Contributions to the Study of Intermittent Contact Haptic Interfaces

Oscar Eduardo de La Cruz Fierro

Sorbonne Université

Doctoral Thesis

Contributions to the Study of Intermittent Contact Haptic Interfaces

by

Oscar Eduardo DE LA CRUZ FIERRO

Thesis submitted in fulfillment of the requirements for the degree of

Doctor of Philosophy

in the Graduate Academic Unit of

Mechanics, Acoustics, Electronics and Robotics Sciences of Paris (ED 391)

Defended on July 8, 2019 before the jury composed of

Thesis Director:	Guillaume Morel, Professor, Sorbonne Université, Paris
Supervisors:	Florian Gosselin, Research Engineer, CEA,LIST, Saclay
	Wael Bachta, Associate Professor, Sorbonne Université, Paris
Reviewers:	Damien Chablat, Research Director, Université de Nantes
	Jean-Pierre Gazeau, Research Engineer, Université de Poitiers
Examiners:	Véronique Perdereau, Professor, Sorbonne Université, Paris
	Nabil Zemiti, Associate Professor, Université de Montpellier

CEA, LIST, Laboratoire de Robotique Interactive
&
Institut des Systèmes Intelligents et de Robotique - Équipe AGATHE

Abstract

Force feedback interfaces are robotic systems allowing natural motion interactions with virtual or remote environments. They are employed in several domains such as remote handling (e.g. nuclear, subsea, space), manufacturing, entertainment, education, medicine and rehabilitation, just to mention the most popular. In virtual reality (VR) applications, the user typically holds a handle that is mechanically linked to the end-effector of the robot. This link has a non-negligible influence since the presence of the robot can be felt (friction, inertia and vibrations of the mechanical structure) even in free space, decreasing the realism of the interaction.

Intermittent-contact haptic interfaces (IC-HIs) represent a promising approach to cope with this issue. These interfaces track and closely follow (without contact) the user movements in free space and come to his/her contact only when force feedback is required. This way IC interfaces aim to improve the realism of the interactions.

The thesis presented concerns the study and improvement of such IC-HIs:

1) First it appeared in our research that the aforementioned improvement of interaction realism has not yet been proven. Indeed, no comparison between classical contact haptic interfaces (CC-HIs) and IC devices had been done so far from a user perception perspective. To this end we decided to perform a series of psychophysical tests based on three elementary VR tasks employing an available state-of-the-art 2 degrees of freedom (DoF) interface that provides finger interactions and allows implementing both CC and IC configurations.

2) Then we noticed that, despite the fact that moving in free space without feeling the presence of the robot invites the user to make faster movements, which in turn tends to produce oscillations when the user avatar enters in contact with virtual objects, this type of movements has attracted, to our knowledge, only little attention in the literature. This prompted us to focus our efforts on the improvement of the control law of the interface, in particular on the transitions between free space and contact modes at high speeds.

3) Finally we noticed that, even though several VR applications are performed by means of a tool (e.g. a virtual scalpel or scissors as in medical simulators), almost all existing IC devices focus on bare fingers interactions. Considering this, and also noticing that tool tracking is far easier than a finger's configuration measurement (variable sizes

and shapes, deformation at contact), we decided to initiate the development of an IC interface allowing tool interactions: the design drivers and sensing approach towards the development of a 6DoF non-contact tool-based tracking system were defined.

Keywords: Haptic interfaces, Virtual reality, Intermittent-contact, Psychophysical tests, Non-contact tracking.

Résumé

Les interfaces à retour d'effort sont des systèmes robotisés permettant d'interagir gestuellement de façon naturelle avec des environnements virtuels ou distants. Ces dispositifs sont utilisés dans différents contextes tels que la téléopération (e.g. nucléaire, sous-marine, spatiale), le manufacturing, les jeux vidéo, l'éducation, la médicine ou la rééducation, pour ne citer que quelques exemples. Pour les applications en réalité virtuelle, les utilisateurs manipulent généralement ces interfaces à l'aide d'une poignée qui est reliée mécaniquement au robot. Ce lien a une influence importante puisqu'il conduit l'utilisateur à ressentir la présence du robot même en espace libre (frottements, vibrations, inertie de la structure mécanique du robot), ce qui réduit le réalisme de l'interaction.

Les interfaces à contacts intermittents (CI) constituent une alternative prometteuse pour essayer de surmonter ces inconvénients. Elles proposent de suivre les mouvements de l'utilisateur à faible distance en espace libre et de ne venir à son contact que lorsque l'on veut appliquer un retour d'effort. Elles visent de cette façon à améliorer le réalisme des interactions.

Cette thèse s'intéresse à l'étude et à l'amélioration des performances d'une telle interface CI :

1) Nous avons tout d'abord constaté que l'amélioration du réalisme des interactions évoqué ci-dessus n'a jamais été prouvé dans la littérature. En effet, il n'existe pas de comparaison entre les interfaces haptiques à contact classique (CC) et les interfaces CI du point de vue de leur perception par les utilisateurs. Nous avons donc décidé d'effectuer une série de tests psychophysiques basés sur la réalisation de trois tâches élémentaires représentatives des interactions usuelles en réalité virtuelle. Ces tests ont été effectués en utilisant une interface existante à 2 degrés de liberté (DdL) permettant d'interagir avec l'index de l'utilisateur et pouvant être utilisée comme une interface CC ou en tant qu'interface CI.

2) Nous avons aussi observé que le fait de se déplacer en espace libre sans ressentir la présence du robot incite les utilisateurs à se déplacer plus rapidement, ce qui a tendance à rendre le robot oscillant lors des contacts entre l'avatar de l'utilisateur et son environnement. Ce type de mouvement n'a pas, à notre connaissance, beaucoup été étudié dans la littérature. Nous avons donc également travaillé sur l'amélioration de la loi de commande de l'interface CI, en particulier lors des transitions entre espace libre et contact.

3) Enfin, nous avons constaté que, bien que différentes applications de réalité virtuelle sont réalisées à l'aide d'un outil (e.g. avec un scalpel ou avec des ciseaux virtuels dans les simulateurs en chirurgie), presque toutes les interfaces CI existantes n'autorisent que des interactions à mains nues. Sur la base de ce constat, et sachant que le tracking d'un outil est beaucoup plus facile que celui des doigts (dimensions et formes variables, déformation au contact) nous avons décidé d'initier le développement d'une interface CI à 6DdL adaptée aux interactions effectuées à l'aide d'un outil. Nous nous sommes plus particulièrement concentrés sur la cahier des charges d'un tel système et sur l'étude des capteurs associés aux système de tracking de l'outil.

Mots clés: Interfaces haptiques, Réalité virtuelle, Contacts intermittents, Tests psychophysiques, Tracking sans contact.

To my family.
To Victor and Lobo.

Acknowledgments

I wish to express my deepest gratitude to my supervisors who gave me the opportunity to undertake this project.

The research work for this doctoral thesis was conducted at the Laboratoire de Robotique Interactive (LRI, Interactive Robotics Laboratory) at the CEA, LIST institute facilities and in collaboration with the Institut des Systèmes Intelligents et de Robotique (ISIR, Institute of Intelligent Systems and Robotics) from Sorbonne Université.

The funding for this project was made possible by the Commissariat à l'énergie atomique et aux énergies alternatives de Saclay (CEA, the French Alternative Energies and Atomic Energy Commision, Center of Saclay) under the scope of a Contrat de Formation par la Recherche grant (CFR, Research Training Contract).

Amongst the numerous individuals and institutions, I would like to express my profound gratitude to the following:

- *Marie-Aude Vitrani* and *Guillame Morel*, for giving me the opportunity to be part of the Assistance to Gesture with Applications to THErapy (AGATHE) team at ISIR as a Research Engineer and for welcoming me during my PhD, a valuable professional opportunity.
- *Guillaume Morel*, Professor at Sorbonne Université and PhD Director, for his interest in the research topic and valuable advice during the development of the project.
- *Wael Wachta*, Associate Professor at Sorbonne Université, for his valuable advice in several technical aspects of the research.
- *Florian Gosselin*, Research Engineer at LRI, for his assiduous supervision and willingness to transmit skillful scientific guidance through these many years.
- *Yann Perrot*, Director of the Laboratoire de Robotique Interactive, for his support to assist to international conferences.
- *Benoît Perochon, Pascal Chambaud, Philippe Pottier, Didier Houche*, permanent members from the Laboratoire de Robotique Interactive, for their support in practical aspects and for the preparation of experiments. I also wish to thank *Elodie Renividaud* for her support in administrative aspects.

- *Michèle Vie, Yves Germain, Ludovic Villard, David Reversat, Florian Richer, Philippe Gauthier*, members of the ISIR Administrative and Engineering staff for their help in administrative aspects during my PhD and technical support during the undertaken experiments at ISIR.

- *Damien Chablat*, Research Director at Université de Nantes, and *Jean-Pierre Gazeau*, Research Engineer at Université de Poitiers, for their keen eye in examining my thesis.

- To my colleagues *Caroline Maureau, Jean-Baptiste Cazneuve, Juan Miguel Alvarez, Omar Islas and Simona Streckaitė*, who contributed by reviewing and providing valuable feedback in their respective technical domains covered under this research.

- Thanks to everyone and to all the personnel who kindly volunteered their valuable time to complete all the proposed user tests.

- To all the people from both laboratories, and beyond, who created a pleasant working atmosphere which made these three years a lively and fulfilling time in my career and left an everlasting memory: *Davinson Castaño-Cano, Juan Miguel Alvarez, Susana Sánchez Restrepo, Ugo Vollhardt, Alexandra dos Santos, Carlos Viña, Omar Islas, Valentin Marcel, Arthur Bouton, Caroline Maureau, Vanessa Zervogianni, Nathaly Ruiz, Alessia Michelotti, Livia Tepshi, Malik Shukeir, Monika Kamińska, Veronica Sorgato, Laure Simon, Jean-Baptiste Cazneuve, Fabien Rodrigues, Bianca Trovo.*

Lastly, I wish to express my warmest thanks to my family, in particular to my parents Blanca Edilia Fierro Rogero and Juan De La Cruz Campa, for their unfailing support and for making me what I am today.

Table of contents

List of figures

List of tables

Introduction

Classical force feedback interfaces, also called here classical-contact haptic interfaces (CC-HIs), are robotic systems allowing natural motion interactions with virtual or remote environments. They are used in several domains such as design, manufacturing, assembly, scientific visualization, entertainment, education, medicine, space, rehabilitation, micromanipulation and molecular biology. In all cases, they should provide adequate kinesthetic (force) feedback, contributing to enhance the sense of presence in the virtual environment.

With CC-HIs, the user is usually mechanically linked to the device's end-effector, typically a handle, whose movements, measured by the robot, are used to know the configuration (position and orientation) of his/her hand. This information is necessary to provide force feedback which is consistent with the virtual scene and the mechanical properties of the virtual object (VO) being touched. The mechanical link that is established when the user manipulates the haptic device has however a non-negligible influence since he/she experiences the friction, inertia and vibrations of the mechanical structure, even in free space where he/she is expected to feel nothing. Such unwanted sensations decrease the realism of the interaction since the user feels all the time the presence of the robot. In addition, the difference between free space and contact is less distinctively felt than in the real world. In order to cope with these issues, several efforts can be made in terms of mechanical design, e.g. use of very lightweight and very stiff structures (even if an optimal trade-off is difficult to attain) and more efficient transmission systems. Another approach consists in installing a force sensor at the level of the robot's end-effector in order to measure and compensate any resisting force in the direction of displacement. However, resisting forces can never be totally cancelled and none of these approaches completely eliminates the feeling of the presence of the robot in free space.

Intermittent-contact haptic interfaces (IC-HIs) represent an original and promising approach aiming to cope with the aforementioned issues. Its principle consists in removing the mechanical link between the human operator and the force feedback interface during manipulations in free space and come at his/her contact only when force feedback is required. This solution implies the need to track and closely follow the user's movements in free space and to prevent him/her to move in the constraint direction when a VO is being touched. This way, the user doesn't feel any force in free space (perfect transparency) and the transitions from free space to contact are deemed to be felt more naturally as

the robot really touches the user at the simulated contact moment. This approach aims to improve the realism of the interactions, however it suffers from several shortcomings. First, its efficiency has not yet been proven in terms of user perception. Second, even if IC interfaces are experimentally proven to be stable at low speeds, they tend to become oscillating at higher speeds. Finally, despite the fact that a lot of tasks are performed by the mean of tools in the real world, most of existing IC-HIs focus on bare finger interactions and are therefore not optimal for simulating tool-mediated tasks.

In the scope of the present PhD work, we propose to systematically address these issues. We first focused our attention on the evaluation of the benefits and identification of the limitations of the IC paradigm based on tests performed with an available state-of-the-art 2 degrees of freedom (DoF) IC-HI that provides finger interactions and allows implementing both CC and IC configurations. Then we worked on the improvement of the stability of such IC interface during interactions at high speeds. Finally, we proposed to extend the IC principle to an interface providing 6DoF interactions through a tool, as it is the case in several virtual reality (VR) applications, e.g. as in medical simulators, overcoming this way some issues associated with finger tracking.

The present PhD dissertation is organized as follows:

Chapter I - Research Context: This chapter introduces the basics of VR and how the human sense of touch contributes in such context to enhance the immersion of the user in a simulated task. Technical specifications of CC interfaces (number of DoF, workspace, inertia, maximum exertable force, etc.) are presented along with the limitations of such devices to provide pure free movements. The IC paradigm is then presented together with developed platforms employing this principle. Its advantages and challenges are also discussed. Finally a description of the performed research based on the IC paradigm is given, focusing on the three above-mentioned key challenges: user perception evaluation, performance improvement for interactions at high speeds and extension of the IC paradigm to tool interactions.

Chapter II - Evaluation of the Benefits of IC-HIs from a User Perception Perspective: IC haptic interfaces aim to provide more realistic interactions with virtual environments since they touch the user only when force feedback is required. This assumption has however not yet been proven. Unfortunately, technical specifications usually available for existing CC and IC interfaces do not allow to directly infer their perceived rendering quality (real interactions and immersion) and do not ensure optimal performances for the completion of a task of interest. Indeed, any evaluation performed without human interaction would not really represent the actual device use. Fortunately, psychophysical tests represent a solution to this problem. They are a useful tool to evaluate the benefits of CC and IC interfaces and compare them. To this end, three psychophysical tests representing elementary VR tasks were performed by a group of volunteers using an available interface that can be configured either as a CC or as an IC interface. The protocol, performance metrics and results are presented for each experiment. Conclusions

and perspectives are also given.

Chapter III - Improvement of Contact Rendering at High Speeds: A good force feedback interface should allow stable interactions, whether the user is moving in free space or getting in touch with a VO. In the case of IC haptic interfaces, this is particularly challenging since, besides displaying a stable behavior in both modes, the control law must ensure a stable transition between free space and contact. Therefore, the IC interface must shift from closely following the user movements to a completely stabilized (usually fixed) position prior to contact. Stable transitions have already been accomplished in a prior work with an existing 2DoF IC interface, but only at speeds up to 0.2m/s. This is a relatively low speed, considering that typical movements in VR environments are performed at speeds up to 4.6m/s, and if the interface is perfectly transparent in free space the user will be tempted to move faster. Being stable only up to 0.2m/s thus limits the scope of possible applications. This chapter presents the contributions made in the control law aiming to improve the free space to contact transitions at higher speeds (tests performed up to ≈ 0.4m/s). In order to evaluate the benefits of the implemented control law, a group of participants was invited to perform a user test consisting in tapping on a vertical wall at low and high speeds. Quantitative and qualitative results are given and discussed. Finally, conclusions and perspectives are drawn.

Chapter IV - Contributions to the Design of an IC-HI Tracking Module for Tool-Based Interactions: The design of an IC haptic interfaces providing finger interactions is particularly challenging due to the variable sizes and shapes of fingers from one person to another as well as deformation at contact. This issue makes tracking of the user particularly complex. Fortunately, several VR applications are performed by means of the manipulation of a tool, e.g. medical simulators, which is much easier to track than fingers (fixed and known geometry, possibility to integrate active components directly in the tool). In this chapter we propose to extend the IC paradigm to a 6DoF tool-based interaction device, which has the advantage of overcoming the above-mentioned issues. An IC device consists in two main parts, a tracking system and a force feedback system. The former system is used to obtain the relative pose (position and orientation) between the user and the robot's end-effector. The later consists in an end-effector which shape and size are suited to provide the corresponding interaction forces at contact. The presented work focused on setting the design specifications of an IC tracking system in terms of dimensions and sensor requirements. Preliminary test and characterization of a proposed sensing strategy are proposed. Finally, conclusions and perspectives are given.

In the very last part of this document, global conclusions and perspectives on the performed work are given.

Chapter 1

Research Context

Contents

1.1 Introduction

In our days, there is an increasing demand for simulators aiming to artificially recreate real world environments. These systems are used for various applications such as assembly verification, e.g. virtually checking that a new system can be easily assembled before launching the production, training, e.g. flight simulators, or simply entertainment, for instance immersive video-games.

An ideal simulation environment should stimulate each one of our senses (sight, hearing, smell and touch) to give us the illusion of being present in the recreated environment (immersion) and allow us to interact with it. However, recreating the corresponding sensations requires complex devices while all of them are not always required.

Indeed, it can be observed in practice that visual and touch feedback are sufficient to cover a wide scope of applications, even when fine interactions are required, e.g. dexterous manipulation of virtual objects (VOs). Visual rendering is obtained with systems ranging from simple monoscopic screens to more complex configurations like head mounted

displays or multi-screen immersive systems such as CAVEs, with techniques allowing to recreate photo-realistic images. The study of the sense of touch is unfortunately less advanced. It is addressed with haptic interfaces, i.e. complex mechatronic devices able to provide either tactile or force feedback.

Force feedback interfaces are widely employed in virtual reality (VR) environments, e.g. for the training of novice surgeons in medicine, for the simulation of a product assembly, for education purposes or for scientific research. However, despite the wide range of applications of these devices, they still require to be improved in order to provide force sensations that are totally realistic.

This chapter introduces our work which, based on these observations focuses on the study of a novel type of force feedback interface aiming to increase the realism of the interactions. It is organized as follows: we will first learn about the concept of VR (see section 1.2), then about the importance of the sense of touch (section 1.3) and how it can be reproduced by force feedback devices to enrich our interaction experience in several VR applications (1.4). Representative characteristics of common force feedback interfaces will be presented in section 1.5, along with the difficulty to obtain a good mechanical transparency (section 1.6). In section 1.7, we will introduce intermittent contact haptic interfaces, a relatively novel and very promising approach aiming to cope with this issue. Finally, we will show in section 1.8 that these systems still suffer from several shortcomings and we will introduce the proposed research.

1.2 Virtual reality

Even though virtual reality sounds as a very modern concept, it has been around for more than half a century.

VR accounts for an interactive computer simulation allowing the user to visualize a virtual environment (VE) which recreates a scene of the real world. Interactive means that such simulation acquires, by means of a tracking system, information on the user's state and is able to provide sensory feedback to one or more senses. The main objective is to make the user feel as being immersed in the VE [Mihelj et al., 2014].

Four basic characteristic elements of VR can be identified: the virtual world (or VE), immersion, sensory feedback (as a response to user's actions) and interactivity.

- A computer-based **VE** contains the description of the simulated objects as well as the rules governing their interactions, e.g. the effect of gravity making virtual objects to fall as it does with those in the real life [Mihelj et al., 2014].

- In the present context, **immersion** implies the notion of "being present" in the VE. In simple words, it is the belief of having left the real world to be "present" inside the VE.

Immersion can be achieved if the VR system is able to provide realistic stimuli to all human senses [Mestre, 2015].

- **Sensory feedback** requires proper displays, e.g. a head-mounted display (HMD, see Fig.1.1 and Fig.1.2) able to visually immerse the user in the virtual world, and a force feedback interface, hold by the user, that will apply on him/her the forces generated when VOs are being touched.

- Finally, **interactivity** refers mainly to the fact that the VE is responsive to the user's actions (inputs). It requires a tracking system able to determine the movements of the user to ensure consistency between the real world and the VE. As an example, the visualized scene will adapt so that the user has the impression to move inside the VE.

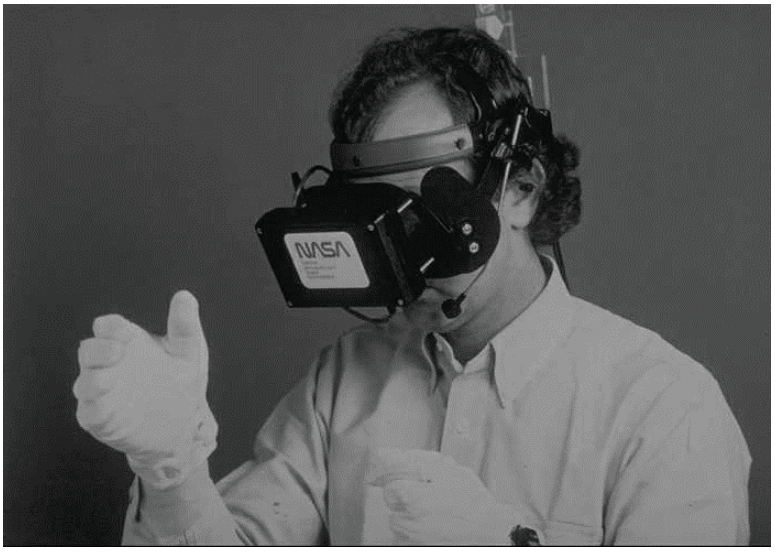

Figure 1.1: NASA's first HDM [Mestre, 2017].

Figure 1.2: Classic HMD and VR glove environment [Havig et al., 2011].

The first practical implementation of the VR paradigm was developed in 1957 and patented in 1962 by Morton Heilig, who is considered as the father of VR. In such a system, known as Sensorama (see Fig.1.3), a single person could perceive, e.g. a motorcycle ride through a city via sight, smell, vibration and wind [Sherman and Craig, 2003].

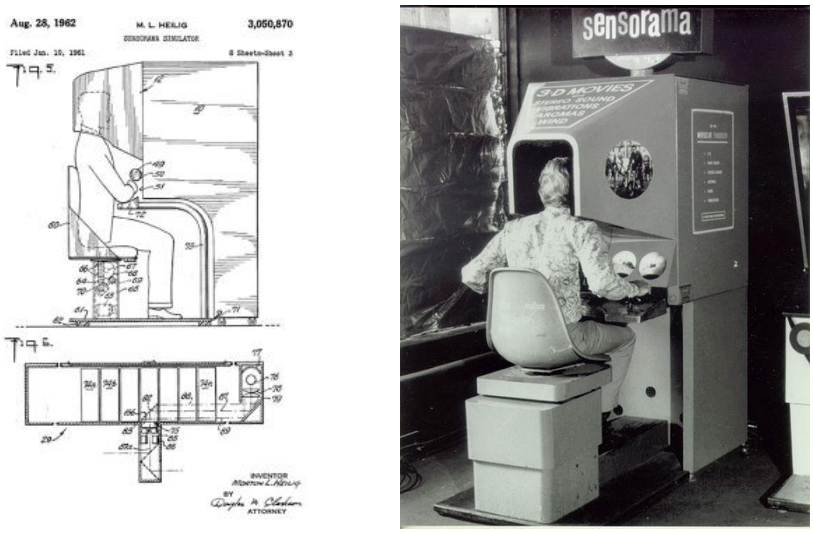

Figure 1.3: First developed and patented VR system.

Several other VR systems were developed. The GROPE I to III systems, created in the late 60s and early 70s, allowed the user to move and feel interaction forces between molecules thanks to a haptic interface (see Fig.1.4). Other examples of VR applications using force feedback will be described in section 1.4.

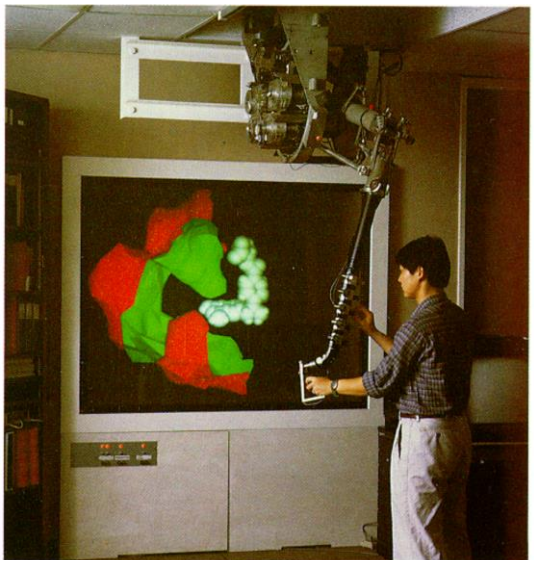

Figure 1.4: GROPE-III haptic display system [Brooks et al., 1990].

As stated in the above paragraphs, one of the main goals of a VR system is to create the sensation of "presence". A step forward in this direction was achieved during the 90s

with the concept of CAVE (Cave Automatic Virtual Environment). It consists of a room whose walls are in fact screens displaying a VE (see Fig.1.5).

Figure 1.5: Example of a CAVE [Havig et al., 2011].

This technology is however very expensive and requires an important volume to be installed, e.g. four equally sized walls of $\approx 1.8\text{m} \times 1.8\text{m}$. As a consequence, the current tendency is to use HMDs instead. This technology have made huge progress in the recent years and is now both efficient and affordable (see Fig.1.6).

HTC VIVE Oculus Rift

Figure 1.6: Commercial HMDs.

Another important concept in VR applications is the notion of **avatar**, which is the virtual representation, for instance, of a human being as well as objects of interest regarding the task or the scene (see Fig.1.7). Finally, figure 1.8 shows how the aforementioned elements are linked.

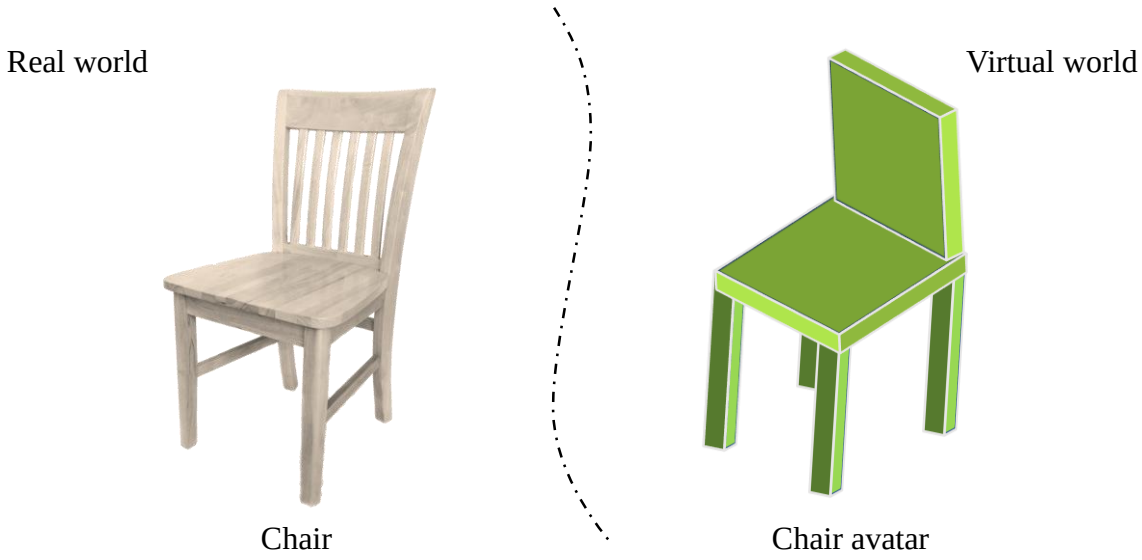

Figure 1.7: Avatar principle.

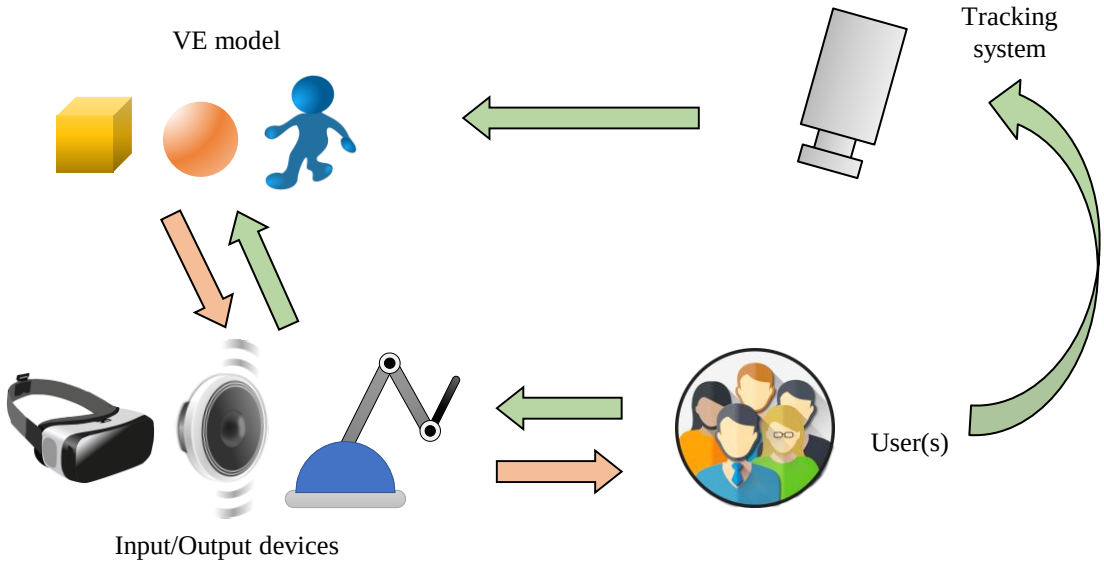

Figure 1.8: VR feedback loop.

The following section will provide an insight on the importance of the sense of touch and, in particular, the role it plays when non-direct manipulation of remote/virtual objects and interaction with VEs takes place.

1.3 Sense of touch and haptic feedback

The sense of touch is of capital importance for our everyday lives. Its lack would make us experience serious difficulties when performing tasks such as grasping and manipulating tools or working in contact with surrounding objects [Robles-De-La-Torre, 2006]. Thanks to this sense, which gives us the ability to perceive the environment physical characteristics

(shape, size, texture) and regulate the forces that we apply on it, we are able to perform a wide scope of tasks with high level of dexterity.

In some circumstances however, the human operator cannot be in direct contact with the object being manipulated, e.g. because the environment is hostile (nuclear, underwater, space) or because it is inaccessible at the user's scale (micromanipulation, microsurgery). In such cases the task can be accomplished by means of a teleoperated system, i.e. a remote robot mimicking the movements of a master arm manipulated by the operator. The ability to control the movements of a remote system is also of great value in VR, the user remotely controlling virtual avatars instead of robots in this case.

The concepts of teleoperation (manipulation of a remote robotic system), VR (controlling a virtual avatar) and telepresence (allowing a person to feel as if he/she were present at a place different from his/her current location) have accentuated the importance for the development of systems that allow a human operator to sense the physical characteristics and forces applied on the objects being remotely (see Fig.1.9a) or virtually (see Fig.1.9b) manipulated [Bergamasco, 1995], i.e. by means of haptic interfaces.

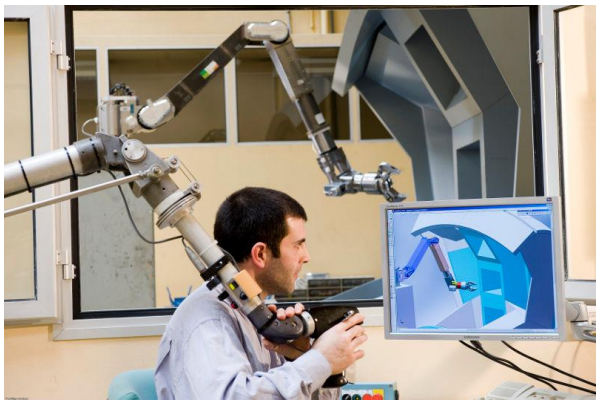

(a) Teleoperation master arm with force feedback in a nuclear context (©CEA/Stropa)

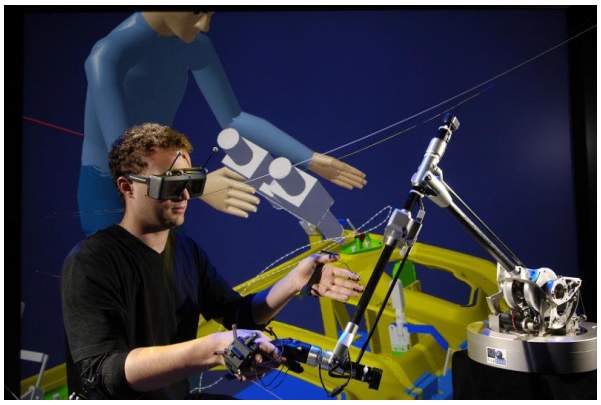

(b) VR assembly testing for the automotive industry (©CEA/Stropa)

Figure 1.9: Teleoperated and virtual reality (VR) systems using force feedback.

Haptics was defined as a "perceptual system that uses both cutaneous (including thermal) and kinesthetic inputs to derive information about objects, their properties, and their spatial layout" [Lederman and Klatzky, 1990]. To stimulate this sense, the user requires dedicated devices called haptic interfaces, i.e. devices allowing motion interactions with remote/virtual environments with a reproduction of the sense of touch, using kinesthetic (force/position) and cutaneous (tactile) receptors [Hannaford and Okamura, 2016].

We can distinguish four methods for creating haptic sensations artificially: vibrotactile devices, force feedback systems, surface displays and distributed tactile displays [Hayward and Maclean, 2007]. The scope of the present work is limited to the force feedback devices category. The following section will describe their main applications with a focus on VR, which is of particular interest for the present work.

1.4 Force feedback devices application examples

Force feedback interfaces find applications in numerous domains (most of them using VR) such as design, manufacturing, assembly, scientific visualization, entertainment, education, medicine, space, rehabilitation, micromanipulation, as well as molecular biology [Hannaford and Okamura, 2016]. The interface should then provide adequate kinesthetic information contributing to enhance the sense of presence in the VE [Reiner, 2004].

In the fields of **design**, **manufacturing** and **assembly**, haptic feedback can contribute to change traditional product development approaches by allowing the users to get the feeling of touching objects, perceiving the nature of their surfaces and their dynamics before producing any real prototype [Xia, 2016]. This way, users can gain a comprehensive understanding and accurate evaluation of the design and manufacturing process (see Fig.1.10a).

In **scientific visualization** (see Fig.1.10b), haptic devices can be used to simulate object's physical properties, e.g. texture and/or interaction forces. This allows direct and immediate control over simulations as well as sensing of the results of the scenario of interest [M. and Taylor, 2005].

The **entertainment** industry has also beneficiated from haptic developments. Force feedback technology enhances the game experience by providing more realistic sensations while playing a game [Orozco et al., 2012].

Haptics is also of great interest in **education**. For example, a multimedia system for learning handwriting of alphabet letters/characters in different languages can make use of a haptic device to provide force feedback to guide the user's gesture at following a pre-recorded letter trajectory (see Fig.1.10c).

In **medicine** also, VR simulation-based training appears as a promising solution for skill transfer. Novice surgeons can acquire and/or improve their skills before operating on a real patient and experienced surgeons can learn new techniques and even rehearse when the patient to operate presents a complicated surgery case (see Fig.1.10d), e.g. a congenital anomaly or a known difficult anatomy [Aggarwal and Ara, 2009].

Force feedback interfaces can also be used to intelligently **guide**/**regulate** the motion of the user during an operation [Bowyer et al., 2014], e.g. preventing the user to move towards a restricted region, contributing that way to improve the security of the patient and postoperative results.

More generally, **robot-assisted minimally invasive surgery** (RMIS) offers advantages to patients such as less trauma, shorter hospital stay and reduced recovery times [Westebring et al., 2008]. Robots in master-slave configuration can cope with motion constraints of surgical instruments, improving surgeon's dexterity [Puangmali et al., 2008]. The surgeon is expected to act and feel as if he/she were holding directly the surgical

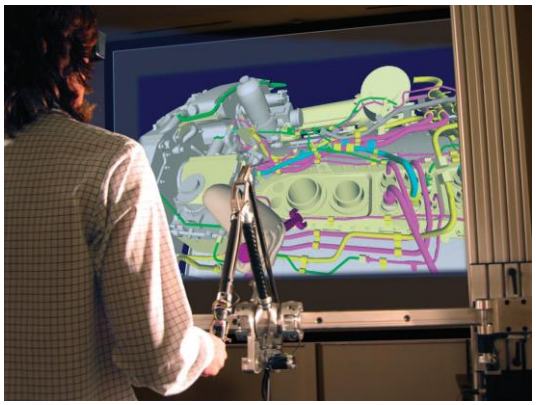

(a)Virtual aircraft engine maintenability operation

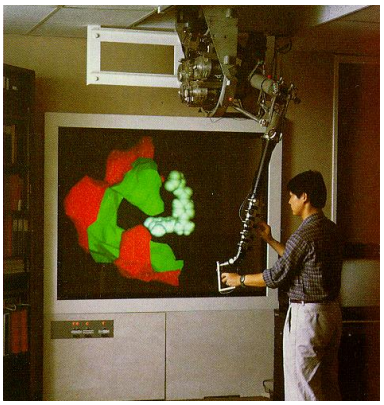

(b) GROPE III system used for scientific visualization

(c) Telemaque platform used for children's handwriting acquisition

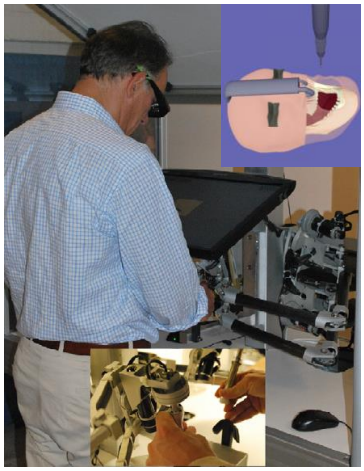

(d) Training platform for maxillo facial surgery

(e) MIT MANUS for shoulder rehabilitation

(f) HUG for VR on-orbit servicing missions

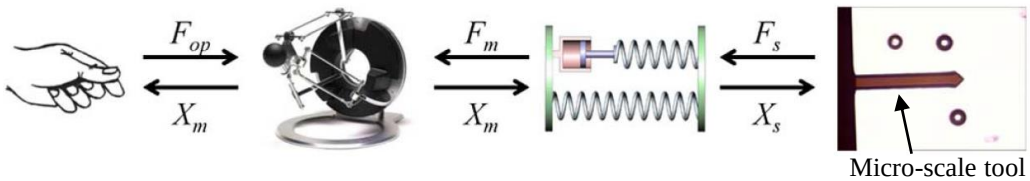

(g) Teleoperation for micromanipulation

Figure 1.10: Applications of force feedback interfaces: (a) [Borro et al., 2004], (b) [Brooks et al., 1990], (c) [Palluel-Germain et al., 2007], (d) [Gosselin et al., 2013], (e) [Burdea, 2008], (f) [Sagardia et al., 2015] and (g) [Bolopion and Régnier, 2013].

tools being in contact with the patient. In such scenarios, any strategy to estimate/ sense the applied force is expected to improve the accuracy and dexterity of the surgeon [Okamura, 2009] and therefore reduce the tissue trauma and organic damage. The development of force sensors for RMIS is thus still an active research topic as reported in [Puangmali et al., 2008].

One can also refer to physical rehabilitation which is a growing field of use for haptic interfaces. Unlike a human therapist, robots can train patients for long periods of time without tiring. Robotic systems coupled with VR simulations also bring additional improvements to today's conventional physical therapy methods, since they introduce objective measures of performance (see Fig.1.10e).

Space is an environment inaccessible to humans where force feedback systems can contribute to train operators and help them performing maintenance, reparation or exploration tasks while preventing and reducing risks. In [Sagardia et al., 2015] for instance, a VR platform for telerobotic on-orbit servicing missions helps to train users (providing visual and haptic feedback) for satellite maintenance tasks (see Fig.1.10f).

When it comes to manipulation of tiny objects, haptic systems allowing the user to interact with objects at the micro scale are needed (see Fig.1.10g). In **molecular biology** for example, the size and complexity of molecular structures make it difficult, if not impossible, to show all of their features in a physical model alone. In combination with augmented reality (AR) and voice commands, haptic feedback provides additional information about these models using a force display [Sankaranarayanan et al., 2003].

All the above mentioned applications require a device compatible with the targeted task. Several examples of such devices are presented in section 1.5, with focus on commercially available interfaces.

1.5 Commercially available force feedback interfaces

Force feedback systems are robotic mechanisms capable to measure the user's movements, this information being used to control the movements of his/her avatar, and deliver a force signal to his/her hand, usually through a stylus or a thimble [Campion, 2011].

The realism of the interaction is strictly related to the capabilities of the device to allow natural movements of the human operator's hands as well as to reproduce adequate stimuli on them. An ideal force feedback system should be transparent: the user should be able to move in free-space without feeling any force, i.e. to make pure free movements, and the device should prevent him/her to move in the constraint direction if a stiff object is being touched, i.e. the device should be able to simulate any type of contacts, even hard ones [Couroussé, 2007].

It is worth noting that a perfect transparency cannot be attained in practice. Fortunately, most of the time it is not necessary to reproduce the whole bunch of physical interactions experienced everyday, and force feedback interfaces can be tuned to the requirements of the tasks of interest. It is thus important to identify what sources of kinesthetic information are relevant for the targeted tasks, and which degree of fidelity is needed [Robles-De-La-Torre, 2006].

Several performance metrics are usually employed to qualify a force feedback interface: workspace, position resolution, continuous force, peak force, friction, apparent stiffness, apparent inertia and bandwidth. All these notions, defined below with reference to e.g. [MPB Technologies Inc., 2018b] contribute to the transparency of the device.

- The **workspace** is the volume that the device can cover, considering both translations (ranges usually expressed in the Cartesian space in mm, cm or m) and rotations (ranges usually expressed in degrees in yaw, pitch and roll).
- The **position resolution** is the smallest amount of movement which can be detected by the arm sensors. It is usually expressed at the level of the handle (i.e. in the Cartesian space) in μm or mm in translation and in degrees or radians for the rotations.
- The **continuous force** is the amount of force/torque that the device can exert for an extended period of time. It is usually expressed in the Cartesian space in N for the translations and in N.m for the rotations.
- The **peak force** is the maximum force that the actuators can exert, e.g. over a small period of time. The peak force can typically be between 2 and 10 times higher than the continuous force for typical actuators usually implemented in force feedback interfaces, allowing to momentarily stop the user against the environment, e.g. when taping or touching a hard object.
- The **friction** is a measure of the resistance of the device to movement. It is expressed in N for translations and N.m for rotations. It should be as low as possible.
- The **apparent stiffness** is the maximum stiffness that can be simulated by the device. It informs on the different types of objects that can be simulated. Indeed many objects in VR environments behave like a spring, i.e. they deform linearly in response to an external force. The apparent stiffness is expressed in N/m for translations and N.m/rad for rotations. The higher it is, the better solid virtual walls can be simulated.
- The **apparent inertia** is a measure of the mass (in kg) and inertia (in kg.cm^2) that is sensed by the user when he/she tries to move the handle of the robot. It should be as low as possible in order to give him/her the impression that he/she moves freely in free space.
- The **bandwidth** is the frequency (in Hz) up to which the device can be properly controlled. It should not be confused with the update frequency of the controller nor

with the bandwidth of the human somatosensory system, i.e. about $300 - 1000$Hz for tactile sensing and $20 - 30$Hz for kinesthetic and proprioceptive sensing.

It is worth noting that, even if the afore-mentioned data are usually given in the Cartesian space, this information can be given instead in the joint space.

Six main manufacturers were identified in the market: 3D Systems, Force Dimension, Haption S.A., Quanser, MOOG Inc. and MPB Technologies Inc. Representative examples of their products will be briefly described below.

The **Touch** device (see Fig.1.11a, left) is a desktop interface providing 3DoF force feedback. This low power device can be used in several applications, including 3D modeling, training, skill evaluation, virtual assembly and robotic control [3D Systems, 2018]. The premium series provide 6 active DoF and cover a vast range of research and commercial applications, e.g. virtual prototyping, maintenance path planning and molecular modeling applications. Within this category, the **Phantom Premium 3.0** provides a range of motion compatible with full arm movement pivoting at the shoulder (see Fig.1.11a, right).

The **omega.6** (see Fig.1.11b,left) provides 3DoF force feedback. It is considered by Force Dimension as the most advanced pen-shaped force feedback device available. Focused on ergonomics, this device enables the rendering of high contact forces and high stiffness thanks to an update rate of 4kHz. The **sigma.7** (see Fig.1.11b, right) is a high-sensitivity 7 active DoF device from Force Dimension that can be used in applications including medical and space robotics, micro and nano manipulation, bi-manual teleoperation, virtual simulations, training systems and research [Force Dimension, 2018].

Haption S.A. provides a wide range of high performance force feedback interfaces. It proposes 3 or 6 DoF devices like the **Virtuose 3D Desktop** (see Fig.1.11c, left) and the **Virtuose 6D TAO** that can be used for VR and teleoperation applications (see Fig.1.11c, right). It is particularly well suited for scale 1 virtual/remote manipulations. It is also used for comanipulation in laparoscopic surgery as well as in rehabilitation [Haption, 2018].

The **High Definition Haptic Device** (HD^2) from Quanser (see Fig.1.11d) is a high-fidelity 6DoF haptic interface for advanced research in haptics and robotics. It is particularly suitable for the development of test beds for various emerging applications such as medical simulators and teleoperation. This haptic interface can track the operator's motion in 6DoF and apply force to the user in 5DoF [Quanser Inc., 2018].

The **Desktop Haptic Interface** from MOOG, Inc. (see Fig.1.11e) is a general purpose haptic interface, providing force feedback in 3DoF. Its admittance control allows to provide realistic crisp touch and feel [MOOG, 2018].

Finally, the **Freedom 6S** (see Fig.1.11f) from MPB Technologies Inc. is a high-fidelity force feedback device operating in 6DoF, providing the user with the sense of touch in both virtual and real-world applications. It is ideally suited for medical and master/slave

robotics [MPB Technologies Inc., 2018a].

The main technical specifications of the above presented force feedback devices are detailed in table 1.1. It is worth noting that the development of haptic devices is part of an increasing market. More and more applications are being imagined every day, generating the continuous need for novel devices.

(a) Touch and Phantom Premium 3.0
from 3D Systems, U.S.A.

(b) omega.6 and sigma.7
from Force Dimension, Switzerland

(c) Virtuose 3D Desktop and Virtuose 6D TAO
from Haption S.A., France

(d) HD2 High Definition Haptic Device
from Quanser, Canada

(e) Desktop Haptic Interface
from MOOG, Inc., U.S.A.

(f) Freedom 6S from MPB
Technologies Inc., Canada

Figure 1.11: Examples of common commercial force feedback interfaces.

Table 1.1: Characteristics of commercial force feedback interfaces. Here the "Ø" (diameter) symbol indicates that the workspace is roughly cylindrical in shape. In the third column, the upper number indicates the total number of (sensed) DoFs, the second one the number of active (motorized) DoFs.

Device	Workspace	DoF	Exertable force	Stiffness	Resolution	Apparent inertia	Friction
Touch	*Translational* >160 x 120 x 70 mm	6 3	*Translational* 3.3N (peak)	*Translational* > 1260 N/m (x) > 2310 N/m (y) > 1020 N/m (z)	*Translational* ≈ 0.055mm		
Phantom Premium 3.0	*Translational* 838 x 584 x 406 mm *Rotational* Yaw - 297° Pitch - 260° Roll - 335°	6 6	*Translational* 22N (peak) *Rotational* Yaw - 515mN.m (peak) Pitch - 515mN.m (peak) Roll - 170mN.m (peak)	*Translational* 1000N/m	*Translational* ≈ 0.02mm *Rotational* Yaw - 0.0023° Pitch - 0.0023° Roll - 0.0080°	-	-
omega.6	*Translational* Ø 160 x 110 mm *Rotational* Yaw - 240° Pitch - 140° Roll - 320°	6 3	*Translational* 12N (cont.)	*Translational* 14500N/m	*Translational* < 0.01mm *Rotational* 0.09°	-	-
sigma.7	*Translational* Ø 190 x 130 mm *Rotational* Yaw - 235x 200° Pitch - 140° Roll - 200° *Grasping* 25mm	7 7	*Translational* 20N (cont.) *Rotational* 400mN.m (cont.) *Grasping* ±8N (cont.)	-	*Translational* 0.0015mm *Rotational* 0.013° *Grasping* 0.006mm	-	-
Virtuose 3D Desktop	*Translational* 520 x 220 x 400 mm *Rotational* 270 x 120 x 250°	6 3	*Translational* 10N/3N (peak/cont.)	*Translational* 1000N/m (peak)	*Translational* 0.023mm *Rotational* 0.35°	-	-
Virtuose 6D TAO	*Translational* 1070 x 458 x 820 mm *Rotational* 330 x 130 x 270°	7 6	*Translational* 42/12N (peak/cont.) *Rotational* 5/1.4N.m (peak/cont.)	*Translational* 2000N/m (peak) *Rotational* 40 N.m/rad (peak)	*Translational* 0.013mm *Rotational* 0.0018°	-	-
HD² / Quanser	*Translational* x: 800 mm y: 250 mm z: 350 mm *Rotational* Yaw – cont. Pitch & Roll - 180°	6 6	*Translational* x: 19.71/10.84N (peak/cont.) y: 19.71/10.84N (peak/cont.) z: 13.94/7.67N (peak/cont.) *Rotational* Yaw, Pitch and Roll 1.72/0.948N.m (peak/cont.)	*Translational* x: 3000N/m y: 3000N/m z: 3000N/m *Rotational* Yaw - 0.05N.m/rad Pitch and Roll – 3.4 N.m/rad	*Translational* x: 0.051mm y: 0.051mm z: 0.051mm *Rotational* Yaw - 0.088° Pitch and Roll – 0.033°	*Translational* x: 300g y: 300g z: 300g *Rotational* Yaw - 0.79g.m² Pitch and Roll – 2.29g.m²	*Translational* x: 0.353N y: 0.353N z: 0.353N *Rotational* Yaw - 0.5N/mm Pitch and Roll – 61.775N/m
Desktop Haptic Interface	*Translational* 70 x 60 x 60 mm *Rotational* Pitch - 130° Roll - 200°	7 3	*Translational* 10/4N (peak/cont.)	*Translational* 1000N/m	*Translational* 10µm	*Translational* 0.1kg	-
Freedom 6S	*Translational* 170 x 220 x 330 mm *Rotational* Yaw - 130° Pitch - 170° Roll - 340°	6 6	*Translational* 2.5/0.6N (peak/cont.) *Rotational* Yaw - 310/88mN.m (peak/cont.) Pitch - 370/105mN.m (peak/cont.) Roll - 150/44mN.m (peak/cont.)	*Translational* 2000N/m *Rotational* Yaw - 2.5N.m/rad Pitch - 4.0N.m/rad Roll - 0.2N.m/rad	*Translational* 2µm *Rotational* Yaw - 0.001° Pitch - 0.001° Roll - 0.001°	*Translational* 125g *Rotational* Yaw - 0.03g.m² Pitch - 0.04g.m² Roll - 0.003g.m²	*Translational* 40mN *Rotational* Yaw - 2mN.m Pitch - 5mN.m Roll - 1mN.m

1.6 Limitations of existing haptic interfaces

As mentioned earlier, the apparent mass of haptic interfaces, as well as their friction, should be as low as possible, in order that the user doesn't feel the presence of the robot in free space. All existing devices were designed to answer this need. However, as can be seen in table 1.1, their values are not negligible. As a consequence, a perfect transparency is not attained.

Transparency in free space could be improved by implementing accompanying control strategies, e.g. measure the force exerted by the operator and exert an additional force in the direction of movement [Diaz et al., 2010]. Such solutions have however their limits and inertia and friction cannot be totally cancelled.

Part of the problem is related to the fact that force feedback interfaces usually require the user to be **mechanically linked** to them in order to know the user's position and provide force feedback that is consistent with the virtual scene. This link has a non-negligible influence as the user experiences the **friction**, **inertia** and **vibrations** of the mechanical structure even when moving in free space. In this case the difference between free space and contact is less distinctively felt and muscular fatigue is expected to appear in case of long manipulations.

Medical simulators are particularly sensitive to this issue. In dentistry training for example, the need for the simulation of hard teeth (high stiffness) and light tools (low inertia) places a great challenge in the design of force feedback interfaces [Zhang et al., 2017].

A relatively novel paradigm known as intermittent-contact aims to cope with the limitations of conventional devices in order to improve the realism of the haptic interaction and relief the user when long manipulations take place. Its principle and the advances in this field of research will be described in the next section 1.7.

1.7 Intermittent-contact paradigm

The intermittent-contact (IC) paradigm proposes to remove the mechanical link between the interface and the user in free space, obtaining a perfect transparency and letting the user touch the haptic device only when a contact occurs in the VE. This way, intermittent-contact haptic interfaces (IC-HIs) aim to improve the realism of the haptic interaction.

Two categories of devices implementing the IC paradigm can be identified. The first one is known as Encountered-Type haptic interfaces (ET-HIs) and the second one as Close-Tracking-type haptic interfaces (CT-HIs). In the former, a robot manipulator, which end-effector has the shape of the simulated object, is controlled to make it be encountered the user's hand at the position where the VO is found. In the later, the device follows the user at a short and constant distance, without contact, and touches him/her only when a VO is reached.

These devices are particularly interesting to reduce the fatigue during long manipulations and to perceive small interaction forces as it is the case in medicine, e.g. the force applied on an organ. Their principle and relevance will be discussed in sections 1.7.1 and 1.7.2 respectively.

1.7.1 Encountered-type haptic interfaces

The ET-HI principle consists in imagining that the virtual space is superimposed with the real environment. The robot is then controlled to be positioned along its surface at the nearest position of the user's hand and simulate the VO properties (see Fig.1.12). This way, the user remains away from the robot in free space and he/she touches its end-effector only when and where he/she is supposed to touch the VO, a perfect transparency is therefore achieved. To do this, the user's position must be tracked, e.g. using video

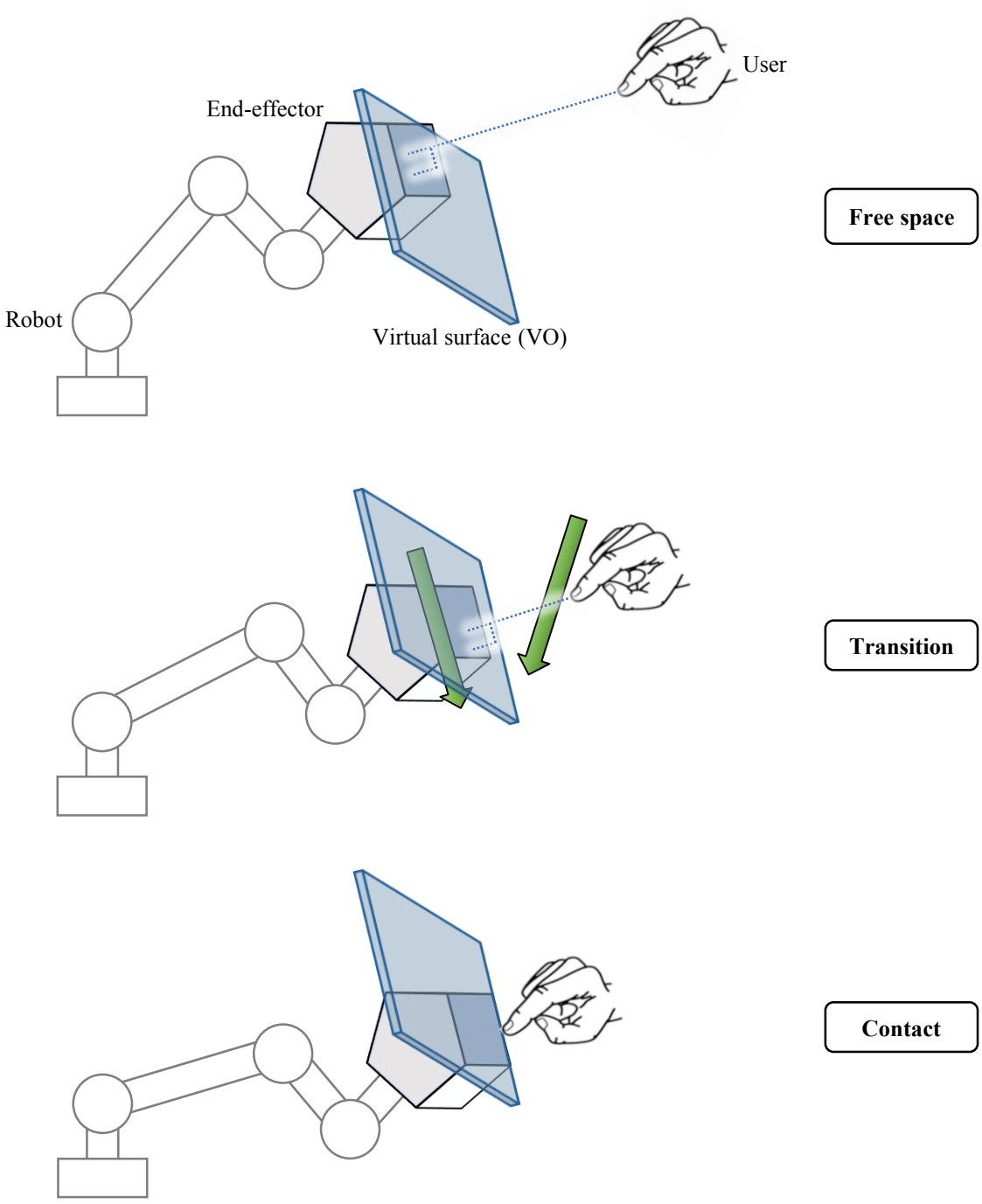

Figure 1.12: Encountered-type haptic interfaces functioning principle.

cameras or body-mounted position tracking sensors, and the robot must be controlled so that it can rapidly and accurately anticipate the user's movement intentions.

The ET-HI approach was first proposed in [McNeely, 1993]: a robot manipulator, which end-effector has the shape of the simulated object, is controlled to make it encounter the user's hand at the position where the VO is expected to be found. This way the user is totally free in free space and he/she can feel the corresponding interaction forces.

The ET-HI approach was also used in [Tachi et al., 1994] for the construction of a haptic space: the user's arm motion is measured by a passive master arm, allowing to compute the position and orientation of the user's fingertip. This information is used by a computer to calculate the nearest object to the user's hand in the virtual haptic space (see Fig.1.13). The local geometry of the simulated object near the contact point and its mechanical impedance are displayed by a 6DoF impedance controlled manipulator and a shape approximation device (SAD). The SAD possesses curved surfaces as well as convex and concave edges and its positioning and orientation are modified in order to simulate the desired object configuration.

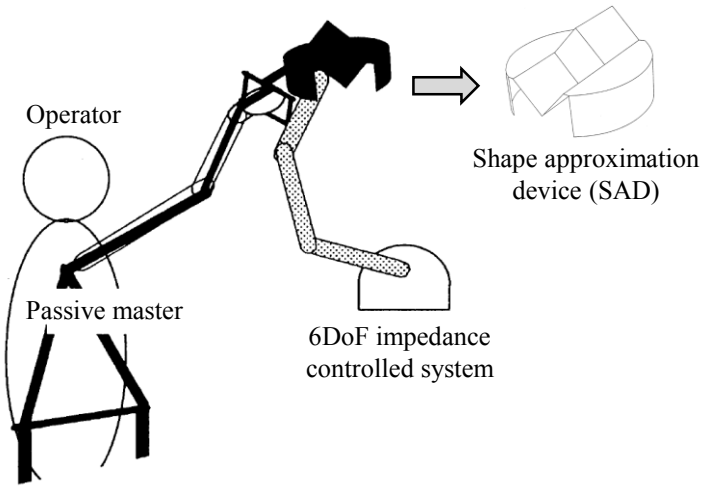

Figure 1.13: Virtual haptic space representation (adapted from [Tachi et al., 1994]).

Another ET-HI system was proposed in [Yokokohji et al., 1996, Yokokohji et al., 1999]. Called WYSIWYF (What You can See Is What You can Feel), this concept allows the user to feel the object precisely where the user sees it. Employing vision-based tracking, the system can blend live video with the virtual scene, i.e. a portion of the user's hand is extracted from the captured image and is superimposed on the virtual scene (see Fig.1.14).

In [Yokokohji et al., 2004], an ET-HI device allowing the simulation of precision grasping tasks using three fingers (thumb, index and middle fingers) was presented (see Fig.1.15). The system consists of two modules, a base module composed of a robot manipulator (see Fig.1.15a) and a specifically designed contact module for finger interaction (see Fig.1.15b), together accounting for the necessary number of DoF to place a local surface patch any-

where in space. The positioning and orientation of the system are predicted based on the measure of the wrist speed profile and aperture distance between the fingers.

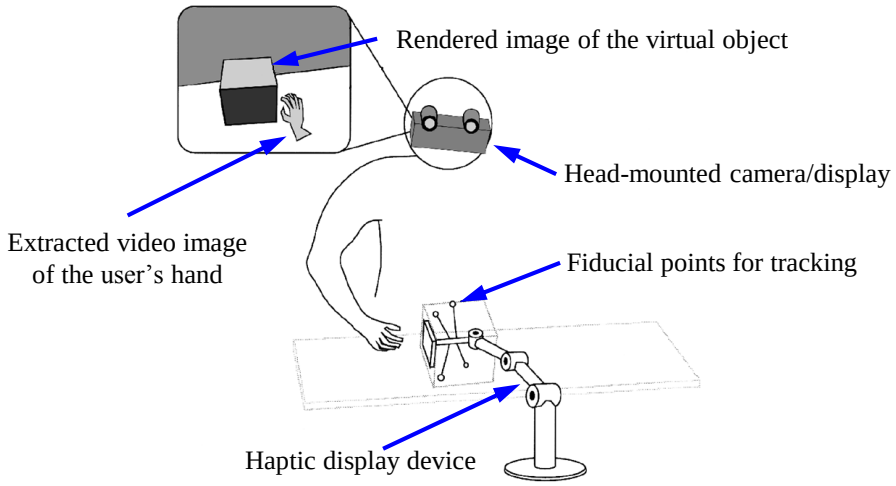

Figure 1.14: WYSIWYF system (adapted from [Yokokohji et al., 1999]).

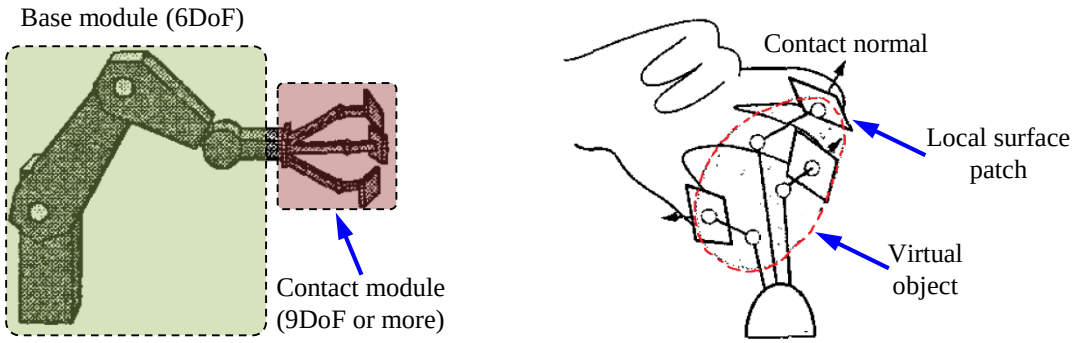

(a) System modules

(b) Contact module diagram

Figure 1.15: Multiple finger ET-HI (adapted from [Yokokohji et al., 2004]).

When working with ET-HI devices, the user's hand is a kind of moving obstacle (see Fig.1.16a) that should be avoided (see Fig.1.16b). Miscalculations or system slowness can lead to painful collisions. In order to cope with this issue, path planning techniques are necessary.

In [Yokokohji et al., 2001], a path planning algorithm for ET-HI devices that renders multiple VOs in 3D space was proposed. Here a convex polyhedron is constructed from the reference points of the virtual objects (see Fig.1.16c). As long as the user's hand is outside the polyhedron, the device stays on its surface. On the other hand, if the user's hand penetrates in it, the device avoids the user's hand and goes inside the polyhedron if necessary. Such algorithm not only considered the security of the user but also the efficiency of the device movement.

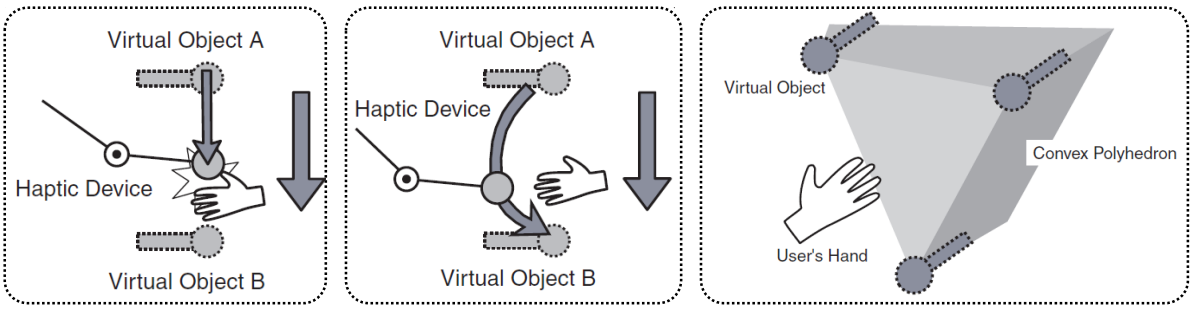

(a) Collisions with careless path-planning

(b) Collission avoidance

(c) Polyhedron principle

Figure 1.16: Path-planning issue in ET-HIs (adapted from [Yokokohji et al., 2001]).

As previously explained, ET-HIs have the advantage over classical type haptic interfaces to be perfectly transparent in free space as they are not at all in contact with the user's hand. With this approach however, the robot may reach very high speeds, which is dangerous for the user, e.g. if bilateral contacts with concave surfaces have to be simulated. Another issue is that the amount of objects that can be simulated is limited to a restricted set of pre-manufactured objects, which often display only very simple mathematical shapes. Despite these limitations, this approach recently found a regain of interest as exemplified by the Lobby-Bot platform from Clarte [Clarte, 2018] used for testing the perception of different materials (see Fig.1.17).

Figure 1.17: LobbyBot ET-HI system.

1.7.2 Close-tracking-type haptic interfaces

The CT-HI approach is another way to implement the IC paradigm. Contrary to the ET-HI principle where the device follows the surface of the VO, it proposes to let

the device follow the user at a short and constant distance, without contact, and touch him/her only when a VO is reached (see Fig.1.18).

The CT-HI principle requires to measure the distance between the device and the user's body (typically his/her finger), using e.g. sensors installed on the end-effector. The device will then closely follow the user's movements without any path planning as long as the user remains in the reachable volume (workspace) of the interface. Despite this limitation, the security of the user is improved. Several examples of such devices will be given below.

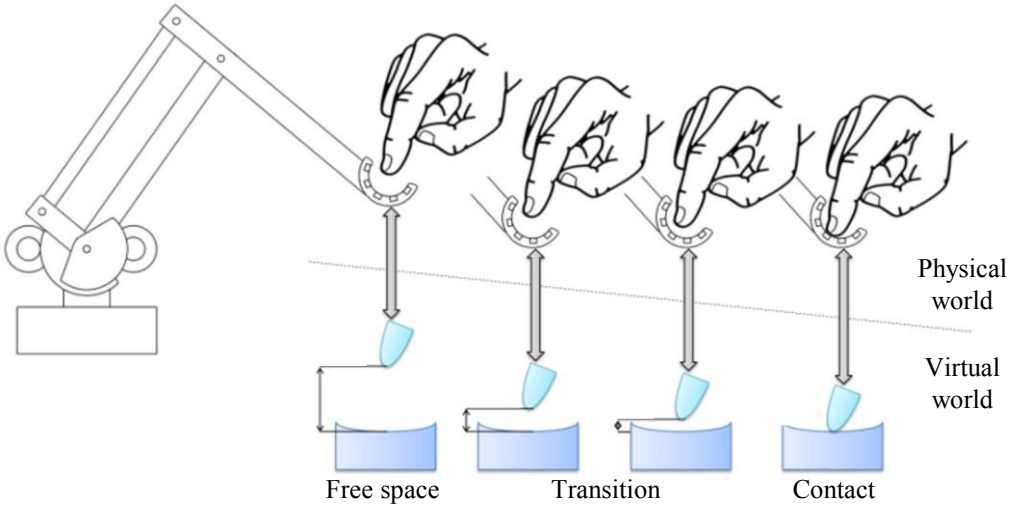

Figure 1.18: Close-tracking-type haptic interfaces functioning principle.

In [Hirota and Hirose, 1993], the existence of an object is simulated thanks to a mechanism for surface displaying (see Fig.1.19). 3DoF tracking of the index finger is accomplished by means of magnetic sensors integrated in a moving head and magnets mounted on the finger (see Fig.1.19a). When the finger is being displaced in free space (i.e. no VO is being touched), the moving force feedback head follows it (tracking mode).

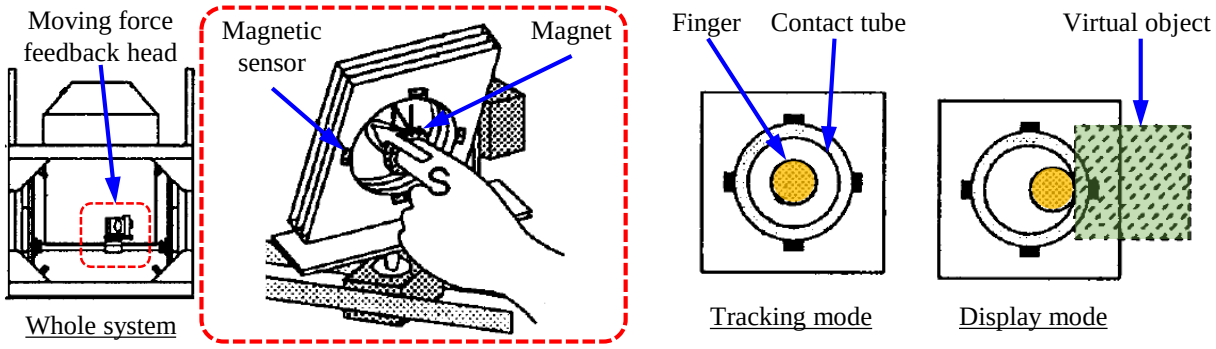

(a) Detail of force feedback head

(b) Control

Figure 1.19: Surface display (adapted from [Hirota and Hirose, 1993]).

When a VO is about to be touched, the display mode is activated, the force feedback head stops at the VO position and waits for the finger to contact its inner surface composed of a tube (see Fig.1.19b).

In [Yoshikawa and Nagura, 1997], a 2DoF arm (see Fig.1.20a) allows finger interaction with virtual worlds thanks to a ring-like end-effector equipped with a set of eight light-weight optical on-off sensors used to roughly estimate the fingertip position in the ring (see Fig.1.20b). When the finger is far away from a VO, the ring's position is controlled to keep the fingertip in its center. When the fingertip is near a VO, the ring moves closer to it. Finally, when the fingertip is in touch with a VO the display mode is activated (see Fig.1.20c). A force sensor placed between the ring and the tip of the arm allows then to measure the force applied by the arm on the fingertip.

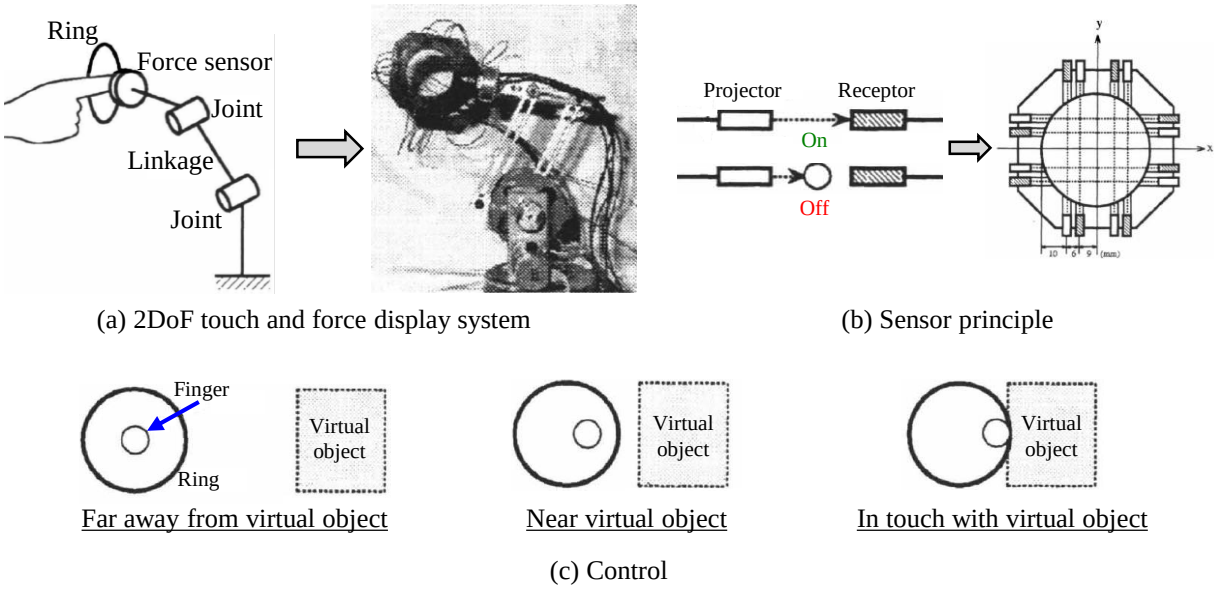

(a) 2DoF touch and force display system

(b) Sensor principle

(c) Control

Figure 1.20: 2DoF CT-HI system from [Yoshikawa and Nagura, 1997].

A similar approach was used in [Gonzalez, 2015] for the development of a 2DoF CT-HI (see Fig.1.21a). The tracking is however improved to get better performances: the end-effector is instrumented with infrared proximity sensors allowing to reconstruct the finger shape and to precisely estimate the position of its center using distance measurements (see Fig.1.21b). The control of the device is more precise, especially regarding the transitions between free space and contact (see Fig.1.21c). Further technical specifications on this CT-HI can be found in appendix A.

In [Yoshikawa and Nagura, 1999], a three-dimensional haptic display composed of two arms and a cap-like end-effector attached to their tips was presented (see Fig.1.22a). The user can insert his/her finger in the cap to interact with the virtual world. The device's sensor system is composed of optical glass-fiber on-off sensors, allowing to roughly estimate the 6DoF configuration (position and orientation) of the finger in the cap (see Fig.1.22b). In free space the device tracks and follows the fingertip without contact. At contact (when

a virtual object is touched), the cap is controlled so its inner surface touches the finger (see Fig.1.22c).

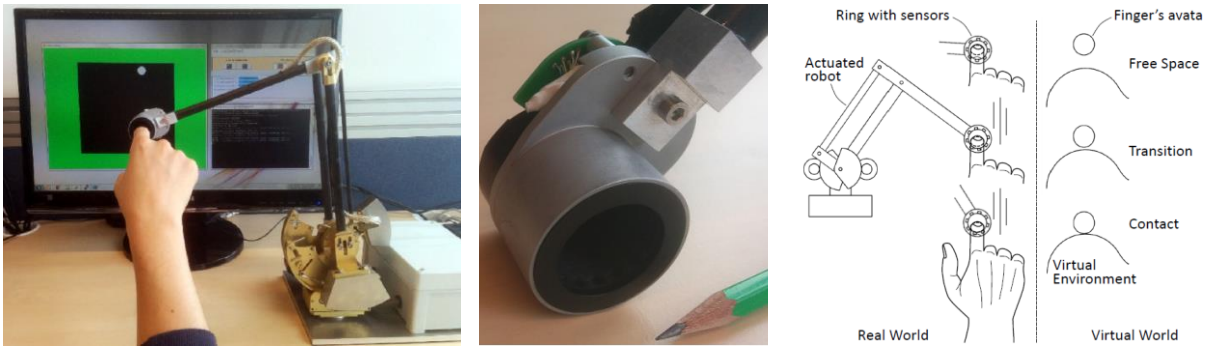

(a) 2DoF close-tracking-type interface (b) End-effector (c) Control

Figure 1.21: 2DoF CT-HI system from [Gonzalez, 2015].

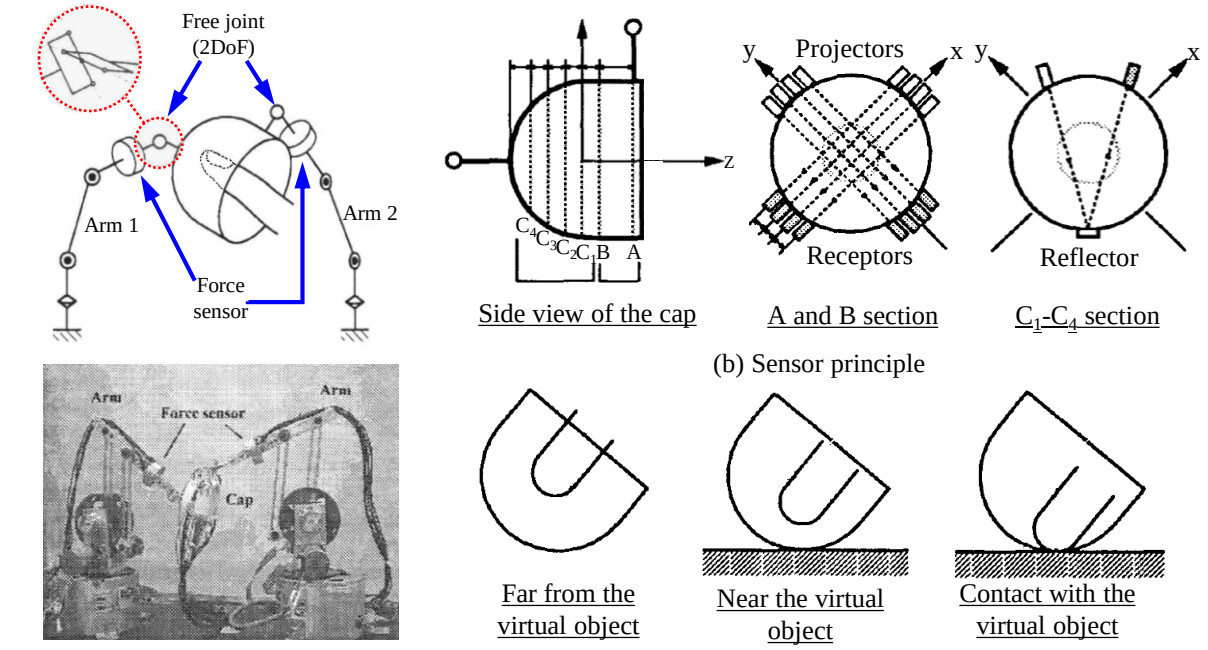

Figure 1.22: 3DoF CT-HI system from [Yoshikawa and Nagura, 1999].

Finally, a recently developed CT-HI presented in [Chabrier et al., 2017] allows two finger dexterous interactions (index and thumb fingertips) with digital mock-ups in VR (see Fig.1.23a). This interface should be able to precisely measure and follow both fingertips remotely without equipping the user with any marker on skin or nail, and serve as a contact surface when force feedback is required. To perform this, two 6DoF end-effectors were specially designed and tested. Each end-effector integrates 9 proximity sensors, 8 placed around the finger in two planes, the last one being in front of it (see Fig.1.23b). A 6DoF (position and orientation) robot is associated with each finger and connected to a

base plate fixed on the hand palm. All these elements are associated with a positioning arm (see Fig.1.23c) in order to allow for as free as possible hand movements.

It is worth noting that the performance of CT-HI devices directly depends on the quality and speed of the measurement of the user's body configuration (typically his/her hand or finger). It is of capital importance to acquire this data with a high precision and at a high frequency in order to allow for the implementation of an efficient control strategy ensuring clean free space to contact transitions. Several techniques can be used therefore. Some of them will be described and discussed in chapter 4.

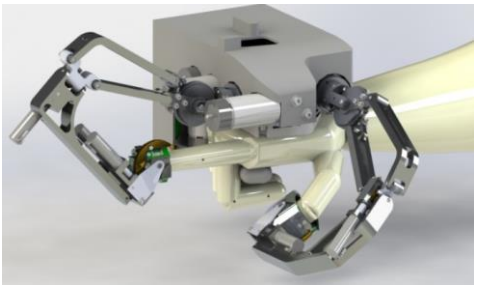

(a) Two fingers close-tracking-type haptic interface

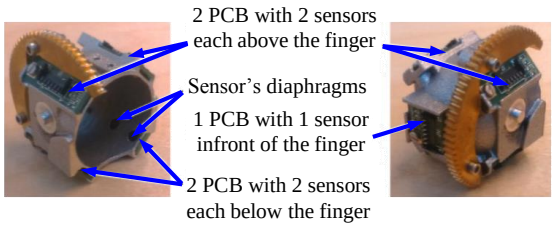

(b) Prototype end-effector with 9 proximity sensors

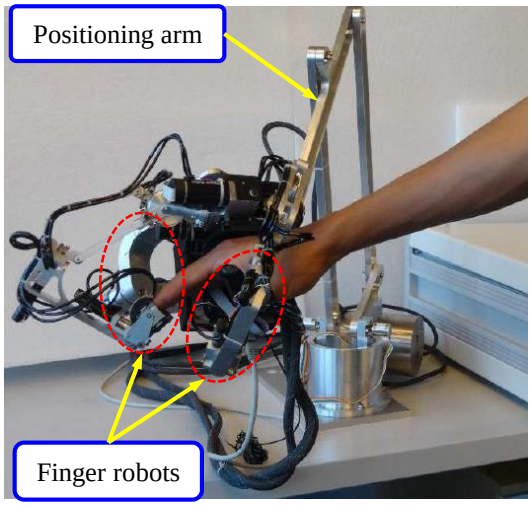

(c) Interface main elements

Figure 1.23: Two finger dexterous CT-HI (adapted from [Chabrier et al., 2017]).

1.8 Proposed research

Force feedback interfaces are intended to allow a user to interact naturally with a virtual/remote environment with haptic feedback. Therefore, they should be both light and frictionless enough so that they do not interfere with the user's movement in free space (transparency) and mechanically stiff to provide realistic force feedback. Several efforts can be made to achieve these goals, e.g. by optimizing the mechanical design or by using force sensors to measure and compensate the resistance of the device to the user's movements in the direction of displacement. These solutions are however not sufficient to achieve a perfect transparency and the performances of current force feedback devices still require to be improved, in particular for tasks lasting long hours and where perception of small forces is important, e.g. for medical simulators employing light tools.

The IC paradigm, presented in section 1.7, aims to solve this problem by physically disconnecting the user for the device in free space and letting him/her touch the robot only

when it is required, this way providing only the necessary amount of interaction forces. This principle can theoretically render force feedback interfaces perfectly transparent, allowing to increase the realism of the interaction. It has been implemented in two ways: ET-HI and CT-HI devices.

In the former approach, the system anticipates the user's movements, positions the end-effector of the robot at the place where he/she is expected to touch a VO and waits for the user to encounter it. User tracking is commonly achieved by means of a motion capture system or a passive mechanical master arm attached to the user's arm. Such approach is however dangerous, as without meticulous path planning, the robot may follow trajectories near the user. Furthermore, if bilateral contacts are simulated the robot may attain very high speeds, compromising the security of the user.

The later approach proposes to closely track (advantageously with a system integrated in the end-effector of the robot) and follow the user's movements (in position and orientation) without contact in free space and stop the robot when a VO is being touched to make the user feel the interaction forces. With this approach, the security of the user is improved, even if his/her movements are restricted to the workspace of the robot. For this reason, in the present work we will focus on close-tracking-type interfaces.

It is worth noting that, despite their potential advantages, CT-HI devices still suffer from several limitations. The objective of the doctoral thesis presented here is to increase knowledge about them. It is organized around three key questions that, according to the explored literature, have not yet been addressed for this type of devices. Each of these issues will be addressed in a specific chapter of this thesis, as explained below.

For practical purposes the term IC-HI will be used as an equivalent of CT-HI in the reminder of the present document.

- **Chapter 2:** Evaluation of the Benefits of IC-HIs from a User Perception Perspective.

When using a force feedback interface in VR, the user should ideally experience what the avatar feels, either nothing when he/she is in free space, or realistic forces during contacts with the environment. He should also feel, a clear distinction between free space and contact modes. Compared to conventional devices, IC-HI interfaces should increase the realism of the interaction as they theoretically provide a perfect transparency in free space, a large range of forces when obstacles are touched and sharp transitions between these two states. These advantages should allow VR to get closer to reality. As a consequence, we would expect that users prefer an IC-HI rather than keep using conventional devices. However, this has not yet been proven.

To answer this question, we made use of an existing 2DoF device developed at CEA, LIST [Gonzalez, 2015] that can be configured either as a classical contact haptic interface (CC-HI) or as an IC-HI. In order to compare the relative merits of both configurations, a series of phsychophysical tests were proposed to a group of volunteers. Three types

of user tests, each one representing an elementary VR task, were performed: stiffness identification, target pointing and obstacle detection. Each test was performed in both configurations (CC-HI and IC-HI), and information about the state of the system but also about the feeling of the user were acquired, allowing us to obtain both qualitative and quantitative results. This work is presented in chapter 2.

- **Chapter 3:** Improvement of Contact Rendering at High Speeds

When designing IC-HIs and their controller, three phases should be considered: free space, contact and transitions between free movements and contact. In free space, the robot tries to keep the user limb, e.g. his/her fingertip, at the center of its end-effector. In practice, the limited dynamics of the robot reduce its capacity to instantaneously follow the user. The role of the controller is then to try to compensate for the resulting position error. IC-HIs usually work quite well in this phase, provided that the available gap between the end-effector and the user limb is sufficient to absorb any position deviation without contact between them.

At contact, IC-HIs work like any other haptic interface. They can be controlled either in admittance or impedance These principles are well known and this phase is not a problem, as far as the controller gains preserve the stability of the device.

Transitions between free space and contact are more tricky. Let's take the example of a fixed obstacle. When the user approaches the vicinity of the VO, the robot's end-effector should be completely stabilized before contact so that the user has the impression of touching an immobile object. As can be seen in the literature, this can be made in various ways, either by abruptly shifting from free space control to contact mode when hitting the VO, or by progressively changing the reference position in the vicinity of the environment, so that the user limb seamlessly moves from the center of the end-effector to its periphery, allowing the user to touch it when required, or by having both mode always active and progressively changing their weight depending on the situation. The last one is the most recent solution and it proves to be the more stable [Gonzalez et al., 2015]. However, it is still not capable to manage contacts at high speeds.

Motivated by this fact, part of our research was concentrated on the improvement of the contact rendering at high speeds. The proposed control strategy aims to dissipate the energy of the interface, prior to contact, by creating a pure damping zone on the frontier of the VO. To evaluate the benefits of this approach, user tests were also performed. Further details can be found in chapter 3.

- **Chapter 4:** Contributions to the Design of an IC-HI Tracking Module for Tool-Based Interactions.

It can be seen in the literature that most existing IC haptic interfaces are intended for bare finger interactions. Despite their advantages, the design of such systems is particularly challenging since the size and shape of human fingers vary for each user. Also,

fingers deform both when bending and during contacts with the environment. This makes it difficult to precisely determine their position, orientation and geometry.

Fortunately, a lot of tasks are performed by means of a tool and do not require direct finger interactions. In surgery simulators for example, the interaction usually takes place through a stylus-like interface. Compared to a finger, a tool is easier to track as it has a fixed geometry, a known size and homogeneous mechanical properties. Furthermore, it can be equipped with active sensors.

As several applications could benefit from an IC-HI interface allowing tool interactions, we initiated the development of such a device. It is worth noting that VR applications are seldom limited to 2DoF. They generally require both translations and rotations in any direction. Hence our work focused on a 6DoF device.

IC-HIs contain both a tracking module and a force feedback module. The former allows to obtain the relative tool/robot position and orientation information, while the latter provides the corresponding Cartesian forces and torques by constraining the user in an appropriate way.

Due to limited time and resources, we focused our work on the tracking module. High-speed response, small size and excellent accuracy are the main design drivers for this system. In the scope of the present research its development was addressed by setting up precise specifications, by studying the state of the art in depth in order to select the most appropriate sensing technology, and by characterizing the response of a 1DoF sensor that can be used as a basis for our 6DoF tracking system. This work is presented in details in chapter 4.

Chapter 2

Evaluation of the Benefits of IC-HIs from a User Perception Perspective

Contents

2.1 Introduction

Since they touch the user only when force feedback is required, intermittent contact haptic interfaces, and in particular close-tracking-type devices (referred here as IC-HIs), aim to provide more realistic interactions with virtual environments than classical contact haptic interfaces (CC-HI). To our knowledge, however, this has not yet been proven. Indeed, the information which is usually available regarding both CC and IC existing interfaces is often limited to technical specifications (number of DoF, workspace, inertia, maximum exertable force, etc.) and example applications. Unfortunately, this is not sufficient to ensure optimal performances for the completion of a VR task of interest nor to directly infer their perceived rendering quality. Such performance assessment requires the presence of the human operator in the loop and any evaluation performed without human interaction would not really represent the actual device use.

Psychophysical evaluation methods appear to be a good solution to this problem. By directly evaluating the perception of an external stimulus provided to a human being through a given device, such approach allows to take into account both the performances of the device itself, the capacities of the user, and their adequacy in the context of a specific task. Results being given with reference to the user, who is independent of the device, this approach also allows to make fair comparisons between two or more force feedback devices. It can be imagined for instance asking a user to perform a given VR task with different devices and measuring/calculating each time the same performance metric, related to the task itself and not to the employed device. The results obtained can be then analyzed to learn which device is better suited for the task of interest.

Psychophysical tests are thus a useful tool to evaluate the relative benefits of CC-HI and IC-HI devices and compare them. In this work, we choose to focus on three tests representing elementary VR tasks. These evaluations, reported in this chapter, were performed by a group of volunteers using an available interface that can be configured either as a CC or as an IC interface.

This chapter is organized as follows: section 2.2 presents an insight on the different existing approaches for the assessment of haptic interfaces performances and the interest of a psychophysical evaluation approach. Section 2.3 will describe the general methods employed during our experiments in order to provide an understanding of the test conditions. Sections 2.4, 2.5 and 2.6 correspond to each experiment. For each case, specific methods (participants, materials, procedure, data processing), results and conclusion are given. Finally the chapter conclusion and perspectives are given in section 2.7.

2.2 Evaluation of haptic interfaces

2.2.1 Performance evaluation approaches

As shown in figure 2.1a, a haptic rendering system, when considered as a whole, is composed of different components, i.e. the VE, the haptic interface itself and the human user. While the performances of each module can be assessed separately, according to different types of evaluation (see Fig.2.1b) and basic criteria (see Fig.2.1c), an ideal performance measurement should consider the whole haptic system.

The level of detail of the **VE** for instance is important for the visual realism of the scene. It increases however in turn the computation time required at each simulation step for the update of the interaction forces, especially if the available resources are limited, thus decreasing the force rendering quality. Taking into account only the VE would not completely reflect the influence of the modeling quality.

Similarly, when considering the haptic interface, it is desired to have a device that provides high transparency in free space and that displays high stiffness when force feedback

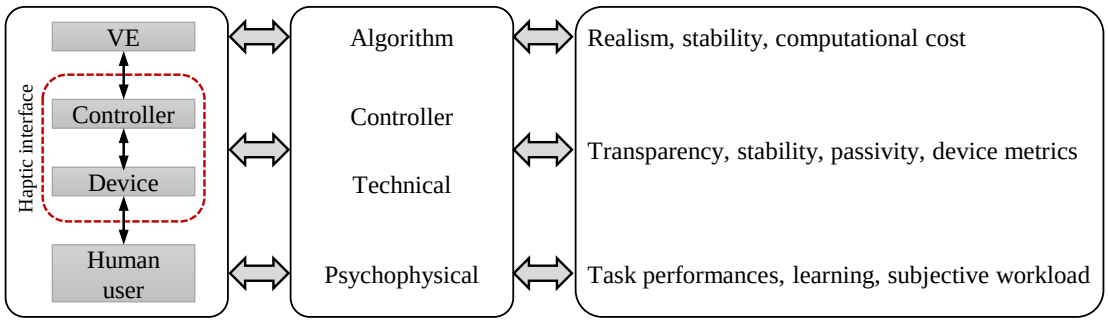

Figure 2.1: Haptic rendering evaluation techniques (adapted from [Samur et al., 2007]).

is provided (contact with a stiff VO). Considering only the **device** technical specifications is not sufficient as the performances of the **controller**, which ensures a proper communication between the VE and device, have also a large influence on the achievable stiffness.

The quality of the immersion and of the perceived interactions thus depend on the quality of both the VE, the controller and the capacity of the haptic device to provide realistic interactions. All these elements should therefore be taken into account for the evaluation of the haptic rendering system. These elements representing research branches by themselves and as a result being in constant evolution, methods being resilient to such evolution is of particular interest in this case. Experiments involving human users may provide a pertinent approach, as will be developed in the following section.

2.2.2 Evaluation based on psychophysical tests

When considering the ability of a user to perform a given VR task requiring force feedback, the following question quickly arises: Which haptic interface better suits the task of interest?

The answer to this question is not straightforward since the device technical specifications (DoF, workspace, inertia, maximum exertable force, etc.) alone do not provide direct information regarding the attainable performances for that task. The task's constraints should also to be taken into account. Whether the interface is intended to be used in a medical simulator or in a video game platform, the requirements will not be the same. Indeed the dynamics of such tasks are totally different and the device should fit them to fulfill the expectations. Similarly, the human operator should also be considered. Indeed, the design of haptic devices should account for the human operator's capabilities, e.g. take into account the size of the hand or the reachable speeds and workspace with his/her arm.

In summary, as a haptic device is meant to be used by a human user to perform various tasks and its performance is highly affected by the user's behavior and tasks constraints [Samur, 2012], all these elements should be taken into account. In this con-

text, psychophysical evaluation represents a pertinent approach. More specifically, device evaluation based on **psychophysical tests** represents an adapted approach for haptic interfaces since it links device performance measures to the limits of human perception, obtaining as a result device-specific limits [Samur, 2012] regarding the task of interest.

Psychophysics has been defined as "the scientific study of the relation between stimulus and sensation" [Gescheider, 2013], e.g. for the senses of vision, hearing and touch. Another more complete definition is "the analysis of perceptual processes by studying the effect on a subject's experience or behavior of systematically varying the properties of a stimulus along one or more physical dimensions" [Bruce et al., 2014].

Haptic rendering systems have been used in a variety of pshychophysical experiments:

- peg-in-hole [Unger et al., 2001],
- tapping [Chun et al., 2004],
- targeting [Oakley et al., 2000],
- haptic training [Avizzano et al., 2002],
- joint task in a shared VE [Basdogan et al., 2000],
- hardness perception [Lawrence et al., 2000] and
- object recognition [Kirkpatrick and Douglas, 2002].

Such experiments can be useful to assess the performances either of the haptic interface or of the haptic feedback itself. In the present work the attention is given to attainable performances with a haptic device.

For a VR task of interest a set of performance metrics can be defined in order to build a standard testbed that can be used with several devices. This should include both **quantifiable** metrics, e.g. speed, force, time travel, and **subjective** performance values, e.g. survey, user's opinion [Samur, 2012].

Testbed evaluation approach aims then to provide general and complete results that can be taken into account in any VR application using the studied task [Samur et al., 2007]. This means that several haptic devices that are potentially interesting for the desired application can go through such testbed evaluation, the device obtaining the highest performances is expected to be used for that application since it will provide optimal performances.

Depending on the nature of the task, it can be classified into two haptic modes: **motor control** and **perception**. A haptic mode is defined as "a distinct style of using the haptic system, characterized by the nature of the user's attention, the path and duration of the movements, and the **skin location** contacting the object of interest"

[Kirkpatrick and Douglas, 2002]. A haptic mode involves then several factors that play a more or less important role depending on the nature of the task. Table 2.1 shows a taxonomy for each haptic mode assuming that the user is using his/her hand. This information can contribute to imagine a pertinent VR-based testbed based on the subtasks.

Table 2.1: Taxonomy of haptic modes (adapted from [Samur, 2012]).

Haptic mode	Generic tasks	Subtasks
Motor control	Travel	*-Targeting* *-Motion selection* *-Input conditions*
	Selection	*-Indication of object* *-Indication to select*
	Manipulation	*-Attachement* *-Positioning* *-Orientation*
Perception	Detection Discrimination	*-Stimulus (position, velocity, force, pressure, stiffness, viscosity)*
	Discrimination	*-Material (texture, hardness, weight)*
	Identification	*-Geometry (size, shape)*

In the literature, a comprehensive evaluation of different CC devices was found in [Samur, 2012]. On the other hand, despite the potential interest of the IC paradigm (which aims to provide a perfect transparency in free space and more realistic transitions between free space and contact) and the fact that it has been around at least since the 90s, it was observed a lack of work to assess its benefits for VR tasks. Motivated by this observation, we decided to implement a certain number of psychophysical experiments based on VR tasks in order to assess the benefits of a recently developed IC-HI device.

Inspired by the taxonomy provided in table 2.1, psychophysical experiments based on three different tasks that can collectively represent the building elements of a realistic haptic application were proposed: (1) stiffness identification, (2) target pointing and (3) blind obstacle detection. Aiming to compare the relative benefits of CC and IC haptic interfaces, all of them were performed in both conditions.

The first experiment, called **stiffness identification**, aimed to answer the following question: Does an IC haptic interface allow to better distinguish different stiffness values than a CC-HI device? This experiment consisted in palpating a reference wall that displays a reference stiffness (unknown to the user) that has to be guessed. To this end, the same wall could be switched to a variable stiffness mode where the user could modify the displayed stiffness. Switching between both modes could be done until both walls were perceived as displaying the same stiffness. This kind of task is commonly performed by veterinarians and novice surgeons to learn palpation skills [Forrest et al., 2009].

In a second experiment we wondered if a target pointing task was easier to perform with an IC-HI or with a CC-HI? In order to obtain elements of answers, this experiment, called **target pointing**, proposed a motor control task which consisted in pointing targets of several sizes, located at different distances from a home position. Well defined metrics to evaluate the performance of this type of experiment have been defined in [MacKenzie, 1995].

The third experiment, called **blind obstacle detection**, aimed to answer the following question: Are free space to contact transitions more realistic employing an IC haptic interface than with a CC device? This experiment proposed a combination of different haptic modes since it asked the user to follow a vertical line (motor control) where he/she would encounter an invisible obstacle located at an unknown position (perception).

The performed experiments searched to provide answers to the above presented questions. While all of them are different, they share however certain common points from an implementation point of view. These elements are presented in the following section 2.3.

For practical purposes in the reminder of the present chapter, the terms "CC condition" (classical-contact condition) and "IC" condition (intermittent-contact condition) will make reference to the use of a CC and an IC device respectively.

2.3 General methods

In this section, some aspects which are common to the three performed experiments will be presented and described: participants (section 2.3.1), materials (section 2.3.2), experimental setup (section 2.3.3), procedure (section 2.3.4) and data processing methods (section 2.3.5).

2.3.1 Participants

A total of thirty people (19 men, 11 women, aged 22-60) were invited to be volunteers for our experiments. They were told that they would have to perform a VR task employing a force feedback interface. A brief description of these two elements was provided in certain cases during the recruitment process, however no concrete details about the experiment were given.

The population was mainly issued from people working in the "Institut des Systèmes Intelligents et de Robotique" (ISIR), a robotics laboratory located in Paris, France. It accounted for administrative personnel, permanent staff, PhD students and interns. Only right-handed volunteers were chosen since, as it will be seen further in section 2.3.2.1, the experimental set-up was better suited for right handed participants.

Each one of the three experiments was assigned to a group of ten participants in a random manner, i.e. a list with proposed time slots was filled in order to make two appointments with each participant, one for the CC interface and another one for the IC interface. This means that each group was asked to perform only one of the three assigned tests using both a CC and an IC interface (see Fig.2.2).

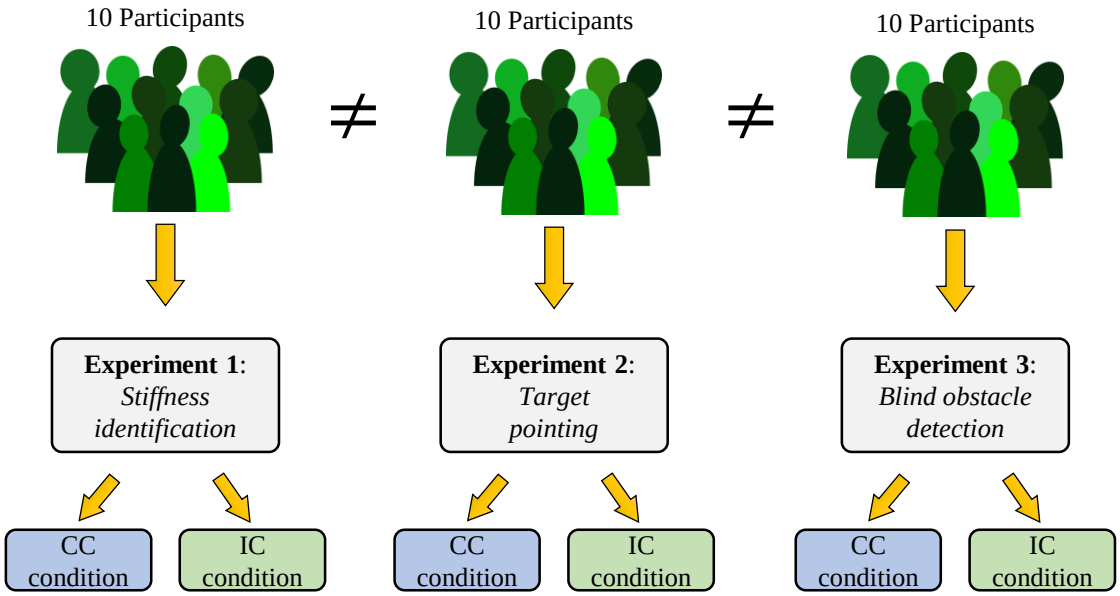

Figure 2.2: Assignment of experiments.

In order to prevent learning effects, a two-days rest interval between the tests performed with CC and IC interfaces was given to the subjects. Calendar shown in table 2.2 provides a representative chronology of the performed experiments for each subject, denoted here as *S*.

Table 2.2: Experiments calendar.

Day 1	Day 2	Day 3	Day 4	Day 5	Day 6
IC Stiffness	**IC** Contact	**CC** Pointing	**CC** Stiffness	**CC** Contact	**IC** Pointing
S1 to S5	*S11 to S15*	*S21 to S25*	*S1 to S5*	*S11 to S15*	*S21 to S25*
IC Pointing	**CC** Stiffness	**CC** Contact	**CC** Pointing	**IC** Stiffness	**IC** Contact
S6 to S10	*S16 to S20*	*S26 to S30*	*S6 to S10*	*S16 to S20*	*S26 to S30*

2.3.2 Materials of the study

In this section the materials employed during the experiments are described. The focus was given here to the elements that allowed to collect/generate data, in particular:

- the **CC** and **IC** haptic interfaces (section 2.3.2.1), which allows to collect information regarding the movements of the user as well as the interaction forces,

- the **VE** (section 2.3.2.2), which definition provides the necessary elements to generate its visual representation and calculate the corresponding interaction forces thanks to the associated **control law** (section 2.3.2.3),

- and finally, a **questionnaire** (section 2.3.2.4), that allows to collect the feeling of the participants on particular aspects of the performed experiment.

2.3.2.1 CC & IC haptic interfaces

One of the main aims of the performed work was to compare the attainable performances in both CC and IC conditions for a same VR task. To perform this an available 2DoF robot was equipped with either a CC or an IC end-effector.

The **robot** is composed of two links 0.25m long each. Its workspace lies in a vertical plane. The actuation of the links is provided by two DC motors and cable capstan reducers allowing a particularly transparent behavior. Encoders (position sensors placed on the motors) are used to track the robot's displacements and counterweights are mounted on each axis to allow for gravity compensation (see Fig.2.3).

Figure 2.3: 2DoF robot employed for experiments.

This platform was originally equipped with an IC end-effector (see Fig.2.4a). This element is composed of a 24mm wide hollow cylinder equipped with 16 infrared proximity sensors used to compute the relative position of the finger with respect to the cylinder, the later being also used as contact surface when force feedback is applied.

In order to provide typical CC feedback, the IC end-effector could be easily replaced by a CC end-effector mounted on the same robot (see Fig.2.4b). It is composed of a thimble that mechanically links the user's finger to the robot. Its internal cup can be replaced with another one of a different inner diameter according to the user's finger's size (five different cups ranging from 15 to 19mm were proposed). In order to avoid finger twisting during manipulations, each cup can freely rotate around the distal phalanx axis.

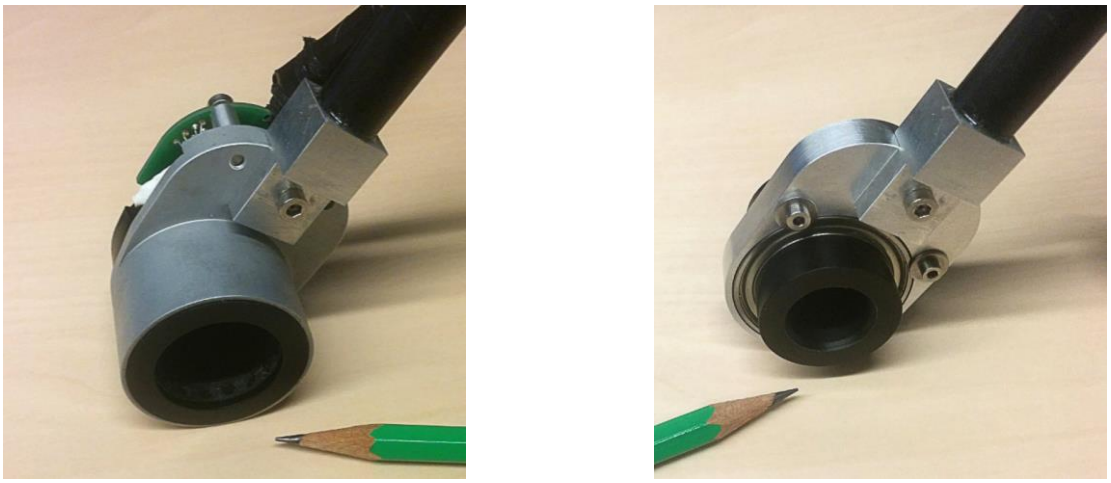

(a) IC end-effector

(b) CC end-effector

Figure 2.4: Employed end-effectors.

Further technical details on the robot equipped with an IC end-effector can be found in appendix A.

2.3.2.2 Virtual environment

A VE recreates a scene of the real world. Its model is used for visualization purposes as well as to calculate the corresponding interaction forces.

In the present case the employed 2D VE consists of a black vertical rectangle (**free space**) surrounded by a thick green contour representing four **virtual walls**. The **home position** is a circular area of the free space employed as a starting point prior to a movement. Finally, user's **finger avatar** was represented with a white circle which displacement was coupled with that of the robot's end-effector. These elements are shown in figure 2.5.

As the interaction with the VE is performed by means of a haptic interface, this VE should be positioned in an area where the device performs well. Here, the VE from figure 2.5 is placed 0.2m in front of the robot's reference frame R_0 and it extends just above it (see Fig.2.6). The dimensions of the free space rectangle are 0.15m $\times$ 0.20m. According to [Gonzalez, 2015], this robot equipped with an IC end-effector shows homogeneous performances in this area.

It is worth noting that figure 2.6 illustrates the VE as it is defined in the haptic space, i.e. the environment used to generate force feedback. It can differ from its visual representation, which can in particular be placed in a different location as shown later in figure 2.12 (the haptic virtual space is located close to the robot as shown on figure 2.6 while its visual representation is shown on a screen in front of the user, far away from the robot).

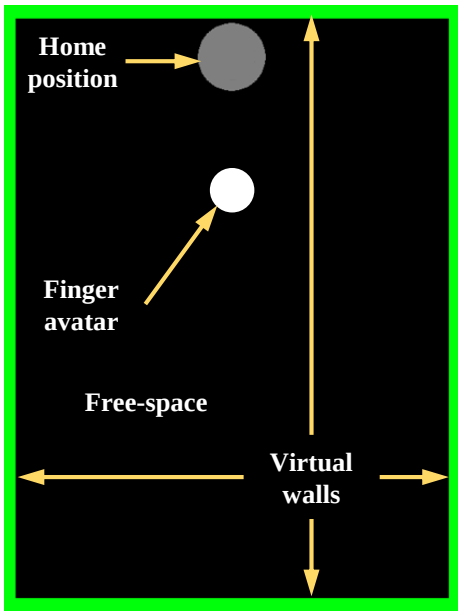

Figure 2.5: VE main elements.

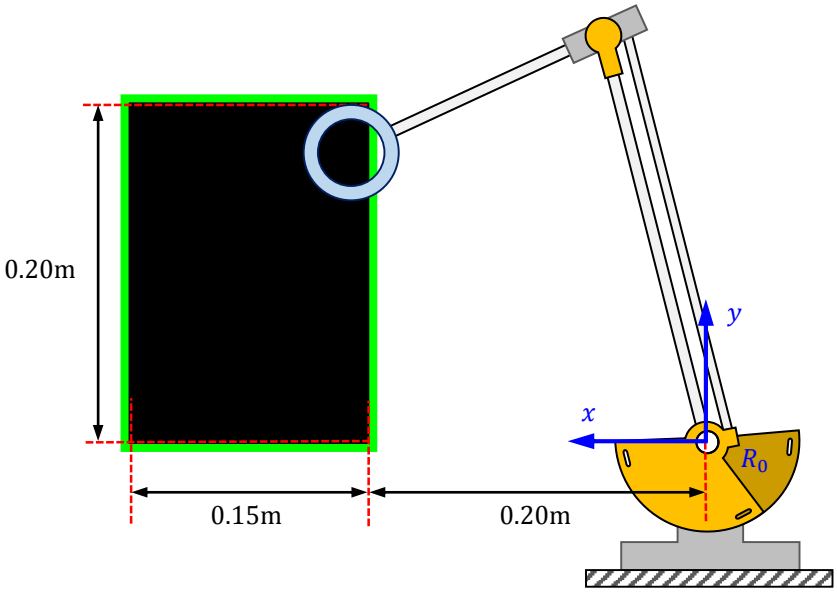

Figure 2.6: VE mapped into real world robot's workspace.

The corresponding interaction force with the VE, e.g. with a virtual wall, denoted here as F_e, is calculated based on its model and acts as a unilateral constraint during

the contact phase. Such principle works for both conditions CC and IC, however control in free space is different. The following section will provide the principle of the control employed on both interfaces.

2.3.2.3 Control of the haptic interface

The control strategy of either the CC or the IC interface (see Fig. 2.4) should manage the behavior of the device during free space and contact modes. In the following paragraphs the employed strategies for both modes as well as the transition between them will be presented, first for an IC-HI and then for a CC-HI.

In free space the IC haptic interface should closely track the user's finger position without touching it. We note here:

$$\boldsymbol{\epsilon_X} = \boldsymbol{X}_{f/0} - \boldsymbol{X}_{r/0} = \boldsymbol{X}_{f/r} \tag{2.1}$$

the tracking error $\boldsymbol{\epsilon_X}$ between the center of the finger $\boldsymbol{X}_{f/0}$ and the center of the ring $\boldsymbol{X}_{r/0}$ (see Fig.2.7, where the finger is modeled as a cylinder). This error can then be expressed in the joint space as follows:

$$\boldsymbol{\epsilon_q} = \mathbf{J}^{-1}(\boldsymbol{q})\boldsymbol{\epsilon_X} \tag{2.2}$$

where $\boldsymbol{q} = [q_1 \quad q_2]^T$ are the joint positions and $\mathbf{J}(\boldsymbol{q})$ the robot's Jacobian matrix expressed in its global reference frame R_0.

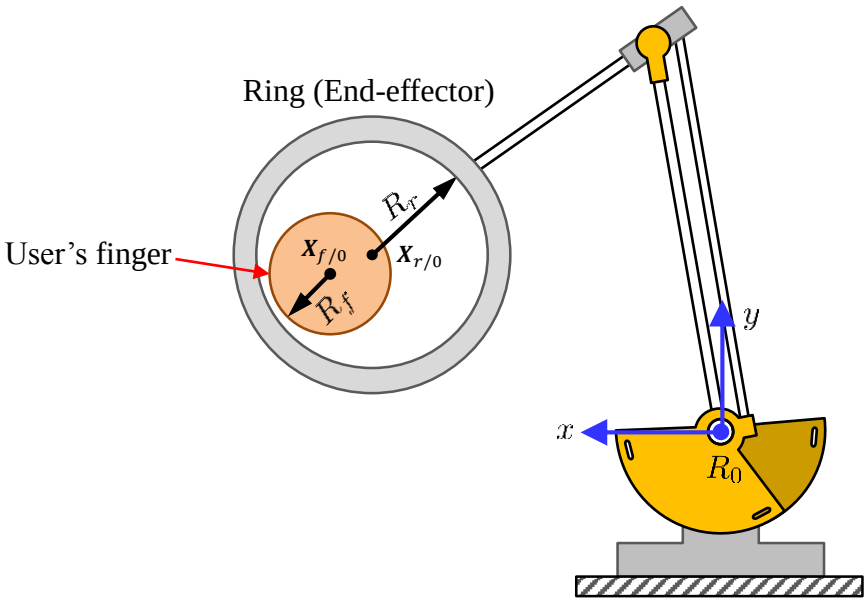

Figure 2.7: User's finger and ring representation in the robot's reference frame R_0.

Error minimization is achieved with a proportional derivative controller, which pro-

vides the robot with a reference tracking torque $\boldsymbol{\tau}_t$ in the Laplace domain:

$$\boldsymbol{\tau}_t = \mathbf{Z}_t \boldsymbol{\epsilon}_{\boldsymbol{q}} = (\mathbf{K}_t + \mathbf{B}_t s)\boldsymbol{\epsilon}_{\boldsymbol{q}}, \tag{2.3}$$

where $\mathbf{Z}_t$ is the impedance expressed in the joint space, $\mathbf{K}_t$ and $\mathbf{B}_t$ the proportional and derivative gains respectively (both diagonal matrices in the joint space) and s the Laplace variable. With this controller, a link equivalent to a spring-damper system is created between the centers of the finger and the ring which have their corresponding avatar representation in the virtual world (see Fig.2.8).

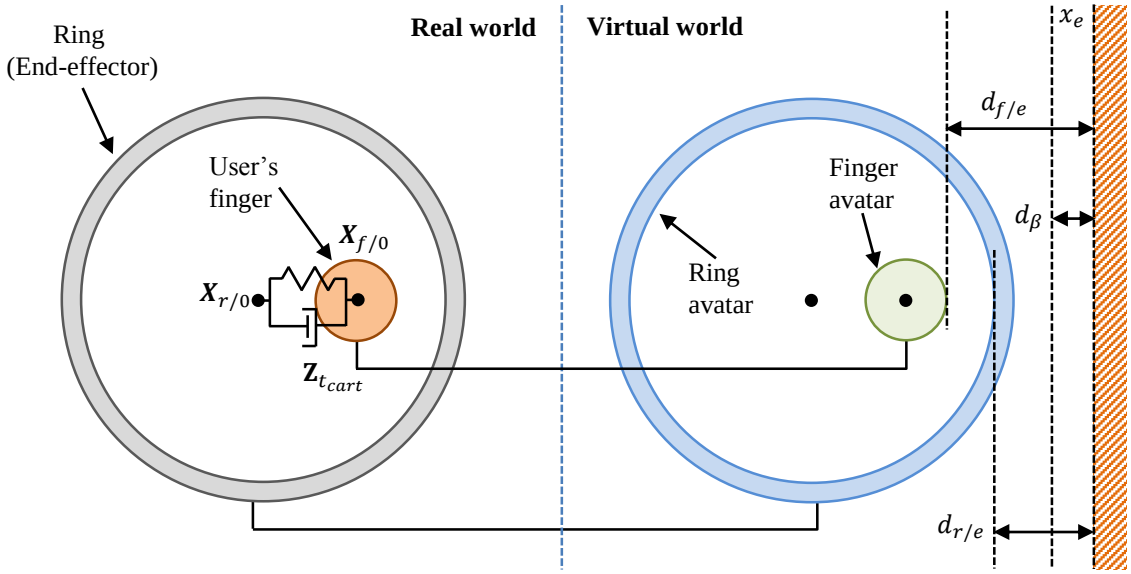

Figure 2.8: Spring-damper coupling between the center of the ring and the finger. Here the finger and ring avatars are approaching a VO located at x_e and are respectively located at a distance $d_{f/e}$ and $d_{r/e}$ from it. In this figure, the impedance $\mathbf{Z}_{t_{cart}}$ is represented in the Cartesian space. It is linked to the joint space impedance $\mathbf{Z}_t$ defined in equation (2.3) by the relation $\mathbf{Z}_{t_{cart}} = \mathbf{J}^{\mathrm{T}} \mathbf{Z}_t \mathbf{J}^{-1}$.

The corresponding PD tracking gains are:

$$\mathbf{K}_t = \begin{bmatrix} 40 & 0 \\ 0 & 40 \end{bmatrix} \text{Nm/rad} \qquad \mathbf{B}_t = \begin{bmatrix} 1 & 0 \\ 0 & 1 \end{bmatrix} \text{Nms/rad} \tag{2.4}$$

When the finger touches a VO, e.g. a wall, the resulting contact force based on its mechanical properties should be displayed to the user. Such force resulting of the interactions with the VE is noted here as $\boldsymbol{F}_e$ and acts as an unilateral constraint. A viscoelastic compliant VE without tangential friction is assumed and a modified Kelvin-Voigt model [Achhammer et al., 2010] is used to calculate the resulting interaction forces as follows:

$$\boldsymbol{F}_e = \begin{cases} \text{if } d_{r/e} < 0 \ \& \ \dot{X}_{r/0} > 0 \text{ then } \boldsymbol{F}_e = -d_{r/e}(\mathbf{K}_e + \mathbf{B}_e s)\boldsymbol{n} \\ \text{if } d_{r/e} < 0 \ \& \ \dot{X}_{r/0} < 0 \text{ then } \boldsymbol{F}_e = -d_{r/e}\mathbf{K}_e\boldsymbol{n} \\ \text{else } \boldsymbol{F}_e = 0 \end{cases} \tag{2.5}$$

where

$d_{r/e}$ is the distance between the ring's avatar inner circumference and the closest point of a VO located at position x_e,
$\boldsymbol{n}$ is an unitary vector normal to the surface of contact and
$\dot{X}_{r/0}$ is the speed of the ring along $\boldsymbol{n}$.

For explanation purposes, $\dot{X}_{r/0}$ is assumed positive in the direction of motion. These elements are illustrated in figure 2.9.

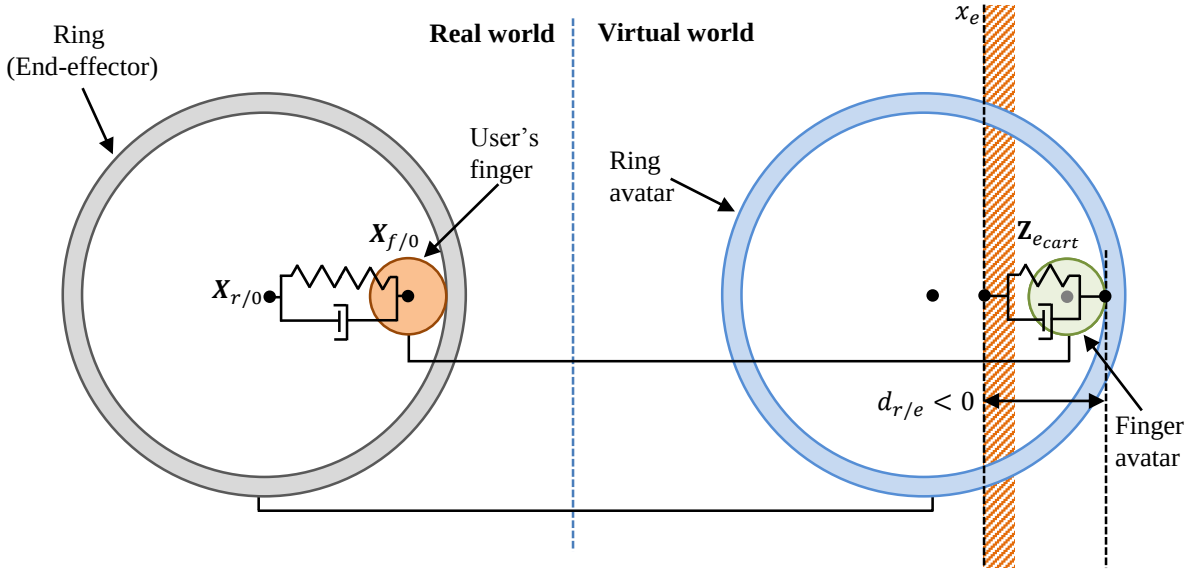

Figure 2.9: Spring-damper coupling between the ring avatar and the virtual wall.

The PD gains $\mathbf{K}_e$ and $\mathbf{B}_e$ for force rendering are:

$$\mathbf{K}_e = \begin{bmatrix} 2500 & 0 \\ 0 & 2500 \end{bmatrix} \text{N/m} \qquad \mathbf{B}_e = \begin{bmatrix} 35 & 0 \\ 0 & 35 \end{bmatrix} \text{Ns/m} \tag{2.6}$$

The transition between free space and contact with the IC-HI is achieved by reducing the influence of the tracking force $\boldsymbol{F}_t$ (send to the robot as a tracking torque $\boldsymbol{\tau}_t$) by a factor β nearby the obstacle, i.e. the tracking force starts decreasing at a distance $d_{f/e} = d_\beta$ from the VO which is located at position x_e. Equation (2.7) shows how β can vary in function of $d_{f/e}$, the distance between the finger's avatar and the VO (distances $d_{f/e}$ and d_β are ilustrated in figure 2.8). However, factor β cannot be totally canceled in the vicinity of

the VO since in this case the ring would not follow the finger when it moves away from it.

$$\begin{cases} \text{if } d_{f/e} > d_\beta \text{ then } \beta = 1 \\ \text{if } d_{f/e} \in [0, d_\beta] \text{ then } \beta = \frac{1-\beta_{min}}{d_\beta} d_{f/e} + \beta_{min} \\ \text{if } d_{f/e} \leq 0 \text{ then } \beta = \beta_{min} = 0.1 \end{cases} \tag{2.7}$$

Here $d_\beta = R_r - R_{f,max} = 1\text{mm}$ (with $R_r = 12\text{mm}$ and $R_{f,max} = 11\text{mm}$ chosen so that $\forall R_f, R_{f,max} > R_f$). [1] This way by the moment the user encounters the ring, the tracking effect is almost canceled and $\|\boldsymbol{F}_e\| \neq 0$. Equation (2.3) can now be expressed as:

$$\boldsymbol{\tau}_t = \mathbf{Z}_t \beta \boldsymbol{\epsilon}_{\boldsymbol{q}} \tag{2.8}$$

The control explained in previous paragraphs, corresponding to the IC haptic interface, is summarized in the control block diagram from figure 2.10. Here the KVM block computes the interaction force based on the modified Kelvin-Voigt model and the block $f(\cdot)$ performs estimation of the relative distances $d_{f/e}$ and $d_{r/e}$. This approach is known as smooth transition based control.

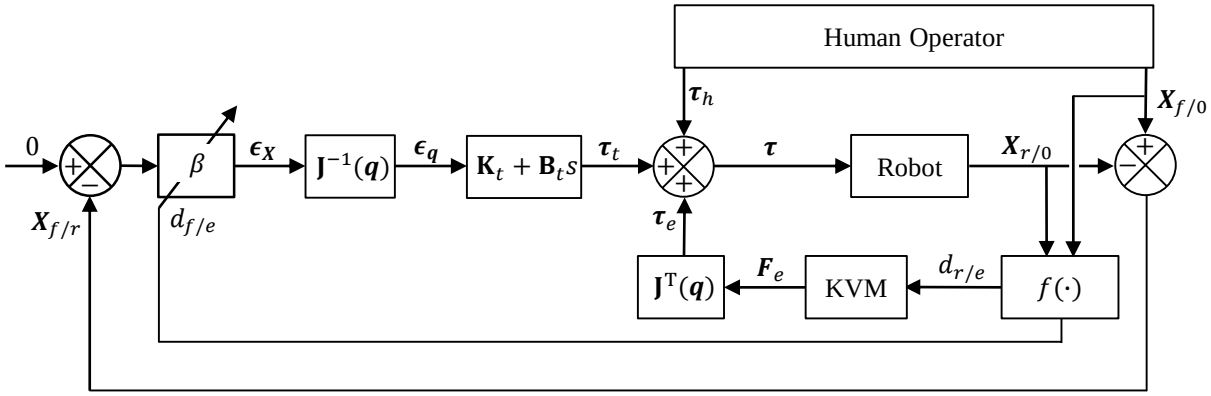

Figure 2.10: Smooth transition-based control block diagram.

In the case of the CC-HI device, the user's index finger is mechanically linked to the robot's CC end-effector (the center of the end-effector and user's finger are coincident). As a result the displacement of the interface in free space is performed thanks to the forces the user applies on it.

As for the contact, force rendering is performed the same way as in (2.5), i.e. the ring avatar is used to compute the interaction forces. Same controller gains were also used.

The control corresponding to the CC haptic interface, is summarized in the control block diagram from figure 2.11.

[1] According to [Grenier, 1991] the perimeter of the largest index is 63mm, which gives a radius of $\approx 10\text{mm}$.

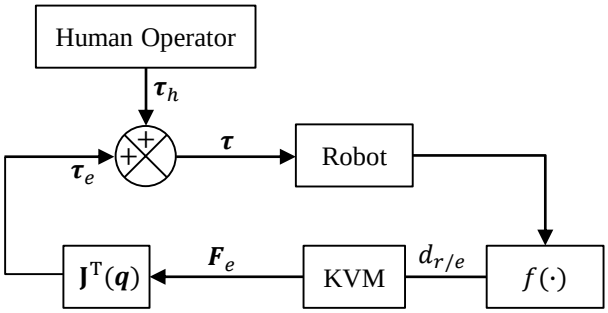

Figure 2.11: CC force rendering control block diagram.

2.3.2.4 Questionnaire

A questionnaire was employed to perform a complementary survey on particular aspects of the performed task at the end of each experiment. Such questionnaire was anonymous and the participants could spend as much time as they needed to fill it. In this section, only the questions which are common to the three experiments are provided. These questions were:

- *Did you find the interface easy to use?*
  1) Strongly disagree
  2) Disagree
  3) Neutral
  4) Agree
  5) Strongly agree

- *Did you find that the interface was tiring to use?*
  1) Strongly disagree
  2) Disagree
  3) Neutral
  4) Agree
  5) Strongly agree

Besides these common questions, 2 or 3 additional questions specific to each experiment were included in the questionnaire (see sections 2.4.2.3, 2.5.2.2 and 2.6.2.2).

2.3.3 Experimental setup

The experimental setup used for the tests was installed in an isolated room of the robotics laboratory ISIR. During each test the **participant** was sitting, wearing headphones and facing a **screen** where the VE is displayed by means of a graphical user interface (GUI). The **robot** was placed on a small table so that the user's right index

finger could be placed comfortably inside the end-effector (no elbow rest was provided). The robot was also hidden from the user's sight by a vertical **wall**. The **experimenter** was positioned in front of a **supervision computer**. This set-up is shown in figure 2.12. Figure 2.13 shows a top view diagram indicating the relative distribution of the different mentioned elements.

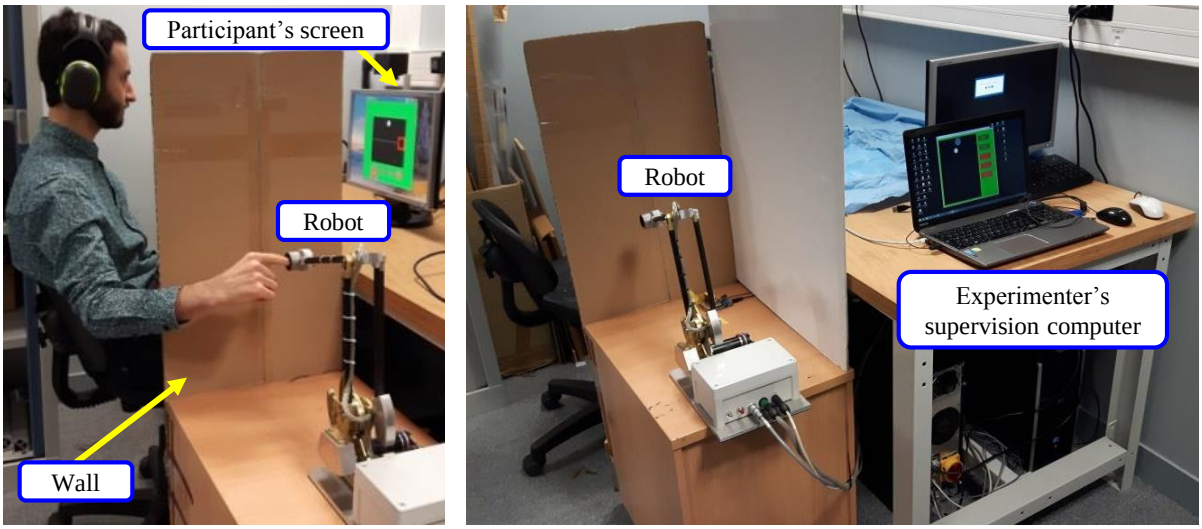

Figure 2.12: Representative experimental setup.

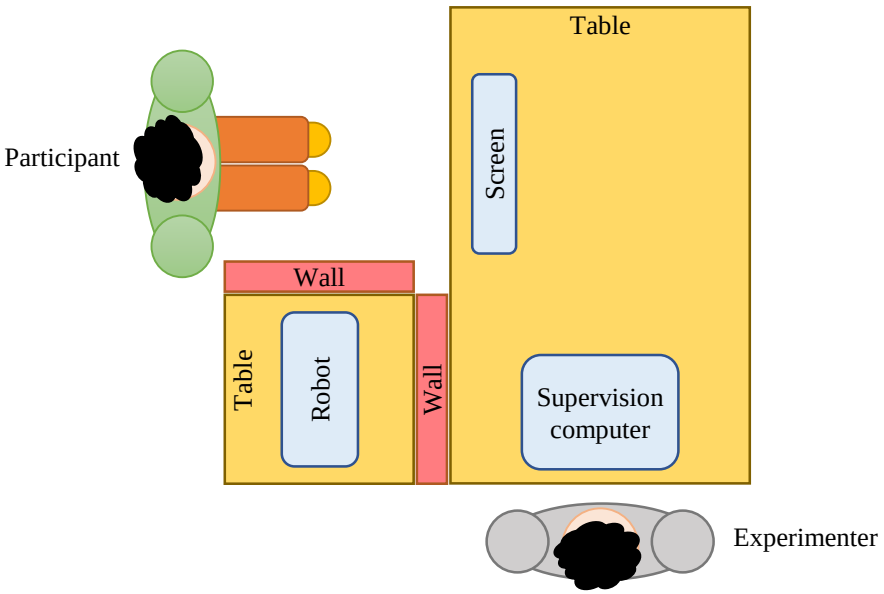

Figure 2.13: Experimental setup top view diagram.

It is worth noting here that the participant visualized a GUI that contained only the VE (as shown in figure 2.5) and that its displayed size was adapted to fit properly the available screen so that it could be clearly visualized from the user's location. A constant finger radius was employed for all participants to define the size of the finger avatar, in practice $R_f = 7.5$mm.

The experimenter visualizes a different version of the GUI, displayed on the supervision computer. It contains additional buttons allowing to turn on/off the force feedback as well as the tracking of the user's finger (in IC condition) and to select the corresponding VE for each task (see Fig.2.14).

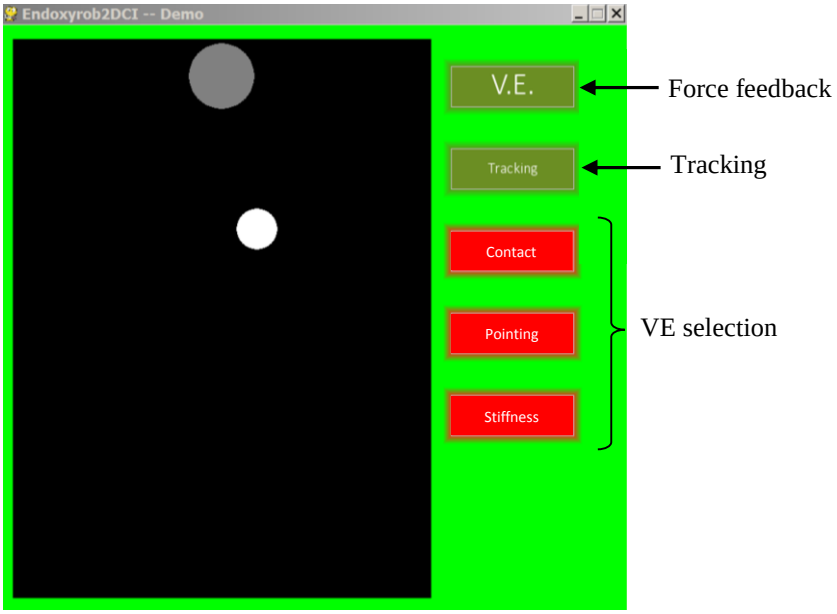

Figure 2.14: Experimenter graphical user interface.

2.3.4 Procedure

This section explains the general procedure for the performed experiments. The procedure describes what happens for each participant since the moment he/she arrives until he/she leaves the room where the experiment took place. The implemented procedure can be divided in several stages that are shown in figure 2.15.

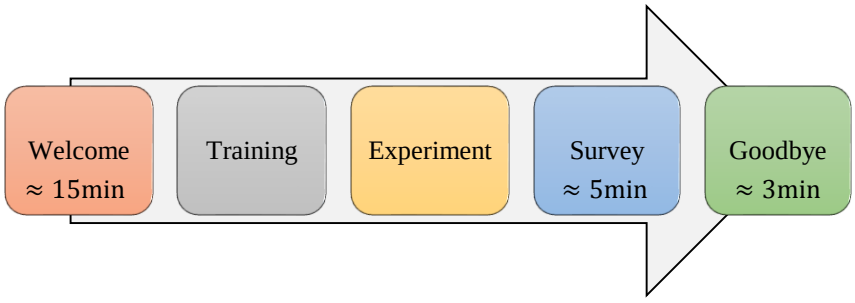

Figure 2.15: Genaral experimental procedure stages.

This figure provides also typical duration times for common stages (welcome, survey and goodbye). Specific typical times for each experiment will be described later in the reminder of this chapter.

2.3.4.1 Welcome

The following stages describe the welcome of a participant:

1. The participant was met at the main hall of the laboratory and taken to the experiment's room.
2. Once in the experiment's room, he/she was invited to take a sit and answer a general information form (profession, age, knowledge about computer tools, human machine and haptic interfaces).
3. The participant was then provided with a letter of consent, which explained the global process of the experiment he/she was about to perform. This letter gave in particular information on the following aspects:
    - the aim of the study,
    - how a haptic interface allows to interact with a VR,
    - a description of the CC and IC devices,
    - a description of the VR task to be performed as well as,
    - the recorded variables.
4. He/she was asked if there were questions about the global process.
    - A brief resume of the letter of consent was explained orally in order to reinforce the understanding of the general procedure.
5. Finally, he/she was asked to sign the letter to agree on the experimental conditions.

Since this was a voluntary participation, he/she was informed that he/she could quit the experiment at any time and because of any reason without generating any particular issue.

2.3.4.2 Training session

The aim of the training session is to provide the participants with practical information on the execution of the experiment and to allow them practicing until they feel confident with it. This training session focused on the following aspects:

- explaining to the participant the experimental conditions,
- teaching him/her how to manipulate the haptic interface according to the experiment to perform,
- explaining the structure of the experiment and
- practicing the corresponding VR task.

These points will be developed in the following paragraphs.

Experimental conditions. During the presentation of the layout of the main elements of the experiment to the participant, it was pointed out that during the experiment he/she was going to be sitting on a chair, wearing headphones and facing a screen where the VE was displayed. In addition to this, he/she was told that the robot (placed on a small table so that his/her right index finger could be placed comfortably inside the end-effector) was going to be hidden from his/her sight by a vertical wall.

The headphones let him/her listen a softened pink noise (not disturbing for the inner ear) during manipulations. This was intended to reduce the influence of surrounding parasitic noises, in particular those eventually generated by the haptic interface.

When any oral communication had to be established between the experimenter and the participant, the former talked to the later through a microphone located on the supervision computer. At this time the pink noise was turned off so the participant could listen to the experimenter's voice in the headphones. This solution allows to avoid removing the headphones each time oral instructions are required.

Haptic interface manipulation. As described in section 2.3.2.1 the employed haptic interface could be equipped either with a CC or with an IC end-effector. The 2DoF nature of this robot had to be taken into account when learning how to manipulate it in both CC and IC conditions, i.e. for displacing the finger avatar in free space, and if required for touching the virtual walls.

During the manipulation of the interface, the participant had to maintain his/her right index finger inside the robot's end-effector and to keep it perpendicular to the robot's working plane without pushing. Such task was somehow complicated, in particular in the IC condition, since in the absence of a mechanical link, nothing prevents the participant from moving his/her finger out the end-effector nor from changing its orientation without noticing it.

The correctness of the participant's gesture was verified by the experimenter and he/she was told to correct it if necessary. Enough time was given to him/her in order to learn how to manipulate the haptic interface.

Structure of the experiment. Each experiment required the participant to perform a VR task. The action of performing such task is denoted here as a **trial**. A **set** consists

then of a defined number of trials and a complete experiment is composed of a defined number of sets. The number of sets for each experiment will be specified later in this chapter. These definitions were explained to the participant prior to practicing the VR task.

Practice of the VR task. The participant had enough time to learn how to perform the VR task. Several trials were performed until he/she felt comfortable with it. In practice, at least one set of trials was performed.

2.3.4.3 Experiment

Prior to the experiment, the experimenter activates the corresponding VE by means of the GUI displayed on the supervision computer. In order to start, the participant is asked to put the headphones and to place his/her right index finger inside the end-effector of the haptic interface.

Oral instructions allowed to perform the transitions between trials. For a single trial, the experimenter proceeded in the following way:

1. The participant is invited to position the finger's avatar over the home position. Examples of employed phrases were:
   (a) "Please go to the home/starting position"
   (b) "O.k.! Let's move back to the starting position"
2. The experimenter activates the data recording and invites the participant to perform the VR task. Examples of employed phrases were:
   (a) "1, 2, 3, Go!"
   (b) "1, 2, 3, Let's go!"
3. Once that the participant had accomplished the task, a small break of 10s was given to him/her . At the same time the experimenter stopped recording data. During this break he/she was free to keep his/her finger inside the robot's end-effector or put it aside. Examples of employed phrases were:
   (a) "O.k.! Time for a break. You can put your arm aside if you wish"
   (b) "O.k. break!"
   (c) "Small rest!"

Once that a set of trials was completed, a longer break took place ($1-2$min). During this time the experimenter asked the participant to put his/her arm aside. The experimenter also asked him/her how he/she was feeling with the execution of the VR task and if he/she had any questions. At the same time complementary instructions were given if

necessary, e.g. in the case his/her gestures to manipulate the interface were not adequate. Once the break was finished, another set of trials started until completing the number of required sets for the whole experiment. A scheme of the building blocks of a typical experiment is shown in figure 2.16.

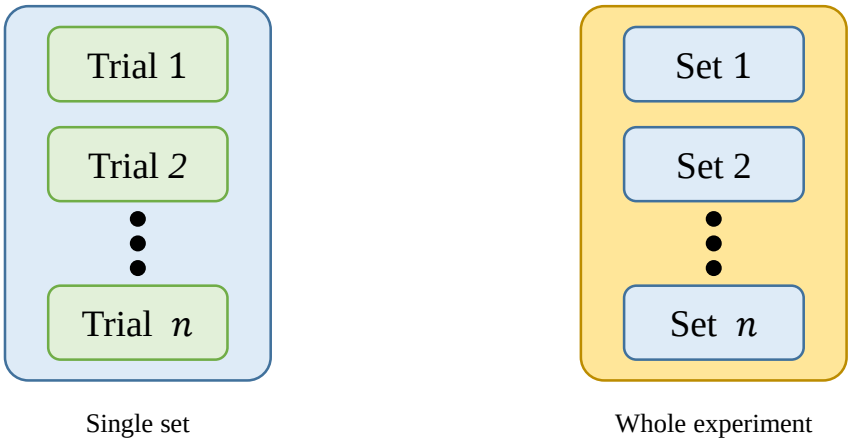

Figure 2.16: Scheme of a typical experiment.

2.3.4.4 Survey & goodbye

At the end of the experiment, the participant was asked to answer a survey. Finally a reward was given, e.g. a chocolate, prior to taking him/her back to the hall of the laboratory.

2.3.5 Data processing

The aim of the data processing was to identify meaningful differences/tendencies between the CC and the IC interface. To this end, a statistical analysis on the performance metrics of interest was performed for each experiment. On the other hand, the perception of the user was measured based on the provided answers during the survey performed at the end of each experiment.

2.3.5.1 Statistical analysis

The generated data were post-processed in order to perform quantitative comparisons. Boxplots were employed to analyze the results. Here the median appears inside the box as a horizontal line, the box represents the first (Q1) and third (Q3) quartiles and whiskers represent minimum and maximum values (see Fig.2.17). This method allows to observe the dispersion of data around the median as well as outliers without making any assumption on the underlying statistical distribution.

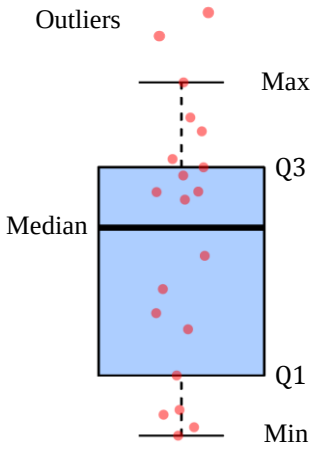

Figure 2.17: Elements of a boxplot.

In a second time, the statistical significance of the performance metrics was studied. To do so, an analysis of variance (ANOVA) was performed. Such test relies on data normally distributed (normality validated with a Shapiro-Wilk normality test) and on the equality of variances (equality validated with a Levene's test). In the opposite case, a non-parametric statistical test was employed (Friedman test).

Finally, in both cases the corresponding post-hoc test was performed.

2.3.5.2 Perception measurement

In order to asses the perception of the participants for each experimental condition, the answers were counted as a five-point Likert scale. Measured perception for each question was calculated using equation (2.9).

$$Pe_i = \frac{\sum_{j=1}^{5} n_{A_j} \cdot j}{\sum_{j=1}^{5} n_{A_j}} \tag{2.9}$$

where:

Pe_i	is the measured perception for question i
j	is the Likert level
A_j	is the selected option corresponding to Likert level j
n_{A_j}	is the number of participants that answered option A_j.

Statistical significance of Pe_i was assessed by means of a Wilcoxon one-tailed rank-sum test.

2.4 Experiment 1: Stiffness identification

This experiment aimed to provide elements of response to the following question: Does an IC haptic interface allow to better distinguish different stiffness values than a CC device? Therefore, it proposed to palpate a horizontal wall (displaying a nominal stiffness value) in order to guess (approximate) its value. To this end, the same wall could be switched to a variable stiffness mode where the user could modify the displayed stiffness. Switching between both modes could be done until both walls were perceived the same.

In the following sections, some elements which are specific to this experiment will be described, in particular the participants (section 2.4.1), the specific employed materials (section 2.4.2) as well as the specific setup (see section 2.4.3). In section 2.4.4 the specific procedure for the execution of the task will be detailed. Section 2.4.5 presents the employed performance metrics. Section 2.4.6 provides the obtained results and observations. Finally conclusions are given in section 2.4.7.

2.4.1 Participants

Ten subjects participated in this experiment: 7 males, 3 females. Their ages ranged from 24 to 36. All of them were right-handed.

2.4.2 Specific materials

2.4.2.1 Virtual environment

The VE employed for this experiment relies on the VE of reference displayed in figure 2.5. It contains however additional elements (see Fig.2.18), in particular a **horizontal wall** located at a distance of 12cm (in the real world) from the bottom and an **invisible zone** that avoids the user from visualizing this wall as well as the finger avatar. The goal of this invisible zone is to avoid the influence of visual feedback when palpating/pushing on the wall. The horizontal wall is modeled the same way as the surrounding green virtual walls, i.e. as a spring-damper system which behavior is defined in equation (2.5). As a consequence, a finger avatar pushing on it would displace downwards a longer distance if a low stiffness is displayed or a shorter distance in case of a high stiffness, allowing the participant to guess the difference from visual cues.

2.4.2.2 Remote control

The horizontal wall described in previous section 2.4.2.1 was employed to alternatively display two different stiffness and damping values defined as:

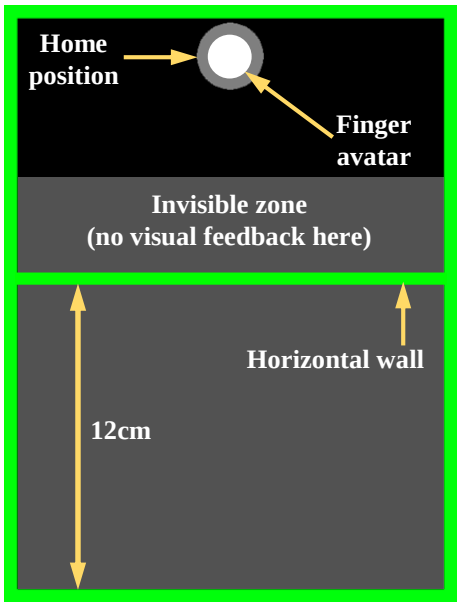

Figure 2.18: Stiffness identification VE.

- K_{ref}, being the displayed reference stiffness (reference mode),
- B_{ref}, being the corresponding damping value (fixed automatically to keep a K_{ref}/B_{ref} ratio roughly equal to 71 as with the gains from section 2.3.2.2),
- K_u, being the stiffness value, fixed by the user (variable mode) and
- B_u being the corresponding damping value, fixed automatically to keep $K_u/B_u \approx 71$.

These values were applied along $\boldsymbol{n}$, referring in this case to a vector normal (pointing upwards) to the horizontal wall.

Switching between both modes as well as other actions could be accomplished by means of the remote control shown in figure 2.19. Such control is composed of three elements:

- the **switch**, that allowed to toggle between the reference and variable modes,
- the **potentiometer**, that allowed, in variable mode, to modify the displayed stiffness of the wall (possible stiffness values ranged from 50 to 2500N/m),
- and finally the **push button** allowed to validate the chosen K_u value.

2.4.2.3 Questionnaire

In order to take into account the user's perception in relation to the experiment, he/she was asked to answer a survey at the end of it. The survey for this experiment included the following questions:

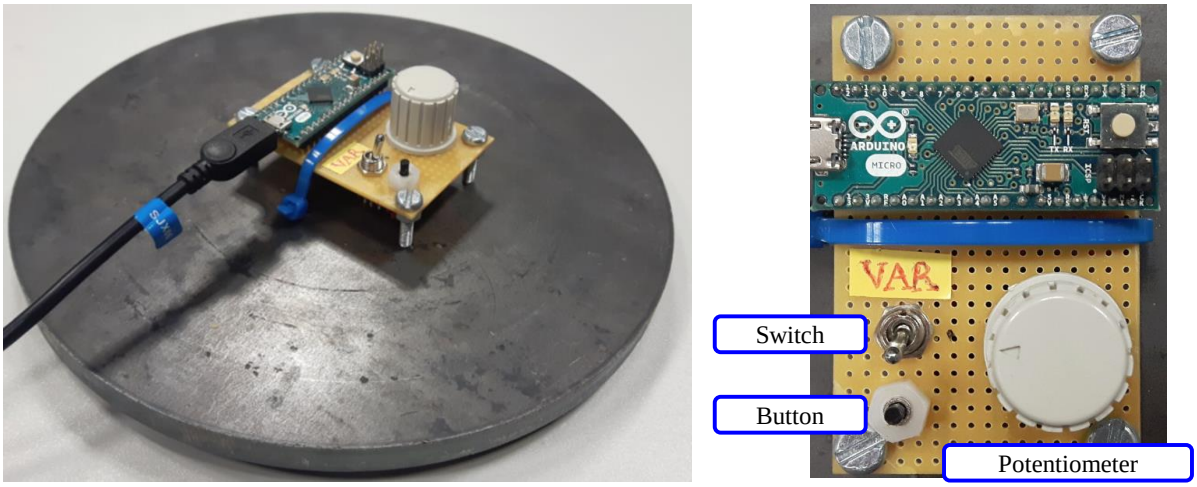

Figure 2.19: Stiffness identification experiment remote control

- **Q1.***Did you find it easy to approximate the variable stiffness value to the perceived reference stiffness when it was low?*
  1) Strongly disagree
  2) Disagree
  3) Neutral
  4) Agree
  5) Strongly agree

- **Q2.***Did you find it easy to approximate the variable stiffness value to the perceived reference stiffness when it was high?*
  1) Strongly disagree
  2) Disagree
  3) Neutral
  4) Agree
  5) Strongly agree

- **Q3.***Did you find the interface easy to use?*
  1) Strongly disagree
  2) Disagree
  3) Neutral
  4) Agree
  5) Strongly agree

- **Q4.***Did you find that the interface was tiring to use?*
  1) Strongly disagree
  2) Disagree
  3) Neutral
  4) Agree
  5) Strongly agree

The same group of questions were asked to each participant at the end of each test in both conditions (CC and IC).

2.4.3 Specific experimental setup

The experimental setup for this experiment required to integrate the remote control so that the participant could easily manipulate it with his/her left hand. Figure 2.20 shows a top view of the experimental setup integrating the remote control.

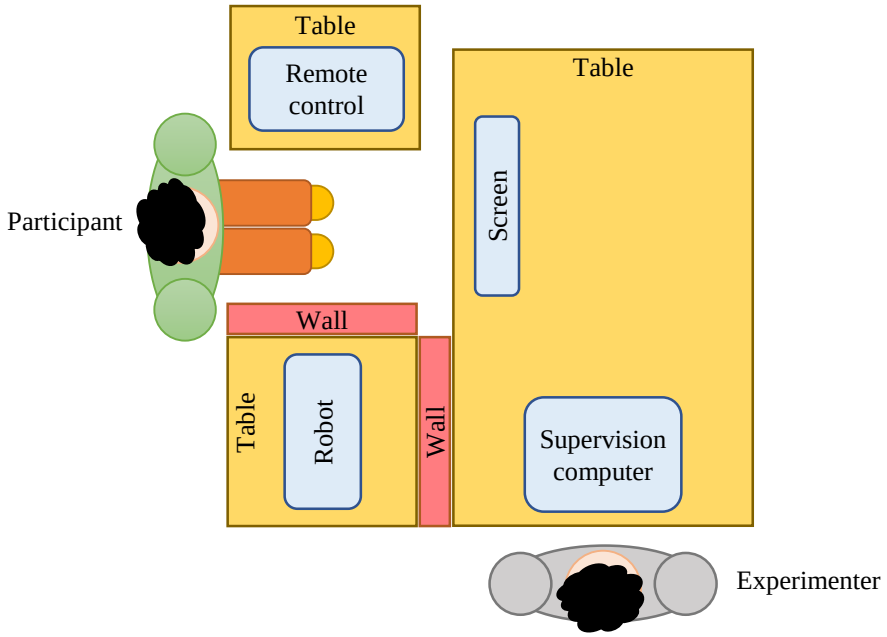

Figure 2.20: Stiffness identification experimental setup.

2.4.4 Specific procedure

In the present experiment a **trial** consisted in the palpation of a horizontal wall in order to guess the displayed reference stiffness. To this end, the same wall could be switched to a variable stiffness mode which current value K_u was retrieved from the potentiometer mounted on the remote control.

For each trial, the user was given a **limited time** (25s) to palpate the horizontal wall (with the index finger inside the robot's end-effector). He/she could switch between both stiffness modes as much as desired in order to make his/her choice of K_u (by pushing the button on the remote control). If the time given to perform the trial was over, the user had to press the button to validate the last K_u defined with the potentiometer. It is worth noting here that contact with the end-effector in the IC condition was allowed any time.

At the beginning of each trial, the reference mode was activated in order to randomly display one of the following five reference stiffness values:

$$\begin{bmatrix} 100 & 200 & 400 & 800 & 1600 \end{bmatrix} \text{N/m}$$

and their corresponding damping values:

$$\begin{bmatrix} 1.4 & 2.8 & 5.6 & 11.2 & 22.5 \end{bmatrix} \text{Ns/m}$$

It is important to mention that in order to apply any change of wall stiffness, including changing the stiffness mode, it was necessary to move the finger avatar to the visible zone, e.g. if the user switched to variable mode and/or modified the potentiometer's position, the finger avatar had to be displaced to the visible zone to apply such changes. The same was also valid when switching to the reference stiffness mode in order to display the reference stiffness value. A visual aid was provided to the participant, the home position being red in reference mode and green in the variable mode (see Fig.2.21).

A **set** was composed here of five trials (one trial per reference stiffness), with a 10s **break** each time. During each set each reference stiffness was presented once to the user. A total of three sets were performed (thus a total of 15 trials, i.e. 3 trials per reference stiffness value) in order to obtain three K_u values for each K_{ref} value (see Fig.2.22).

Prior to the experiment, the subjects had a **training** phase (15min). During this phase he/she was taught how to manipulate the interface with appropriate gestures and practiced the aforementioned sequence of actions in real experimental conditions. A representative flow of all building phases is shown in figure 2.23. Giving a representative time of $\approx$ 48min to pass the whole experiment, either in the CC or in the IC condition.

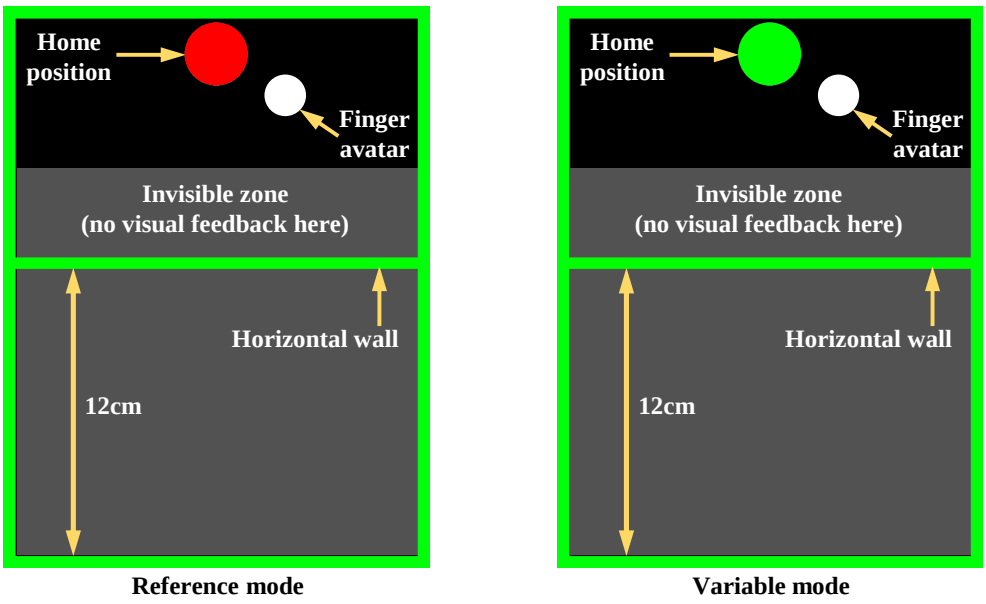

Figure 2.21: Stiffness identification visual aids.

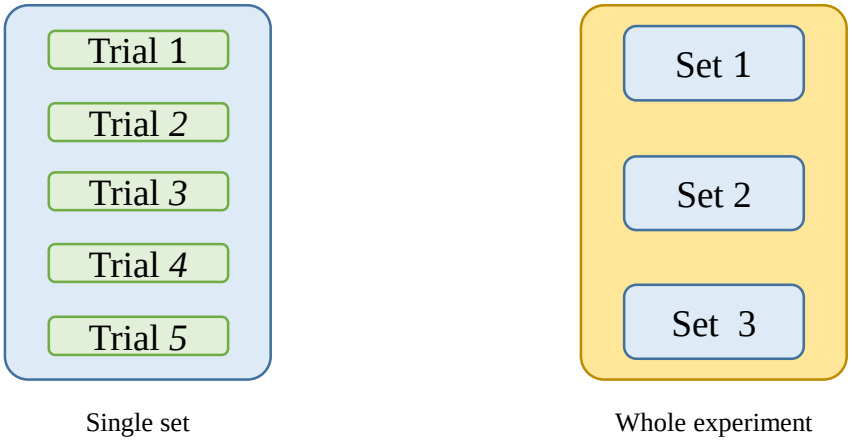

Figure 2.22: Stiffness identification experiment blocks.

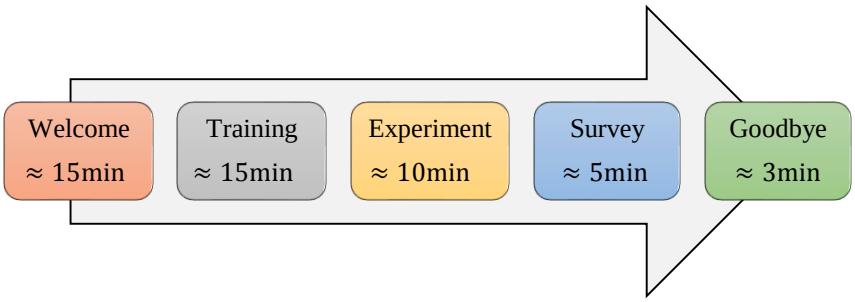

Figure 2.23: Stiffness identification procedure stages.

Transitions between trials and sets were performed by means the oral instructions introduced in section 2.3.4.3.

2.4.5 Performance metrics

The employed performance metric was based on the following formula:

$$D_s = \frac{K_{ref} - K_u}{K_{ref}} \times 100 \tag{2.10}$$

where D_s represents the difference, in percentage, between the reference and user stiffness values. A D_s value close to zero indicates a better approximation of the K_{ref} value, therefore a better performance.

2.4.6 Results & observations

As stated in section 2.4.5, the value D_s was defined as the performance metric of interest for the present experiment. We remind here that this metric expresses the difference, in percentage, between the reference stiffness K_{ref} and the user stiffness K_u.

Figure 2.24 shows the boxplot that allows to compare the behavior of the different samples in each case. It can be noticed that the data were grouped according to the condition (CC and IC) and according to the reference stiffness. Here each point represents the mean of the three trials performed by each user at each K_{ref} value. Several observations can be made based on this resource.

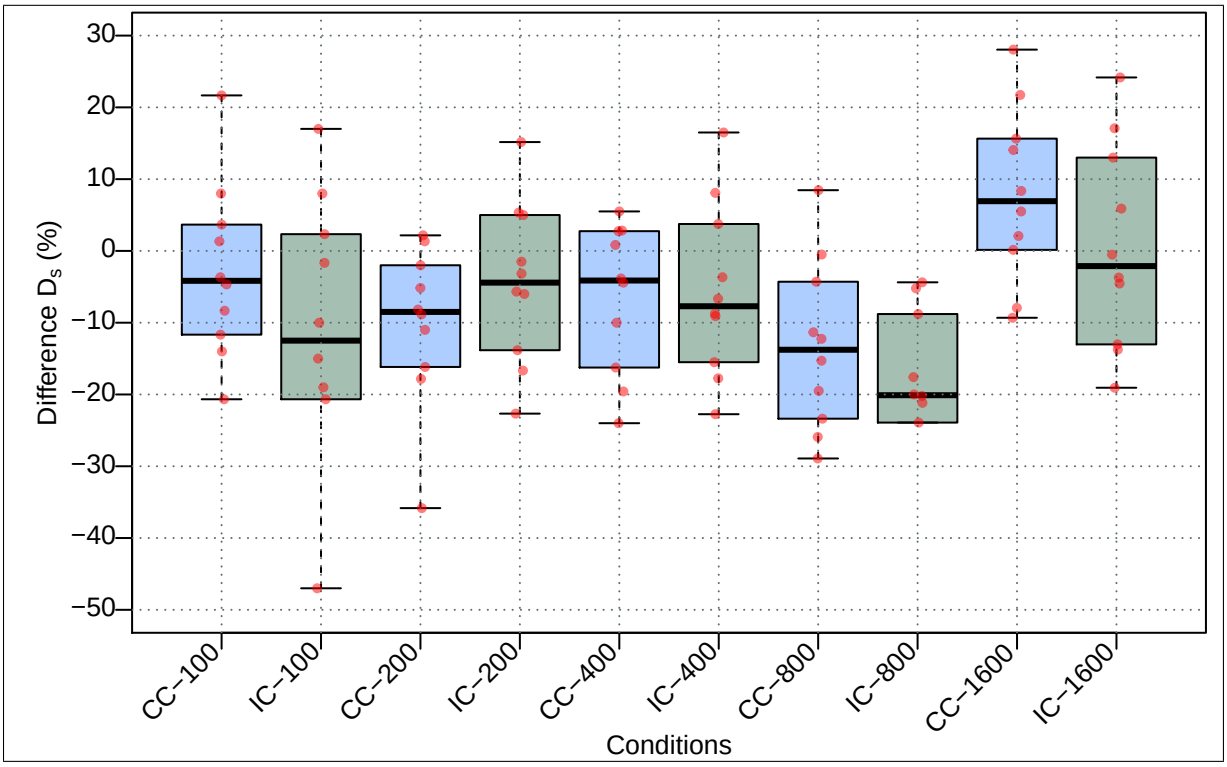

Figure 2.24: Difference D_S vs reference stiffness K_{ref} boxplot.

For low reference stiffness values ($K_{ref} = [100, 200, 400]N/m$), both interfaces show a D_s value spread quite similar. Around one third of the data points are found between 0% and 20%. Positive values imply an under estimation of the stimuli K_{ref}. On the other hand, around half of the data points are between -20% and 0%. Negative percentages imply that the user over estimated the stimuli K_{ref}.

For a medium stiffness value ($K_{ref} = 800N/m$), it can be stated that most of the data points are negative in both conditions. For this case there was a clear over estimation of K_{ref}.

Finally for a high stiffness value ($K_{ref} = 1600N/m$) the data points moved toward positive values. It can be seen that the tendency was to under estimate the stimuli, meantime in the IC condition over and under estimation of the stimuli looked similar. In this case the fact of not being mechanically linked to the interface may have influenced the results with data points similarly distributed around the reference stimuli.

In general, based on the results presented in figure 2.24, it is difficult to infer a clear difference between both interfaces. A post-hoc analysis of the Friedman test showed that

there was not a statistically significant difference between both interfaces ($p - value > 0.05$).

The measured perception P_e for this experiment is shown in figure 2.25. The chart shows the measured perception and the ideal value is highlighted by a dotted line. Based on this resource it can be noticed that the perception of participants of low K_{ref} values (Q1) was better in the CC condition. On the other hand no particular difference was observed in the perception of high K_{ref} values (Q2). It can be also noticed that the participants found the CC interface easier (Q3) and less tiring to use (Q4).

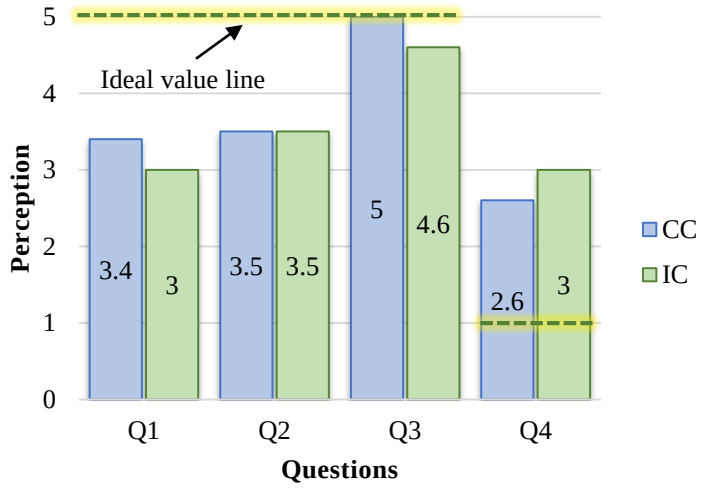

		P_e	$\tilde{x}$	*p-value*
Q1	**CC**	3.4	4	0.763
	IC	3	2.5	
Q2	**CC**	3.5	4	0.5828
	IC	3.5	4	
Q3	**CC**	5	5	0.9873
	IC	4.6	5	
Q4	**CC**	2.6	2.5	0.8622
	IC	3	3	

Q1: Did you find it easy to approximate the K_u value to the K_{ref} value when it was low?

Q2: Did you find it easy to approximate the K_u value to the K_{ref} value when it was high?

Q3: Did you find the interface easy to use?

Q4: Did you find that the interface was tiring to use?

Figure 2.25: Measured perception for 10 subjects for the stiffness identification task.

The table shows the corresponding median $\tilde{x}$ and the p value for a Wilcoxon rank-sum test. Despite the above provided observations, no statistical significant difference was reported ($p > 0.05$ in all cases).

2.4.7 Conclusion

A stiffness identification task was performed by a group of subjects in order to compare the benefits of an IC interface to those of a CC interface. During the experiment the subjects had to palpate a horizontal wall and manage to approximate a K_u stiffness to a K_{ref} stiffness, the performance metric for this experiment being the value D_s.

Results shown in a boxplot allowed us to observe that for low values users tended to over estimate the stimuli, meantime the opposite trend was observed for high values ($K_{ref} = 1600$N/m). After data processing, no statistical significant differences were reported between both interfaces. This was also the case for the measured perception.

From a general point of view, it can be concluded that the usage of an IC interface did not significantly modify the capacity of the subjects to perceive stiffness during a palpation task.

2.5 Experiment 2: Target pointing

A second experiment was proposed to answer the following question: is a target pointing task easier to perform with an IC haptic interface than with a CC device? In order to provide elements of response to this question, this experiment proposed a motor control task involving travel and targeting. Starting from an initial (home) position, the user had to point several targets of different sizes and located at various distances from the initial position.

In the following sections, some elements which are specific to this experiment will be described, related in particular to the participants (section 2.5.1) and to the specific employed materials (section 2.5.2). In section 2.5.4 the specific procedure for the execution of the task will be detailed. Section 2.5.5 presents the employed performance metrics. Section 2.5.6 provides the obtained results and observations. Finally, conclusions are given in section 2.5.7.

2.5.1 Participants

Ten subjects participated in this experiment: 5 males, 5 females. Their ages ranged from 22 to 60. All of them were right-handed.

2.5.2 Specific materials

2.5.2.1 Virtual environment

The VE employed for this experiment relies on the VE of reference presented in figure 2.5. It contains however additional elements (see Fig.2.26), in particular the **target**. The visualized target (bottom gray circle) is vertically aligned with the home position (top gray circle). In order that it is not hidden by the finger's avatar, its size is expanded. In practice, the diameter of the visualized target is equal to the nominal diameter of the target (W for width, in cm) plus the diameter of a reference finger $2R_f$ ($R_f = 0.75$cm). The relative distance between the center of the home position and the center of the target is called A.

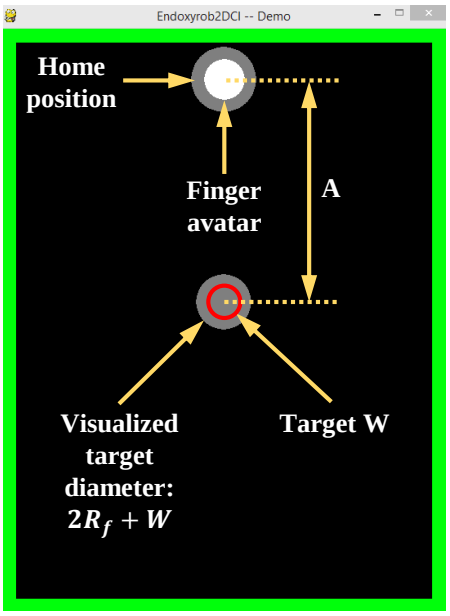

Figure 2.26: Target pointing VE.

2.5.2.2 Questionnaire

In order to take into account the user's perception in relation to the experiment, he/she was asked to answer a survey just after it. This survey included the following questions:

- **Q1.** *Were you able to reach the target easily?*
  1) Strongly disagree
  2) Disagree
  3) Neutral
  4) Agree
  5) Strongly agree

- **Q2.** *Were you able to reach the target rapidly?*
  1) Strongly disagree
  2) Disagree
  3) Neutral
  4) Agree
  5) Strongly agree

- **Q3.** *Did you find the interface easy to use?*
  1) Strongly disagree
  2) Disagree
  3) Neutral
  4) Agree
  5) Strongly agree

- **Q4.***Did you find that the interface was tiring to use?*
  1) Strongly disagree
  2) Disagree
  3) Neutral
  4) Agree
  5) Strongly agree

2.5.3 Specific experimental setup

The setup employed for this experiment is the one previously described in section 2.3.3.

2.5.4 Specific procedure

In the present experiment a **trial** consisted in displacing the finger avatar, from the home position to the center of the target and to remain there until obtaining the message "Target validated!". No particular instructions were given to the subject in terms of speed of the movement, however in order to obtain a valid trial the only constraint was to start and finish the movement performing a vertical movement, without moving sideways.

For each trial a limited time (10s) was given to move from the home position towards the target. The user had to manage to keep the finger avatar inside the target until visualization of the validation message. After validation, the user was asked to move his/her finger avatar back to the home position and wait (without removing his/her finger from the interface) for instructions to perform the next trial.

Different position and size values allowed to generate nine targets. The values employed for the position A of the target were:

$$\begin{bmatrix} 4 & 8 & 16 \end{bmatrix} \text{cm}$$

the values employed for the size W of the target were:

$$\begin{bmatrix} 0.25 & 0.5 & 1 \end{bmatrix} \text{cm}$$

Therefore in the present experiment a **set** was composed of nine trials, corresponding to the different possible combinations of distances and target sizes (as will be further explained below, these values were chosen in order to span a large range of tasks, from easy to very hard). A total of three sets were performed (27 trials in total, i.e. 3 trials per target configuration). This structure is illustrated by figure 2.27.

Prior to the experiment, the subjects had a **training** phase (15min). During this phase

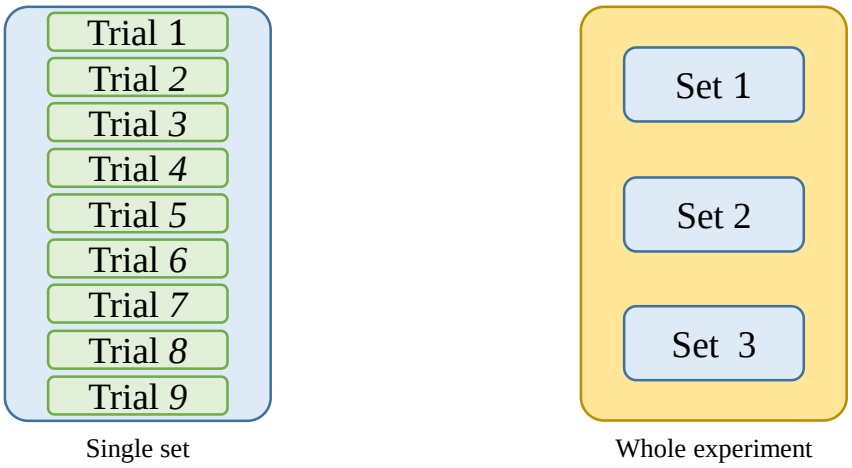

Figure 2.27: Target pointing experiment blocks.

he/she was taught how to manipulate the interface with appropriate gestures and practiced the aforementioned sequence of actions in real experimental conditions. A schematic representation of the flow of all building phases is shown in figure 2.28. The total time required for the whole experiment was ≈ 43min.

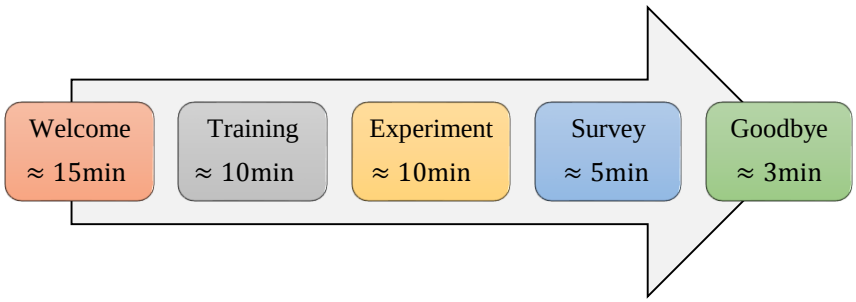

Figure 2.28: Target pointing procedure stages.

It is worth noting that, during the experiments performed with the IC haptic interface, the user was instructed to try to avoid touching the robot's end-effector. Transitions between trials and sets were performed by means the oral instructions, as explained in section 2.3.4.3.

2.5.5 Performance metrics

This experiment aims to assess the relative benefits of both interfaces when trying to perform a travel and targeting task. Within this context, Fitts's law provides a comprehensive set of metrics that can be used in this case [MacKenzie, 1995].

According to this law, the difficulty of a target pointing task can be quantified by means of information theory (measured in "bits"), that is:

$$ID = \log_2(2A/W) \tag{2.11}$$

where:

- ID is called the index of difficulty (in bits),
- A is the distance or amplitude to move (cm) and
- W is the width or tolerance of the region within which the move terminates (cm).

The A and W values presented in section 2.5.4 were chosen in order to sample a wide range of indexes of difficulty, giving as a result nine different combinations (targets). The chosen values allowed five difficulty levels denoted here as easy ($ID = 3$), medium-easy ($ID = 4$), medium ($ID = 5$), medium-hard ($ID = 6$) and hard ($ID = 7$). The corresponding ID values for each (A,W) combination are shown in table 2.3.

Table 2.3: Index of difficulty ID for each (A, W) combination.

Combination	A (cm)	W (cm)	ID (bits)	Level
1	4	1.00	3	Easy
2	4	0.50	4	Medium-easy
3	8	1.00	4	
4	4	0.25	5	Medium
5	8	0.50	5	
6	16	1.00	5	
7	8	0.25	6	Medium-hard
8	16	0.50	6	
9	16	0.25	7	Hard

The time to complete a movement task can be predicted using a linear equation function of ID:

$$MT = a + b \cdot ID \tag{2.12}$$

where:

- MT is the movement time (in s),
- a is the ordinate at origin (in s) and
- b is the slope coefficient (in s/bits).

Movement time values were recorded for each trial. Parameters a and b are constants that can be determined from experiments employing linear regression. Since these parameters are system dependent they could be used as benchmark metrics for performance comparisons between haptic devices [Samur, 2012].

These results allowed us to compute the index of performance IP which is of particular interest since it represents the amount of processed information per unit of time (bits/s), that is:

$$IP = \frac{ID}{MT} \tag{2.13}$$

2.5.6 Results & observations

During the experiment, several variables were recorded, including: the amplitude A of the movement, the target size W and the Cartesian position of the user's finger center $\boldsymbol{X}_{f/0}$. The later was used to compute the movement starting and end times, both allowing to calculate the movement time MT.

It is worth mentioning that the data of two subjects could not be taken into account for data analysis due to inappropiate manipulation of the IC interface. One of them continuously grazed the wall when performing the movement while the other grasped the IC end-effector using his/her index finger and the thumb.

Figure 2.29 shows the boxplot that allows to compare the different IPs at each ID for both haptic interfaces. It can be noticed that the data set was grouped according to the condition (CC and IC) and according to the index of difficulty ID. Each data point represents the mean of trials of each subject at each level of difficulty.

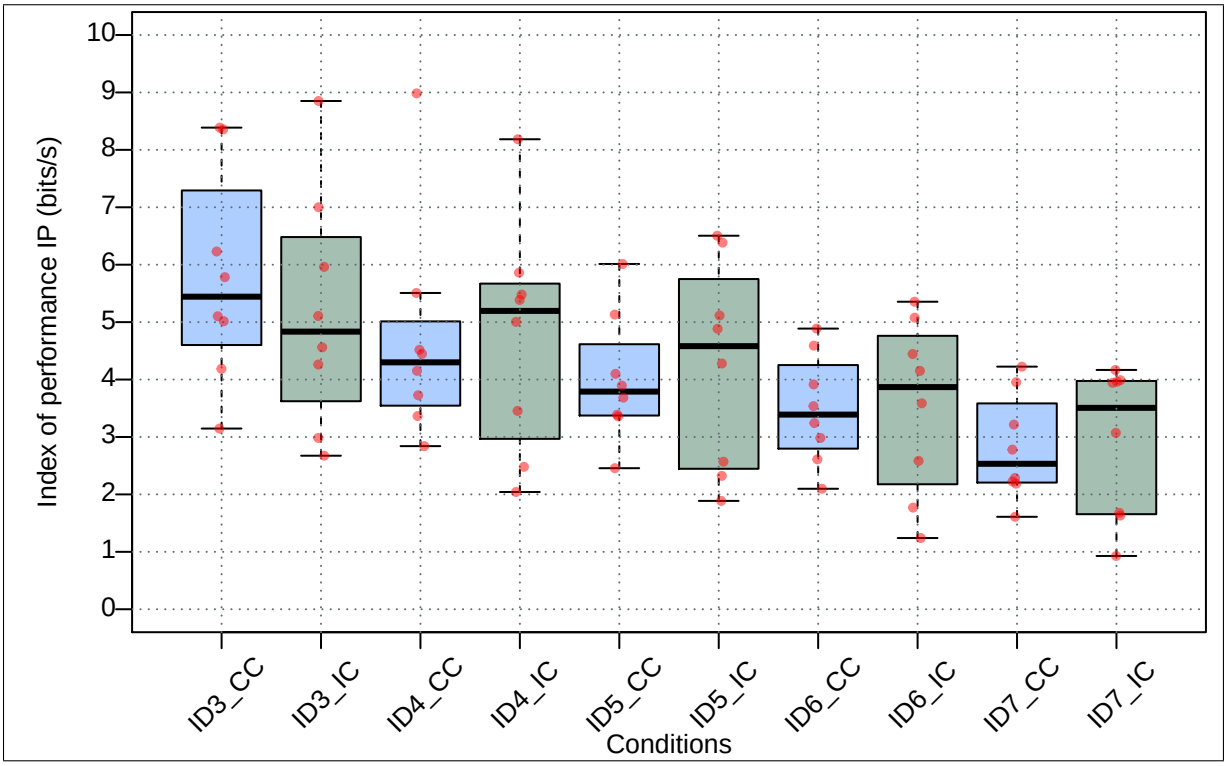

Figure 2.29: Index of performance IP vs. index of difficulty ID boxplot.

By looking at the boxes in the case of a task with the easiest level ($ID = 3$bits), it can be observed that the CC condition obtained a higher median than the IC condition. For a medium-easy task ($ID = 4$bits), IP median and data points show higher values in the

IC condition. Such tendency was also observed for medium ($ID = 5$bits), medium-hard ($ID = 6$bits) and hard tasks ($ID = 7$bits).

Friedman test was employed to assess the statistical significance of IP, however results did show that there was no statistical significant difference between both conditions ($p > 0.05$ in all cases).

The measured perception P_e for this experiment is shown in figure 2.30. The chart shows the measured perception and the ideal value is highlighted by a dotted line. Question Q1 aims to provide information about the task difficulty which is related with the ID. Question Q2 provides information related to the movement time MT. Questions Q3 and Q4 are generic questions regarding the employed interface.

Based on this resource it can be noticed that the participants found the target easier to reach in the IC condition (Q1), on the other hand similar speeds (Q2) were perceived in both conditions. The IC interface was perceived to be easier to use (Q3) and less tiring (Q4) than the CC one. In general the measured P_e values are close to each other, not showing a clear difference with the exception of Q4.

The table shows the corresponding median $\tilde{x}$ and the p value for a Wilcoxon rank-sum test. Despite the above provided observations, no statistical significant difference was reported ($p > 0.05$ in all cases).

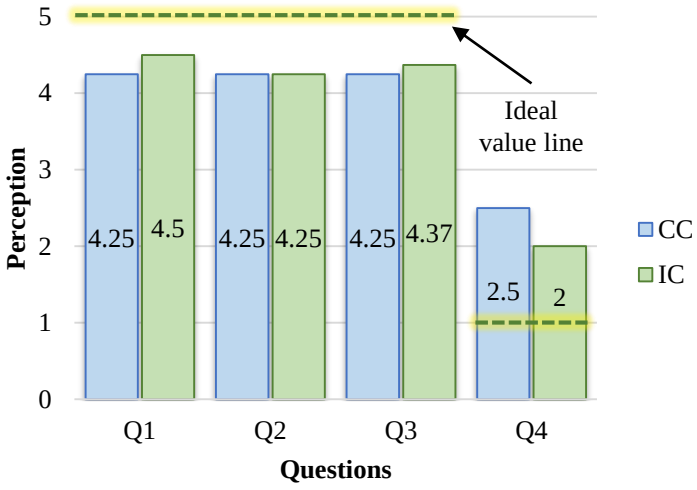

		P_e	$\tilde{x}$	*p-value*
Q1	**CC**	4.25	4	0.1573
	IC	4.50	5	
Q2	**CC**	4.25	4	0.6088
	IC	4.25	4	
Q3	**CC**	4.25	4	0.5000
	IC	4.37	4	
Q4	**CC**	2.50	2	0.3839
	IC	2.00	2	

Q1: Were you able to reach the target easily?
Q2: Were you able to reach the target rapidly?
Q3: Did you find the interface easy to use?
Q4: Did you find that the interface was tiring to use?

Figure 2.30: Measured perception for 8 subjects for the target pointing task.

2.5.7 Conclusion & perspectives

In the present section, a travel/targeting experiment was presented. The reported results showed that the index of performance trended to be higher in the IC condition.

The perception of the user regarding the experiment itself showed to be similar for both conditions in terms of ease and speed to reach the target. A similar feeling was reported in terms of ease to manipulate both interfaces. On the other hand, the IC interface was perceived as less tiring to manipulate.

Statistical analysis performed on the index of performance IP and on the measured perception P_e stated however that there was no significant difference between both conditions.

The fact of not being mechanically linked to the interface in the case of the IC condition may have influenced the user to displace faster during the movement. This may explain why the IP value trended to be higher for several IDs. To better compare the precision of the pointing task, the position of the user's finger relative to the center of the reached target could be studied.

It is worth noting that the proposed task did not include any free space to contact transition. An interesting complement to this study could be to add force feedback to the pointing task, e.g. to implement a serial tapping task as used by Fitts, i.e. a participant who taps as quickly and accurately as possible between two targets for several width W and distance A values. This kind of experiment would involve free space to contact transitions, therefore potentially revealing more realistic manipulations since breaks would only be done between each set and not between each trial, which in the performed experiments was judged to break the rythm of participants.

2.6 Experiment 3: Blind obstacle detection

Our last experiment aims at allowing to answer the following question: are free space to contact transitions more realistic employing an IC haptic interface than a CC interface? In order to provide elements of response to this question, this experiment proposed a blind obstacle detection task, which combines motor control and perception haptic modes: the user was asked to follow a vertical line (motor control) where he/she would encounter an invisible obstacle (horizontal wall) located at an unknown and variable position (perception).

In the following sections, the elements which are specific to this experiment will be described, in particular the participants (section 2.6.1) and the specific employed materials (section 2.6.2). In section 2.6.3, the specific procedure for the execution of the task will be detailed. Section 2.6.4 presents the employed performance metrics. Section 2.6.5 provides the obtained results and observations. Finally conclusions are given in section 2.6.6.

2.6.1 Participants

Ten subjects participated in this experiment: 7 males, 3 females. Their ages ranged from 24 to 28. All of them were right-handed.

2.6.2 Specific materials

2.6.2.1 Virtual environment

The VE employed for this experiment relies on the VE of reference presented in figure 2.5. It contains however additional elements, in particular a **horizontal wall** or obstacle (invisible to the user) located at a distance from the bottom of the VE which can be $x_{obs} = 0, 2, 4, 8$ or 12cm. This VE is shown in figure 2.31.

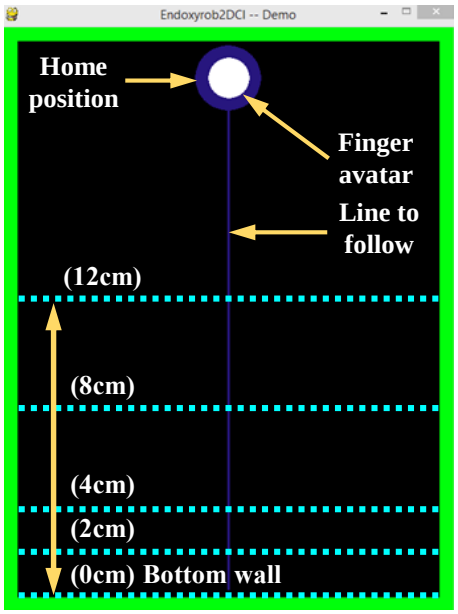

Figure 2.31: Blind obstacle detection VE.

2.6.2.2 Questionnaire

In order to take into account the user's perception in relation to the experiment, he/she was asked to answer a survey at the end of it. The survey for this experiment included the following questions:

- **Q1.** *Were you able to detect the obstacle easily?*
  1) Strongly disagree
  2) Disagree
  3) Neutral

4) Agree
5) Strongly agree

- **Q2.***Did you manage to not press too hard on the obstacle?*
  1) Strongly disagree
  2) Disagree
  3) Neutral
  4) Agree
  5) Strongly agree

- **Q3.***Did you rapidly stop as soon as the obstacle was detected?*
  1) Strongly disagree
  2) Disagree
  3) Neutral
  4) Agree
  5) Strongly agree

- **Q4.***Did you find the interface easy to use?*
  1) Strongly disagree
  2) Disagree
  3) Neutral
  4) Agree
  5) Strongly agree

- **Q5.***Did you find that the interface was tiring to use?*
  1) Strongly disagree
  2) Disagree
  3) Neutral
  4) Agree
  5) Strongly agree

2.6.3 Specific procedure

During each **trial**, the user was instructed to move his/her finger avatar along a vertical line (index finger inside the robot's end-effector) until he/she encounters a horizontal wall (obstacle, invisible to the user) which was positioned at an unknown variable distance from the bottom of the VE. No particular instructions were given regarding the speed of the movement.

For each trial the user was given a limited amount of time (10s) to start moving from the home position and encounter the obstacle. As soon as the user encountered the obstacle, he/she was asked to move back the finger avatar to the home position before having a 5s break (here the user was invited to keep his/her index right finger inside the interface). Once back in the home position, another trial could take place.

Five obstacle positions were presented randomly ($x_{obs} = 0, 2, 4, 8$ and 12). Therefore in the present experiment a **set** was composed of five trials (one per obstacle position). A total of four sets were performed (20 trials in total, i.e. 4 trials per obstacle position), with a one minute break between sets. This structure is illustrated by figure 2.32.

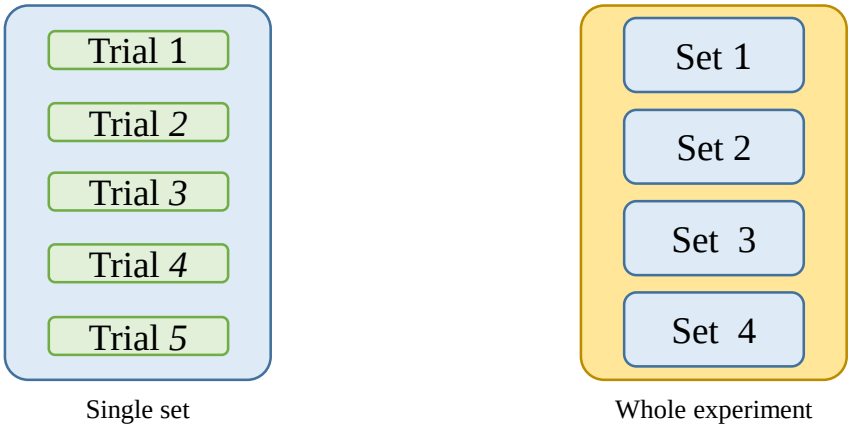

Figure 2.32: Blind obstacle detection experiment blocks.

Prior to the experiment, the participants had a **training** (10min). During this phase they were taught how to manipulate the interface by employing appropriate gestures (as an example, in order to ensure good functioning when using the IC interface, it was important to keep the index finger perpendicular to the robot's 2D workspace, without changing its orientation and without moving it out of the robot's end-effector). It was also told to the user that the robot's end-effector shouldn't touch him/her in free space when using the IC interface. A schematic representation of the flow of all building phases for this experiment is shown in figure 2.33. The total time required to perform it was about $\approx$ 45min.

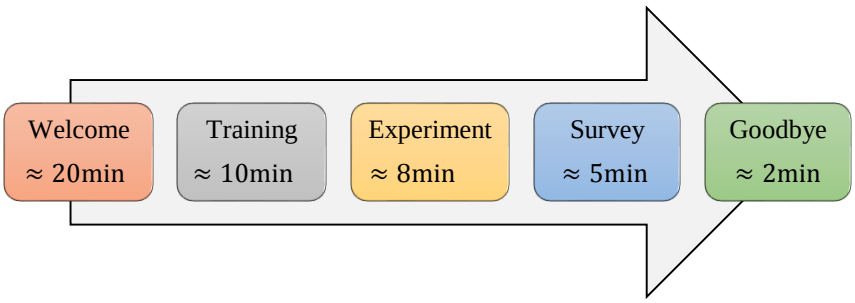

Figure 2.33: Target pointing procedure stages.

Transitions between trials and sets were performed by means of oral instructions as introduced in section 2.3.4.3.

2.6.4 Performance metrics

During the experiment, several data were recorded, including the obstacle position x_{obs}, the finger position $\boldsymbol{X}_{f/0}$ and its velocity $\dot{\boldsymbol{X}}_{f/0}$, the ring position $\boldsymbol{X}_{r/0}$ and its velocity

$\dot{\boldsymbol{X}}_{r/0}$ as well as the interaction force with the VE $\boldsymbol{F}_e$ (the later being computed from the obstacle and ring positions in the absence of direct force measurement).

These data allowed to calculate the following performance metrics for this experiment:

- $v_r(t_{cs})$, which corresponds to the speed (along the vertical axis) of the interface's end-effector (ring) when its avatar encounters the obstacle, i.e. when contact starts (the corresponding time denoted here as t_{cs}). This would provide the speed of the user in CC condition (since a mechanical link exists) and approximate user's speed in IC condition (since the end-effector is closely tracking and following the user).

- t_{cont}, represents the amount of time the user stays in contact with the obstacle. It is defined as the difference $t_{cf} - t_{cs}$, with t_{cf} being the instant of time when contact was finished. This data informs on the user's reaction time.

- $F_{e_{max}}(t)$ (with $t \in [t_{cs}, t_{cf}]$) corresponds to the maximum estimated force (along the vertical axis) during contact.

High user speeds are deemed to be the signature of a highly confident user. On the other hand, long contact times and high forces would to indicate that the contact was hard to detect.

2.6.5 Results and observations

The analysis of the benefits of both interfaces was assessed based on the performance metrics provided in previous section 2.6.4.

The data of three subjects had to be discarded for data analysis due to unexpected situations that generated extreme metric values. For instance, the recorded $F_{e_{max}}$ values for one of them were zero for nearly half of the trials, while two other subjects manipulated the CC or the IC interface several times at much higher speeds ($\approx 0.4m/s$) than the rest of the subjects (≈ 0.10m/s), hence completely different position and force profiles. Therefore data processing was based on data corresponding to only 7 subjects.

Figure 2.34 shows a boxplot where each v_r point represents the mean of all trials for each subject at each obstacle position x_{obs}. It can be observed that most of speeds remained lower than $|v_r| = 0.15$m/s (taking into account the speed's absolute value, all speeds being negative as the user was moving downwards). Based on the medians, we can state that the participants reached in general higher speeds when manipulating the CC interface. This observation raises the following question related to the manipulation of the IC interface: why participants move slower in this case? A possible answer could be that they concentrated more on the gesture (which was difficult to perform in this configuration, i.e. follow a vertical line, with the right index finger inside the end-effector

and perpendicular to the robot's working plane while at the same time avoiding to touch the robot) than on the task itself.

Figure 2.35 shows a boxplot where each t_{cont} point represents the mean of all trials for each subject at each obstacle position x_{obs}. In general, it can be observed a clear trend to stay longer in contact with the obstacle with the IC interface (lower medians in the CC condition). It can be also noticed that the t_{cont} value slightly increases in both conditions when the distance between the home position and the obstacle becomes shorter (the closer the obstacle, the longer the contact).

Figure 2.36 shows a boxplot where each $F_{e_{max}}$ point represents the mean of all trials for each subject at each obstacle position x_{obs}. Here it can be observed that less force was applied with the IC interface. This is somehow interesting since in this case the participant did not require to apply a lot of force to detect the obstacle, which is closer to reality.

Friedman test was employed on the presented data sets in order to asses for a statistically significant difference between both interfaces. The performed tests on each of the performance metrics did not show any significant difference between CC and IC haptic interfaces ($p > 0.05$ in all cases).

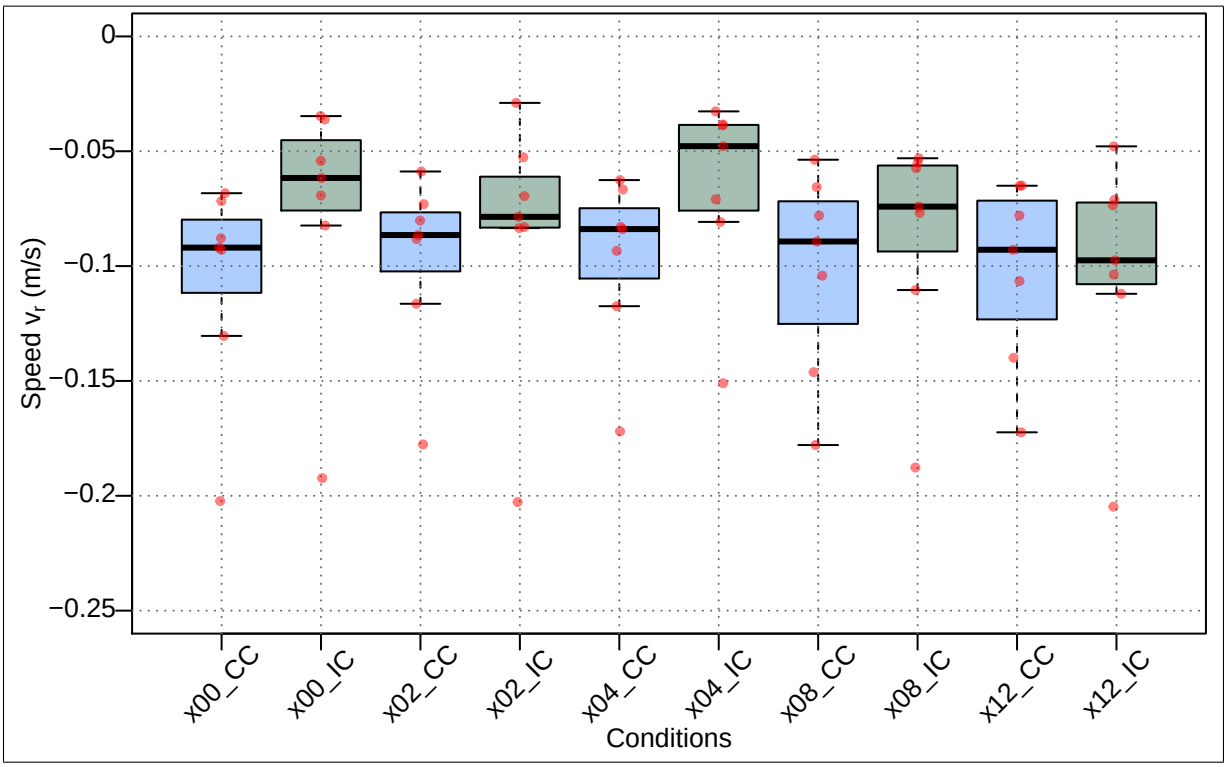

Figure 2.34: End effector's speed v_r vs. obstacle's position x_{obs} boxplot.

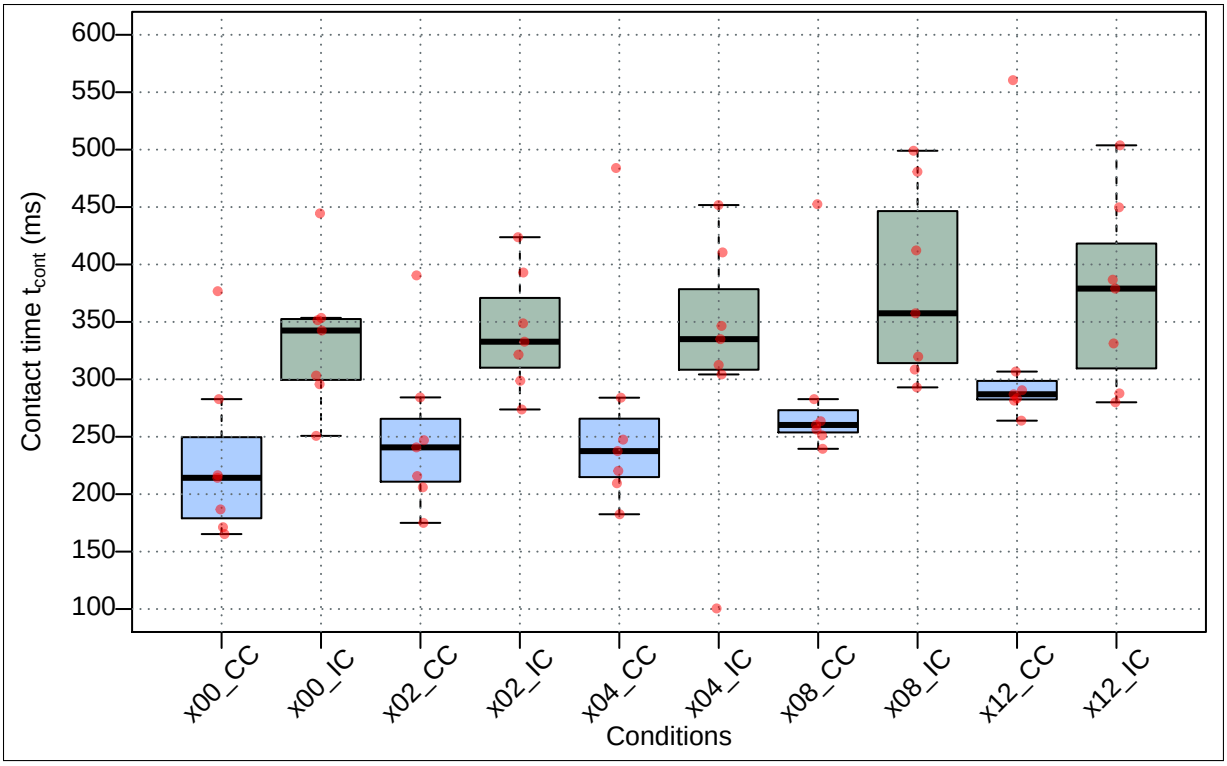

Figure 2.35: Time in contact with the obstacle t_{cont} vs. obstacle's position x_{obs} boxplot.

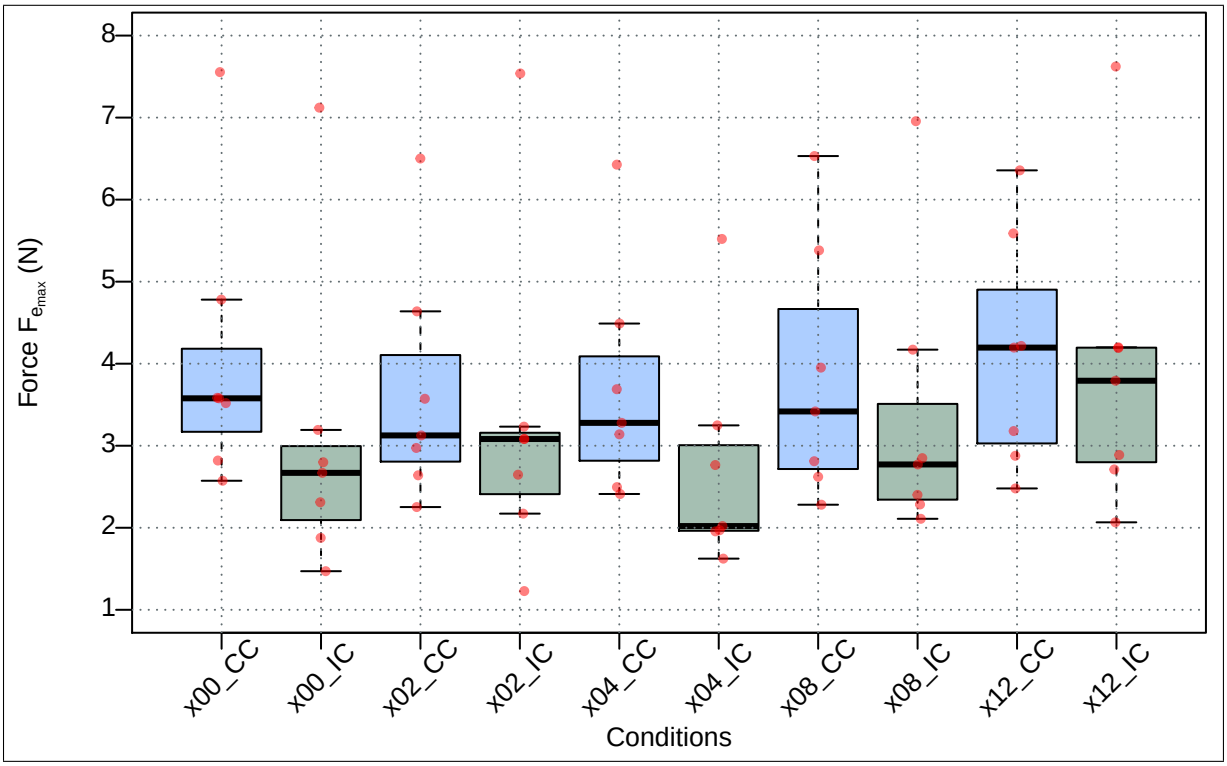

Figure 2.36: Maximum estimated force during contact $F_{e_{max}}$ vs. obstacle's position x_{obs} boxplot.

The measured perception (computed from the results of the survey) is shown in figure 2.37. It can be observed that subjects reported similar ease to perceive contact with both

interfaces (Q1). On the other hand, they estimated that they applied smaller forces (Q2) using the IC interface (this being consistent with the observations reported in Fig.2.36). Participants considered that their reaction time was faster in the IC condition (Q3), which is inconsistent with the results reported in figure 2.35. Finally users found the CC interface easier (Q4) and less tiring (Q5) to use.

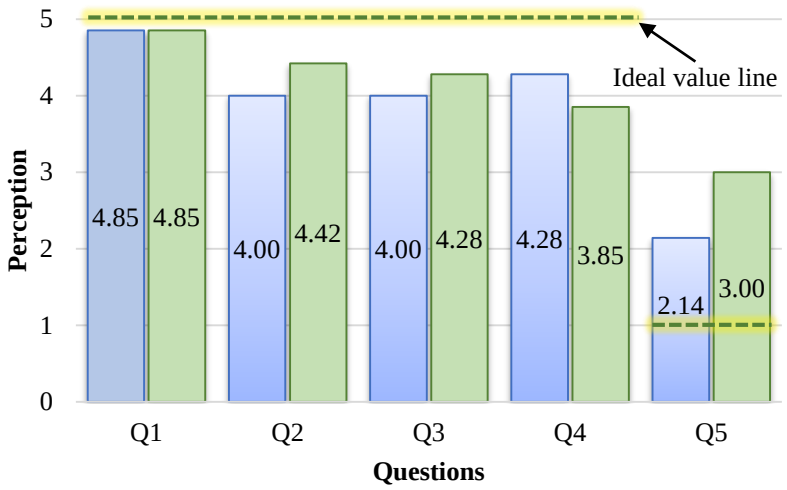

		P_e	$\tilde{x}$	*p-value*
Q1	**CC**	4.85	5	0.7692
	IC	4.85	5	
Q2	**CC**	4.00	4	0.2043
	IC	4.42	5	
Q3	**CC**	4.00	4	0.3164
	IC	4.28	4	
Q4	**CC**	4.28	4	0.7529
	IC	3.85	4	
Q5	**CC**	2.14	2	0.9528
	IC	3.00	3	

Q1: Were you able to detect the obstacle easily?

Q2: Did you manage to not press too hard on the obstacle?

Q3: Did you rapidly stop as soon as the obstacle was detected?

Q4: Did you find the interface easy to use?

Q5: Did you find that the interface was tiring to use?

Figure 2.37: Measured perception for 7 subjects for the blind obstacle detection task.

2.6.6 Conclusion

Generally speaking, no significant difference between both interfaces was found, however certain tendencies could be observed. For example, longer contact times and smaller user speeds prior to contact with the IC interface were unexpected but somehow not stunning since learning to use this kind of device was not straightforward. The presented experiment highlighted the fact that a mechanical link, even in free space, as is only present with the CC interface, reassures the user. For an IC interface, any slight haptic stimuli may be necessary to bypass this issue. On the other hand, this tendency appears quite logical. Indeed, in the IC conditions, the user has a bare finger and must be cautious while in the CC condition he has a kind of protecting layer which could unconsciously reassure him (with such a protection he can move quickly without risks of injuries). It would be interesting to test this hypothesis in a future test campaign.

2.7 Chapter conclusion and perspectives

Choosing a force feedback interface is not a straightforward task. Besides taking into account the device's metrics (DoF, workspace, inertia, maximum exertable force, etc.), it is fundamental to evaluate its performances in real conditions, i.e. while being manipulated by an user. To this purpose, device evaluation based on psychophysical tests (linking the device performance measures to the limits of human perception) represent a pertinent approach.

This is also true for IC haptic interfaces. Indeed, while the IC paradigm theoretically provides perfect transparency in free space and more realistic haptic interactions at contact, the benefits of this type of devices are still not clearly known. Learning about their benefits was the purpose of the presented research.

To this end, we performed three experiments: stiffness identification, target pointing and blind obstacle detection. It was concluded from the first experiment that the usage of an IC interface did not significantly modify the capacity of the subjects to perceive stiffness. On the other hand, the target pointing and the blind obstacle detection experiments highlighted somehow that a mechanical link plays an important role to reassure the user, particularly when manipulation occurs in free space. However none of the presented experimental results showed a significant difference on performance metrics regarding both types of haptic interfaces.

This is encouraging because it means that, even though an IC interface is less intuitive to manipulate when considering only 2DoF movements (such movements are difficult to perform in this configuration as the user has to move along a given trajectory while maintaining his/her finger inside the end-effector and perpendicular to the robot's working plane while at the same time avoiding to touch the robot), its employ did not impoverish the capacity of the participants to perform the proposed tasks.

In order to encourage the development of more performing IC interfaces it is important to learn on current devices capacities. Ergonomics of IC devices indeed plays an important role since users are intended to use them in the most natural possible way, e.g. the user should concentrate on the task itself and not on how to position his/her hand to make the device work properly. The development of IC haptic interfaces with higher degrees of freedom ($\geq$2DoF) is thus expected to provide more natural manipulations. This will release the aforementioned usage difficulties, and one can reasonably make the assumption that in this case IC interfaces will outperform CC devices. Further developments are however necessary to validate this hypothesis.

Finally, IC interfaces remain, from our perspective, a promising approach. We may think of a variety of IC devices configurations, among which end-effectors that can fit already existing robotic arms (using the IC paradigm, even those ones that were not designed for haptic interactions can be employed for this purpose).

Chapter 3

Improvement of Contact Rendering at High Speeds

Contents

3.1 Introduction

A good force feedback interface should allow stable interactions, whether the user is moving in free space or getting in touch with a VO. In the case of IC haptic interfaces, this is particularly challenging since besides displaying a stable behavior in both modes, the control law must also ensure a stable transition between free space and contact (see Fig.3.1).

First tested control strategies for IC-HIs were reported in [Hirota and Hirose, 1993], [Yoshikawa and Nagura, 1997] and [Yoshikawa and Nagura, 1999]. Such approaches relied on an abrupt transition between free space and contact modes. While simple, this solution can generate oscillations (based on non-passive energetic exchanges) and therefore a non-realistic contact sensation, especially when encountering a VO at high speeds. On the contrary, an ideal IC interface must switch from closely following the user's movements to a completely stabilized (and usually fixed) position prior to be contacted by the user. As abrupt transitions do not fulfill this requirement, smooth transition strategies

were proposed later. This way, stable transitions have already been accomplished in a previous work [Gonzalez, 2015] with an existing 2DoF IC interface (see section 2.3.2.1 or appendix A for more details on the interface), however only at speeds up to 0.2m/s. For faster movements, oscillations unfortunately reappear.

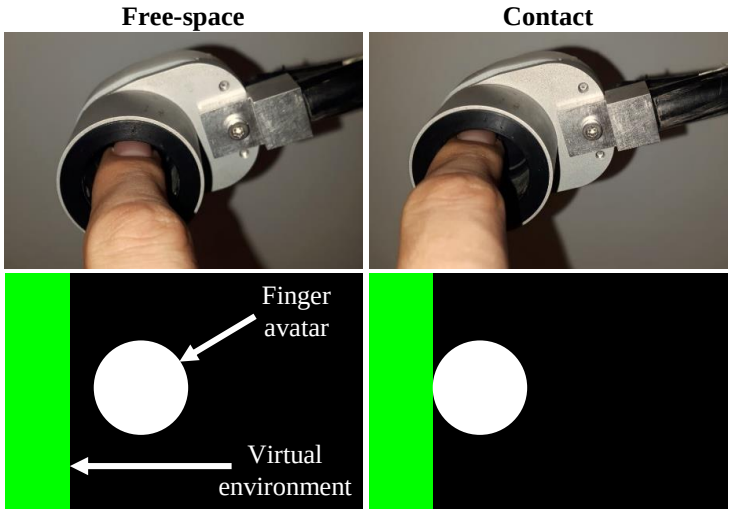

Figure 3.1: Free space to contact transition in real and virtual worlds.

This is relatively embarrassing since in practice typical movements in VR environments are performed at speeds up to 4.6m/s [Elgendi et al., 2012b]. Providing stable free space to contact transitions only up to 0.2m/s thus limits the scope of possible applications.

In order to allow for a larger range of applications, oscillations must be reduced even for high speed contacts. This is the goal of the work presented in this chapter which introduces a contribution aiming to improve the free space to contact transitions at higher speeds (tests performed up to $\approx$ 0.4m/s). The efficiency of our approach was validated using quantitative performance metrics. As we were also interested in evaluating how natural the contact was perceived, we performed user tests as well. To this end, a group of six participants was invited to perform a certain number of taps on a virtual wall at low and high speeds, employing an existing 2DoF IC haptic interface in order to test the current implemented control law (smooth transition strategy) and the novel approach we proposed.

The present chapter is organized as follows: in section 3.2 the current control law implemented on the available 2DoF IC interface (already presented in section 2.3.2.3) is briefly recalled. In section 3.3 the proposed strategy allowing to perform stable free space to contact transitions at higher speeds ($>$ 0.2m/s) is detailed. Section 3.4 presents results of the preliminary comparison cases between both control laws and section 3.5 presents the description and results obtained from user tests. Finally, conclusions and perspectives are drawn in section 3.6.

3.2 Smooth transition-based control

As detailed in section 2.3.2.3, the control of the IC-HI relies on two modes: free space and contact. The goal of the control in free space is to reduce the tracking error $\boldsymbol{\epsilon_X}$ in order to closely track and follow the user's finger without touching it (see Eq.(2.1)). Such error minimization is achieved with a proportional derivative controller, which provides the robot with a reference tracking torque $\boldsymbol{\tau}_t$ (see Eq.(2.3)).

On the other hand, the goal of the contact mode is to display to the user the mechanical properties of the VO being touched. Such force $\boldsymbol{F}_e$ is calculated as an unilateral constraint assuming a viscoelastic compliant VE without tangential friction (see Eq.(2.5)).

Finally, the smooth transition between free space and contact modes is achieved by reducing the influence of the tracking force $\boldsymbol{F}_t$ (send to the robot as a tracking torque $\boldsymbol{\tau}_t$) by a factor β nearby the obstacle. Such transition is illustrated in figure 3.2.

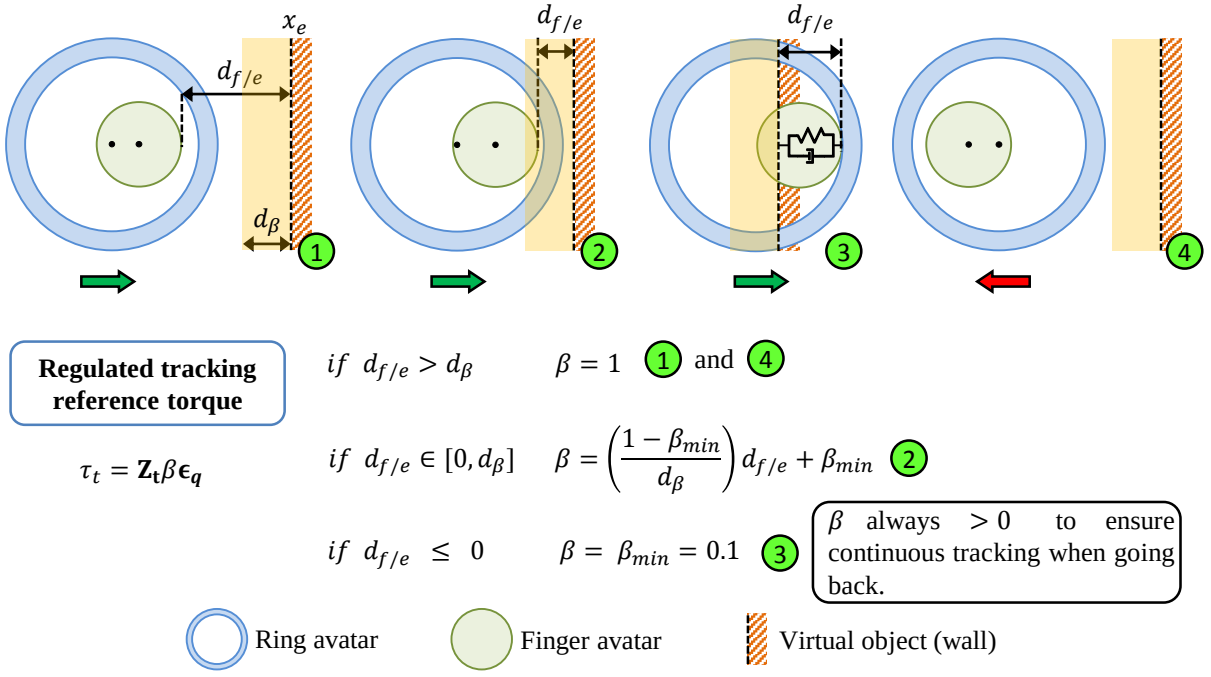

Figure 3.2: Smooth transition-based control illustration.

While allowing a smooth transition between free space and contact, this algorithm presents in practice an undesired behavior when contacting a VO at high speeds (>0.2m/s): oscillations appear when the ring encounters a VO and therefore an unnatural contact is perceived by the user when his/her finger encounters the interface's end-effector, giving the impression of touching a moving object instead of a static one as in real life.

As it will be noticed, the contribution described in the remaining of the present chapter focuses on the transition strategy.

3.3 Offset transition-based control

Smooth transition-based control proved to be stable with interactions occurring at low speeds (≈ 0.2m/s) [Gonzalez, 2015]. However at higher speeds (> 0.2m/s) the problem is not completely tackled and the sensation felt at contact may be non-realistic.

In the present section we propose a different strategy to perform stable free space to contact transitions for faster movements. Taking the smooth transition-based approach as a base, the proposed approach adds bilateral damping contributing to the stabilization of the robot's end-effector before application of the force feedback. As will be shown later, this comes at the price of a slight shift of the virtual constraint, which remains however imperceptible for most users as proved by the results of our evaluations. Such approach is denoted here as offset transition-based control law.

3.3.1 Principle of the offset transition-based control

In free space, the user can move the interface freely, i.e. no interaction force exists. When the ring's inner periphery penetrates in a VO, we propose to completely stop it before displaying the VO properties. To do this, a dissipative force is applied on the ring until the interface is static (in practice until $|\dot{\boldsymbol{X}}_{r/0}| < v_{th}$, with v_{th} a threshold introduced to cope with the noise of the speed signal).

In practice, the speed threshold is tuned experimentally. It was set here at $v_{th} \approx 0.02$m/s, which corresponded to a static interface with a finger inside the ring. When the mentioned condition was true, the new VO position x_ε was defined as the coordinate of the distal point on the inner periphery of the ring, then the VO properties ($\mathbf{K}_e$ and $\mathbf{B}_e$) were rendered to the user.

This algorithm was implemented using a Finite State Machine (FSM) as shown in figure 3.3. Each state description is presented below.

- **Transparent state:** this state becomes active when the relative distance between the ring avatar to the VO is greater than d_β, i.e. $d_{r/e} > d_\beta$. In this mode only the tracking force $\boldsymbol{F}_t$ acts on the ring, implying $\boldsymbol{F}_e = 0$. As soon as the interface approaches the VO and the inner periphery of the ring penetrates into it ($d_{r/e} < 0$) the braking state becomes active.

- **Braking state:** in this state a bilateral force $\boldsymbol{F}_d$ is exerted on the ring (see Eq.(3.1)) with $\mathbf{B}_d$ being the dissipation gain. When $|\dot{\boldsymbol{X}}_{r/0}| < v_{th}$ the VO state becomes active.

$$\boldsymbol{F}_d = -\dot{\boldsymbol{X}}_{r/0}\mathbf{B}_d\boldsymbol{n} \tag{3.1}$$

- **VO state:** in this state the VO properties (the same as implemented in the original control law) are displayed.

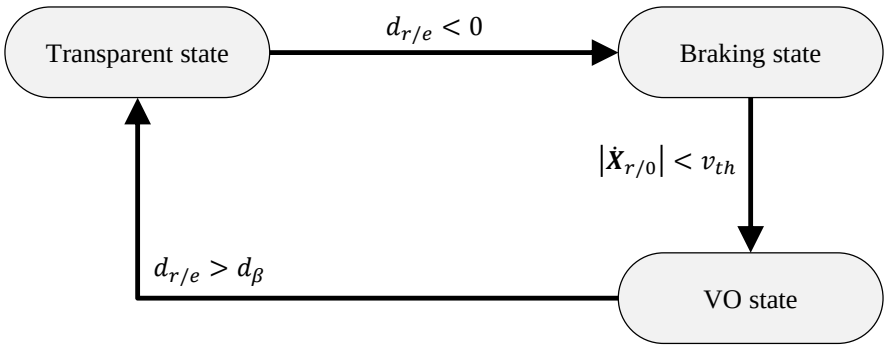

Figure 3.3: Finite State Machine governing the proposed control law.

Equation (3.2) defines $\boldsymbol{F}_e$ in reference to the VO new position x_ε, where $d_{r/\varepsilon}$ represents the relative distance between the ring inner periphery and this new constraint.

$$\boldsymbol{F}_e = \begin{cases} \text{if } d_{r/\varepsilon} < 0 \ \& \ \dot{\boldsymbol{X}}_{r/0} > 0 \text{ then } \boldsymbol{F}_e = -d_{r/\varepsilon}(\mathbf{K}_e + \mathbf{B}_e s)\boldsymbol{n} \\ \text{if } d_{r/\varepsilon} < 0 \ \& \ \dot{\boldsymbol{X}}_{r/0} < 0 \text{ then } \boldsymbol{F}_e = -d_{r/\varepsilon}\mathbf{K}_e\boldsymbol{n} \\ \text{else } \boldsymbol{F}_e = 0 \end{cases} \tag{3.2}$$

3.3.2 Management of the tracking force

As previously explained, the influence of the tracking force must diminish when the ring touches the wall, however it must be strong enough for the interface to follow the user's finger when it moves away from the VO. Also, it is important to have a continuous tracking force to ensure that the interface will behave correctly during transitions between free space and contact modes.

In the original control law the influence of the tracking force $\boldsymbol{F}_t$ decreased by a factor β function of $d_{f/e}$ (relative distance between the finger avatar and the virtual environment), to ensure its continuity. This approach makes factor β to reach its minimum value β_{min} when the finger avatar is in contact with the VO.

For the control algorithm presented in section 3.3.1 we proposed to decrease factor β in function of an augmented avatar of the finger. By making its radius equal to R_r (that of the inner radius of the ring), the minimum value of $\boldsymbol{F}_t$ is already reached by the time the ring's avatar penetrates in the reference wall x_e. Indeed, because of the tracking error $\boldsymbol{\epsilon_X} \neq 0$, the finger's center position is always in advance to that of the ring in the direction of the motion. This way, the finger avatar will first penetrate in the reference (x_e) then in the offset (x_ε) VO boundary. This strategy, as well as the corresponding applied forces are illustrated in figure 3.4.

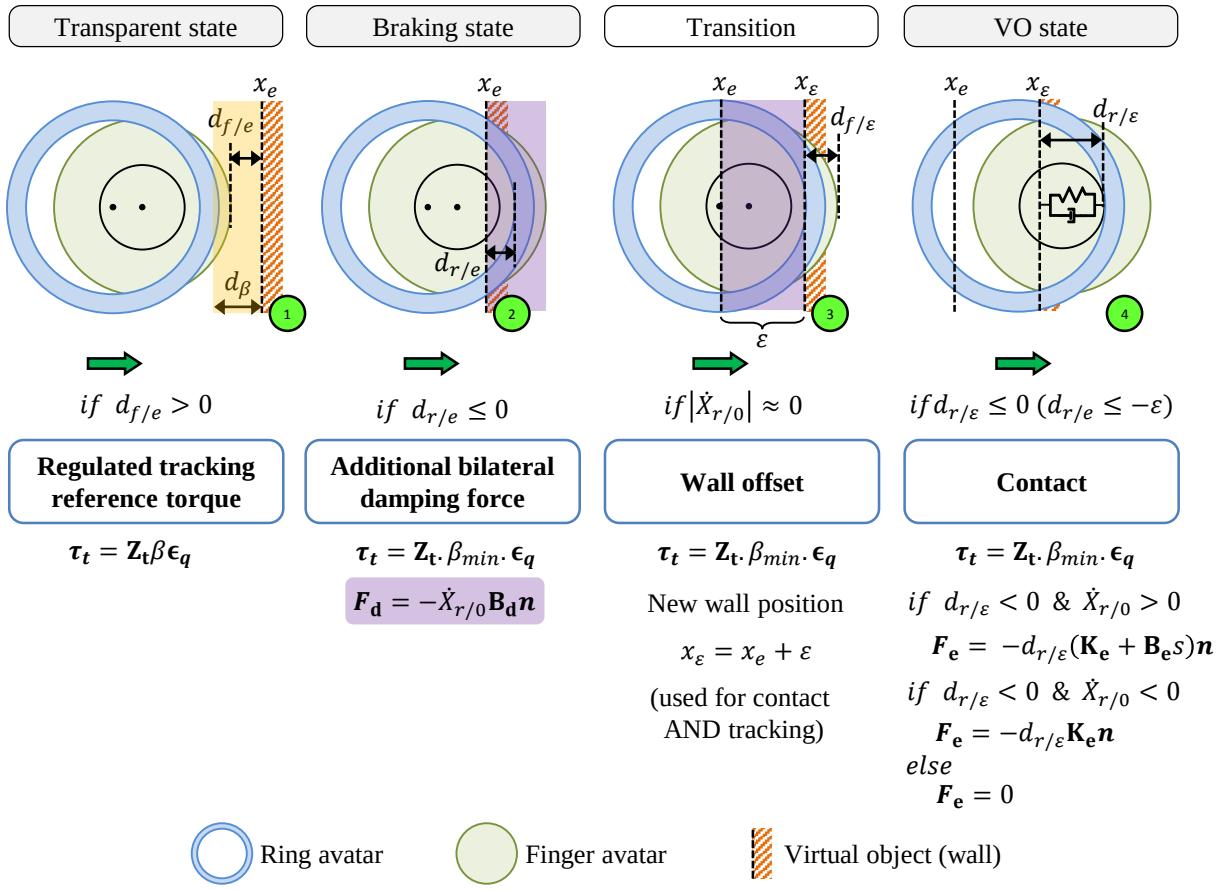

Figure 3.4: Approaching phase of the offset transition-based control.

When the VO takes its new value at x_ε, the augmented finger's avatar is already penetrating into it. At this moment β varies in function of $d_{f/\varepsilon}$ (see Eq.(3.3)), following the same principle as in (2.7) and illustrated in figure 3.2, ensuring the continuity of $\boldsymbol{F}_t$.

$$\begin{cases} \text{if } d_{f/\varepsilon} > d_\beta \text{ then } \beta = 1 \\ \text{if } d_{f/\varepsilon} \in [0, d_\beta] \text{ then } \beta = (\frac{1-\beta_{min}}{d_\beta})d_{f/\varepsilon} + \beta_{min} \\ \text{if } d_{f/\varepsilon} <= 0 \text{ then } \beta = \beta_{min} = 0.1 \end{cases} \tag{3.3}$$

When moving away from the VO located at x_ε, the augmented finger avatar can be far enough from it in order too fully reactivate the tracking force $\boldsymbol{F}_t$, i.e. $d_{f/\varepsilon} > d_\beta$. When the ring comes back in transparent state ($d_{r/e} > d_\beta$) we make β vary again in function of $d_{f/e}$. This way the continuity of the tracking force is ensured when moving away from the virtual object (see Fig.3.5).

The offset transition-based control block diagram is shown in figure 3.6. Here the KVM block computes the interaction force based on the modified Kelvin-Voigt model. The block $f(\cdot)$ provides the estimation of the robot's end-effector speed $\dot{\boldsymbol{X}}_{r/0}$ and relative distances $d_{r/\varepsilon}$ and $d_{f/e,\varepsilon}$ according to the active state. Here $d_{f/e,\varepsilon}$ means that β will be function either of $d_{f/e}$ or $d_{f/\varepsilon}$, according to the active state.

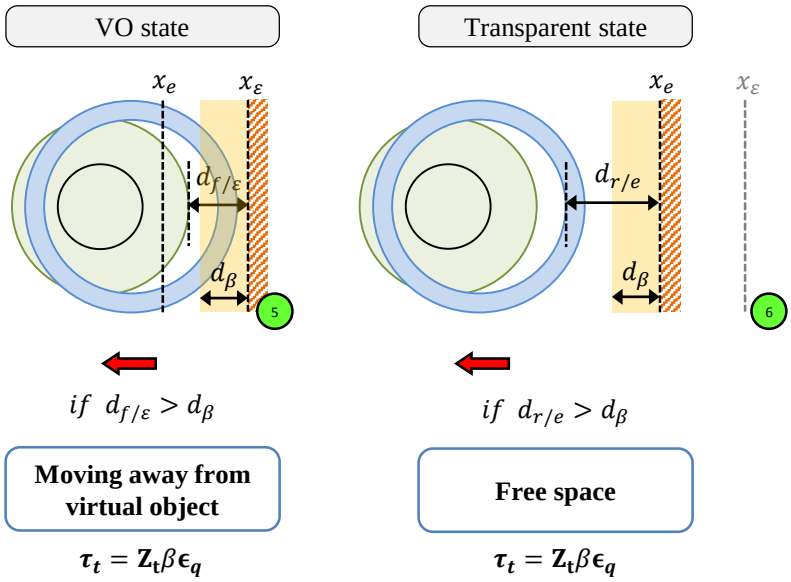

Figure 3.5: Moving away from the virtual object. When any of the distances $d_{f/\varepsilon}$ or $d_{f/\epsilon}$ is bigger than a distance d_β, in reference to x_ε or x_e respectively, $\beta = 1$.

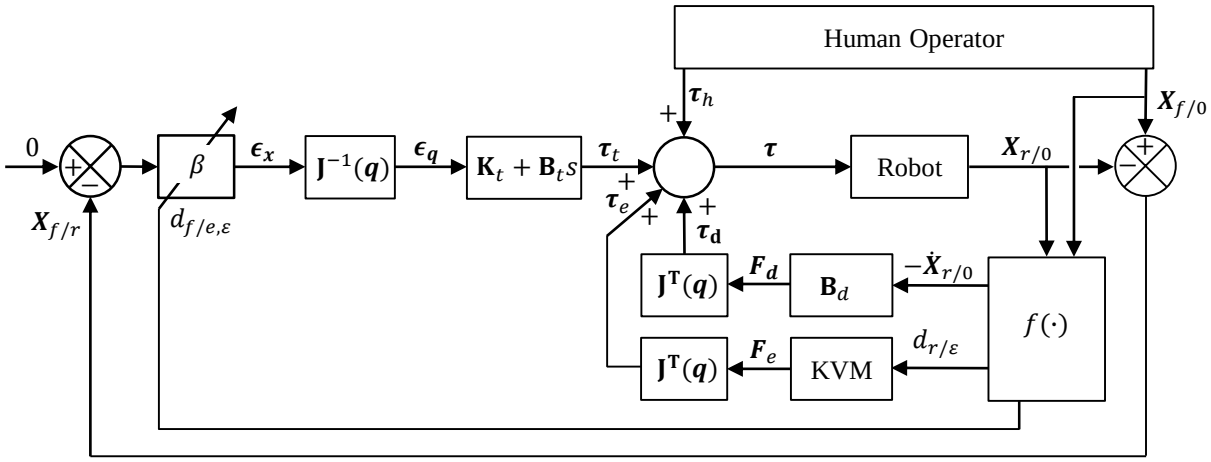

Figure 3.6: Offset transition-based control block diagram.

3.4 Preliminary comparison of control strategies

The aim of this section is to make a preliminary comparison between the smooth transition-based (existing approach) and the offset transition-based (newly proposed approach) control laws.

In order to get valuable results, we will focus here on contacts with a static VO occurring at high speeds (> 0.2m/s), since in such conditions oscillations at contact were observed with the smooth transition based approach.

We are more specifically interested in answering the following questions:

1. to which extent the oscillations are reduced with the offset transition-based approach?,
2. how long does it take to the IC interface to reduce its speed to ≈ 0m/s before the user touches it? and
3. how realistic the contact with a VO object is perceived?

Considering this, a VR tapping test on a static VO, i.e. a wall, was proposed to evaluate both approaches. In order to make quantitative comparisons between both approaches, specific metrics allowing to compare their respective performances during a typical encounter were defined.

For the sake of simplicity, in the reminder of this chapter, the smooth transition-based approach will be denoted here as VO-A, standing for virtual object A, and the offset transition-based approach will be denoted as VO-B, standing for virtual object B.

3.4.1 Performance metrics for the comparison between different control laws during a typical encounter

In order to compare both control laws, our attention was focused on the behavior of the IC interface when it encounters a VO with a certain speed (low or high as defined in section 3.4.2). We were particularly interested in the Cartesian speed and displacement of the IC-HI end-effector (or ring) during a typical encounter. We focused on two instants of time:

- $t_{r/vo}$: instant of time at which the ring's inner periphery encounters the static VO at x_e and
- $t_{f/r}$: instant of time when the user's finger contacts the ring (contact detected by means of a capacitive sensor covering the inner surface of the ring).

Therefore the corresponding speeds:

- $v_r(t_{r/vo})$: speed of the ring when it encounters the VO at x_e and
- $v_r(t_{f/r})$: speed of the ring when it first encounters the user's finger.

As for displacement, we were interested in the amplitude of the very first oscillation (rebound) after the encounter with the VO took place, as well as the maximal speed of the ring during this rebound. Based on this, we defined:

- d_{max}: amplitude of the very first rebound of the ring after encountering the VO and
- $v_{r_{max}}(> t_{f/r})$: maximum speed during the first rebound.

The above proposed metrics apply for both control strategies. In the case of the VO-B approach, we defined the following additional metrics:

- $t_{v_r \approx 0}$: time taken by the interface to stabilize (time to reach a speed $v_r \approx 0$) and
- ε: offset added on the virtual constraint of reference x_e.

The above-defined metrics are related to questions stated in previous section 3.4 regarding the reduction of the oscillations at contact and the time it takes for the interface to stabilize.

3.4.2 Proposed study cases

The experiments were performed using the 2-DoF IC-HI presented in Chapter 2 (see Fig.2.3). Preliminary tapping tests allowed to observe the behavior of the device in conditions VO-A and VO-B for movements performed at different speeds: a user was invited to manipulate the 2DoF IC-HI in order to approach the left vertical wall of the VE of reference (see Fig.2.5).

Due to the dynamics of the robot, the user entered in contact with the ring before reaching the wall for speeds > 0.5m/s. For this reason, a value of 0.4m/s was chosen as the maximum speed tested (called here **high speed**). To span a large range of experimental conditions, we also performed the same tests at a much lower speed. A value of 0.2m/s was chosen as a **low speed** to remain significantly lower than the high speed value.

The robot's gains were adjusted experimentally in order to ensure an efficient finger tracking while minimizing oscillations at contact. Their values in free space and during contacts are given in (3.4) and (3.5) respectively. We use the same gains $\mathbf{K}_t$, $\mathbf{B}_t$ and $\mathbf{K}_e$, $\mathbf{B}_e$ in both conditions VO-A and VO-B. The dissipative gain $\mathbf{B}_d$ is defined in (3.6). A high value is chosen in order to stop the interface as fast as possible (in practice in < 20ms, see Table 3.2). With these values, no noticeable oscillations were observed.

$$\mathbf{K}_t = \begin{bmatrix} 40 & 0 \\ 0 & 40 \end{bmatrix} \text{Nm/rad} \qquad \mathbf{B}_t = \begin{bmatrix} 1 & 0 \\ 0 & 1 \end{bmatrix} \text{Nms/rad} \tag{3.4}$$

$$\mathbf{K}_e = \begin{bmatrix} 2500 & 0 \\ 0 & 2500 \end{bmatrix} \text{Ns/m} \qquad \mathbf{B}_e = \begin{bmatrix} 100 & 0 \\ 0 & 100 \end{bmatrix} \text{N/m} \tag{3.5}$$

$$\mathbf{B}_d = \begin{bmatrix} 100 & 0 \\ 0 & 100 \end{bmatrix} \text{N/m} \tag{3.6}$$

It is worth noting that the speed of movement is imposed by the user. In order to ensure that it is close to the aforementioned values, the speed prior to contact was recorded for each displacement to verify that its value was as close as possible to the defined low and high speeds.

3.4.2.1 Low speed case

The graphical representation of the device's position and speed for a typical encounter obtained at low speed is illustrated in figures 3.7 and 3.8 for each condition. Performance metrics defined in section 3.4.1 are employed here to illustrate the first rebound and the corresponding speed of the interface.

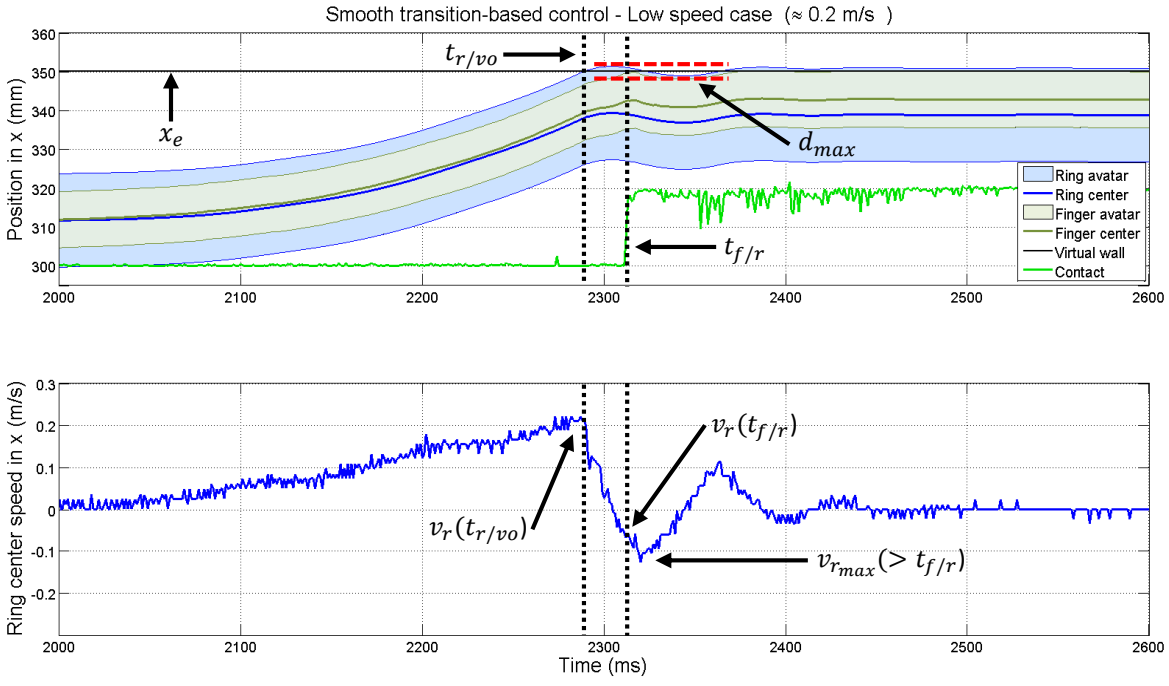

Figure 3.7: Typical encounter with a vertical virtual wall at a low speed in condition VO-A.

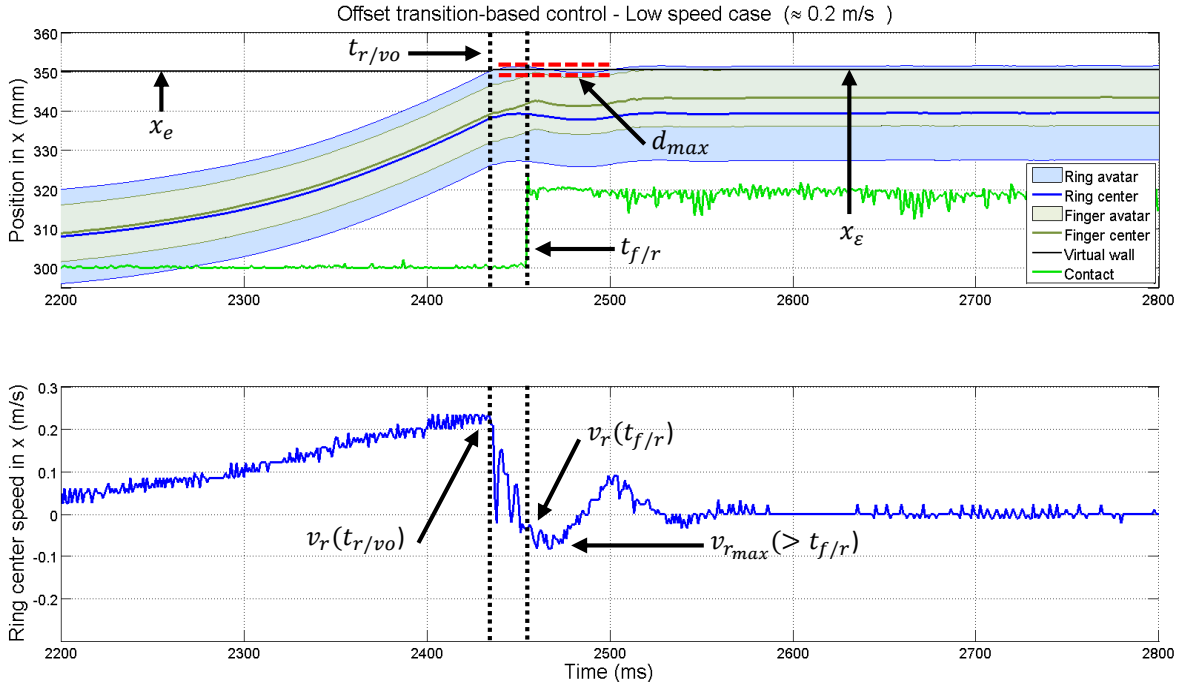

Figure 3.8: Typical encounter with a vertical virtual wall at a low speed in condition VO-B.

No noticeable difference can be observed between VO-A and VO-B conditions. In both cases, the ring's speed and the first rebound show a similar profile and also similar orders of magnitude for d_{max} and v_r values.

Based on these results, we conducted that the behavior of both control laws is very similar at low speeds.

3.4.2.2 High speed case

The graphical representation of the device's position and speed for a typical encounter obtained at high speed is illustrated in figures 3.9 and 3.10 for each condition. It can be observed that by the time the user's finger encounters the ring (at $t_{f/r}$), the corresponding ring's speed is closer to 0 in VO-B than in the VO-A condition. A reduction of the speed $v_r(t_{f/r})$ was observed with the proposed approach VO-B.

It can also be observed that the d_{max} value is smaller in the VO-B condition (important oscillations appeared with VO-A). As for the rebound speed $v_{r_{max}}(> t_{f/r})$ it can also be seen that its absolute value $|v_{r_{max}}(> t_{f/r})|$ is bigger in VO-A than in VO-B.

These observations let us make the hypothesis that the sensation felt by the user would be more representative of a static object, therefore more natural, if the VO-B is employed.

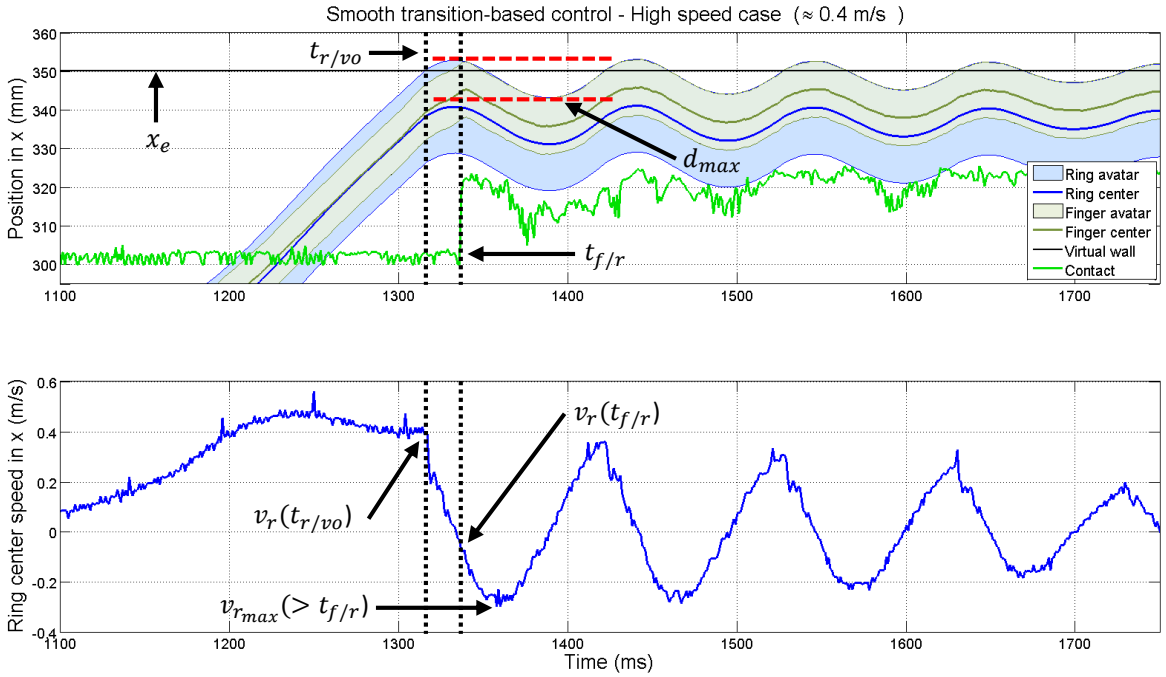

Figure 3.9: Typical encounter with a vertical virtual wall at a high speed in condition VO-A.

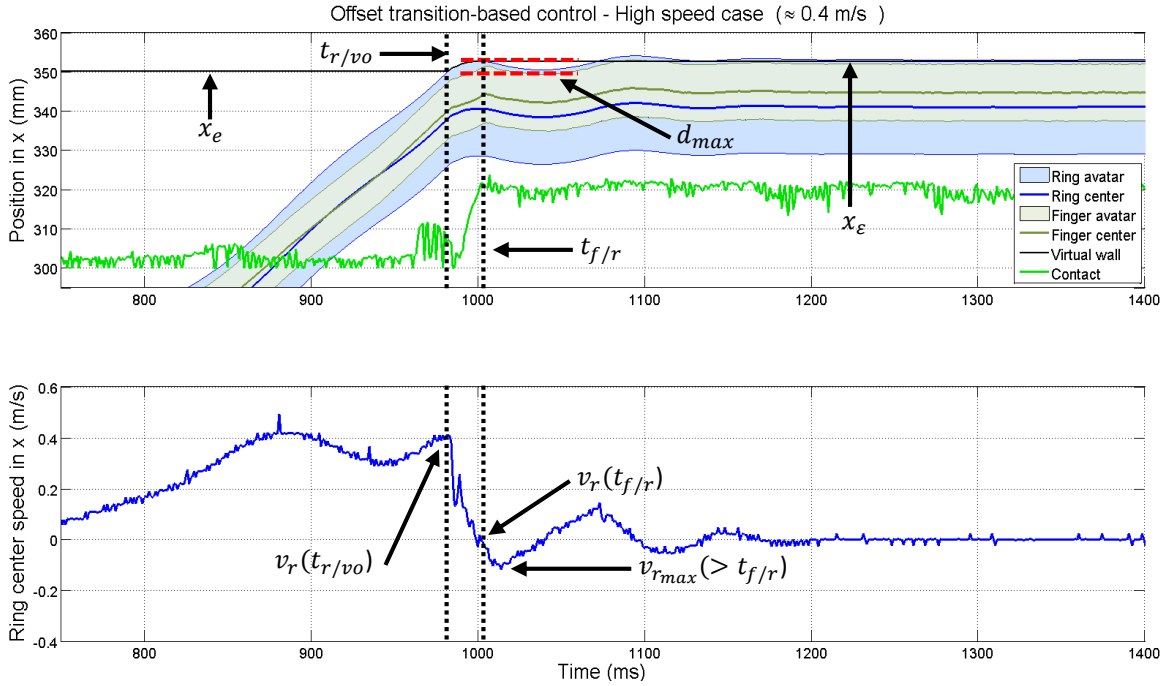

Figure 3.10: Typical encounter with a vertical virtual wall at a high speed in condition VO-B.

3.4.3 Conclusion

Preliminary taps on a vertical wall were performed at low and high speeds. Taps at low speed allowed us to observe that the behavior of the interface was similar in both approaches. Taps at high speed allowed us to observe a reduction of oscillations with the newly proposed approach.

3.5 User-test-based comparison of control strategies

Preliminary tests let us to make the hypothesis that the speed of the ring when the finger encounters it $|v_r(t_{f/r})|$, the amplitude of the first rebound d_{max} and the maximum ring's speed during the rebound $|v_{r_{max}}(> t_{f/r})|$ are smaller in VO-B condition compared to VO-A. The aim of the tests presented in this section is to test our hypothesis. To this end, a group of six subjects was proposed to perform a tapping test at low and high speeds in both conditions.

This section is organized as follows: details regarding the participants are given in section 3.5.1, the employed materials are presented in paragraph 3.5.2, the experimental setup in paragraph 3.5.3, the procedure in paragraph 3.5.4 and the proposed data processing in paragraph 3.5.5. Finally, results and elements of discussion are provided in section 3.5.6.

3.5.1 Participants

A total of six people (3 men, 3 women, aged 23-33) were invited to perform the VR tapping task employing an IC haptic interface. A brief explanation of VR and what a haptic interface is was provided during the recruitment process. However, no concrete details on the experiment were given.

This population was composed of people working in the Interactive Robotics Laboratory from CEA, LIST. It accounted for administrative personnel, permanent staff as well as PhD students.

The participants affirmed to be familiar with computer technology tools, e.g. office software and multimedia content. Some of them were familiar with specialized software, tactile screens as well as joysticks. On the other hand, most of them already knew what a haptic interface was but most of them had never used one.

Only right-handed volunteers were chosen since the employed IC-HI is mainly suited for this profile. Each participant performed the proposed experiment during one single visit.

3.5.2 Materials employed for the study

In this section the materials employed during the experiments are presented. The focus is given here to those elements that allowed to collect/generate data, in particular: the IC haptic interface, the VE and a questionnaire employed to perform a survey at the end of each experiment.

3.5.2.1 IC haptic interface

A description of the IC-HI employed for the user tests can be found in section 2.3.2.1 and in appendix A.

3.5.2.2 Virtual environment

The VE employed in this experiment is shown in figure 3.11. It is similar to the VE presented in Chapter 2 (see Fig.2.5). This 2D VE consists of a black vertical rectangle (free space) surrounded by a thick green contour representing four virtual walls, the left wall being used as the obstacle where the user has to tap. The user's finger avatar is represented with a white circle which displacement is coupled with that of the robot's end-effector. In addition, a vertical line is displayed in order to indicate where to start the displacement for a single tap. This line is positioned at a specific distance according to the tested condition, i.e. 4cm (for low speed) and 8cm (for high speed). Such distances were defined experimentally, allowing to reach the low and high speeds of interest at the moment of contact with the left wall.

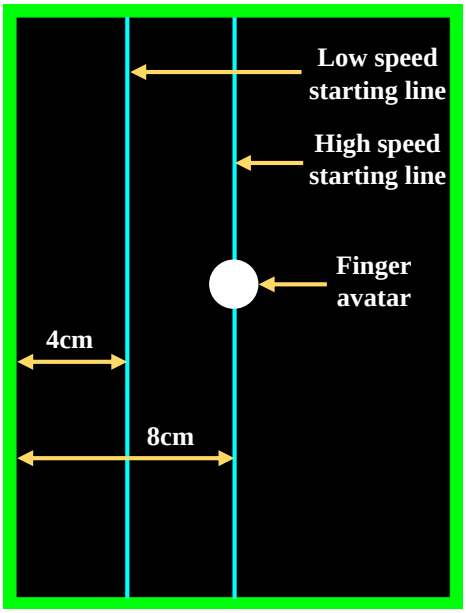

Figure 3.11: Virtual environment employed for the tapping test.

It is worth noting that the VO-B approach introduces an offset ε on the virtual constraint x_e. Visualizing such offset may have an impact on the way the contact is perceived. It was thus decided to display the finger avatar as stopping at the original virtual wall position irrespective of its real location (see Fig.3.12). Such action introduces a potential visuo-haptic delay, i.e. the user may see his/her finger avatar touching the obstacle before really filing the contact. Fortunately, as was emphasized by [Vogels, 2004] and [Knorlein et al., 2009], such visuo-haptic delay is imperceptible if it is lower than 45ms,

which is the case here since as it will be seen in section 3.5.6.2 the interface stabilizes in less than 20ms.

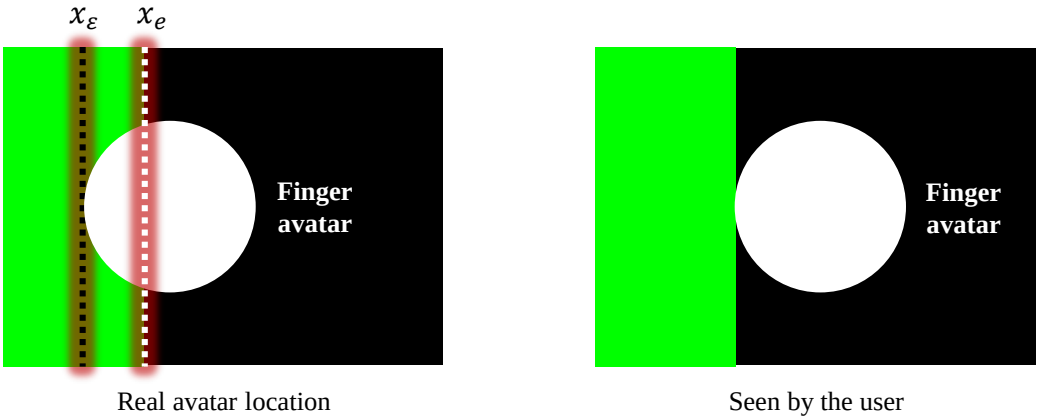

Figure 3.12: Finger avatar location in VO-B approach.

3.5.2.3 Questionnaire

A questionnaire was employed to perform a survey on particular aspects of the performed task. This questionnaire was anonymous and the participants could spend as much time as they needed to fill it. The employed questions were the following:

- **Q1.** *Was the contact perceived*
  1) well before the finger's avatar reaches the wall?
  2) slightly before?
  3) at the moment the avatar reaches the wall?
  4) slightly after?
  5) well after?

- **Q2.** *At contact, the wall was perceived as*
  1) clearly moving to the left?
  2) moving to the left?
  3) being static?
  4) moving to the right?
  5) clearly moving to the right?

- **Q3.** *The sensation at contact was perceived as*
  1) very natural?
  2) natural?
  3) neutral?
  4) unnatural?
  5) very unnatural?

3.5.3 Experimental setup

The experiment was performed in an isolated room. The **participant** was standing up, facing the **screen** and wearing an anti-noise **helmet**. The **haptic interface** was placed on a table so that the user could comfortably place his/her right index finger inside the end-effector and so that a horizontal movement towards the left could be performed easily.

The interface was hidden from the user's sight by a vertical **wall**. These elements are illustrated in figures 3.13 (picture of the setup) and 3.14 (top view diagram showing the placement of the main elements).

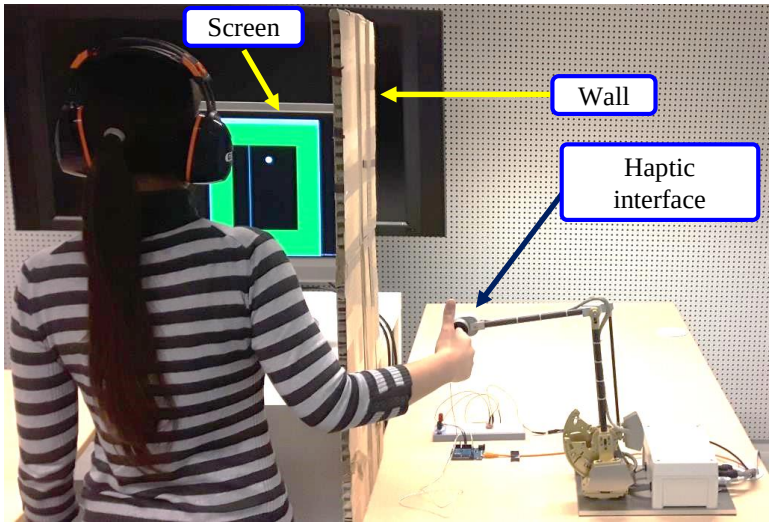

Figure 3.13: Main elements of the experimental setup (picture).

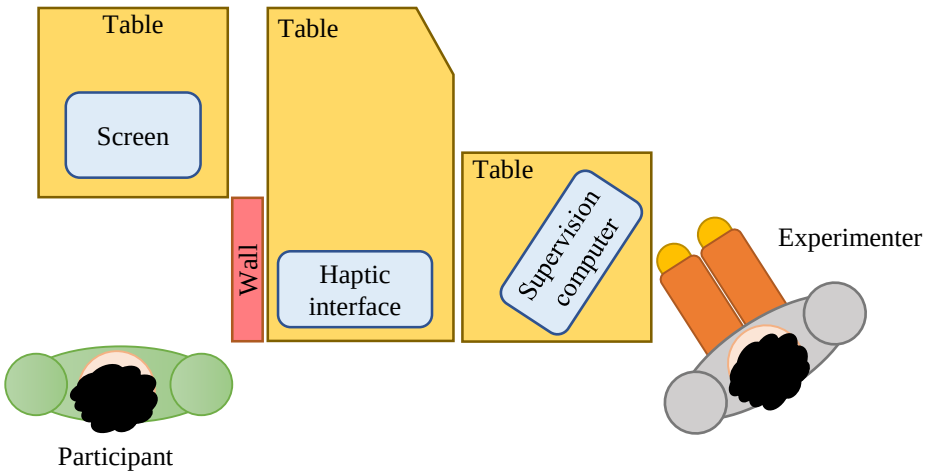

Figure 3.14: Main elements of the experimental setup (top view diagram).

It is worth noting here that the participant visualized a GUI that contained only the VE presented in section 3.5.2.2 whose displayed size was adapted to cover the largest possible portion of the participant's screen. The finger's avatar size was proportional to the participant's index finger diameter.

The experimenter visualized a different version of the GUI displayed on a supervision computer. It contained additional options allowing to turn on/off either the VO-A or the VO-B control laws, the force feedback as well as the tracking of the user's finger. Such additional options were not visible for the participant.

3.5.4 Procedure

This section explains the general procedure followed by each participant to perform the proposed experiment. This procedure describes the performed actions since the moment the participant arrives until he/she leaves the room where the experiment takes place.

The user is asked to perform a certain number of taps on a vertical wall located on his/her left at low and high speeds ($\approx$ 0.2m/s and $\approx$ 0.4m/s respectively) using VO-A and VO-B approaches. This generates four test conditions:

- VO-A Low,
- VO-B Low,
- VO-A High and
- VO-B High.

As shown in figure 3.15, the implemented procedure can be divided in several stages: welcome, training, experiment-survey stage (for each condition) and a goodbye.

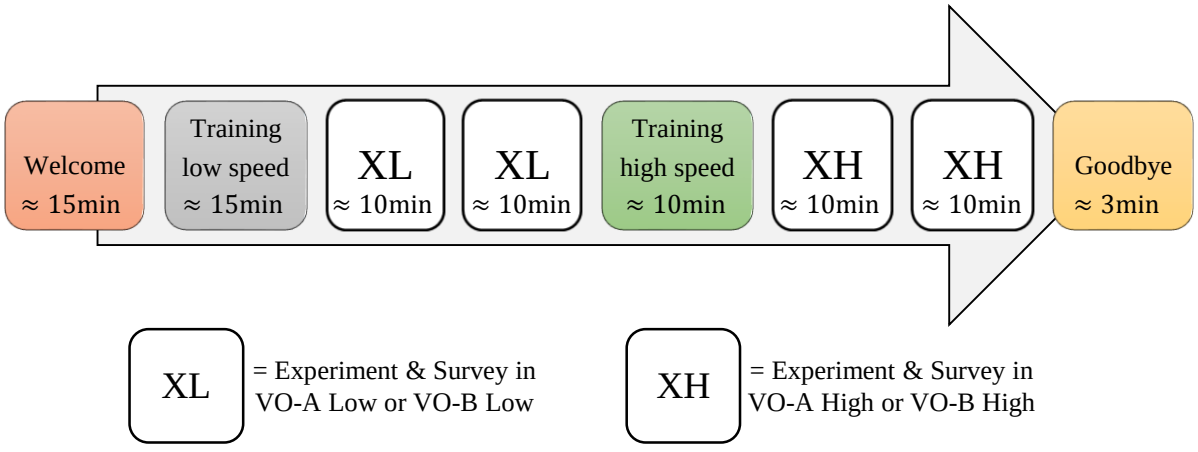

Figure 3.15: Experimental procedure stages and representative times.

In this figure, it can be observed that a specific training session was planned for each speed, i.e. for low and high speeds. This would allow the user to remember the sensation of moving at low or high speeds prior to the experiment.

Two XL blocks account for the experiments and survey at low speeds, and two XH blocks for those at high speeds. It is worth noting that the survey is filled in each XL or XH block. This way questions on the performed task are easier to answer, rather that answering everything at the very end of the experiment. The average length of the whole experiment was around 1h30.

3.5.4.1 Welcome

The following stages describe the welcome of a participant:

1. The participant is met at the main hall of the laboratory and taken to the experiment's room.
2. Once in the experiment's room he/she is invited to take a sit and is provided with a letter of consent which explains the global process of the experiment he/she is about to perform and gives details on the following aspects:
    - The aim of the study.
    - An explanation on how a haptic interface allows to interact with a VR.
    - A description of the IC haptic interface.
    - A description of the VR task to be performed
3. The participant is asked if there are any questions regarding the global process.
    - At this moment a brief resume of the documents is given orally in order to reinforce the understanding of the general procedure.
4. Finally, he/she is asked to sign a letter of consent to validate his/her agreement with the terms of the procedure.

Since this was a voluntary participation, he/she was informed that he/she could quit the experiment at any time and for any reason without generating any particular issue.

3.5.4.2 Training

As stated at the beginning of section 3.5.4, two training sessions were proposed for each participant: one at low speed and one at high speed. The goal was to train the user to move his/her arm at speeds close to ≈ 0.2m/s (in the low speed case) and ≈ 0.4m/s (in the high speed case).

The training focused on the following aspects:

1. Explaining the **experimental conditions** to the participant:

   Upon presentation of the layout of the different elements of the experimental setup, it was explained to the participant that during the experiment he/she was going to be standing up, wearing an anti-noise helmet and facing a screen where the VE was displayed by means of a GUI. In addition to this, it was told him/her that the robot (placed on a contiguous table so that he/she could comfortably place his/her right index finger inside the end-effector) was going to be hidden from his/her sight by a vertical wall.

   The anti-noise helmet allowed to reduce the influence of surrounding parasitic noises, in particular those eventually generated by the haptic interface. When any oral communication had to be established, the experimenter talked louder to the participant so that he/she could listen to his voice, even while wearing the helmet. This would avoid to remove it each time oral instructions were required.

   Also, the user's finger diameter was measured prior to the haptic interface manipulation stage, for the purpose of adjusting the size of his/her finger's avatar.

2. Teaching him/her **how to manipulate the haptic interface** according to the experiment to perform:

   The 2DoF nature of the haptic interface had to be taken into account when learning how to manipulate it. Here, it was of crucial importance that the user kept his/her right index finger inside the end-effector (straight and perpendicular to the working plane of the robot) with the finger pad oriented to the left, so that it can make a full contact with the wall (see Fig.3.16).

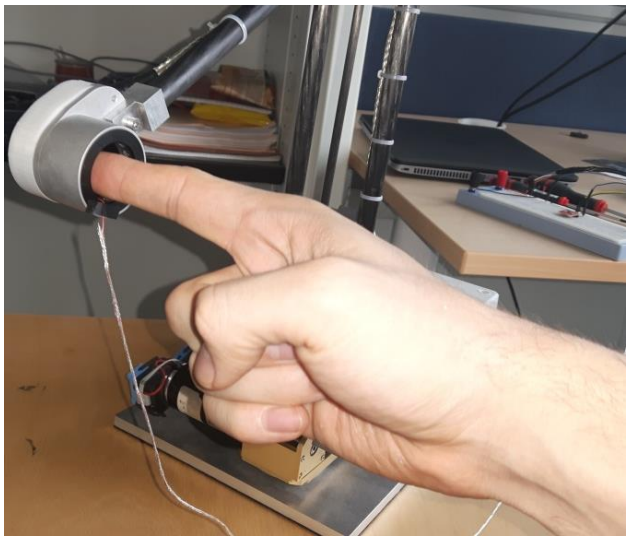

Figure 3.16: User's hand expected positioning during manipulations.

The non-respect of the above-described gesture would impact the user's perception and the quality of the data recorded with a contact sensor installed in the inner surface of the ring. The correctness of the participant's gesture was verified by the experimenter

and he/she was told to correct it if necessary. Enough time was given to him/her in order to learn how to manipulate the interface.

3. Explaining the **structure of the experiment**:

   The experiment requires the participant to perform a VR tapping task. The action of performing one single tap is denoted here as a **trial**, this trial being considered as valid if the tap is performed at the expected speed, either low or high. A **set** corresponds to the fact of performing at least three valid trials for each one of the four conditions (VO-A Low, VO-B Low, VO-A High and VO-B High). Finally, a complete experiment is composed of a defined number of sets (here four sets corresponding to the four experimental conditions). These definitions were explained to the participant prior to practicing the VR task.

4. **Practice** of the VR task:

   The participant was given enough time to learn how to perform the VR task and and feel comfortable with it.

Stages (1-4) were performed during the first training session. During the second training session, points (2-3) were briefly reminded and the attention was given to point (4). In all cases, the participant only knew if it was low or high speed and no information about the VO being touched was provided.

3.5.4.3 Experiment

According on the condition in which training took place (either VO-A or VO-B), the experiment started with a different condition. This is illustrated in table 3.1. Each case represents a complete experiment session. Cases were employed alternatively for each participant, e.g. participant 1 performed the experiment using the order stated in case 1, participant 2 performed the experiment using the order stated in case 2, etc. Performing this way would help to avoid any learning effects regarding the VO being touched.

Table 3.1: Experiment structure cases.

Case 1
Training – VO-A Low
Experiment – VO-B Low
Experiment – VO-A Low
Training – VO-A High
Experiment – VO-A High
Experiment – VO-B High

Case 2
Training – VO-B Low
Experiment – VO-A Low
Experiment – VO-B Low
Training – VO-B High
Experiment – VO-B High
Experiment – VO-A High

Prior to the experiment, the experimenter activated either the VO-A or VO-B condition (selection of the corresponding control law) by means of the GUI displayed on the supervision computer. In order to start the experiment, the participant was asked to put

the helmet and to place his/her right index finger inside the end-effector of the haptic interface.

Oral instructions allowed to perform the transitions between trials. For a single trial, the experimenter proceeded in the following way:

1. The participant was invited to position the finger's avatar approximately at the center of the starting line. Examples of employed phrases were:

   (a) "Please go to the starting line"

   (b) "O.k.! Let's move back to the starting line"

2. The experimenter activated the data recording and invited the participant to perform the VR task (to tap on the left vertical wall of the VE). Examples of employed phrases were:

   (a) "1,2,3, go!"

   (b) "1,2,3, let's go!"

3. Once that the participant had accomplished the VR task, he/she was invited to come back to the starting line (if he/she felt tired he/she could remove his/her finger from the interface, however it was preferred no to do this so he/she kept in mind the sensation of moving at the low or high speed). At the same time the experimenter stopped recording data and verified speed and contact sensor data.

The correctness of the participant's gestures was inspected visually during each trial. Data was also recorded for each single tap and its exploitability was verified in situ to verify the validity of the trial, i.e. correct speed (either ≈ 0.2m/s or ≈ 0.4m/s) and absence of contact with the ring before touching the obstacle. If needed, he/she was told to move slower or faster in order to better approximate the expected speed. Steps (1-3) were repeated until the obtention of at least three valid trials for each of the four conditions.

Once a set of trials was completed, the user was asked to take an obligatory break, e.g. $1-2$min. During this time, the experimenter asked the participant how he/she was feeling with the execution of the VR task and if he/she had any questions. After this, he/she was asked to answer to the survey before keep on going with the next set. An example of scheme of the building blocks of a typical experiment (without the welcome, training and goodbye blocks) is shown in figure 3.17 for case 2 from table 3.1.

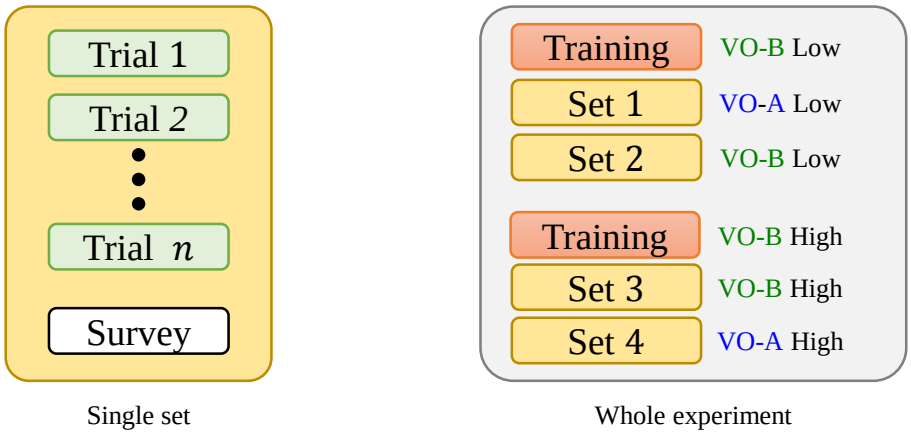

Figure 3.17: Scheme of a typical experiment in a case 2 structure.

3.5.4.4 Goodbye

At the end of the experiment, a reward was given to the participant before taking him/her back to the hall of the laboratory.

3.5.5 Data processing

The generated data were post-processed in order to perform quantitative comparisons. Box-plots were employed to analyze the results. Here the median appears inside the box as a horizontal line, the box represents the first (Q1) and third (Q3) quartiles and whiskers represent minimum and maximum values (see Fig.3.18). This method allows to observe the dispersion of data around the median as well as outliers without making any assumption on the underlying statistical distribution. Boxplots were applied on the following performance metrics: $v_r(t_{r/vo})$, $v_r(t_{f/r})$, d_{max} and $v_{r_{max}}(> t_{f/r})$.

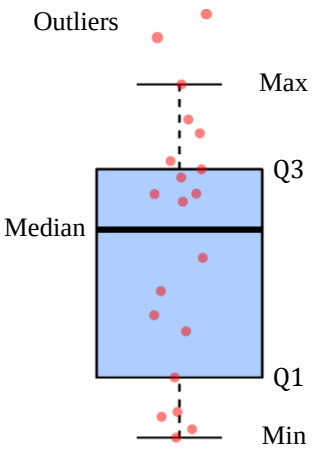

Figure 3.18: Elements of a boxplot.

In order to assess the perception of the participants and get complementary qualitative

comparisons for each experiment condition, we used the results of the survey. The answers were counted as a five-point Likert scale. Measured perception for each question was calculated using equation (3.7).

$$Pe_i = \frac{\sum_{j=1}^{5} n_{A_j} \cdot j}{\sum_{j=1}^{5} n_{A_j}} \tag{3.7}$$

where:

Pe_i	is the measured perception for question i
j	is the Likert level
A_j	is the selected option corresponding to Likert level j
n_{A_j}	is the number of participants that answered option A_j

3.5.6 Results and discussion

Between 10 and 15 taps were necessary in each case to obtain three valid taps. With a population of 6 participants, this implies that a total of 18 trials were employed for data analysis in each condition, i.e. 3 taps $\times$ (VO-A or VO-B) $\times$ 6 participants.

3.5.6.1 Performance evaluation

Figure 3.19 illustrates the boxplot corresponding to the speed of the ring when it encountered the VO ($v_r(t_{r/vo})$). It can be observed that the movements were performed

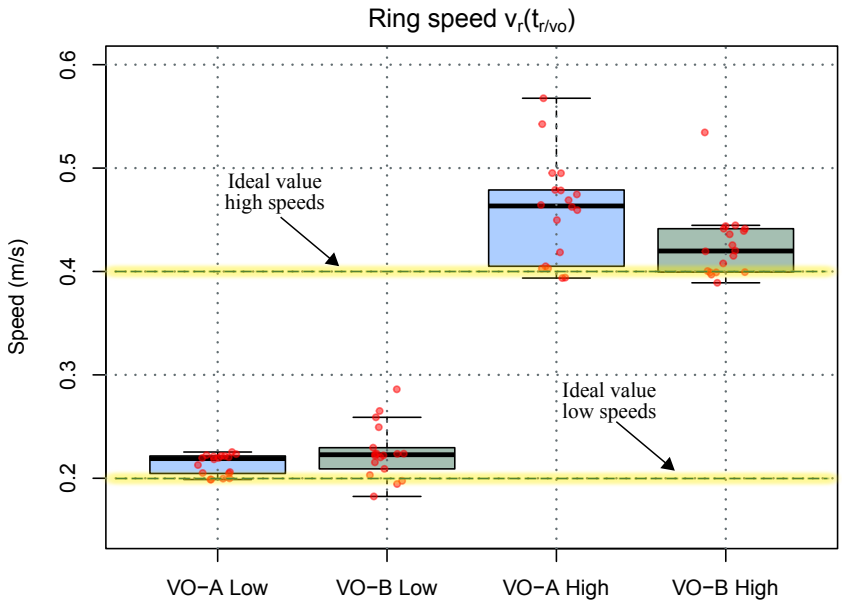

Figure 3.19: Speed of the ring at time $t_{r/vo}$.

close to the defined low and high speeds, i.e. $\gtrapprox$ 0.2m/s and $\gtrapprox$ 0.4m/s respectively (a positive value indicates that the ring moves in the same direction as of the user's movement).

Figure 3.20 shows the obtained results for the speed of the ring when it encounters the user's finger ($v_r(t_{f/r})$). Its absolute value should be as low as possible to realistically simulate a static wall. It can be observed that, at low speeds, the spread of the data is similar in both conditions. At high speeds, a noticeable shift of the spread of this value for the VO-B condition evidences smaller absolute values than in the VO-A condition.

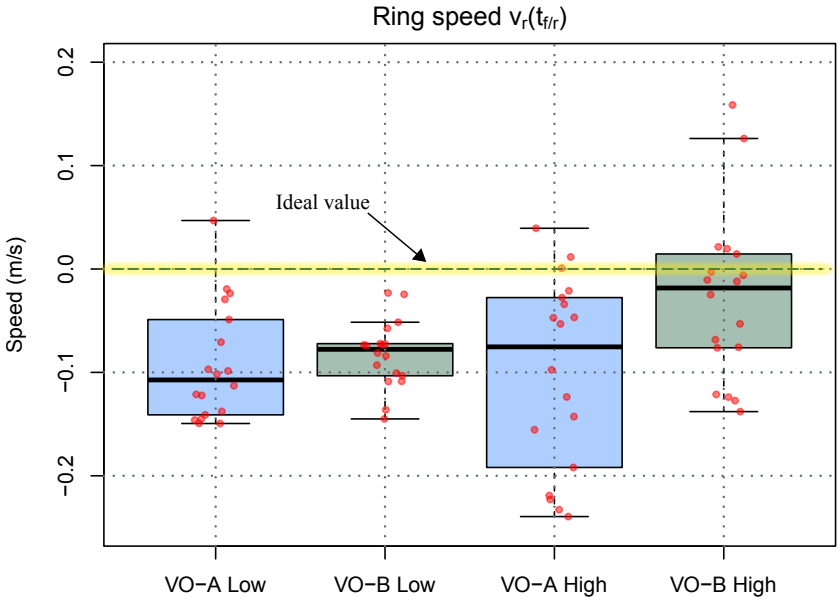

Figure 3.20: Speed of the ring at time $t_{f/r}$.

Figure 3.21 resumes the retrieved amplitudes d_{max} of the first rebound of the ring against the wall. This value should be as small as possible to reduce unnatural perceived

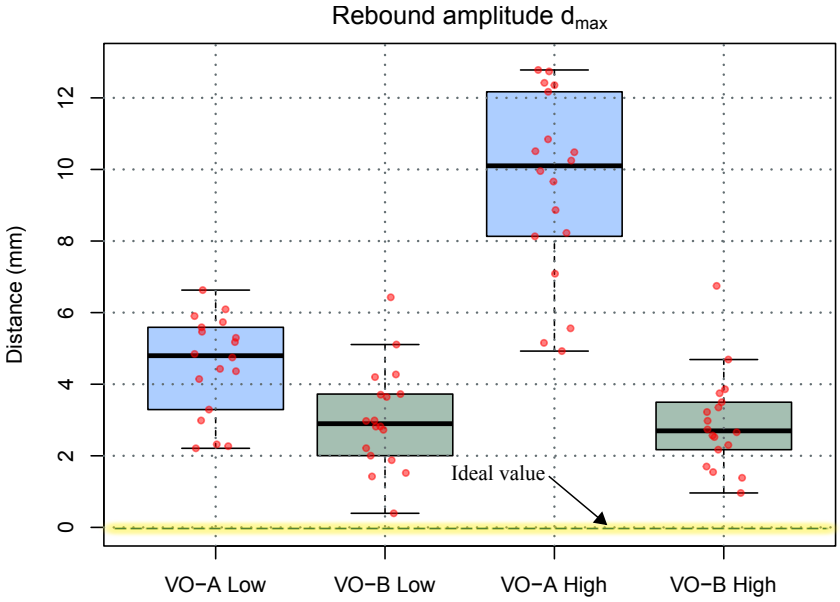

Figure 3.21: Rebound amplitude d_{max}.

oscillations. At low speeds, a slight reduction of this value can be observed for the VO-B case. At high speeds, such reduction is maintained. It is worth mentioning here that the orders of magnitude of d_{max} are similar at low and high speeds, meaning that there may be possible improvements to do at low speeds for the VO-B approach.

Finally, figure 3.22 illustrates the obtained results regarding the rebound maximum speed $v_{r_{max}}(> t_{f/r})$. It can be inferred from these results that the ring is moving against the user (negative speeds). At low speeds, the absolute value of this speed is slightly smaller in the VO-B condition than in the VO-A case. At high speeds the absolute value in VO-A is higher than in the VO-B case.

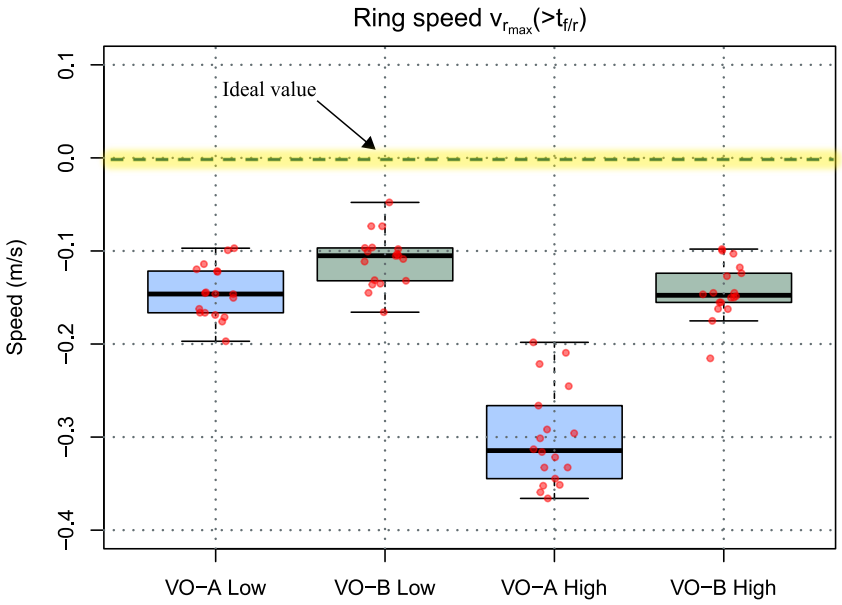

Figure 3.22: Speed of the ring center at a time $> to_{f/r}$.

3.5.6.2 Stabilization of the interface

The proposed approach VO-B stabilizes the interface at the price of slightly modifying the position of the VO. Table 3.2 provides mean and standard deviation for the stabilization time $t_{vr\approx 0}$ and the generated offset ε at low and high speeds.

Table 3.2: Mean and standard deviation for $t_{v_r\approx 0}$ and ε.

mean (std)	$t_{v_r\approx 0}$ (ms)	ε (mm)
Low speed	3.38 (2.90)	0.45(0.28)
High speed	13.55 (1.97)	2.21(0.37)

Results show that, in average, the ring stabilizes in ≈ 3ms at low speed and ≈ 13ms at high speed. On the other hand the offset ε remained lower than 3mm. As according to [Vogels, 2004] and [Knorlein et al., 2009], a visuo-haptic delay is imperceptible if it

is lower than 45ms, we can expect here that a human operator wouldn't realize these differences when performing a tap.

3.5.6.3 Perception of the participants

The participants were asked to answer three questions upon completion of at least three valid taps in each condition. Results for the measured perception are given in figure 3.23.

Q1 asks if the user perceived the contact before (score 1 or 2), just when (3) or after (4 or 5) the finger's avatar touched the virtual wall. It provides information on the perception of the visuo-haptic delay (ideal result is 3). Results tend to prove that, both at low and high speeds, the delay of the haptic signal introduced by the VO-B approach tends to not be perceived, in particular at high speeds. This can be correlated to the fact that $t_{v_r \approx 0} < 45$ms.

Q2 asks if at contact the touched wall was perceived as moving to the left (score 1 or 2), being static (3) or moving to the right (4 or 5). It tells us if the user was perceiving the rebound (ideal result is also 3). At low speeds, the VO was perceived as similar in both conditions. At high speeds, the perception of the VO-B was felt as being more static.

Finally, Q3 asks if the sensation at contact was felt very natural (1), natural (2), neutral (3), unnatural (4) or very unnatural (5). At low speeds no remarkable difference was observed. At high speeds, the contact with the VO-B was perceived as more natural.

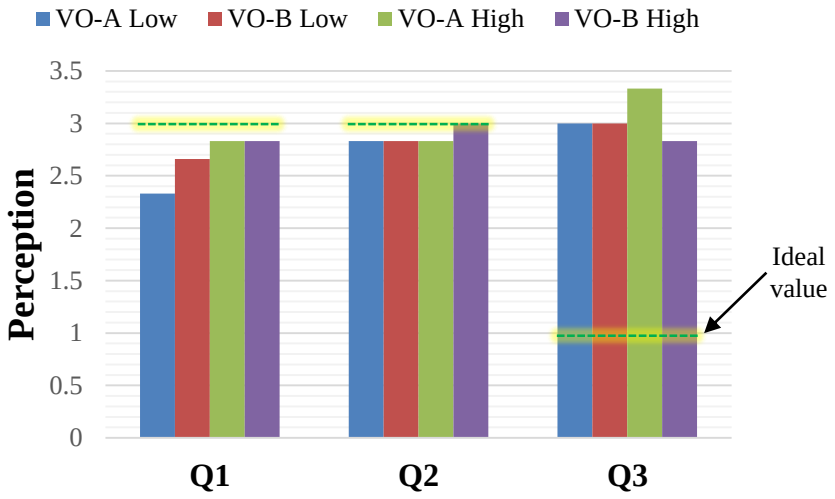

Figure 3.23: : Survey scores.

3.6 Chapter conclusions and perspectives

3.6.1 Conclusions

In this chapter, a new control law intended to improve the contact rendering with an IC haptic interface was introduced. The results of our experiments show that the proposed offset transition-based control allowed to reduce the speed of the end-effector before the user's finger encountered it. The rebound amplitude after contact was also reduced. As a consequence, the contact is perceived as more natural.

The proposed approach stabilizes the interface at the price of slightly modifying the position of the VO, therefore generating a delay of the haptic signal. We found however that the stabilization times remained under the perceptible visuo-haptic delay time, therefore it was not perceived by the participants.

3.6.2 Perspectives

The observed results allowed to notice that with the proposed approach applied on the available IC-HI, some improvement on the stabilization of the interface and realism of the perceived VO was accomplished. It would be interesting to extend the population of participants, e.g. up to 10 or 15 subjects, and perform statistical analysis to reinforce the significance of the results.

Also, the presented approach was a specific development based on the dynamics of the available IC-HI. Different other strategies could be investigated as well, e.g. start applying the dissipative force prior to reach the VO, in order to stop the ring against it without any offset.

In all cases, it would be worth performing a sensitivity study, i.e. a generalized study of the influence of the different parameters of the interface on its performances for the different approaches that allow to stabilize an IC haptic interface. To this end, it would be interesting to develop a 1DoF IC-HI with optimal performances as it would allow to span a larger set of parameters than the existing 2DoF device, thus allowing to perform a deeper study of a typical encounter.

Chapter 4

Contributions to the Design of an IC-HI Tracking Module for Tool-Based Interactions

Contents

4.1 Introduction

Until now, we have seen that an IC haptic system is composed of three main elements:

- the tracking system able to compute the user's configuration,
- the force feedback system which constraints the user when a virtual object (VO) is being touched and
- a control law that manages close following in free space, force feedback at contact and the transitions between these two modes.

An efficient tracking and clean free space to contact transitions depend mainly on the performances of these three elements, i.e. the quality of the tracking information, the adopted control strategy and the ability of the device to follow the controller orders.

Among these elements, the tracking system appears as particularly important as it is the entry point of the system. As an example, to ensure optimal transitions, the configuration of the user must be known precisely and at very high rates so that contacts in the virtual and real worlds are seen and felt at the same time, i.e. allowing to ensure that any existing visuo-haptic delay is imperceptible to the user.

In practice however, the tracking systems of most existing IC haptic interfaces are imprecise. One reason for this is that such devices are often used to interact with the VE using bare fingers [Yoshikawa and Nagura, 1999]. As a precise estimation of the configuration of a finger is a complex task, due to large variations in shape and size depending on the user and on the configuration of the hand, its position and orientation are only roughly estimated. Fortunately, several VR tasks are performed employing a tool instead of bare fingers, e.g. dentistry simulators. For such applications, which are very common in VR, it is more interesting to develop IC interfaces providing virtual tool based interaction, hence the requirement of a dedicated tool tracking system.

The following sections aim to provide a methodology towards the design of such a tracking module. We will first present the tool interaction paradigm for IC haptic interfaces (see section 4.2) as well as different strategies for measuring the relative configuration of a handle in reference to the robot (see section 4.3). Then we will define precise design drivers for the tracking system (see section 4.4). To answer these needs, we will first make a comprehensive review of representative characteristics of common existing tracking systems (see section 4.5) and sensing technologies (see section 4.6), keeping in perspective the design of an IC non-contact tracking system. Then, we will present the results of a preliminary experimental characterization of a sensor, which was found to be suited for our application (see section 4.7). Finally in section 4.8 conclusions are given.

4.2 Tool interaction paradigm for IC haptic interfaces

A close-tracking-type interface (referred here as IC interface) requires a robot end-effector equipped with sensors that allows to measure (to track), without contact, the configuration of the user (position or position + orientation) relative to the robot. Thanks to this information the robot will be able to closely follow the user's movements, e.g. his/her finger position and orientation in free space. When a VO is being touched, the IC interface should be able to come into physical contact with the user and provide force feedback according to the VO mechanical properties, e.g. the object's stiffness, ensuring realistic physical interaction between the user and the interface.

To date, developers of IC haptic interfaces have concentrated their efforts on de-

vices providing interactions directly on the user's hand, as in [Gonzalez et al., 2015, Chabrier et al., 2017]. In such approach, precise tracking of the user becomes a complex task since a finger has variable sizes and morphologies depending on the user. Furthermore, it deforms at contact. Estimation of the finger's configuration and shape without contact requires then the employ of a precise and high frequency measuring system, which is ideally as small as possible. Such system introduces in turn the need for precise, high frequency and small unitary sensors that, properly arranged in a defined volume, will provide raw data that will be converted into meaningful configuration information thanks to any adapted data treatment strategy. It is worth noting that it could be theoretically possible, if necessary, to obtain a very precise information about the finger configuration and shape. This would however require an increase of the number of sensors and therefore an increase of the size of the tracking system, as well as of the time needed to treat the data, which is not desirable as it would result in a bulky and heavy measurement system.

Fortunately, as it can be observed in chapter 1, tracking a finger is not always mandatory. Indeed, several VR applications employ haptic interfaces that are manipulated by means of a pen-like end-effector (a handle which is represented in the virtual world by an avatar of a desired shape, e.g. a surgical instrument), allowing kinesthetic (force/position) interactions with the VE. This is much easier to track than a finger as it has a known and fixed shape and as it can be equipped with embedded sensors. The development of IC interfaces providing interaction by means of a handle (which avatar can represent any desired tool) is thus very interesting and promising.

As shown in figure 4.1, the tracking system (which can be local or external, see section 4.3) ensures the measurement of the handle configuration without contact in free space. The robot controller uses this information to closely follow it. At contact, the robot will move so that its end-effector stops where the VO is expected to be, waiting for the handle (hold by the user) to encounter it and provide the corresponding interaction forces.

IC interfaces using a tool-based interaction paradigm aim to simplify the tracking and force feedback tasks. Indeed a tool, on the contrary to a finger, has fixed size, shape and mechanical properties. Such characteristics should allow to increase the precision of the configuration calculation. The detection of collisions with surrounding VOs and the calculation of the interaction forces are also simplified since the handle avatar shape is known. Furthermore, kinesthetic and tactile feedback are made naturally thanks to the mechanical link established between the user's hand and the handle [Salisbury et al., 2004].

Such a tool based paradigm can find a particular interest in several applications, in particular for dentistry simulators. In such systems, simulation of light tools used to interact with hard teeth requires haptic devices providing both low inertia (in free space) and high stiffness (at contact) [Zhang et al., 2017]. While classical haptic interfaces can hardly answer these requirements, being either very transparent in free space but unable to render high stiffness and large forces or vice-versa, an IC interface would allow to render hard contacts while remaining very transparent as the user can manipulate a handle

(representing the dental tool) in free space without feeling the presence of the robot. This would guaranty the natural execution of the task and provide realistic force feedback with better control of the exerted force on teeth and tissues.

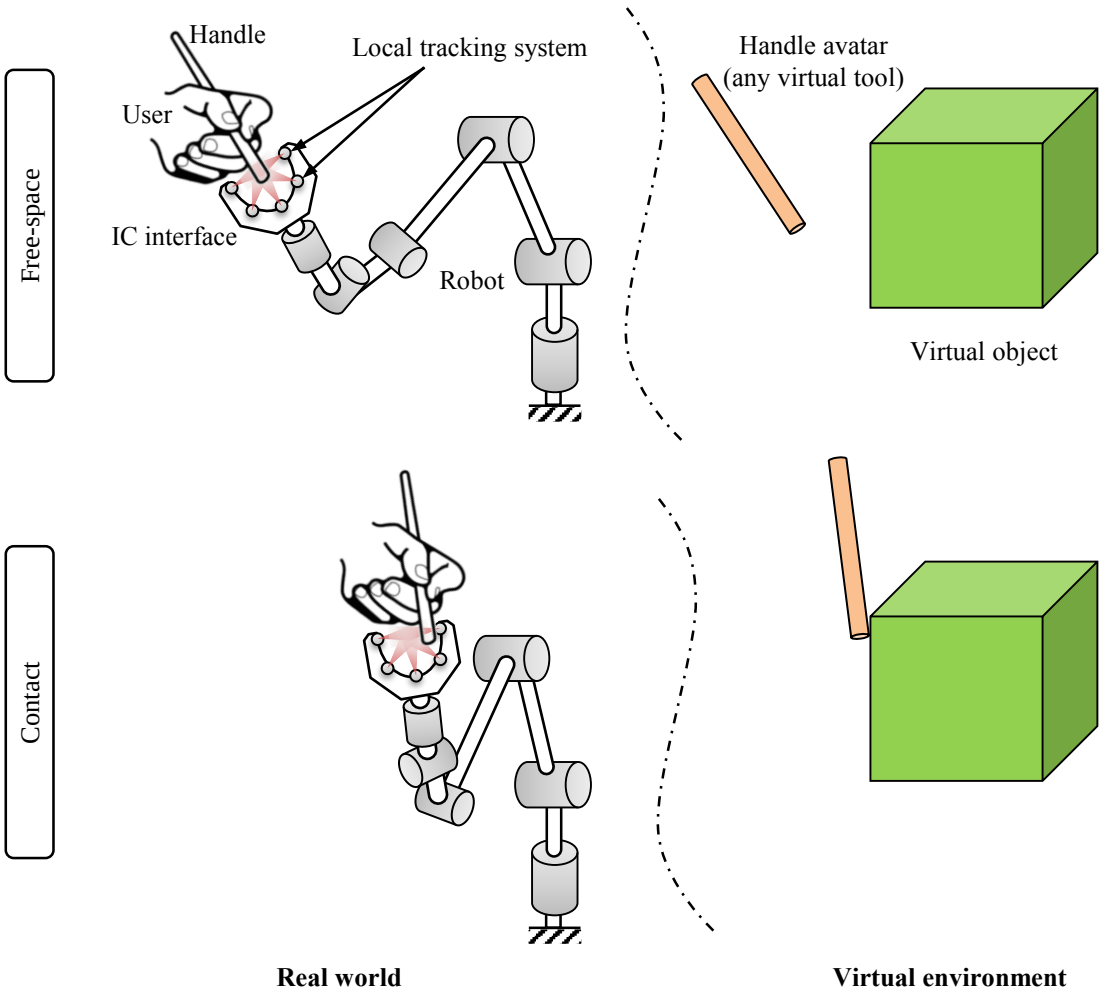

Figure 4.1: IC interface using tool-based interaction paradigm with local tracking system.

As previously mentioned for finger-based IC-HIs, a precise estimation of the handle configuration is also fundamental here to improve the quality of the interaction since this information is used to control the robot behavior in free space and at contact. To answer this requirement, a study of different tracking approaches to measure the relative handle/ robot configuration is presented in the following section.

4.3 Handle/robot non-contact tracking

Several paradigms can be used to track the handle's configuration relative to the robot's end-effector (here IC haptic interface and robot end-effector will be used indistinctly). Three possibilities can be imagined.

4.3.1 External tracking system

One can use a **camera based motion capture** system to measure the global configuration of the handle and the robot (see Fig.4.2). The information of interest, i.e. their relative configuration, would then be obtained at any instant of time by combining these data. This solution is very simple to implement and allows to obtain synchronized measurements of all data. With this approach however, it would be necessary to equip the handle and the end-effector with markers allowing to keep a better track of it. Also, except if using costly high end systems, accuracy and bandwidth are limited. Last but not least, errors associated with the handle and end-effector add up when calculating their relative configuration.

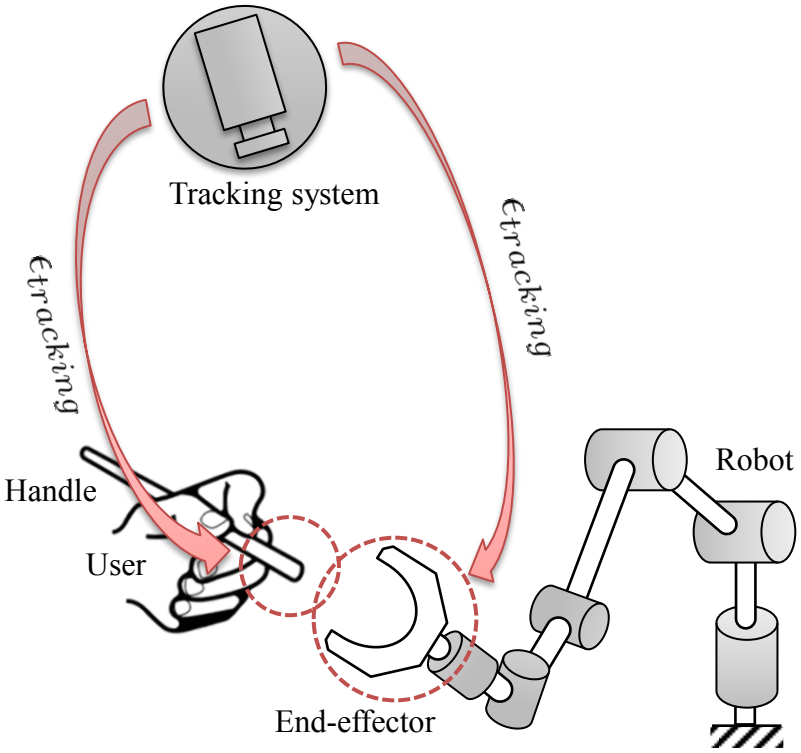

Figure 4.2: External tracking approach, based on a camera motion capture system, and associated errors.

4.3.2 Hybrid tracking system

Another solution is to use a **motion capture system** to measure the configuration of the handle **and** the **joint sensors** of the robot to compute the position and orientation of the end-effector. This solution is relatively simple to implement since it does not require to modify the robot (see Fig.4.3). Moreover, compared to the previous approach the information on the end-effector is more precise and acquired at a higher bandwidth. However, the same limitations remain for the handle and the measure of interest (the relative handle/robot configuration): it is once again calculated by combining both infor-

mation. In such conditions, inaccuracies of both systems add up, being in certain cases relatively important. In fact, it is generally assumed that the robot will move at low speeds, allowing to compute the end-effector's configuration using the joint sensors data combined with the robot kinematic equations. This solution is however not very precise. In order to precisely calculate the configuration of the robot's end-effector, it would be necessary to employ the flexible dynamic model of the robot [Jubien, 2014] which risks to be complex and needs computing resources to be calculated at a haptic rate ($\geq$ 1kHz). In addition, motion capture system's bandwidth are usually lower than those employed in robot controllers, introducing the need to use interpolation and/or predictive filters to ensure that both systems work properly together.

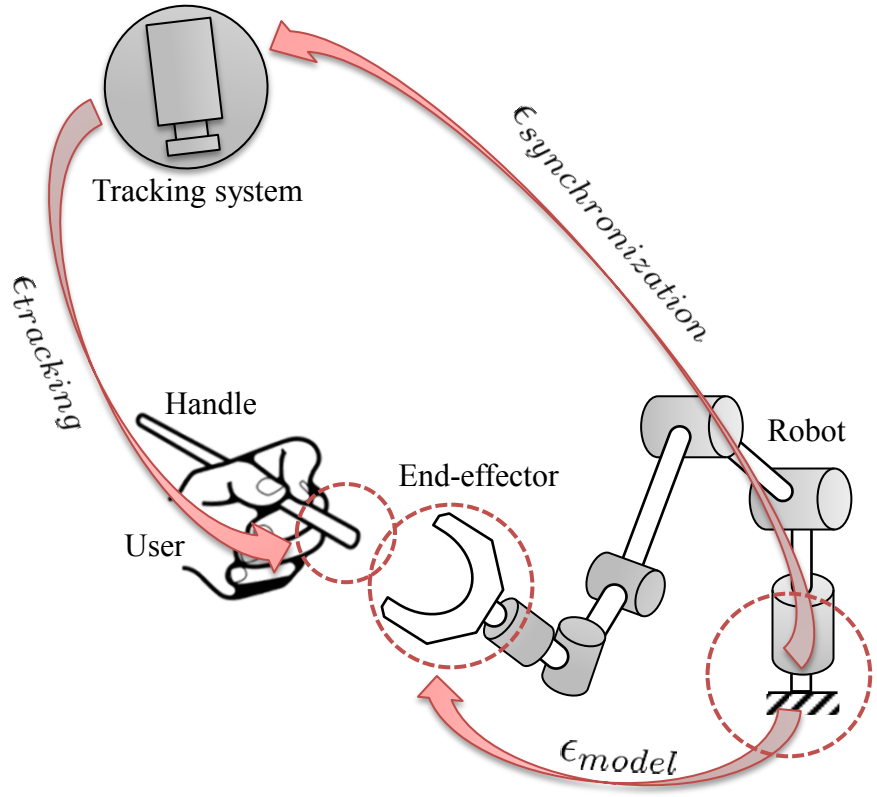

Figure 4.3: Hybrid tracking approach, combining data from motion capture tracking system and robot joint sensors, and associated errors.

4.3.3 Local tracking system

The last and most interesting approach consists in integrating **non-contact short range** sensors (providing displacement information) directly in the end-effector. This solution gives a direct access to the information of interest and, provided an informed selection of sensors, this information is very precise and fast.

This approach was used in [Yoshikawa and Nagura, 1997], [Gonzalez, 2015] as well as in [Chabrier et al., 2017]. In the former, the ring is equipped with a set of eight light-weight optical on-off sensors used to roughly estimate the user's fingertip position

in a ring-like end-effector at a frequency of 2kHz. In the second, the end-effector is instrumented with sixteen infrared proximity sensors allowing finger shape reconstruction and precise estimation of its position at a frequency of 300Hz. In the later, nine infrared proximity sensors are used to identify the relative configuration between the fingertip and the surrounding cap in 5DoF at 1kHz. Therefore, eight sensors are positioned around the finger in two planes perpendicular to the finger axis and the last one is placed in front of the finger.

Despite the fact that it requires the development of a specific measuring system, this approach was considered the best suited for our application since the tracking of the handle would be done with a single measure, reducing the accumulation of tracking errors.

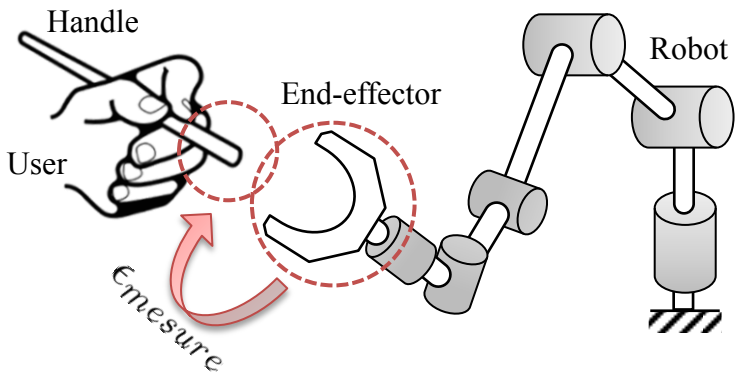

Figure 4.4: Equipped end-effector employed as a local tracking system and associated errors.

4.4 Design drivers of an IC haptic interface tracking system

4.4.1 General considerations

The tracking system of an IC-HI is in charge of measuring, without contact, the relative configuration between the handle held by the user and the robot, either in 3DoF (position) or 6DoF (position and orientation). Its aim of is to provide the robot with the necessary information so that it can compensate for any position difference and follow the handle's trajectory in free space and so that it can properly manage contacts with VOs.

These demands are partially similar to the requirements associated with motion capture systems usually used in VR to measure precisely and at a high frequency rate the 6DoF configuration of different parts of the user's body (e.g. head, eyes, arms, hands, fingers, trunk, legs and/or feet depending on the targeted application). Indeed this information is also used to control the configuration of the user's avatar and manage the contacts with the environment. This is also true for haptic interfaces, with a mechanical link between the user and the robot and with focus on the hand however.

In all cases, the global aim is to avoid tracking technologies that bothers the user and, as a consequence, reduces the immersion and quality of the interactions with the VE. In the case of haptics, "a mechanical influence of the sensor on the system has to be avoided for haptic applications, specially kinaesthetic ones" [Hatzfeld and Kern, 2009]. In the case of IC haptic interfaces providing tool based interactions, mechanical influence of the tracking system is somehow forbidden. It is then not advisable to add heavy tracking systems to the hand of the user since this will potentially make the user uncomfortable and/or fatigue faster.

In summary, despite the fact that there is no universal tracking system (different technologies, which are more or less complex and performant, exist), VR applications and IC interfaces tracking systems share common requirements. An ideal tracking device would need to meet a series of criteria, sometimes not compatible between each other. These requirements are shown in figure 4.5

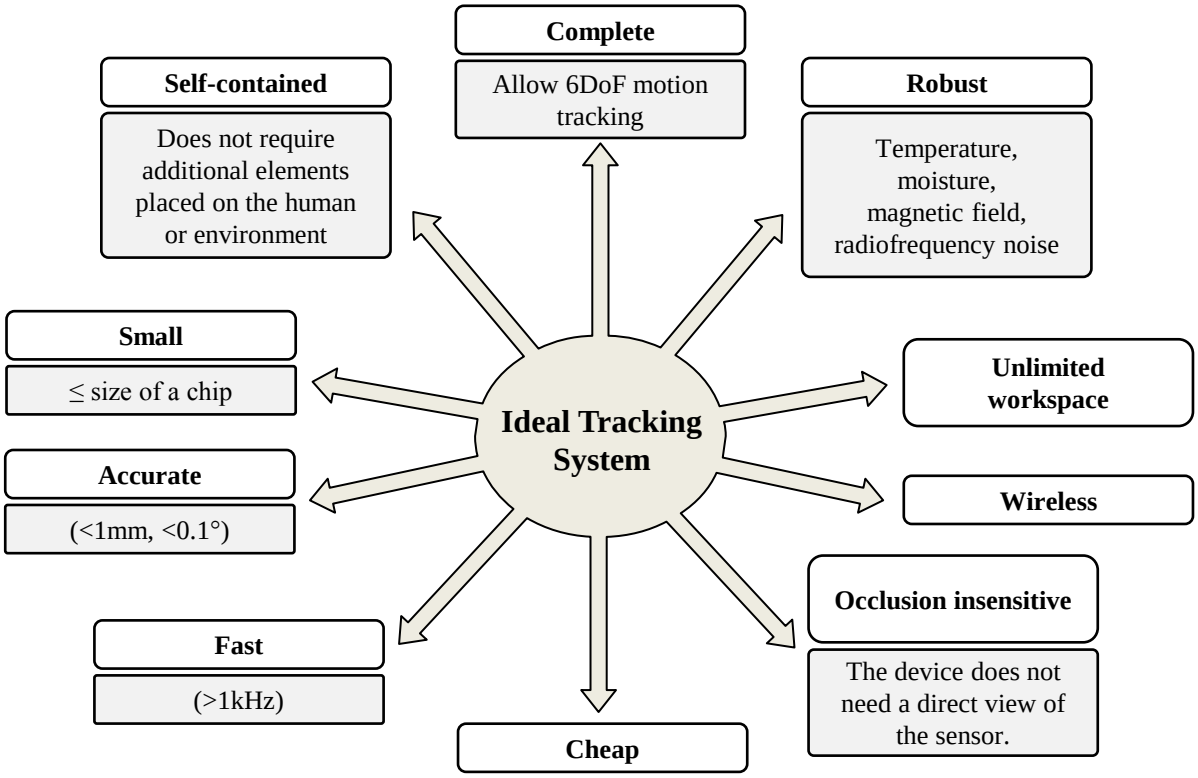

Figure 4.5: Ideal tracking system requirements (adapted from [Mihelj et al., 2014]).

4.4.2 Adaptation to the case of an IC-HI

Previously mentioned requirements hold for any VR tracking system. Some of them remain however quite general and require to be more specifically instantiated in the context of an IC-HI local tracking systems. Each of the above mentioned criteria will be further discussed in the sequel.

4.4.2.1 Completeness, robustness, cost and size

These requirements are still valid in the context of an IC-HI local tracking system. They hold as stated in figure 4.5.

4.4.2.2 Self-containment and wires

The use of a tool as interaction-media (instead of a finger or any other body part) allows to equip the handle, if necessary (e.g. to allow for a higher measurement precision), with active elements (e.g. active emitters or receivers). A special care should however be taken to keep the handle wireless in order to avoid any additional effort caused by the cables. Fortunately, this can be easily avoided by supplying the active elements mounted on the handle with small embedded batteries.

4.4.2.3 Occlusions, workspace and accuracy

With a local tracking system, the handle is always kept in front of the end-effector (provided an adapted control of the device). As a consequence, there are inherently no occlusions. The counterpart of this advantage is that the workspace is directly limited by the robot's range of motion. This means that the robot should be selected adequately for the tasks of interest. Also, a sufficient space should be left between the handle and the end-effector, so that the robot has a sufficient time to react to any user's movement in free space and follow them without handle/robot collision. This introduces in turn some constraints on the local tracking system range of measurement and precision.

4.4.2.3.1 Tracking accuracy The IC paradigm implies that force feedback should be provided to the user only when he/she touches the IC interface in order to provide clear free space/contact and contact/free-space transitions synchronized with the virtual scene.

From a control point of view, the robot is governed by two laws (or modes): the free space mode (that ensures tracking and close following of the handle) and the contact mode (responsible for providing the corresponding interaction forces with VOs). The transition between these two control modes is made when the handle avatar (HA) makes contact with a VO, i.e. when the minimum distance $\boldsymbol{d}_{HA/VO}$ between them becomes negative. In the real world, it should correspond to the exact moment of the physical contact between the handle and the IC interface. A perfect synchronization of these two events in both real and virtual worlds is the goal to attain even if it is not that easy to achieve.

In order to reach an acceptable synchronization (i.e. an imperceptible visuo-haptic delay) it is necessary to precisely determine the distance $\boldsymbol{d}_{handle/robot}$ between the handle and the robot (see Fig.4.6) in order to provide a force feedback that corresponds to the

virtual scene.

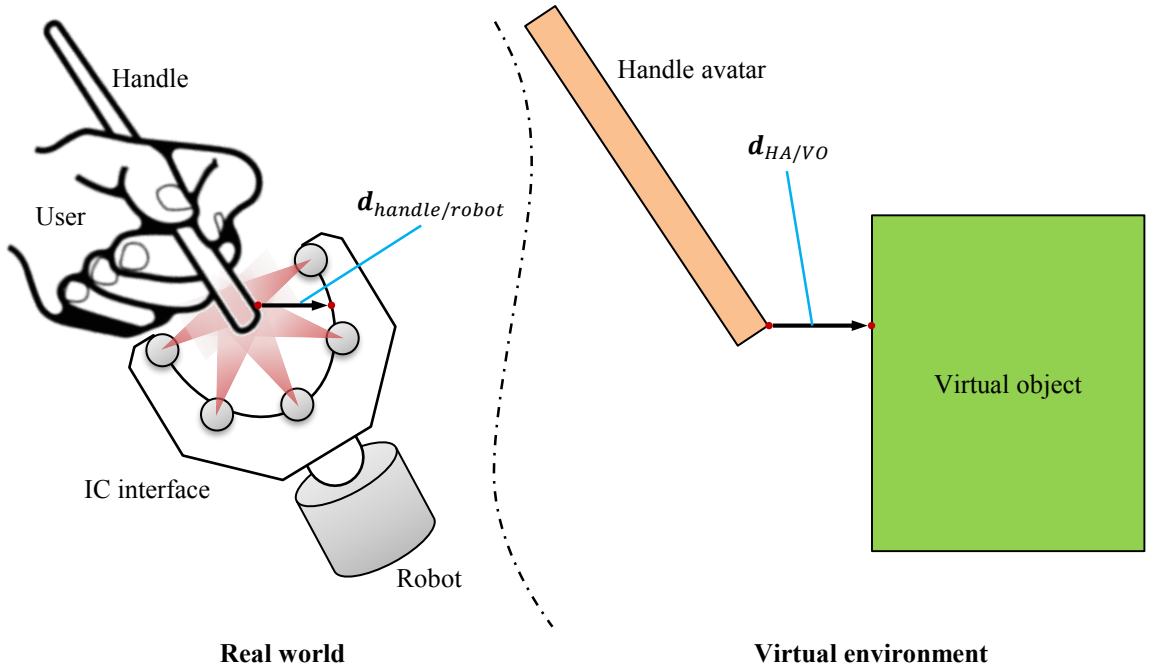

Figure 4.6: Minimum distance in real world and virtual environment prior to contact.

From our experience, a tracking accuracy of about 0.1mm as in [Gonzalez, 2015] and 1° as in [Chabrier, 2018] is sufficient to ensure an efficient control.

4.4.2.3.2 Minimum distance of measurement

In order be able to precisely control the free space to contact and contact to free space transitions, the tracking of the handle should be ensured for any handle position within the end-effector, up to the situation where it encounters the IC interface, i.e. even when $\boldsymbol{d}_{handle/robot} = 0$. It is worth noting however that, in such a system, the sensors are usually hidden behind small diaphragms protecting them from direct contacts against the tracked object (finger or handle). In existing systems, the thickness of the protecting contact surface varies from 0.5mm in [Chabrier, 2018] (metallic end-effector) to about 1mm in [Gonzalez, 2015] (plastic end-effector), the minimum distance between the sensors and the tracked object varying between 0.75 and 1.25mm (due to integration constraints). We will use here a similar value as design driver, i.e. 1mm.

4.4.2.3.3 Maximal range of measurement

The goal of the IC interface tracking system is to provide the configuration of the tool (in 3DoF or 6DoF) to the robot so that it can follow it, i.e. to maintain the center of the IC interface inner volume as close as possible to the handle.

In practice however, "perfect following" of the handle is almost impossible. Indeed the data from the tracking system's unitary sensors need first to be filtered and treated

to calculate the configuration of the tool. Next, the handle configuration is sent to the robot's controller which calculates the necessary torques that should be sent to the robot's actuators to cope with the handle displacement and reduce the position and orientation tracking error (see Fig.4.7 for an illustration of the position tracking error $\vec{\epsilon}_{\boldsymbol{X}}$). Of course, the robot will not react immediately, its reaction time depending on the actuators and robot's dynamics. As a whole, this measurement and tracking process introduces an inherent delay. As a consequence, the robot won't move exactly at the same time as the handle does.

This tracking error must be taken into account when defining the size of the inner volume size of the IC interface. This volume should be large enough to avoid the handle touching the robot while the user is manipulating it in free space. The IC haptic interface should however also remain as small and light as possible for an easy integration on a robot. A careful optimization should thus be performed in order to find the best possible tradeoff between a small end-effector and an end-effector sufficiently large to ensure movements without handle/robot collisions in free space. Within this context, a gap between the handle and the IC interface just larger than the maximum tracking error appears as the best solution.

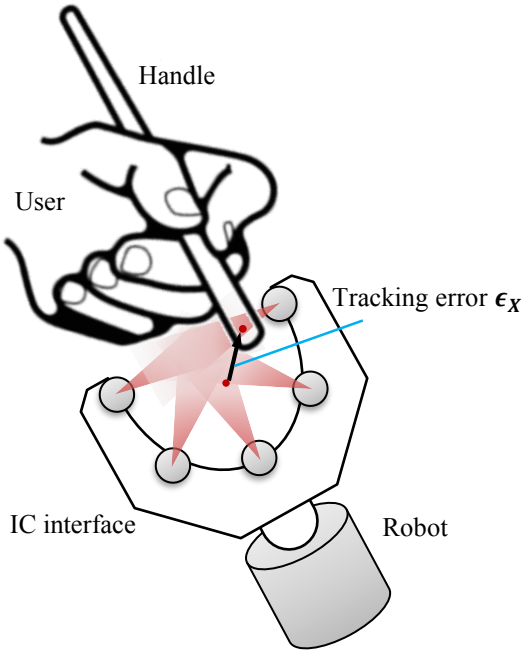

Figure 4.7: Tracking error vector between the handle and the IC haptic interface.

One may think of employing a real robot to perform a tracking error identification task, i.e. make the robot to follow a known trajectory with well defined speeds and accelerations, and identify the maximum tracking error $\boldsymbol{\epsilon}_{\boldsymbol{X}_{max}}$ for such platform. Such an experiment would however be complex to set-up.

Another method that is simpler (especially if the robotic platform is not available at the moment of the design) and that consumes less resources is to simulate the behavior

of the whole system to identify the maximum tracking error. Therefore, it is necessary to make some assumptions regarding both the operator's dynamics (which will constrain the handle's movements), the control law and the robot (which will constrain the following dynamics). It is worth noting that, in a first step, a 1-DOF simulation is sufficient. Such approach that consists in simulating a trajectory-follow task employing a 1DoF IC haptic device model, which characteristics are representative of a whole force feedback device, has been employed in [Gonzalez, 2015] to dimension a 2-DOF IC-HI's end-effector.

Regarding the operator's dynamics, the movement of the user's hand can be modeled using a mathematical model that matches observed straight unconstrained point to point arm movements [Tamar and Neville, 1985]. This model, which results in a minimum jerk trajectory, was slightly modified in its notation by [Gonzalez, 2015] and its formula is given here in (4.1).

$$x_h(t) = x_A + (x_B - x_A)(6t_{rel}^5 - 15t_{rel}^4 + 10t_{rel}^3) \tag{4.1}$$

where

$x_h(t)$	is the hand position,
x_A and x_B	are the start and end positions respectively and
$t_{rel} = t/t_B$	is the motion relative time (with t_B the end time and $x_h = x_A$, when $t = 0$s).

From equation (4.1), the arrival position x_B which corresponds to a motion time t_B can be expressed in function of the human speed $\dot{x}_{h,max}$ and acceleration $\ddot{x}_{h,max}$. Their mathematical expressions are given in equations (4.2) and (4.3) respectively.

$$x_B = \frac{128\dot{x}_{h,max}^2}{45\sqrt{3}\ddot{x}_{h,max}} \tag{4.2}$$

$$t_B = \frac{16\dot{x}_{h,max}^2}{3\sqrt{3}\ddot{x}_{h,max}} \tag{4.3}$$

Speed $\dot{x}_{h,max}$ and acceleration $\ddot{x}_{h,max}$ order of magnitudes should be representative of reasonable human arm movements. A non-exhaustive research allowed us to identify some reference values of typical hand's speeds and accelerations related to VR applications (see in Table 4.1). From this table, we chose medium values of speed and acceleration for our simulations, i.e. 1.6m/s and 23m/s^2.

Regarding the controller, we used a PD coupling scheme between the handle and the robot. Proportional-Derivative controllers are usually employed with force feedback devices. One main reason is that it allows to efficiently simulate stiff surfaces (with a PD controller, the surface of virtual objects appears as if they were modeled by a Mass-Spring-Damper, which can be used to simulate a large variety of typical environments).

Also, provided the PD gains are chosen adequately, the system is passive, i.e. stable for any user behavior.

Table 4.1: Human hand speeds and accelerations in VR applications. Values taken from (1):[Tamar and Neville, 1985], (2): [Elgendi et al., 2012a], (3):[Nagasaki, 1989] and (4):[Gonzalez, 2015].

Movement description	Body parts involved	Speed [m/s]	Acceleration [ms^{-2}]
(1) Two-joint voluntary unconstrained point-to point planar arm movement.	Whole arm	0.79, 1.0	0.7, 1.98, 3.38, 3.96
(2) Rising up right hand in curved motion at slow, medium and high speeds.	Whole arm	0.75, 1.6, 4.5	8.33, 16.66, 62.5
(3) Pointing movement involving arm flexion at slow, medium and high speeds.	Forearm	0.58, 1.08, 3.39	0.26, 0.84, 7.23
(4) Average values for hand movements.	Hand	1.41, 1.86	22

Finally, regarding the robot, we chose to use the Skills haptic device as a reference. This haptic interface was developed at CEA, LIST for the simulation and training of maxilla facial surgery procedures [Gosselin et al., 2011]. It was more specifically tailored to meet the requirements of corticotomy surgical procedure [Hassan et al., 2010] in terms of range of motions, forces and stiffness encountered in this surgical procedure. Such intervention is considered by surgeons as representative of delicate interventions requiring highly sensitive skills, mainly in haptics and audition. In this context, an IC haptic interface is of high-interest to improve the realism of the interaction, e.g. for the transfer of skills from VR training platforms to real world. The 1DoF equivalent of the Skills haptic interface was thus used in the simulation. Its main characteristics are shown in table 4.2.

Table 4.2: Skills haptic interface main characteristics.

Parameter	Value
Peak translational effort: F_{pk}	25N
Apparent mass: m	0.460kg
Robot link length: l_r	0.300m

The block diagram of the simulated robot (implemented in Matlab Simulink) is shown in figure 4.8. The simulation takes as a set point the human's hand position x_h. The tracking error ϵ_X is calculated by subtracting the sensed position of the robot x_r^* from x_h. The Cartesian error is then used to compute the error at the joint level, which serves as an input for the PD controller to calculate the joint torque τ and then the saturated torque τ_s^*, which maximal and minimum values are fixed by the peak torque

$\tau_{pk} = \pm F_{pk} \cdot l_r = \pm 7.5\text{N} \cdot \text{m}$. Angular acceleration $\dot{\omega}$ allows to calculate the angular position θ which is finally used to compute the robot's position x_r. The position of the robot is sensed with a delay of 2ms in order to take into account the haptic loop servo rate and other delays.

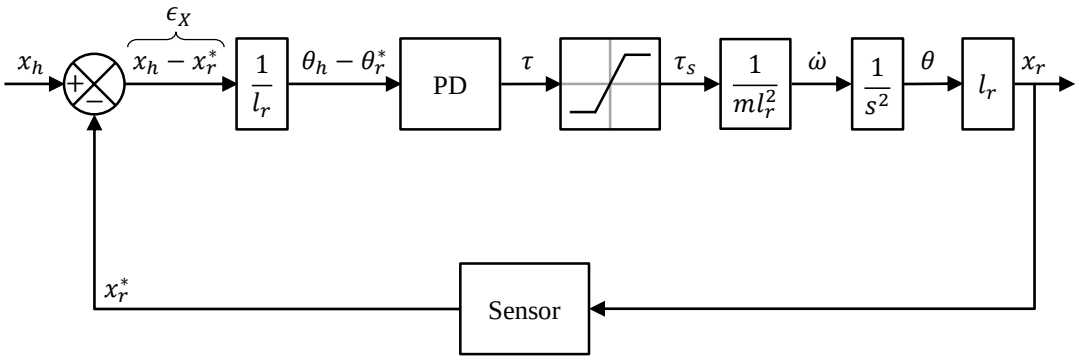

Figure 4.8: 1DoF IC interface control block diagram.

The expression of the PD controller at the joint level is given in equation (4.4). In order to identify the controller gains providing the smallest possible tracking error $\epsilon_{X_{min}}$ (i.e. the smallest of the maximum tracking error values generated at each simulated round-trip displacement), a large range of values were tested in order to observe the error distribution. The proportional gain was chosen between $0 \leq K_p \leq 10000\text{N/m}$ with a step of 100N/m and the derivative gain between $0 \leq K_d \leq 100\text{Ns/m}$ with a step of 1Ns/m. Using this step sizes 10000 tracking error ϵ_X values were obtained. Their distribution is shown in the abacus from figure 4.9.

$$\tau_t = K_p l_r^2(\theta_h - \theta_r^*) + K_d l_r^2(\dot{\theta}_h - \dot{\theta}_r^*) \tag{4.4}$$

These results show that the smallest tracking error that can be attained is $|\epsilon_{X_{min}}| \approx 3.7\text{mm}$. This value is obtained when employing gains equal to $K_p = 3636\text{N/m}$ and $K_d = 90\text{Ns/m}$.

It is worth noting however that these gains cannot be attained in practice. Referring to the Skills technical documentation [Gosselin and Louveau, 2010], it was noticed that the gain K_d that proved to be stable on real platform is limited to $K_{d\theta} = 4\text{Nm/rad/s}$ at the joint level, which corresponds here to $K_d = K_{d\theta}/l_r^2 \approx 45\text{Ns/m}$, which is half of the one obtained in simulation. Simulation results for a round trip movement using these gains are shown in figure 4.10. The corresponding tracking error value is equal to $|\epsilon_X| \approx 4.6\text{mm}$.

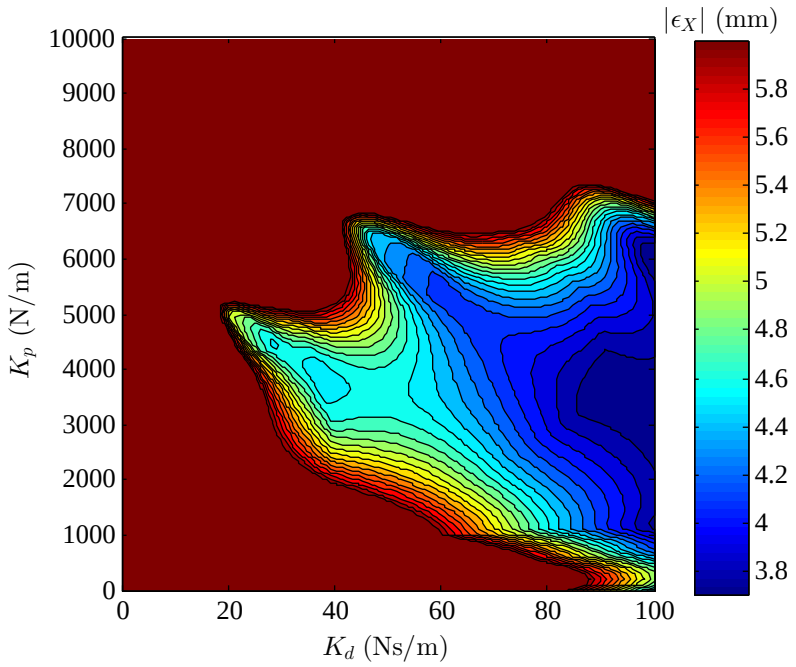

Figure 4.9: Maximal tracking error abacus for different values of K_p and K_d.

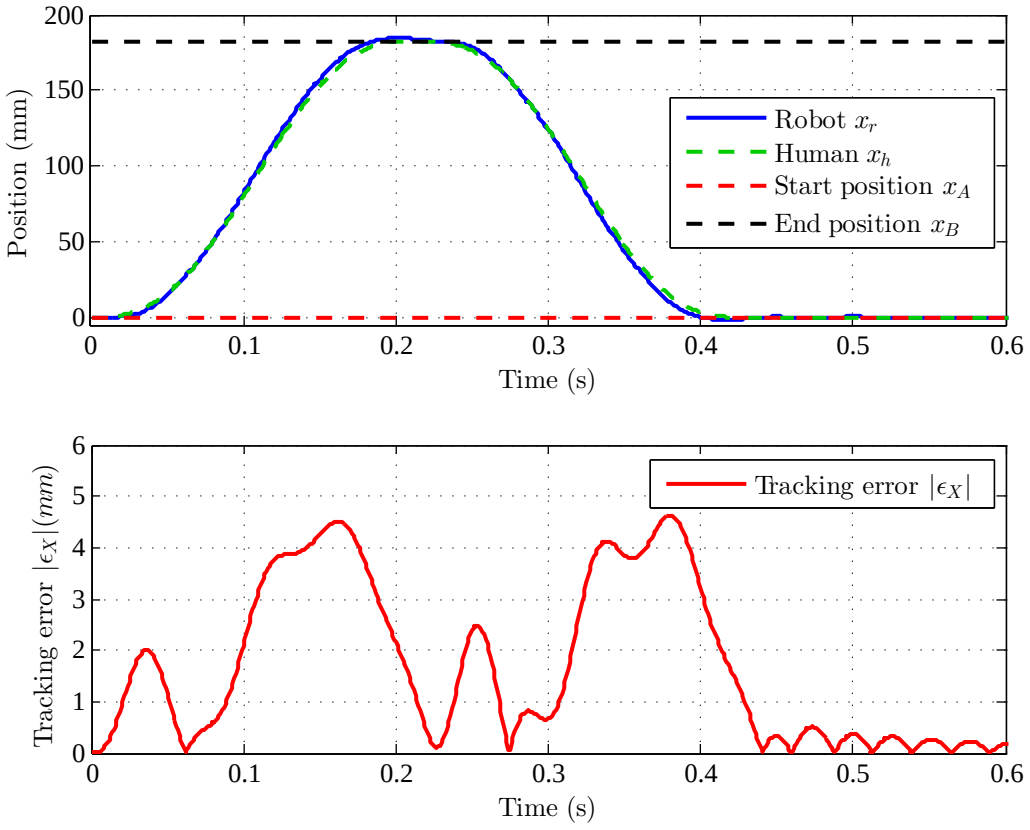

Figure 4.10: Simulated trajectory and tracking error between hand (for medium values $\dot{x}_{h,max} = 1.6\text{m/s}$ and $\ddot{x}_{h,max} = 23\text{m/s}^2$) and the robot (1DoF Skills platform equivalent).

It can then be said that a spherical volume of radius $r \approx 4.6$mm should be taken into account in the process of defining the size of the inner volume of the IC end-effector. For practical purposes, a sphere with a diameter of 1cm will be taken into account.

4.4.2.4 Working frequency

It is known that a servo rate of 1kHz is commonly employed for adequate haptic rendering [Salisbury et al., 2004]. This value appears to be a good compromise allowing to present reasonably complex objects with reasonably stiff values. Higher stiffness, e.g. to provide crisper contacts, would require to increase the working frequency, which implies to reduce the complexity of simulated objects or to employ more powerful computers.

4.4.3 Specifications of an IC interface

An IC haptic interface allowing tool based interactions should be equipped with an adapted end-effector. For this design, it is important to take into account the following aspects:

- The handle, hold directly by the user's hand, should be light and easy to manipulate.
- The handle should be adapted to the tasks of interest. Here, with focus on surgery, we will make the assumption that the handle has a cylindrical pen-like shape, with a comfortable diameter of around 15mm.
- The tracking system's weight should be as small as possible so that the robot is able to displace it and provide expected tracking and force feedback behaviors. Weight has an influence on the stability of the haptic loop.
- The end-effector should allow to constrain the handle in all directions (in position only or position and orientation).

The tracking system (providing 3 or 6 DoF information) requires to be placed between the haptic device and the handle being manipulated by the user. For the former, four main design drivers were identified: minimum distance of measurement (allowing to precisely control the transitions between free space and contact), range of measurement (which should be sufficient to cope with any user's movement), high working frequency (for a stable control of the haptic device) and high accuracy (to reduce error accumulation). The corresponding values are summarized in Table 4.3.

Designers usually use several unitary 1DoF sensors for the realization of such tracking system, however it remains interesting to explore already available tracking systems possibly suiting the development of an IC handle tracking system. Principle and representative characteristics of common existing tracking systems will be presented in next section 4.5.

Table 4.3: IC tracking system design specifications.

IC end-effector design drivers	Value
Minimum distance of measurement	1mm
Range of measurement	≥ 1cm*
Working frequency	1kHz
Position/orientation accuracy	$< 10^{-1}$mm/1°

* i.e. an inner spherical volume of diameter $d = \epsilon_X(1\text{cm}) + \text{handle diameter } (1.5\text{cm})$

4.5 Review of common motion tracking systems

Localization of objects or persons is a common problem faced in several fields of applications. For instance, it is necessary to localize airplanes for air traffic control. It can also be interesting to localize a person which mobile phone has a GPS or to propose him/her location based services or to localize an object in space thanks to the information provided by several cameras observing the scene. Each application may need one or more sensing technologies which data are employed to determine the information of interest. The required sensing technology, accuracy, size, working frequency and resolution will depend mainly on the measuring necessities and on the constraints of the environment where such sensors will be employed.

In the present section, our interest focuses on the tracking systems mainly employed in robotics and in VR applications. Its goal is to open a discussion towards the choice of tracking systems possibly suiting the development of an IC handle tracking system.

The question is then what kind of sensing technologies/approaches are compatible with the targeted application? A comprehensive taxonomy of existing tracking methods is shown in figure 4.11. The most promising will be discussed in the following paragraphs.

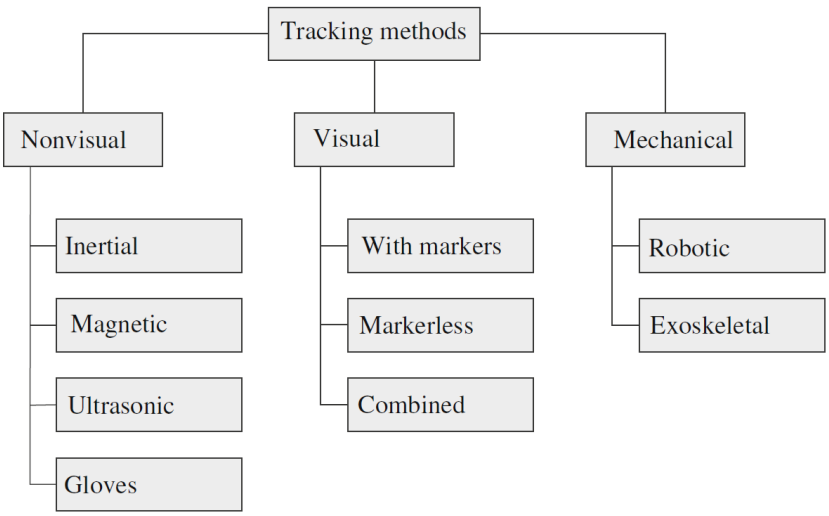

Figure 4.11: User motion tracking methods (taken from [Mihelj et al., 2014]).

4.5.1 By mechanical linkages

4.5.1.1 Principle

This approach assumes a direct physical connection between the target (here the handle manipulated by the user) and the measurement device which commonly consists in several segments connected by joints which angles are measured with articular sensors (encoders or potentiometers). Such principle is illustrated in figure 4.12.

The mechanism's geometric model is used to compute the pose (position and orientation) of the last element of the chain (end-effector) relative to a reference frame, using the articular positions provided by the encoders. This paradigm is commonly used in conventional force feedback interfaces and exoskeletons.

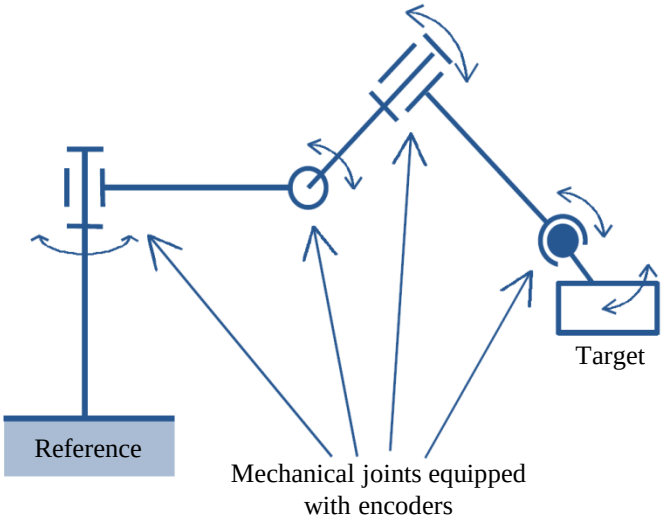

Figure 4.12: Mechanical linkage tracking paradigm (adapted from [Rolland et al., 1999]).

4.5.1.2 Conclusion

Despite the efficiency of a tracking system employing mechanical linkages (e.g. high resolution and high frequency), this approach is not suited to perform the tracking of the handle of an IC haptic interface, since the IC paradigm relies on obtaining the relative handle/robot configuration without any contact at all. This approach will thus not be further discussed.

4.5.2 By Ultrasonic waves

Ultrasonic sensors composed of co-localized emitter/receiver pairs are commonly used in mobile robotics and in the automotive industry as proximity sensors. In such case however, only the distance to the nearest object is required and obtained, and not the distance to a specific point or object of interest.

For precise tracking purposes, it is necessary to be able to compute the distance to specific points or surfaces. This can be made using separate ultrasonic emitters and receivers, as will be exemplified below with the time of flight method, or by purposely associating different emitter/receiver pairs with specific surfaces of the target, as will be explained in section 4.5.2.2 for the phase-shift method. Both methods and their respective merits will be discussed hereunder.

4.5.2.1 Time of flight method

By simply measuring the duration of the travel of an ultrasound wave between an emitter and separate receiver (i.e. the time of flight t_{tof}) it is possible to compute the distance between them. Knowing the travel speed of ultrasonic waves (which depends on the physical medium, e.g. in dry air with a temperature of 20°C, the speed of sound is $c = 343.2\text{m/s}$). The traveled distance l can be calculated using (4.5).

$$l = ct_{tof} \tag{4.5}$$

As shown in figure 4.13, three non-collinear receivers are needed to calculate the position of an emitter in space. In this figure, the equations provided to compute the position of the emitter $E[x_E, y_E, z_E]$ employ the distance calculated using (4.5).

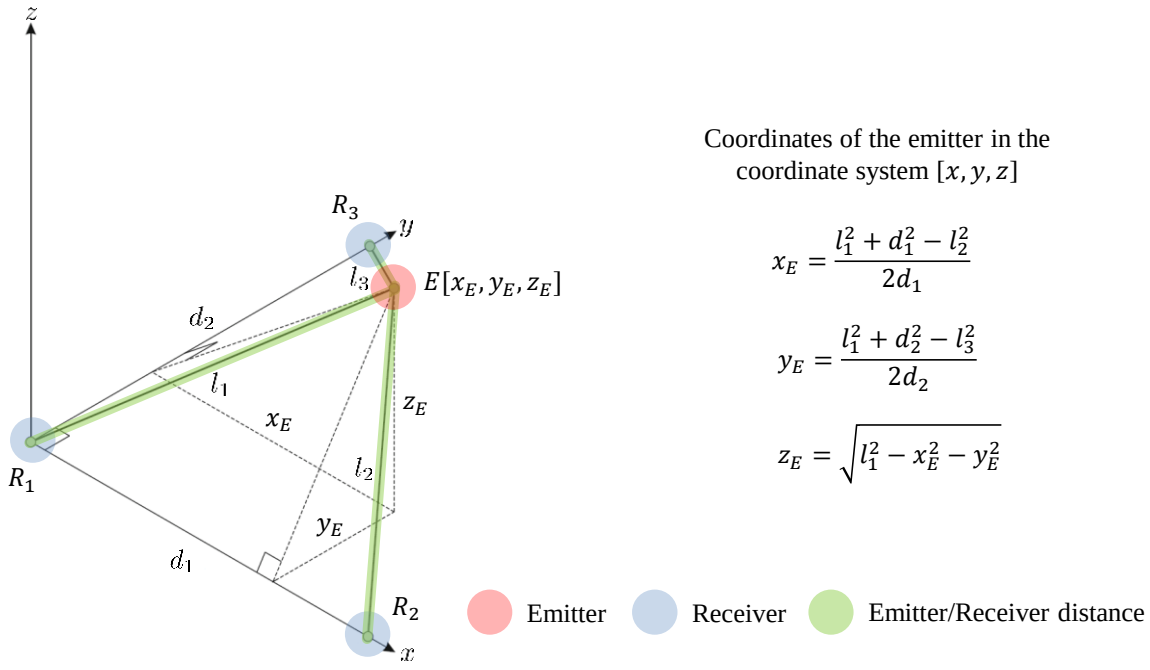

Figure 4.13: Calculation of the position of a point based on ultrasonic distance measurements. Receivers $[R_1, R_2, R_3]$ are located at fixed positions along the axes of a Cartesian coordinate system (adapted from [Mihelj et al., 2014]).

In order to obtain orientation information, it is necessary to calculate the 3D position of at least three non-collinear emitters located on the object of interest. This scenario

is shown in figure 4.14. Here, three receivers measure the ultrasonic pulses sequentially generated by the emitters, generating nine travel times, that way allowing to determine the location and orientation of the target.

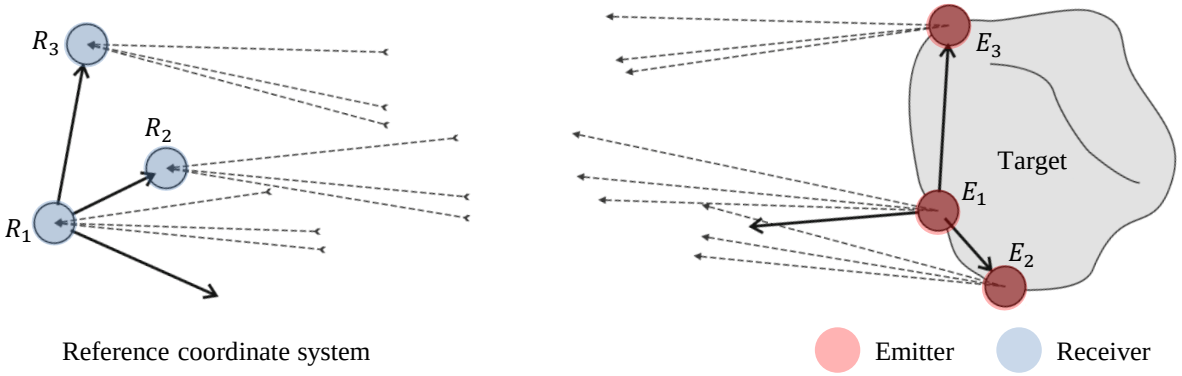

Figure 4.14: Ultrasonic sensor arrangement paradigm to estimate the complete pose of a target (adapted from[Mihelj et al., 2014]).

Table 4.4 provides time of flight distance measurement representative performances based on ultrasonic sensors.

Table 4.4: Time of flight distance measurement representative performances based on ultrasonic sensors [Rolland et al., 1999, Mihelj et al., 2014, MaxBotix, 2018, Farnell, 2018]

Sensor type	Ultrasonic
Measured variable	Distance based on time of flight of an acoustic wave
Physical phenomenon	Transmission or reflection of acoustic waves
Weight / Size	Lightweight / Diameter in the order of 1cm
Measuring range	Few centimeters up to few meters, e.g. 20mm-10000mm
Working frequency	Imposed by the pulse trip time, e.g. for c = 343.2m/s and l_u = 10cm: t_{tof} ≈ 0.3ms ➔ f ≈ 3.3kHz (for separate emitters and receivers) t_{tof} ≈ 0.6ms ➔ f ≈ 1.6kHz (for co-localized emitters and receivers)
Accuracy	Depends on the constancy of the velocity of sound
Needs to equip target?	Target is preferably equipped with ultrasonic emitters
Degrees of freedom (DoF)	- Distance measurement (1DoF) - 6DoF pose calculation based on an arrangement of sensors
Implementation	Requires optimized target design to allow reconstructing the target pose from the distance measurements if using co-localized sensors.
Occlusion sensitive	Yes
Price	Low cost
Strengths (✓) / Weaknesses (✗)	✓: Elementary sensors are simple, low cost and relatively small ✓: Not affected by color or other visual characteristics ✓: Longlasting ✗: Sensitive to temperature, pressure and humidity which affects the velocity of sound thus the accuracy of measured distances ✗: Sequential triple emission of sound signals and speed of sound in air limit the update rate ✗: Signal losses energy with the traveled distance, which limits the measuring range
Applications	Medical imaging, parking systems of cars, liquid level detection, robotics

It is worth noting that it is also possible to use classical ultrasonic sensors composed of co-localized emitters and receivers. This solutions appears however less interesting here. Indeed, in this case the time of flight t_{tof} will not represent the time required for the acoustic wave to travel from the emitter to the receiver but the time required to travel from the emitter to the target on which the ultrasonic wave is reflected plus the time required for this wave to travel back to the receiver, i.e. $l = (ct_{tof})/2$. As a consequence, the acquisition frequency is divided by a factor of 2. Also, it is required either to use different frequencies for each sensor or to separate the sensor/reflecting surfaces pairs in order to avoid cross talk between the different sensors. Finally, the geometry of the target must be precisely dimensioned and manufactured so that the 3D or 6D pose of the target can be computed from the different measurements which are potentially coupled and which can vary non-linearly with the elementary target movements (e.g. a translation in a given direction or a rotation around a given axis).

4.5.2.2 Phase-shift method

Another strategy allowing to calculate the distance between an ultrasonic sensor and a target consists in measuring the phase-shift between a reference signal produced by the emitter and the same signal reflected by the target (see Fig.4.15). Here, the reflected waves are detected with a separate receiver.

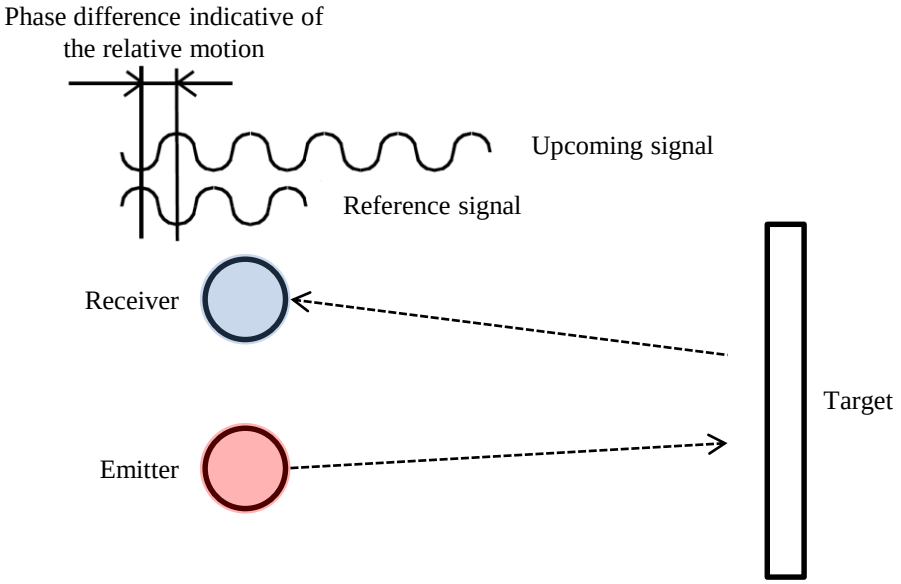

Figure 4.15: Phase-shift distance measurement principle (inspired from [Rolland et al., 1999]).

Contrary to the TOF technique which relies on emitted pulses, here a continuous signal is being measured to determine the phase difference, allowing to obtain high update rates [Rolland et al., 1999]. On the other hand, the relative motion between two measurements will be limited by the size of the wavelength of the signal. Furthermore, cumulative errors appear during the measuring process.

Generally speaking, this method is more accurate, however it requires complex hardware able to measure the phase-shift [Gueuning et al., 1996]. Also, as for TOF sensors using co-localized emitters and receivers, this solution allows only to measure the distance between a sensor and a surface, not the distance between the sensor and a specific point of the target. As emphasized in the previous paragraph, it is then complex to infer the configuration of the target from such measurements.

Table 4.5 provides representative characteristics of the phase-shift approach based on on ultrasonic sensors.

Table 4.5: Phase-shift distance measurement representative performances based on ultrasonic sensors [Gueuning et al., 1996, Rolland et al., 1999, S. Huang et al., 2002]

Sensor type	Ultrasonic
Measured variable	Phase shift
Physical phenomenon	Acoustic pulse propagation
Weight / Size	Lightweight / Diameter in the order of 1cm
Measuring range	4mm to 1500mm
Working frequency	Since a continuous signal is being measured, higher sample rates can be obtained
Accuracy	Higher accuracy than employing TOF technique
Needs to equip user/env	Not required
Degrees of freedom (DoF)	- Distance measurement possible (1DoF) - 6DoF pose calculation based on a sensor array is possible
Implementation	- Requires complex hardware to measure the phase - Requires optimized design of the target to allow reconstructing the target pose from the distance measurements
Occlusion sensitive	Yes, ultrasonic waves are reflected on obstacles.
Price	Low cost
Strengths(✓) /Weaknesses (✗)	✓: Simple, cheap and relatively small ✓: Not affected by color or other visual characteristics ✓: Longlasting ✓: More accurate than TOF technique ✓: Higher sample rates than with TOF can be attained ✗: Sensitive to temperature, pressure and humidity which affect the propagation of the sound thus the accuracy of measured distances ✗: Signal losses energy with the traveled distance, which limits the measuring range ✗: Error cumulation due to relative distance measurements ✗: Range of measurement limited by the wavelength

4.5.2.3 Conclusion

Representative performances attainable with ultrasonic sensors were presented in tables 4.4 and 4.5. Considering the design drivers for an IC haptic interface defined in section 4.4, we conclude that ultrasonic sensors are not adapted to this application for several reasons explained in the following lines.

First of all, the implementation of a 6DoF tracker based on ultrasonic sensors would occupy an important volume, as these sensors are relatively cumbersome. It would not

be possible to integrate several sensors necessary for a 6DoF measurement in a volume of few centimeters. As an example, using 3 emitters and 3 receivers as shown in figure 4.14 would require a handle with a diameter of a least 2cm if the emitters are about 1cm large, hence an inner volume of the end-effector in the order of 3cm as the range of motion of the handle is equal to ±0.5cm. The minimum distance of measurement of such sensors being 2cm, they should be placed on a 7cm diameter sphere. The receiver's size being also about 1cm, the resulting end-effector diameter would be at least 9cm, probably without taking into account integration constraints. This is much more than what is acceptable for a small haptic interface like the Skills robot.

Also, the reported measuring ranges are not adapted to our application (few millimeters to several centimeters). On the other hand, an accuracy below 1mm can be obtained by combining TOF and phase shift techniques [Gueuning et al., 1996]. Still 0.1mm as required here is challenging. Furthermore phase-shift technique is limited by the wavelength size.

Finally, it is difficult to ensure that the working frequency of ultrasonic sensors, which is imposed by the distance separating the sensor from the target and by the speed of sound in the physical medium between them, will be compatible with what is required in a haptic control loop (1kHz). Sampling rate can be improved by employing the phase-shift approach, however ultrasonic waves remain influenced by the enviromental perturbations as temperature, pressure, humidity and unwanted obstacles. Even if a single measurement can be made at a very high frequency at a short distance (e.g. 17kHz for non-colocated emitters and receivers separated by a distance of 2cm, i.e. the minimum distance of measurement for such sensors), this frequency will quickly drop with the distance and the number of DoFs as the different targets have to be acquired sequentially. The sampling rate can be improved employing the phase-shift approach. However in both cases ultrasonic waves remain influenced by the environmental perturbations such as temperature, pressure, humidity and unwanted obstacles.

4.5.3 By magnetic field

The principle of operation of an electromagnetic sensor consists in measuring the local magnetic field produced by an emitter in the sensor's surroundings. Even if the magnetic field of the Earth can be employed as a reference, such measurement would not be accurate enough in practice. For this reason, it is necessary to use an emitter to create the reference magnetic field for measurement purposes.

This principle can be used to design 6DoF contactless sensors. The most important points related to the 6DoF tracking of a target based on magnetic fields are explained in [Mihelj et al., 2014] and will be presented in the following section.

4.5.3.1 6DoF magnetic induction based tracking

As shown in figure 4.16, when a current flows through a wire, a magnetic field is created (if such wire is shaped in order to become a coil with several loops, the intensity of the resulting magnetic field will be more concentrated and stronger than with a single loop).

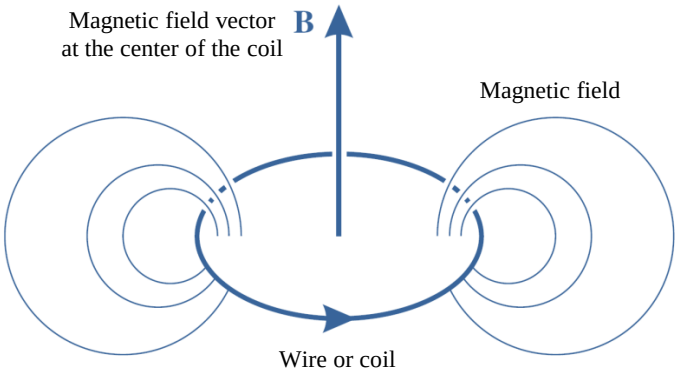

Figure 4.16: Magnetic field of a simplified coil (adapted from [Mihelj et al., 2014]).

It is worth noting that the magnetic field vector vary in space both in direction and magnitude. At the center of the wire/coil, the magnetic field vector $\boldsymbol{B}$ is normal to the coil and its magnitude is proportional to the field's strength $\boldsymbol{H}$. The relationship between $\boldsymbol{B}$ and $\boldsymbol{H}$ is given in (4.6), where μ_0 is the magnetic constant.

$$\boldsymbol{B} = \mu_0 \boldsymbol{H} \tag{4.6}$$

Outside the wire/coil axis and at a distance R from its center, the magnetic field vector $\boldsymbol{B}$ is given by the equation (4.7).

$$\boldsymbol{B} = \frac{\mu_0 M}{4\pi R^3}(2\boldsymbol{a}_R \cos\varphi + \boldsymbol{a}_\varphi \sin_\varphi) \tag{4.7}$$

where

$M = NI\pi b^2$ (with N the number of loops of the coil, I the current flowing through it and b its radius) is the magnetic dipole (assuming $R \gg b$, the coil can be approximated as a magnetic dipole),

R is the distance between the center of the coil and the point of interest,

φ is the angle between the normal to the coil and a vector linking the coil center to the point of interest,

$\mathbf{a}_R$ and $\mathbf{a}_\varphi$ are the radial and tangential unit vectors.

All these parameters are illustrated in figure 4.17.

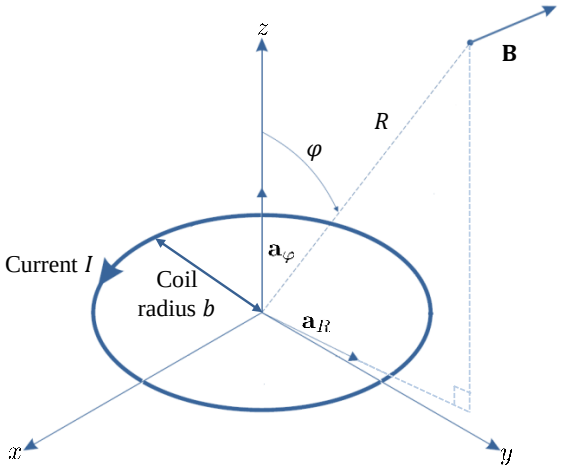

Figure 4.17: Magnetic field density vector near the coil (adapted from [Mihelj et al., 2014]).

Motion tracking based on the electromagnetic principle relies on the phenomenon of coupling, i.e. if a second coil (used as sensor) is inserted in the reference magnetic field produced by the coil of figure 4.17 (used as a source), a current is generated in the former. The amplitude of this signal being function of the reference magnetic field's local intensity and direction (known from Eq. (4.7)) as well as of the relative orientation between both coils, it is possible to infer information on their relative configuration from the measured current.

Of course, a single source/sensor pair is not sufficient to compute a 6DoF configuration. To determine the position and orientation of a target in space, a magnetic tracking system employs in practice three orthogonal active coils on the source side and three orthogonal passive coils organized in a similar but usually smaller configuration on the target. A changing magnetic field is sequentially generated in each coil of the source. These signals generate electric currents in the passive coils located on the target. The measurement of these currents finally allows to estimate the 6DoF relative configuration between the source and the sensor (see Fig. 4.18).

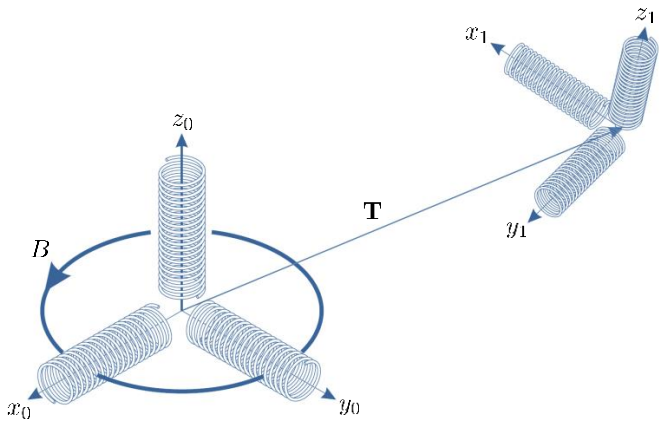

Figure 4.18: 6DoF tracking principle based on magnetic field measurements (adapted from [Mihelj et al., 2014]).

Several magnetic tracking systems are commercially available (see Fig.4.19). As an example, the representative performances of magnetic trackers manufactured by the company Polhemus are provided in table 4.6.

FASTRAK® 6DoF Motion tracker

Figure 4.19: Commercial 6DoF magnetic tracking system (pictures taken from [Polhemus Inovation in Motion, 2018]).

Table 4.6: Polhemus products representative performances (information retrieved from [Polhemus Inovation in Motion, 2018]).

Sensor type	Electromagnetic
Measured variable	6DoF Target pose
Physical phenomenon	Magnetic field emission
Size	Sensor: 2.3 × 2.8 × 1.5cm, Source: 10.3 × 10.3 × 10.16cm
Measuring range	76cm – 106cm (accuracy guaranteed in this range)
Working frequency	50Hz - 240Hz per sensor
Accuracy	0.76mm – 7.62mm (position) / 0.15° – 1° (orientation)
Target instrumentation	Sensors are mounted on the target
Degrees of freedom (DoF)	6DoF pose calculation possible
Occlusion sensitive	No
Price	Expensive
Strengths (✓) / Weaknesses (✗)	✓: Not sensible to occlusion ✓: Sensors easy to attache ✗: Accuracy depends on how far sensors are ✗: Measurements perturbed by any ferromagnetic materials ✗: Too large for an IC-HI
Applications	High accuracy head tracking, EEG localization, training and simulation, eye tracking, neuroscience, biomechanics

Such magnetic sensors are usually considered as small and light. This is true in the field of VR and motion tracking, however not regarding our requirements. First of all, sensors are mainly wired (inconvenient for pure free movements). Furthermore, their acquisition bandwidth is limited by the sequential nature of the excitation of the source's coil, all the more that in practice, the magnetic field in a source's coil must dissipate completely before a magnetic field can be generated in the next coil. Also, their precision decreases with the magnetic field's amplitude hence with the distance from the source. Last but not least, the magnetic field is perturbed in the presence of ferromagnetic materials in the workspace, which is prohibitive when considering their association with a haptic interface.

4.5.3.2 Conclusion

Even though a magnetic tracking system is able to directly measure the pose of a target without contact, their bandwidth and accuracy do not meet the defined design drivers for an IC haptic interface. Furthermore, they are mainly wired (inconvenient for free space movements) and magnetic sensors measurements are perturbed by metal parts which are typically part of a robot.

4.5.4 By optics

Several types of optical sensors, usually used for 6DoF measurement in VR and/or robotics, can be envisaged for the tracking of the handle of an IC-HI. Their principle of operation and respective merits will be introduced below.

4.5.4.1 Motion capture system

Motion capture (MOCAP) is regularly employed in several application domains, e.g. computer animation, biomechanics, robotics, cinema, video games, anthropology etc. Three main types of optical motion tracking systems exist, based on the following paradigms [Field et al., 2011].

MOCAP with **passive markers**. Here at least two fixed cameras are used to compute, by triangulation, the 3D position of one or more passive markers placed on the target. Provided the relative position of at least three targets is fixed, it is possible to reconstruct the 6D pose information of the target. IR lighting and high-speed IR cameras are usually used to avoid visual pollution, e.g. visible light. The markers are also usually coated with a retroreflective tape or painting to increase the image's contrast. With such systems, tracking frequencies of up to 2kHz can be obtained.

Ono main advantage of this solution in the context of human MOCAP is that the target, in this case the user, is not weighted with batteries or cables. Its main disadvantage is related to occlusions. As soon as a target cannot be seen by at least two camera, its position cannot be computed. Occlusion problems can be overcome with the use of more than two cameras and/or supplementary markers, however it augments the processing time. Such system also suffers from non-portability and limited workspace. Figure 4.20 shows a Vicon motion capture system employing passive markers. This system is used in conjunction with a humanoid robot aiming to match the user poses in real time.

When considering the tracking of the handle of an IC-HI, the occlusion problem vanishes. Indeed, it can be hypothetized that the design of the system will ensure that the targets are always in front of the cameras, all the more that the range of motion of the handle is limited. However new disadvantages appear. First, the size of the targets, usually in the range of 2mm to 1cm, would result in a cumbersome handle. Second, the

integration of lighting systems and cameras in the robot's end-effector would make it large and complex. Finally, the minimum range of measurement, usually in the order of few tens of centimeters, is not adapted in our case. Even if it could be reduced with a dedicated design and optics with shorter focal lengths, it would probably remain around at least a few centimeters. Globally, this solution does not seem very well suited for the local tracking of the handle of an IC-HI.

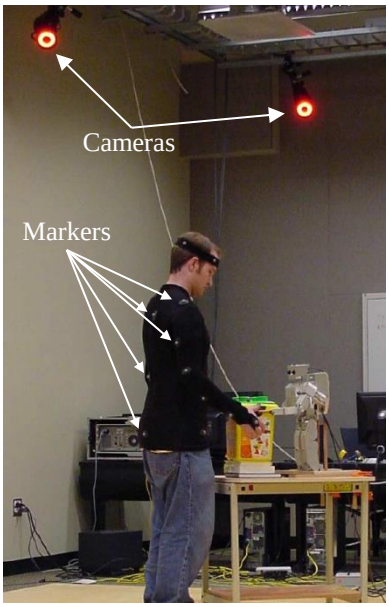

Figure 4.20: Vicon motion capture system (adapted from [Shon et al., 2007]).

MOCAP with **active markers**. Here the markers are infrared emitting diodes (IRED) acting as light sources. Their light is usually multiplexed and as a result the frequency of the acquisition is divided by the number of sources to detect. Even though this solution has the advantage that each light source can be individually identified, this approach limits the measurement frequency.

Within the context of human MOCAP, this method has the advantage over the previous one that, since it employs active markers, the measurement area is theoretically higher than with passive ones. In this case however, the user should be equipped with batteries and wires allowing the light sources to work, which contribute to impede motion.

When considering the tracking of the handle of an IC-HI, this is no more a disadvantage since the handle can be equipped with a small battery locally supplying power to the IREDs which are usually small enough to be integrated on the device. However, the problem remains on the side of the robot, with cameras which will require a large and complex end-effector, even if in this case the problem is a little less acute as the IR lightning system is no more required.

Markerless MOCAP. This paradigm represents an active area of research and employs only one set of camera(s) from one angle of view without requiring to mount any type of markers on the tracked object. This approach relies upon image segmen-

tation techniques to find human posture which may be matched to a human template [Sigal et al., 2009]. Other common approaches employ background scene substraction techniques to extract a silhouette as in [Li et al., 2008] as well as learning algorithms as in [Elgammal and Lee, 2009]. These techniques are noisy, generally not real-time and are highly sensitive to lightning conditions. They do not seem well suited for the tracking of the handle of an IC-HI.

Table 4.7 summarizes representative performances of systems employing both types of markers (markerless techniques being out of the interest of the present work).

Table 4.7: Representative performances of tracking systems employing markers [Field et al., 2011].

Sensor type	Motion capture
Measured variable	Targets positions
Physical phenomenon	(Emitted or reflected) IR light intensity measurement
Weight / Size	Cumbersome (requires at least two cameras)
Measuring range	Minimum distance of measurement in the order of few centimeters for a dedicated design
Working frequency	Image capture up to 2kHz. With **active** markers the camera speed is divided by the number of markers to detect.
Precision	< 1mm
Target instrumentation	Yes (only the targets and their supports with passive markers, with additional batteries and cables with active markers)
Degrees of freedom (DoF)	6DoF pose calculation possible
Occlusion sensitive	Yes in the context of human MOCAP, not for the tracking of the handle of an IC-HI, provided a specific design
Price	Expensive
Strengths (✓) / Weaknesses (✗)	**Passive/active** ✓: High precision ✗: Post-processing latency **Passive** ✗: Large size of the targets mounted on the handle ✗: Large size of the multiple cameras and lightning sources **Active** ✓: Higher range than passive ✗: Frequency divided by the number of sensors ✗: Relatively large size of the targets mounted on the handle ✗: Large size of the multiple cameras
Applications	Virtual reality, entertainment, biomechanics and sport, tracking for virtual sets, clinical sciences

4.5.4.2 Laser triangulation

Laser triangulation finds its origins in metrology and allows to perform accurate measurement of object distances or thicknesses. Its principle is illustrated in figure 4.21. Here a camera, located at a distance d_p from a laser source and inclined of an angle φ with respect to its emitting axis, senses the laser light reflected by a moving object. It can be observed that a displacement d_x of the object causes a displacement d_y of the reflected laser light. Provided the direction in which the object moves in known, its position can

then be deduced from its measurement.

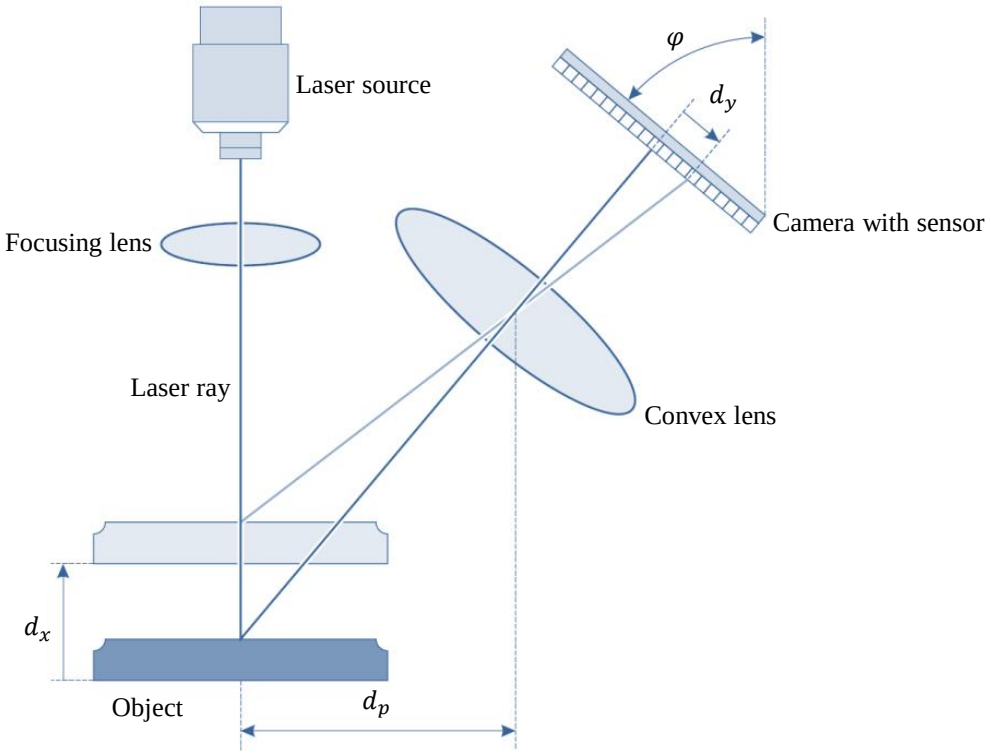

Figure 4.21: Laser triangulation principle (adapted from [Mihelj et al., 2014]).

The camera sensor is usually made of high resolution linear discrete photodiodes, commonly a CCD (charged-coupled device) or a CMOS (complementary metal-oxide semiconductor) row. These systems provide a working frequency higher than 1kHz and an accuracy below $< 10\mu$m [Hatzfeld and Kern, 2009]. However, compared to other optical sensors, this technique remains expensive as a detection row with a sufficient resolution highly impacts its cost.

Table 4.8 provides representative characteristics of triangulation based laser sensors, manufactured by the company Micro-Epsilon, and figure 4.22 shows a representative diagram of these sensors.

While very precise and having a high bandwidth, this technology does not seem very well suited for the tracking of the handle of an IC-HI. Indeed laser triangulation only provides 1DoF information. In order to get the 6DoF pose of the handle, at least 6 similar systems would be required, hence a very large and expensive system. Also, as was explained in the section related to ultrasonic sensors, the handle would have to be properly designed in order to ensure a proper reflection of the different lasers without cross-talk nor a too complex transformation matrix between the sensor's measurement and the handle pose.

Table 4.8: Laser sensor (triangulation) representative performances [Micro-Epsilon, 2018].

Sensor type	Laser sensor (triangulation)
Measured variable	Displacement, distance and thickness
Physical phenomenon	Light reflection
Size	[46 × 20 × 30mm] - [200 × 48 × 83mm]
Measuring range	2mm – 1000mm
Working frequency	2kHz – 100kHz
Resolution	0.2μm – 100μm
Target instrumentation	No
Degrees of freedom (DoF)	1DoF
Occlusion sensitive	Yes
Price	Expensive
Strengths (✓) /Weaknesses (✗)	✓: High bandwidth and precision ✗: Cumbersome
Applications	Monitoring of fragile parts, e.g. parts with surfaces easily damaged, inspection of dynamic materials, e.g. monitoring the dimensions of a tire while rotating at high speed, monitoring vibrations, close control loop of pouring of molten metal

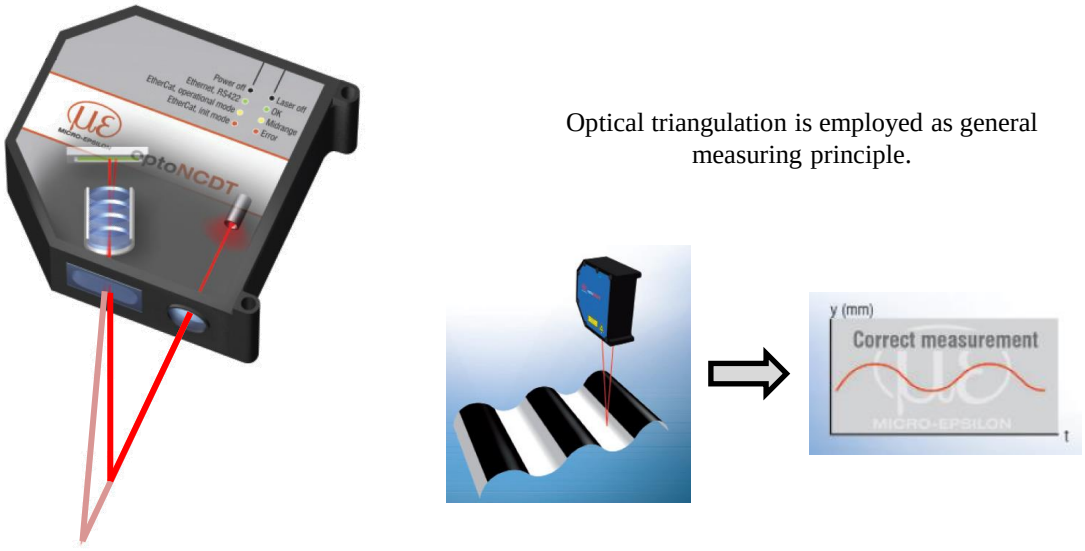

Figure 4.22: Sample diagram of triangulation based laser sensor from Micro-Epsilon (adapted from [Micro-Epsilon, 2018]).

4.5.4.3 Laser time of flight

The distance to an object can also be measured using an optical distance sensor. A diode or laser serves as a light source and illuminates the distant object, and a photodiode, CCD or CMOS sensor, placed either close to the emitter or on the target, is used to detect this light signal. The TOF measurement principle is then used in the same way as with an ultrasonic sensor, except that here the signal of interest is light instead of sound.

Laser rangefinders belong to this category of sensors allowing to measure a distance by TOF with a light source. In such systems, the sensor is just beside the illumination

system, and the target does not need any equipment. However, they are usually relatively cumbersome and fitted to medium (i.e. few meters) to long range (i.e. few hundreds of meters) 1DoF distance measurement in the field of construction and public works. They do not seem adapted for the measurement of short distance 6DoF tracking of the handle of an IC-HI and will not be further discussed here.

It is worth noting however, that very compact and close range ToF sensors were recently announced. An interesting technology based on the flight time of an infrared wave for short-range measurement is the ST microeletronics VL6180 sensor which reference information can be found in [ST Microelectronics, 2016]. Unfortunately, this sensor suffers from a low accuracy (measurement noise up to 2mm between 0 and 100mm). It is also sensitive to temperature (up to 15mm drift) and voltage (up to 5mm). This low accuracy is prohibitive for precise handle tracking.

4.5.4.4 Light pattern projection

The light pattern projection principle consists in illuminating an object of known geometry with a known pattern of light and taking a picture of this object. Its configuration is then computed by matching this image with a model of the illuminated object. A simple pattern consists in parallel stripes projected onto the object of interest. A camera, which is displaced by a certain triangulation angle, perceives the same stripes as curves running along the surface of the object. With the use of mathematical algorithms, the three-dimensional shape of the object can be determined (see Fig.4.23).

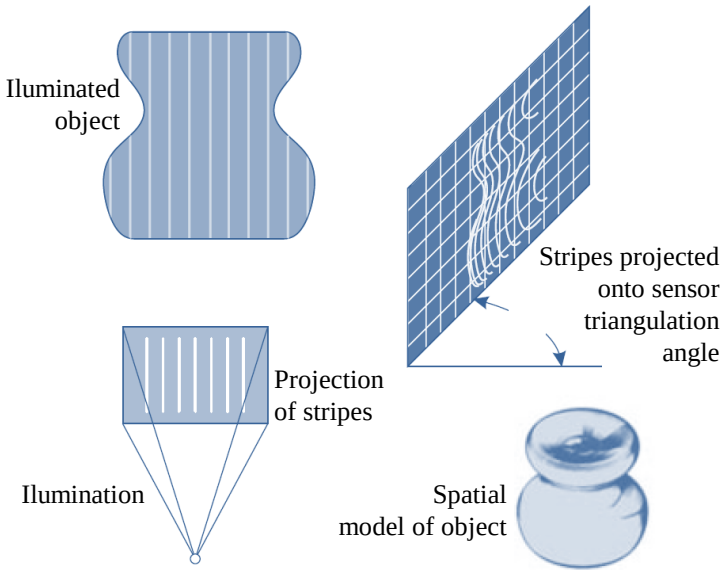

Figure 4.23: Pattern projection principle (adapted from [Mihelj et al., 2014]).

Table 4.9 provides representative characteristics of 3D imaging systems based on light pattern projection.

The present strategy can be classified as part of the **outside-in** paradigm which

Table 4.9: Light pattern projection representative performances [Geng, 2011].

Sensor type	Camera
Measured variable	Distance (3D points)
Physical phenomenon	Light projection
Weight / Size	Relatively big (requires one projector and one camera in a dedicated room)
Measuring range	Limited by the energy of light projection
Working frequency	Around 30 FPS + image post-processing time
Accuracy	3D imaging systems may have different accuracies in different (x,y,z) directions because of the inherent design properties of the systems
Target instrumentation	No
Degrees of freedom (DoF)	6DoF pose calculation possible
Occlusion sensitive	Yes
Price	Expensive
Strengths (✓) / Weaknesses (✗)	✓: Does not require target instrumentation ✗: Bandwidth decreased because of image post-processing times ✗: Cumbersome and requires a controlled environment
Applications	3D Facial recognition, 3D dental imaging, 3D imaging techniques for plastic surgery, 3D model of ear impression for custom hearing aid, imaging for reverse engineering

consists on the employ of video cameras placed on a reference and that record features of the target (see Fig.4.24).

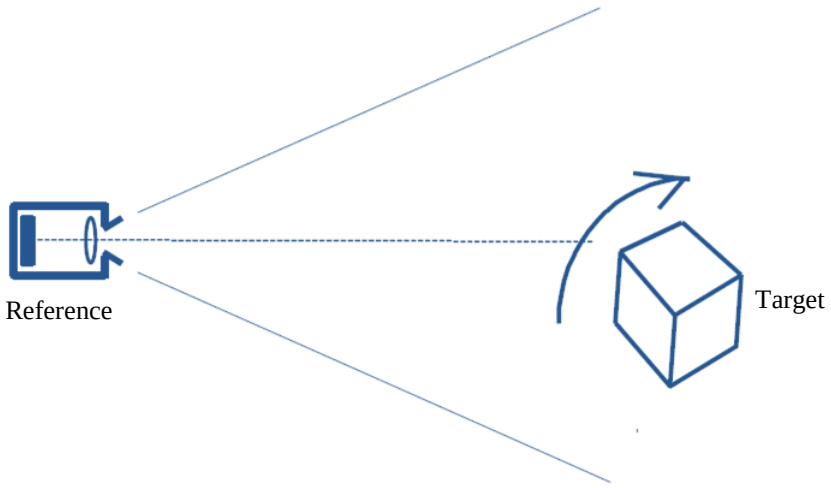

Figure 4.24: Outside-in paradigm (adapted from [Rolland et al., 1999]).

It has the advantage of directly allowing to estimate the 6DoF pose of an object, without any target instrumentation. However, this technique requires a light source allowing the projection of a pattern on the target, making the sensor cumbersome. An important computer processing capacity is also required, and even so the acquisition frequency remains too low for our application.

4.5.4.5 Videometric principle

This principle, applied for example in the field of VR and AR, consists in using several cameras placed on the target, e.g. the head of a user, to take pictures of the surrounding environment, e.g. the ceiling panels, which are equipped with reference patterns. Thanks to the 2D projections of the patterns on the sensors, it is possible to define a vector going from the sensor to a specific feature of each pattern. The position and orientation of the target can then be calculated using at least three vectors constructed from the sensor(s) to the features (see Fig.4.25).

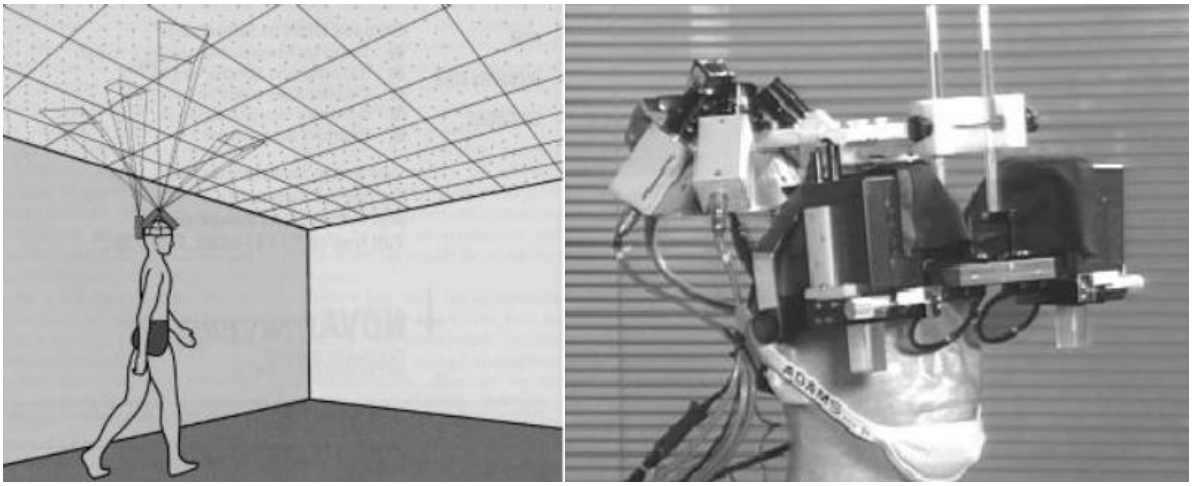

Figure 4.25: Videometric principle (adapted from [Rolland et al., 1999]).

This approach is part of the **inside-out** paradigm, in which the sensor is mounted on the target and the emitters are on the reference as shown in figure 4.26.

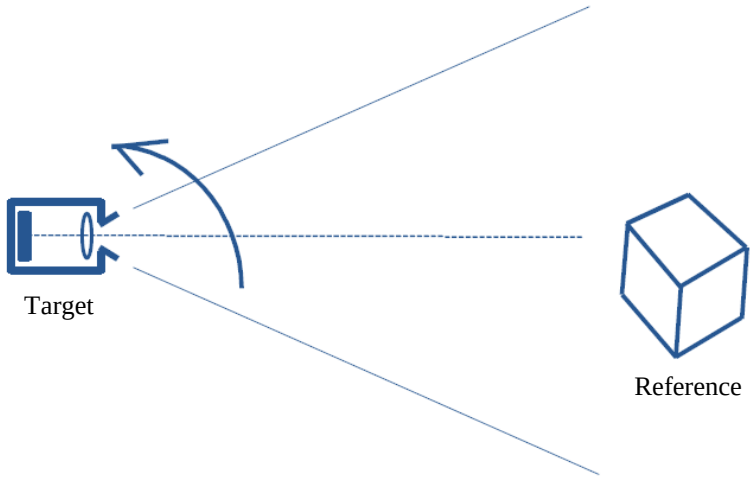

Figure 4.26: Inside-out paradigm (adapted from [Rolland et al., 1999]).

This approach has reported usage in [Janin et al., 1995] for head tracking in augmented reality applications. A similar system employing lateral-effect photodiodes (LEPDs) that

looked upward at a regular array of infrared LEDs installed in precisely machined ceiling panels was reported in [Azuma and Ward, 1991]. In this case, the user is weighted with acquisition and communication electronics. A more recent development applying the inside-out paradigm has been reported in [Welch et al., 2001] where the HiBall tracking system is described (see Fig.4.27a). HiBall was designed as a single, rigid, hollow ball having dodecahedral symmetry, with lenses in the upper six faces and LEDs on the insides of the opposing six lower faces (see Fig.4.27b). This system shows remarkable improvements in terms of size and weight. Despite this, this system remains unfortunately too large and heavy for our application. Also, its accuracy is insufficient for the precise tracking of the handle of an IC-HI. Representative characteristics of reported videometric tracking systems are provided in Table 4.10.

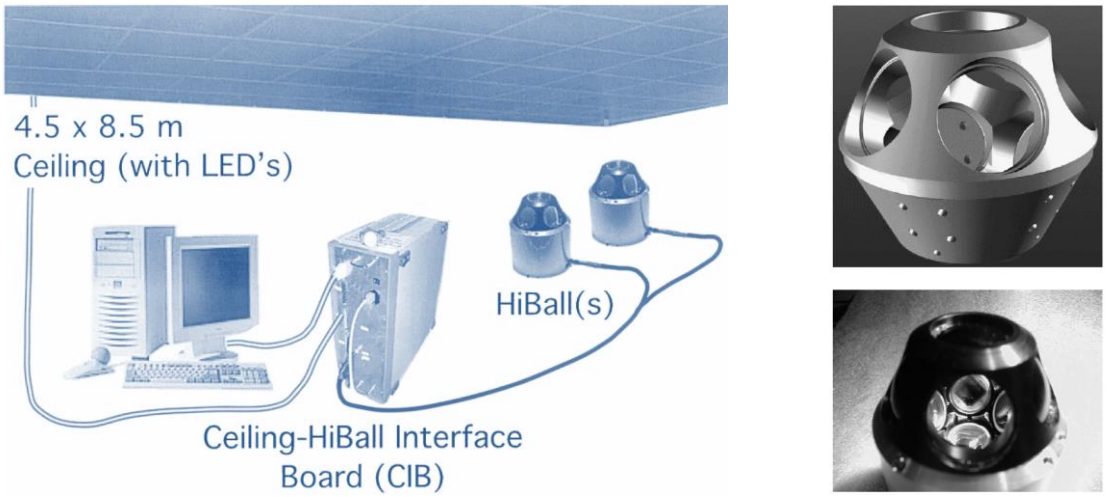

a) HiBall tracking system

b) HiBall

Figure 4.27: HiBall tracking system [Welch et al., 2001]).

Table 4.10: Representative characteristics and performances of reported videometric tracking systems [Janin et al., 1995, Welch et al., 2001].

Sensor type	Camera
Measured variable	Position and orientation
Physical phenomenon	Image acquisition
Weight / Size	Depends on the mounted sensors, e.g.300g for HiBall
Measuring range	Working volume depends on the number of landmarks, e.g. room of 4.5m × 8.5m for the HiBall system ensuring reported absolute error
Working frequency	≈ 2kHz, e.g. HiBall
Absolute error	< 0.5mm and 0.03°, e.g. HiBall
Target instrumentation	Yes
Degrees of freedom (DoF)	6DoF pose calculation possible
Occlusion sensitive	Yes
Price	Expensive
Strengths (✓) / Weaknesses (✗)	✓: Current systems are less cumbersome ✓: Workspace can be as large as required depending on the amount of installed landmarks ✗: Heavy sensors have to be mounted on the target
Applications	Object tracking in virtual and augmented reality

4.5.4.6 Depth cameras

In its simplest implementation, a depth camera is a multiple pixels range (distance) sensor. Range measurement can be accomplished by means of several physical principles. As an example, a type of range sensor known as LIDAR (for Light Imaging Detection And Ranging or for LIght and raDAR) estimates range (distance or depth) by measuring the time-of-flight (TOF) of collimated laser beams illuminating a target (the reflected light being detected by a purposely arranged photodetector). LIDAR technology requires to be combined with some sort of scanning in order to obtain several horizontal and vertical depth measurements, e.g. by employing rotating mirrors (see Fig.4.28a). However field of view and resolution are limited.

Another approach consists in emitting a light that will spread on the scene of interest, that will be then reflected back and that will be finally imaged onto a two-dimensional array of photodetectors (Flash LIDAR depth camera, see Fig.4.28b).

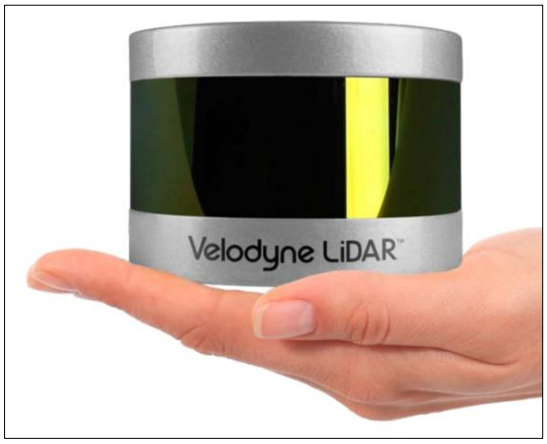

a) VLP-16 LIDAR range scanner
(by Velodyne)

b) DragonEye 3D Flash LIDAR Space Camera
(by Advanced Scientific Concepts Inc.)

Figure 4.28: Examples of depth cameras [Velodyne, 2018, Advanced Scientific Concepts Inc., 2018].

This technology relies on two measurement principles, 1) direct measure of the time taken for a light pulse to travel from the device and to come back after reflection on the target (**pulsed-light** cameras) and 2) deduction of the travel time from a measure of the phase difference between the emitted and received signals (**continuous-wave modulated-light cameras**).

Tables 4.11, 4.12 and 4.13 show that this kind of sensors is not adapted for our application. The measuring range is too large, and the accuracy and acquisition frequency are limited. They will not be further discussed in this document.

Table 4.11: LIDAR range scanner representative performances [Velodyne, 2018].

Sensor type	LIDAR
Measured variable	Time of flight
Physical phenomenon	Laser effect
Weight / Size	590g – 12.7Kg / [7 × 9]cm to [18 × 28]cm
Measuring range	Up to 120m
Working frequency	600,000 to 2,200,000 points per second Rotation rate between 5 to 20Hz
Accuracy / Resolution	Range accuracy between ±2cm to ±3cm / Vertical resolution between 0.33° and 2°
Target instrumentation	Not necessary
Degrees of freedom (DoF)	1DoF since it acquires distance measurements
Installation	Requires to be mounted
Occlusion sensitive	Yes
Strengths (✓) / Weaknesses (✗)	✓: Large measurement ranges ✗: Cumbersome ✗: Limited vertical field of view ✗: Low range accuracy regarding the design of an IC-HI
Applications	Car security, autonomous trucking, drones, robotics

Table 4.12: 3D flash LIDAR cameras representative performances [Horaud et al., 2016, Advanced Scientific Concepts Inc., 2018].

Sensor type	3D Flash LIDAR camera
Measured variable	Time of flight
Physical phenomenon	Reflection of light pulses
Size	[11 × 11,2 × 12,1cm] - [14 × 20,6 × 16,5cm]
Measuring range	7m– 1100m
Working frequency	Between 10 – 450 Frames per second (FPS)
Resolution	[128 × 128] to [1280 × 1024] pixels
Target instrumentation	Not required
Degrees of freedom (DoF)	Provides point cloud of depth measurements
Occlusion sensitive	Yes
Price	Expensive
Strengths (✓) / Weaknesses (✗)	✓: Can perform outdoors, under adverse conditions ✓: Target does not require to be equipped ✗: Cumbersome ✗: Measuring range too big ✗: Low working frequency
Applications	Collision avoidance, adaptive cruise control, surveillance, day-night-rain-fog imaging, automated rendezvous and docking in space, unmaned ground/air vehicles

Table 4.13: Continuous-wave modulated-light cameras representative performances [Horaud et al., 2016, Sony, 2018].

Sensor type	Continuous-wave modulated-light camera
Measured variable	Phase-difference
Physical phenomenon	Reflection of continuous light waves
Weight / Size	[6.5 × 6.5 × 6.8cm] - [24 × 4 × 5cm]
Measuring range	Up to 10m
Working frequency	Up to 60 Frames per second (FPS)
Resolution	[160 × 120] to [512 × 424] pixels
Target instrumentation	Not required
Degrees of freedom (DoF)	Provides point cloud of depth measurements
Occlusion sensitive	Yes
Price	Expensive
Strengths (✓) / Weaknesses (✗)	✓: Target does not require to be equipped ✗: Cumbersome ✗: Low working frequency
Applications	Close and far interaction interfaces with no-touch body tracking, logistics, surveillance and security, machine vision and robotics, medical and biometric

4.5.4.7 Systems employing PSDs

Most of the aforementioned techniques were developed for applications outside the field of haptics. A couple of tracking systems specifically developed for contactless measurement of the 6DoF configuration of the handle of manual human-machine interfaces were also identified in literature. The systems in question are the SPACE MOUSE and the Maglev haptic interface which will be described in the following paragraphs. Both employ position sensitive detectors (PSDs) to obtain non-contact 6DoF displacement information. These sensors are basically large photodiodes providing 1D or 2D coordinates of a spot light hitting their active surface.

Developed in the mid-80s by the German Aerospace Center (known as DLR or Deutsches Zentrum für Luft- und Raumfahrt in German) [Hirzinger, 1999], the **SPACE MOUSE** is a 3D-input device used for CAD and robot control. It employs an arrangement of 6 one-dimensional PSDs, slits and light emitting diodes (LEDs) to measure the displacement of a handle in a small workspace (see Fig.4.29a). The inner moving ring is composed of the LEDs and slits. Each slit faces a 1D PSD which is perpendicularly oriented. Although not shown in figure 4.29a, the ring with PSDs is fixed inside the outer part and connected via springs with the inner ring. The springs bring the inner ring back to an initial position when no forces are applied.

Developed in the late 90s [Berkelman, 1999], the **Maglev** is a tool-based interaction haptic interface (see Fig.4.29b) relying on a magnetic levitation approach. It allows high frequency position measurement and it can provide high frequency force feedback in 6DoF thanks to a non-contact frictionless actuation. Position sensing is obtained by means of three 2D PSDs placed on an outer structure that remains static. They allow to measure

the positions of light spots generated by the light emitted by three LEDs mounted on the moving flotor. A collimating lens is positioned in front of each PSD ensures a proper illumination of its photosensitive area of 44.5mm of diameter. This tracking system provides six independent values (x and y on each PSDs/lens combination) which together allow to compute the 6DoF pose of the flotor.

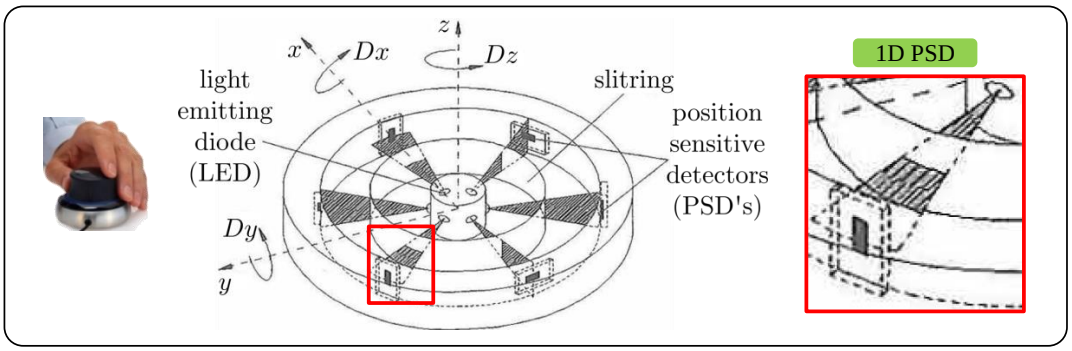

(a) SPACE MOUSE

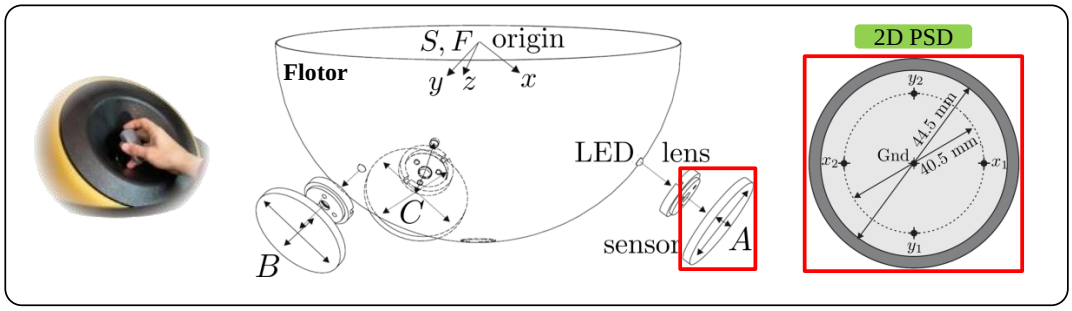

(b) Maglev

Figure 4.29: 6DoF sensors employing emitter/detector pairs based on PSDs.

The Maglev haptic interface provides the following characteristics:

- **workspace:** ±12.5mm (translation) and ±7.5° (rotation),
- **working frequency:** 1.45kHz (max) and
- **resolution:** $5 - 10\mu$m.

Such technologies appear very well suited for our application. However, in their current implementation, they are still too large and would require a complete redesign before they can be integrated in an IC-HI for the purpose of tracking the handle without contact.

4.5.4.8 Conclusion

Based on the performances of the explored tracking systems, the following conclusions arised.

The range of tracking systems based on optical principles is very varied. Most of them find their origins and applications in VR/AR or industry. The former are well suited for

human body tracking or environment reconstruction but their range of measurement is often too large, and their acquisition frequency and accuracy too low for the tracking of the handle of an IC-HI. On the contrary, industry-oriented sensors require high accuracy and acquisition frequency. However, existing systems are limited to 1 DoF measurement and the design of a 6DoF tracker would result in a complex, expensive and cumbersome device

The most interesting approach remains the triangulation principle based on simple optical emitter/detector pairs, in particular IRED/PSD pairs with slits. This solution is compact and can work at high frequencies since PSDs are analog sensors.

4.5.5 Global conclusion on existing motion tracking systems

None of the existing systems appears to be well adapted for the tracking of the handle of an IC-HI. As a consequence, we decided to develop a non-contact tracking system that complies with the design drivers of an IC-HI from scratch. The most promising approach being the triangulation principle based on simple 1D or 2D emitter/detector pairs, we first performed a comprehensive review of such sensors, in order to learn on their principle, characteristics, performances as wells as on their respective advantages and disadvantages. This review is presented in the following paragraph.

4.6 Non-contact displacement or distance sensors for the design of an IC-HI tracking system

4.6.1 Introduction

The study of existing tracking systems presented in section 4.5 has shown that none of them complies with the design drivers defined in section 4.4. This observation led to the conclusion that the design of a new tracking system for IC-HIs was necessary. Our analysis also led us to favor a design based on the combination of several 1 or 2 DoFs elementary position or distance sensors to get the 6DoF pose of the handle.

A similar approach was used in [Diallo, 2014]. A prototype that computes the 6DoF pose of a handle without contact was developed using elementary displacement sensors. This system made use of three linear optical sensors (mounted on a receptacle) to measure the position of the spots produced by thin slit oriented perpendicularly to the sensors and sequentially illuminated by three IR light sources mounted on the handle. This system allows to compute the 3D position of each source based on planes intersections. The 6DoF configuration of the handle is then easily calculated from the positions of the three sources (see appendix B for more details). Despite its limitations which do not allow to fit our requirements (it was quite cumbersome and its acquisition frequency was <300Hz), this

prototype had a suitable workspace and a high precision (10^{-1}mm). It inspired thus our work which was oriented towards the development of a similar system, however improving its performances. To this end it is necessary to find faster, more precise and smaller elementary sensors.

To allow for an informed choice of these sensors, it is of fundamental importance to investigate the characteristics of the different available sensor technologies. Our ultimate goal is to allow for a quick and precise calculation of the 6DoF pose of a handle without contact. We defined the associated design drivers in section 4.4, it is however difficult to translate these design drivers into requirements for each elementary sensor, as we do not know their arrangement in space at the beginning of the design process. Still, in order to guide the sensor's comparison, we will use as a first approximation the same design drivers as for the whole device, i.e. a range of measurement of at least 10mm (in order to cope with the user's and robot's dynamics), with a lower range of measurement as close as possible to 1mm (in order to allow for an as compact as possible design, without having to place the sensors at a longer distance from the handle), an accuracy of 0.1mm and an acquisition frequency around 1kHz. All these sensors should be studied principally in terms of these design drivers, i.e. measuring range, working frequency, precision and of course size.

The following sections aim to provide a review of existing elementary sensor technologies potentially interesting to our application, e.g. ultrasonic, capacitive, magnetic, inertial as well as optical sensors. The working principle and characteristics of each type of sensor will be provided and their pertinence evaluated.

4.6.2 Ultrasonic sensors

4.6.2.1 Principle and characteristics

Ultrasonic sensors generate high frequency acoustic waves (> 20kHz) that can travel and be reflected by an obstacle (see Fig.4.30a).

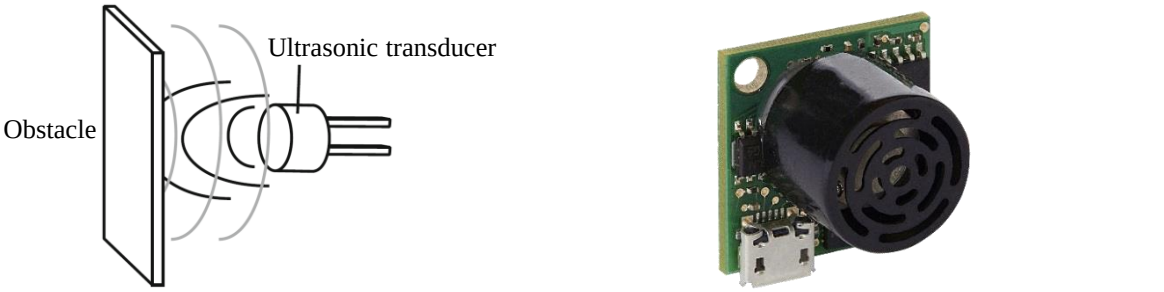

a) Ultrasonic sensor principle

b) HRUSB-MaxSonar® - EZ™ Series from MaxBotix Inc.

Figure 4.30: (a) Reflected waves generated by an ultrasonic transducer (adapted from [Hatzfeld and Kern, 2009]) and (b) Commercial ultrasonic sensor.

These transducers employ therefore piezoelectric materials to convert an electrical current into mechanical oscillations (emitter) and to convert oscillations created by a reflected wave into an electrical current (receiver). This way, ultrasonic transducers allow to perform presence detection or distance measurements, the later being achieved either by evaluating the time of flight (TOF) or by determining the phase shift (difference) between the emitted and received signals (see sections 4.5.2.1 and 4.5.2.2).

Numerous ultrasonic ranging sensors are available on the market (see Fig.4.30b for an example). Most of them employ the TOF principle to provide distance measurements. Table 4.14 shows representative characteristics of ultrasonic rangefinders issued from the MaxBotix Inc. catalogue, which is one of the main manufacturers of these sensors, located in the state of Minnesota, U.S.A. The rest of the characteristics are issued from other sources [Gueuning et al., 1996], [Rolland et al., 1999], [Hatzfeld and Kern, 2009].

Table 4.14: Ultrasonic rangefinder representative characteristics [Gueuning et al., 1996, Rolland et al., 1999, Hatzfeld and Kern, 2009, MaxBotix, 2018].

Sensor type	Ultrasonic rangefinder
Measured variable	Distance
Physical phenomenon	Reflexion of acoustic waves
Weight / Size	Lightweight / Sphere of ≈ 1.5cm diameter
Measuring range	- Minimal: $[15-50]$cm - Maximal: $[3.5-16.5]$m
Working frequency	- Imposed by the pulse trip time, e.g. for $c = 343.2$m/s, $l = 10$cm: $t_{tof} \approx 0.3$ms ➔ $f \approx 3.3$kHz (for separate emitters and receivers) $t_{tof} \approx 0.6$ms ➔ $f \approx 1.6$kHz (for co-localized emitters and receivers) - If phase-shift method, higher sample rates can be obtained since continuous signals are being measured
Accuracy **Repeatability** **Resolution**	- Minimum measurement accuracy possible in transversal direction is $\lambda/2$ (depends on the frequency used and the density of the medium, e.g. air) e.*g.* for an ultrasonic wave of $f = 40$kHz traveling in air at a speed $c = 343.2$m/s we obtain $\lambda = 8.5$mm thus an accuracy of 4.25mm - Some tenths of the ultrasonic wave - $[1-25.4]$mm
Needs to equip target?	- Yes (if separate emitters and receivers) - No (if co-localized emitters and receivers)
Degrees of freedom (DoF)	- Distance measurement (1DoF) - 6DoF pose calculation can be otained based on an arrangement of sensors
Occlusion sensitive	Yes
Price	Low cost
Strengths (✓) / Weaknesses(✗)	✓: Simple, cheap and relatively small. ✓: Not affected by color or other visual characteristics ✓: Longlasting ✗: Sensitive to temperature, pressure and humidity which affect the velocity of sound and thus the accuracy of measured distances ✗: Signal losses energy with the traveled distance, which limits the measuring range
Applications	Parking systems of cars, liquid level detection, robotics

4.6.2.2 Conclusion

Ultrasonic rangefinders are relatively simple and cheap sensors employed in applications as parking systems of cars, liquid level detection and robotics among others. Regarding the design of an IC-HI tracking system, interesting acquisition rates can be attained at close distances ($>$ 1kHz). However, these sensors suffer from several prohibitive disadvantages. When comparing their characteristics with the specifications of an IC-HI tracking system as defined in section 4.4.3 it can be observed that:

- The minimal reported measuring range (15cm) is too big.
- The reported order of magnitude for accuracy do not comply with the searched value ($< 10^{-1}$mm).
- Finally, using ultrasonic rangefinders in order to calculate the 6DoF pose of a target would require a cumbersome arrangement and would provide low accuracy pose measurements.

In conclusion, despite the interesting characteristics of this technology, ultrasonic rangefinders are not adapted to be employed in an IC-HI tracking module.

4.6.3 Capacitive sensors

4.6.3.1 Principle and characteristics

A capacitor consists in two parallel conductive plates (electrodes) placed face to face near each other, separated by a non-conductive substance (dielectric) [Terzic et al., 2012]. Examples of dielectric materials are air, ceramic or fuel, just to mention few of them.

When the circuit from figure 4.31 is closed and thus a voltage is applied across the terminals of the capacitor, the electrodes will start storing energy until attaining the same voltage as the source.

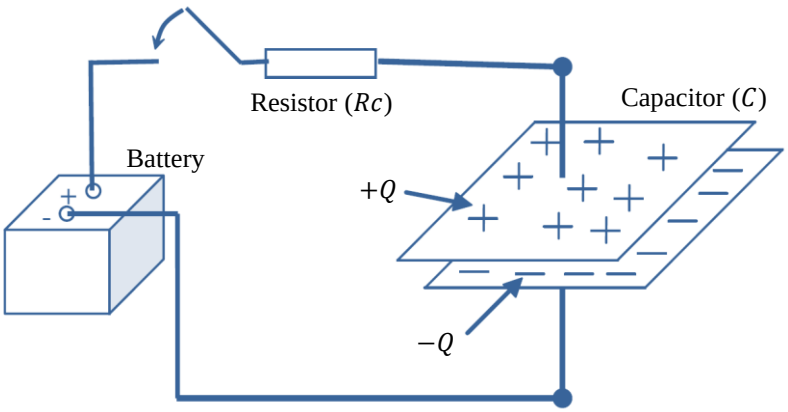

Figure 4.31: Capacitor principle [Terzic et al., 2012].

The time required to charge a capacitor is determined by the time constant $\tau_C = RcC$, where Rc is the resistance (in ohms, Ω) of a resistor connected in series with the capacitor which capacitance (in farads, F) is denoted C. Such time represents how long it takes to a capacitor to store 63% of its total capacity. The stored energy will then remain unless it is consumed by another component.

Equations (4.8) and (4.9) formalize the aforementioned relationships. In (4.8) Q is the charge of the capacitor (in Coulomb, C), C its capacitance (in farads, F) and V the voltage (in volts, V).

$$Q = CV \tag{4.8}$$

$$C = \frac{E_0 E_R A}{D} \tag{4.9}$$

In (4.9) E_0 represents the dielectric permittivity of vacuum (which is a constant equal to $8.85.10^{-12}$F/m), E_R is the relative permittivity of the material placed between the plates (as an example, for the air $E_R = 1$), A is the area of the plates (expressed in square meters, m^2) and D is the distance (in meters, m) between them. From these equations, it can be seen that the charge Q is influenced by the distance between the plates. By measuring Q (either through measuring the current flowing through it or the voltage between its electrodes), it is then possible to infer this distance.

In practice, capacitive sensing technologies allow to obtain either proximity or displacement information from an approaching object. In the present case, our interest is focused on displacement capacitive sensors.

A displacement capacitive sensor can be modeled by two parallel plates where one of them represents the sensor and the other one the object of interest (target). Such devices are used to measure the relative displacement between these two parallel plates (see Fig.4.32).

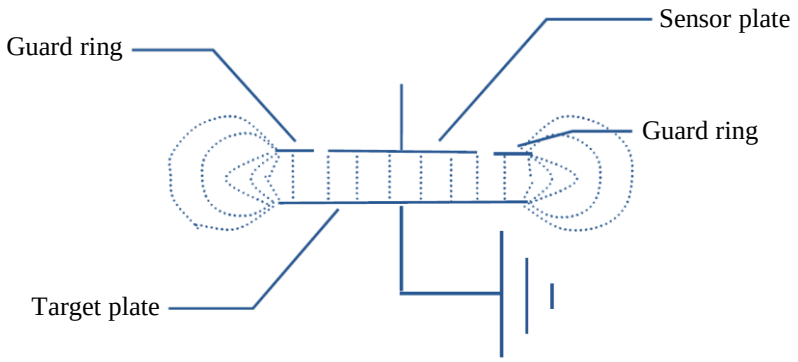

Figure 4.32: Capacitive sensor principle [MicroSense, 2018].

These sensors are typically manufactured as probes and can be either passive or active.

Passive sensors do not contain embedded electronics meanwhile active sensors do. For instance, figure 4.33 shows a commercial passive capacitive position sensor manufactured by the company MicroSense.

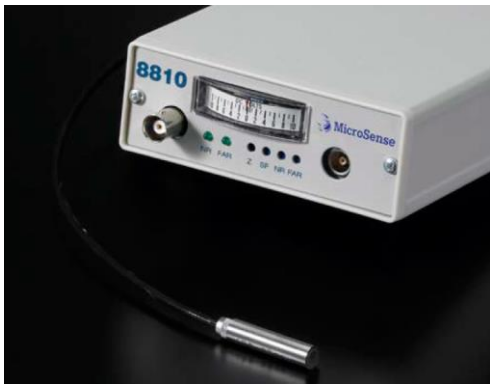

Figure 4.33: High resolution non-contact capacitive position sensor 8810 from MicroSense.

Displacement capacitive sensors allow high precision, high bandwidth, non-contact displacement measurement over modest ranges. This and other representative characteristics issued from MicroSense technical notes are presented in table 4.15.

Table 4.15: Capacitive displacement sensors representative performances [MicroSense, 2018, RS Components, 2018].

Sensor type	Capacitive
Measured variable	Current or voltage
Physical phenomenon	Change of capacitance
Size	Probe diameters between 0.5mm and 10mm
Measuring range	Between $\pm$10µm to $\pm$1000µm
Working frequency	- Up to 100kHz for active sensors - Up to 20kHz for passive sensors
Resolution	$<$ 1nm
Needs to equip target?	No
Degrees of freedom (DoF)	1DoF (small displacements)
Occlusion sensitive	Yes: the presence of other targets will impact the measured capacitance.
Price	Expensive
Strengths (✓) / Weaknesses (✗)	✓: High resolution and bandwidth ✗: Dirty particules on the sensor can affect the measurement ✗: Highly dependent on the permitivity of the medium between the plates, e.g. it can be strongly influenced by dust or humidity ✗: Small measurement ranges **Passive** ✓: Flexibility in probe configuration, stability and lower costs ✗: Cable length restrictions ($3-7$m) **Active** ✓: Do not depend on a cable length ✓: Work at higher frequencies ✗: Less flexible and higher costs
Applications	Positioning, run out measurement, autofocus and nulling, distance and displacement measurement, thicknes and vibration measurements, contact detection

4.6.3.2 Conclusion

Capacitive displacement sensors provide highly interesting characteristics for high resolution and bandwidth tracking systems. However this technology is not of great interest for the intended application (development of the tracking system of an IC-HI) since measuring ranges are very small. Furthermore, commercially available sensors are usually cylindrical and of relatively large sizes. As a consequence an eventual arrangement of several probes would become cumbersome. In conclusion, displacement capacitive sensors are not adapted to our case.

4.6.4 Magnetic field sensors

Magnetic sensors are very varied and employ many aspects of physics and electronics. They can be divided in two categories [Lenz and Edelstein, 2006]: sensors that measure the total magnetic field amplitude and sensors that allow measuring all its vector components. Common technologies used in both cases are shown in figure 4.34. Some of their advantages are stability and low cost. Furthermore they are a very simple, reliable and maintenance free.

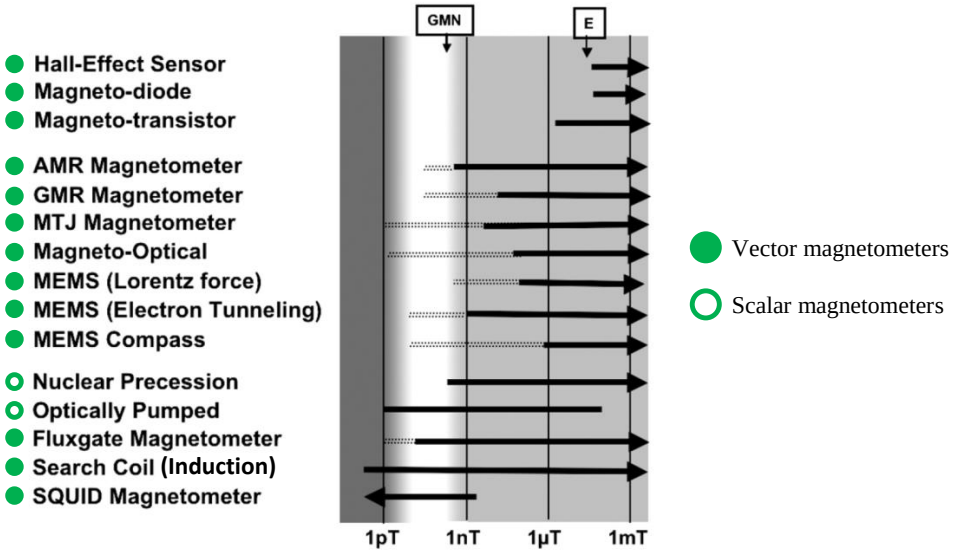

Figure 4.34: Common types of magnetic sensors and their estimated sensitivity [Lenz and Edelstein, 2006].

A review of modern magnetic field sensors [Tumanski, 2013] has concluded that among these sensors four main types of technologies are dominating: SQUID sensors (for very small magnetic fields), flux-gate sensors (for small magnetic fields), MR sensors (for medium values) and Hall effect sensors (for high values). What is important is then the range of measured magnetic field, in particular the smallest measurable value which has a direct influence on the sensor's cost (e.g. AMR sensors, which are a particular type

of MR sensors, are cheaper than SQUIDs). The principle and performances of these four types of sensors will be discussed in the following sections.

4.6.4.1 SQUID sensors

The superconducting quantum interference devices (SQUIDs) work based on the interactions between electric currents and magnetic fields observed when certain materials are cooled below what is called the superconducting transition temperature. This means that at these temperatures these materials show superconductive properties, in particular zero electrical resistance. These transducers convert the magnetic flux threading the SQUID loop into a voltage across the device [Drung et al., 2007]. In practice, it consists in a superconducting ring with one or two Josephson junctions (see Fig.4.35). Two types of SQUIDs can be distinguished: direct current (dc) and radio frequency, with two and one Josephson junctions respectively. The later are less expensive to produce but less sensitive.

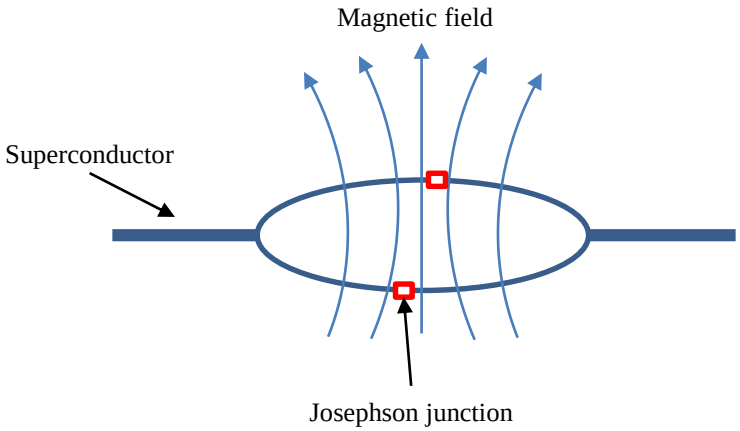

Figure 4.35: DC SQUID simplified diagram.

SQUID sensors are the most sensitive of all sensors for measuring a magnetic field at low frequencies (< 1Hz) [Lenz and Edelstein, 2006]. They are employed to measure extremely small magnetic field changes. Most of the SQUID sensors are integrated in biomagnetic systems [Clarke and Braginski, 2005], e.g. in a magnetoencephalography system which is often installed in a magnetically-shielded room since the brain signals are very week (on the order of few femtotesla). Another example is magnetocardiography which consists on a noninvasive characterization of local magnetic activity of the heart muscle that is generated by currents. Such technique allows to study heart disorders. Other techniques include liver susceptometry (to monitor the accumulation of excess iron in the human liver) and gastro-magnetometry (ingested magnetic markers that are tracked through the gastro-intestinal tract).

SQUID sensors seem to be very specialized sensors. They are supplied by only few manufacturers in the world. Supracon® for example, located in Germany, is one of them.

Their portfolio comprises current sensors, magnetometers and gradiometers (gradient measurement). Figure 4.36 shows some examples.

(a) Current sensors

(b) Magnetometer

Figure 4.36: Commercial SQUID sensors from Supracon®.

Some representative characteristics of SQUID sensors are provided in table 4.16.

Table 4.16: Representative performances of SQUID sensors.

Sensor type	SQUID
Measured variable	Current, magnetic field
Physical phenomenon	Superconducting ring with one or two Josephson junctions
Size	Chip size: $[2.5 \times 2.5]\text{mm}^2$ to $[4 \times 4]\text{mm}^2$
Measuring range	Not reported
Working frequency	< 1Hz
Accuracy / Resolution	Not reported
Needs to equip target?	No
Degrees of freedom (DoF)	Not reported
Occlusion sensitive	Not reported
Price	Expensive
Strengths (✓) / Weaknesses (✗)	✓: Provides the highest available sensitivity ✗: Expensive
Applications	Biomagnetic applications as measurement of magnetic fields emitted by the brain and heart or tracking of magnetic markers in the digestive system.

4.6.4.2 Fluxgate magnetometers

A fluxgate magnetometer is composed of a ferromagnetic material wound with two coils (a drive and a sensor coil) [Lenz and Edelstein, 2006]. It uses magnetic induction and the property of all ferromagnetic materials to become saturated when exposed to high magnetic fields, i.e. when the applied magnetic field cannot further increase the magnetization of the material. For example, if a large sinusoidal current is applied in the drive coil, the core is magnetized up to saturation once each half-cycle. When saturation has been reached, the reluctance (opposition to magnetic flux) of the core to any external magnetic field being measured becomes greater, avoiding any magnetic field to pass through the core. When the core goes out of saturation, the magnetic flux of the incoming magnetic field is attracted to the core and detected by the sense coil. The sensor winding

is driven by a current induced by the passing magnetic field. The voltage at this coil is then measured to find the field [Primdahl, 1979]. This principle is illustrated in figure 4.37.

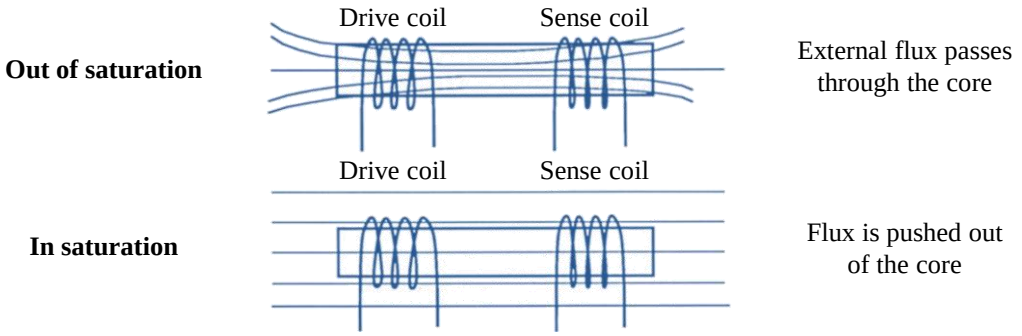

Figure 4.37: Fluxgate magnetometer operating operating principle (adapted from [Lenz and Edelstein, 2006]).

Fluxgate magnetometers are able to directly measure the vector components of the magnetic field with high accuracy [Primdahl, 1979]. Figure 4.38 shows some examples of commercially available sensors and table 4.17 provide common characteristics of this type of sensors.

(a) IC sensor from Texas Instruments

(b) TFM1186 sensor from Metrolab

Figure 4.38: Commercial fluxgate magnetometers.

Table 4.17: Fluxgate sensor representative characteristics ([Tumanski, 2013, Keller, 2018, Texas Instruments, 2018]).

Sensor type	Fluxgate magnetometer
Measured variable	Intensity and orientation of magnetic field
Physical phenomenon	Magnetic induction and saturation of a ferromagnetic material
Size	From [4mm × 4mm] to [30mm × 32mm × 70mm]
Measuring range	1µT to 1mT
Working frequency	1kHz – 47kHz
Accuracy **Resolution / Sensitivity**	Up to 1000 ppm (parts per million): 1000µT 10pT / 10mV/nT
Needs to equip target?	Yes, these sensors could be mounted on the target evolving in a magnetic field emitted by a fixed source
Degrees of freedom (DoF)	1DoF or 3DoF
Occlusion sensitive	No
Price	Relatively cheap
Strengths (✓) / Weaknesses (✗)	✓: Great sensitivity ✓: Single or multi axis measurements ✓: Robust and low power consumption ✗: Range limited to low fields ✗: Relatively limited bandwidth ✗: Large sensor ✗: Perturbing fields are measured
Applications	Military applications, space research, linear positioning sensing, motor reliability diagnosis, overcurrent detection.

4.6.4.3 Magnetoristive magnetometers

Magnetoresistive magnetometers employ a change in resistance ΔR provocated by an external magnetic field [Lenz and Edelstein, 2006]. While there exist several magnetoresistive effects [Tumanski, 2013], only three main effects are commonly used:

- Anisotropic magnetoresistive (**AMR**) effect, as was first observed by William Thomson in 1857. The resistivity of ferromagnetic materials depends on the angle between the direction of an electric current and the orientation of the applied magnetization [Jogschies et al., 2015]. This can be represented by a Hunt element in which a flowing current $\boldsymbol{I}$ and a magnetization vector $\boldsymbol{M}$ form the angle α. A magnetic field $\boldsymbol{H_y}$ coupled into the sensor material will generate a change on the resistivity of the stripe, which is verified by current measurement (see Fig.4.39).

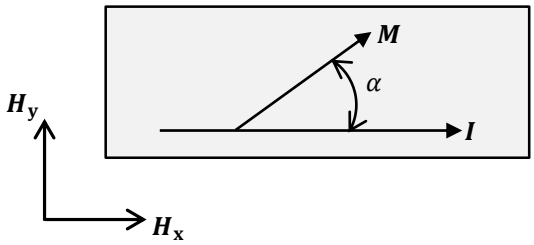

Figure 4.39: Hunt element (adapted from [TE Connectivity Sensors, 2018a]).

- Giant magnetoresistive (**GMR**) effect, discovered in 1988 [Jogschies et al., 2015]. It was given this name since changes in magnetoresistance were larger than in AMR. GMR sensors consist in a four layer structure composed of two thin ferromagnets separated by a conductor. The fourth layer is an antiferromagnet which inhibits the rotation of one of the ferromagnetic layers [Lenz and Edelstein, 2006].

- Introduced in 1995 [Lenz and Edelstein, 2006], Magnetic tunnel junction (**MTJ**) sensors have a structure similar to that of GMR sensors. However the two ferromagnets are separated by an intervening layer which in this case is an insulator. In MTJ, conduction occurs by tunneling of the electrons through the insulator.

Figure 4.40, shows commercially available angular and position AMR sensors from the Swiss company TE Connectivity. For simplification purposes, only AMR sensors characteristics will be presented here. Table 4.18 provides representative characteristics issued from the TE Connectivity catalogue.

KMT37 Angular AMR sensor
from TE Connectivity

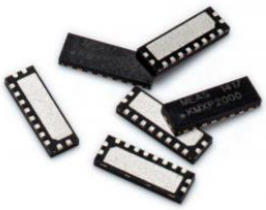

KMXP series linear AMR sensor
from TE Connectivity

Figure 4.40: Comercial AMR angular and position sensors.

Table 4.18: AMR sensors representative characteristics [TE Connectivity Sensors, 2018b, TE Connectivity Sensors, 2018c].

Sensor type	Magnetoresistive magnetometers
Measured variable	Angle/Position
Physical phenomenon	Change in resistance caused by external magnetic field
Size	In the order of a 5mm × 5mm × 2mm package
Measuring range	1 – 5mm
Working frequency	Not reported
Accuracy **Repeatability**	0.1deg / 10 to 50µm 0.1deg
Needs to equip target?	Yes, these sensors could be mounted on the target evolving in a magnetic field emitted by a fixed source
Degrees of freedom (DoF)	1DoF
Occlusion sensitive	No
Price	Cheap
Strengths (✓) / Weaknesses (✗)	✓: Excellent repeatability ✓: Fast response time ✓: Ideal for harsh environments ✗: Quadratic behavior ✗: Sensitivity vanishes for low external field
Applications	Contactless angular or position sensor

4.6.4.4 Hall effect sensors

Hall sensors are the most popular magnetic sensors on the market. They are based on the hall effect, which is a physical phenomenon that was discovered more than 100 years ago (1879) by Edwin H. Hall [Lenz and Edelstein, 2006].

In the absence of a magnetic field, the current flowing through a plate of a conductive material follows a regular path. However when this material is put under the influence of a strong magnetic field perpendicular to it, the current flow is deviated [Tumanski, 2013] as the electrons moving through the magnetic field experience a force, known as Lorentz force, which is perpendicular to the direction of motion and to the direction of the magnetic field. As a result, a voltage difference, known as Hall voltage, is created (see Fig.4.41). This voltage allows then to determine the intensity of the magnetic field since the amount of current flowing through the material is known.

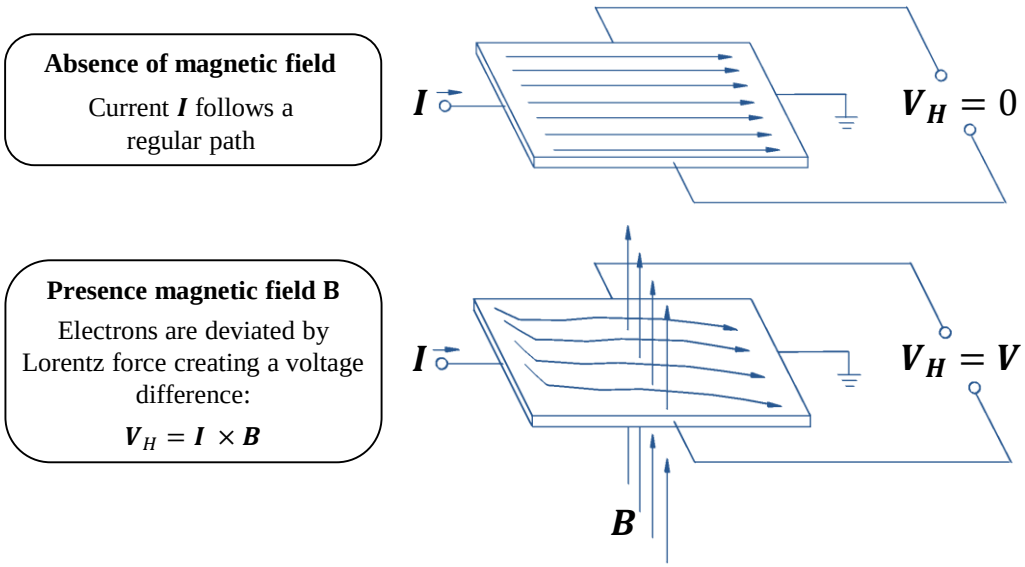

Figure 4.41: Hall-effect sensor operation principle (adapted from [Honeywell, 2018a]).

Figure 4.42 shows some commercial Hall-effect sensors developed by Honeywell. In addition, table 4.19 provides representative characteristics of Hall-effect sensors issued from the Honeywell catalogue.

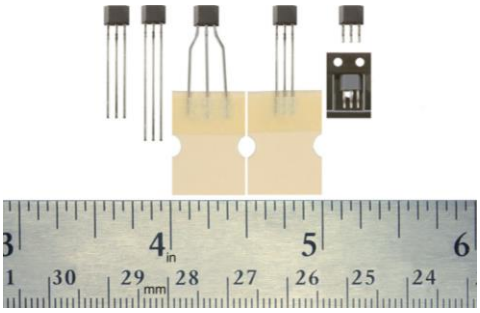

Figure 4.42: Linear Hall-effect sensors ICs from Honeywell .

Table 4.19: Hall-effect sensor representative characteristics [Honeywell, 2018c].

Sensor type	Hall-effect sensor
Measured variable	Magnetic field intensity
Physical phenomenon	Hall effect
Size	In the order of 4mm × 1.6mm × 19mm
Measuring range	±420 Gauss - ±1000 Gauss
Working frequency	Time response in the order of 3µs (333kHz)
Sensitivity	1.4 mV/Gauss - 5.4 mV/Gauss
Needs to equip target?	Yes, these sensors could be mounted on the target evolving in a magnetic field emitted by a fixed source
Degrees of freedom (DoF)	1DoF
Occlusion sensitive	No
Price	Cheap
Strengths (✓) / Weaknesses (✗)	✓: Linear ✓: Cheap ✗: Other magnetic fields can interfere and bias the measurement of the current flow ✗: Temperature affects the sensitivity ✗: Offset voltage in the absence of a magnetic field
Applications	Basic current sensing, simple linear or angular displacement

4.6.4.5 Conclusion

Sensors measuring the magnetic flux density in a magnetic field offer a wide variety of interesting options according to the targeted application. In previous sections, representative characteristics of SQUID sensors, fluxgate magnetometers, magnetoresistive magnetometers as well as hall-effect sensors were explored. The following paragraphs will provide elements of conclusion regarding the intended application: the development of an IC-HI tracking system.

SQUID sensors are very specialized and expensive sensors supplied by only few manufacturers. It was reported that they work at very low temperatures and low frequencies (< 1Hz). These factors make that this type of sensors won't be further explored regarding the intended application.

Fluxgate magnetometers and Hall-effect sensors offer interesting characteristics in terms of size and working frequency. However, since accuracy and resolution are provided in terms of magnetic flux density units (either Tesla or Gauss), it is difficult to infer for the accuracy of position measurements. A test bench for one of these sensors would have to be built in order to be able to determine an order of magnitude of the attainable position accuracy.

Finally, commercial AMR technology offers angular and position sensors with interesting reported accuracy and repeatability. However, the reported measuring ranges in the case of position sensors are too low, i.e. in the order of few millimeters.

It appears from this study that, among the proposed sensors, only Fluxgate magnetometers and Hall-effect sensors could potentially be used to design a 6DoF sensor that fits our application. To do so, an arrangement of the discussed sensors could be mounted on a target evolving in a magnetic field sufficiently big to cover the desired workspace. This solution would however require a prototype as the sensors' datasheets do not directly inform on the attainable precision. In all cases, these sensors would remain sensitive to disturbances being originated from ferromagnetic and metallic elements present in the vicinity of the target. They would also be disturbed by the magnetic fields generated by the motors of the nearby haptic interface. As a consequence, none of the above reported magnetic field sensors would comply with the design drivers of an IC-HI tracking system.

4.6.5 Inertial sensors

4.6.5.1 Principle and characteristics

The 6DoF pose of an object can also be reconstructed by employing inertial measurements [Mihelj et al., 2014]. Commercial inertial measurement units (IMUs) have been largely studied since it represents a cost-effective technology in application cases where optical technologies are not adapted [Filippeschi et al., 2017]. Inertial measurement units

typically combine:

- **Gyroscopes** for the measurement of angular velocities. Three major categories are distinguished [Passaro et al., 2017]: mechanical, optical and vibrating-mass based gyroscopes.

  Mechanical gyroscopes are usually composed of a spinning wheel that is linked to a basis through two gimbals (see Fig.4.43a). Provided the wheel is rotated at a high angular speed, it will tend to keep its axis at a constant orientation despite any rotation of the basis due to the conservation of its angular momentum (a mass that is rotating at high angular speeds conserves its angular momentum if no external moments act on it) [Passaro et al., 2017]. The axis of rotation of the wheel (whose orientation is constant is space) being used as a reference, it is possible to measure the orientation of the basis by using joint sensors in the gimbals. However since these elements are mechanically linked, they are subject to friction, which causes a drift in the direction of the wheel axis with time.

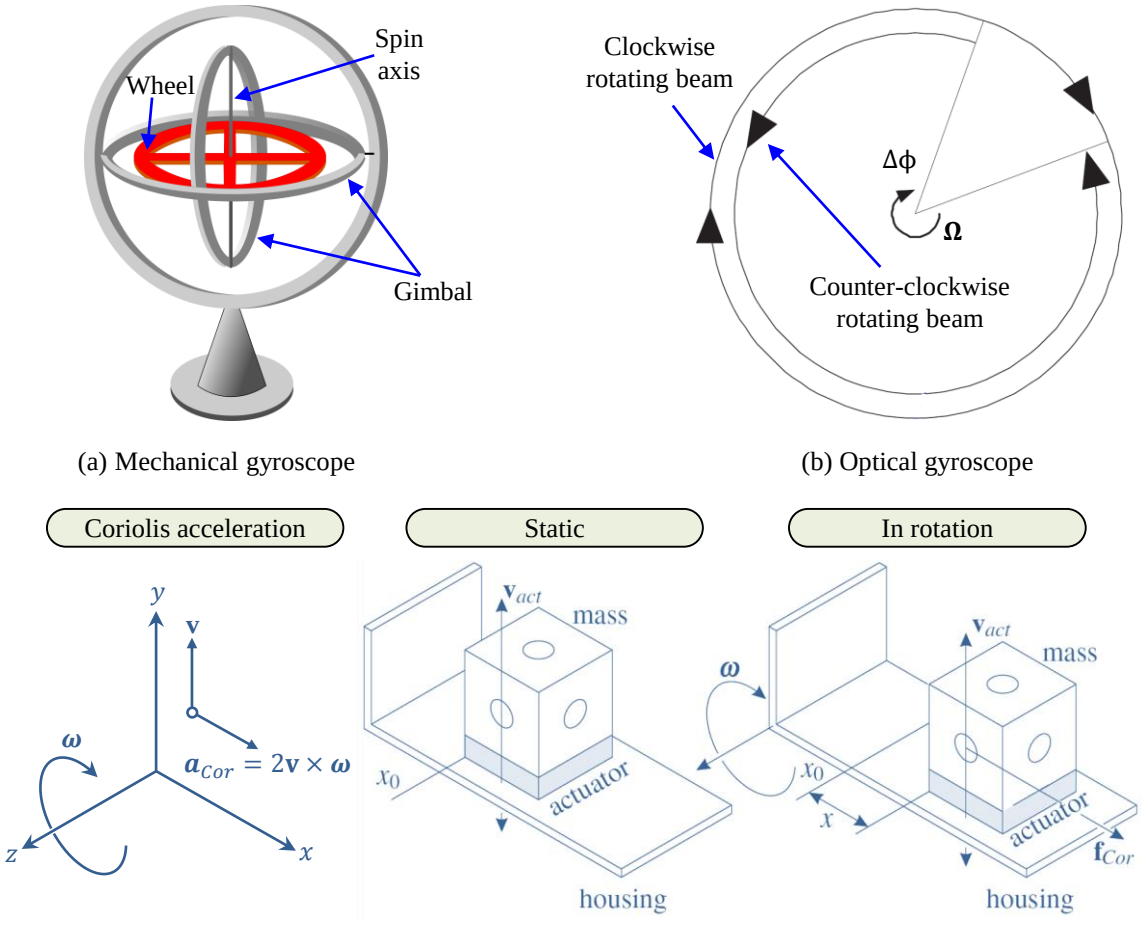

(a) Mechanical gyroscope

(b) Optical gyroscope

(c) MEMS gyroscope

Figure 4.43: Main categories of gyroscopes. Figure (c) taken from [Mihelj et al., 2014].

Optical gyroscopes work based on the Sagnac effect: a light is split by a beam-splitter into two beams: one propagating clockwise and the other one propagating counter-

clockwise [Shamir, 2006]. If the system is static, the two beams travel through the same optical path and return in phase to their origin. If the system turns clockwise with an angular velocity $\mathbf{\Omega}$, the origin turns with it. As a consequence the beam which is rotating clockwise will travel a longer distance to reach the origin than the one traveling counter-clockwise and a phase shift $\Delta\phi$ will be generated (see Fig.4.43b). Such difference in phase can be measured by means of an interferometer (an instrument that merges two or more sources of light to create an interference pattern that can be measured and analyzed).

Gyroscopes based on a **vibrating mass** are generally based on micro-electro-mechanical systems (MEMS). Their working principle consists in a vibrating mass that is affected by the Coriolis acceleration caused by the rotation (see Fig.4.43c). This results in secondary vibrations that are perpendicular to the primary ones and to the angular velocity vector. By measuring the secondary vibrations, it is possible to determine the angular velocity [Mihelj et al., 2014].

- **Accelerometers** for the measurement of linear accelerations. An accelerometer consists in a mass m connected to a rigid housing by means of springs with stiffness k, the whole being affected by the damping d (see Fig.4.44). When the housing is accelerated, it creates a tension on the spring as the mass does not immediately follow it. This system can be modeled as a second order mass-spring-damper system (see Eq.(4.10)), where the product ma represents the force acting on the mass.

$$m\ddot{x} + d\dot{x} + kx = ma \tag{4.10}$$

The acceleration can then be measured by knowing the relative mass/housing displacement and the mechanical tension generated on the spring.

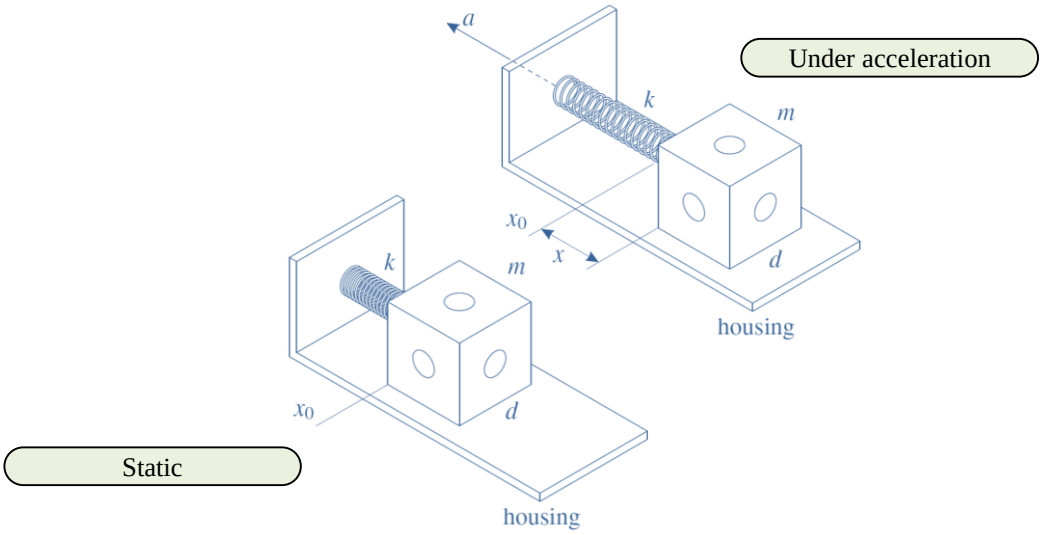

Figure 4.44: Accelerometer principle (taken from [Mihelj et al., 2014])

- **Magnetometers** to measure the orientation relative to the Earth's magnetic field.

The principle of a magnetic sensor won't be described here since the most common types of such sensors have already been described in section 4.6.4. The orientation with reference to a magnetic field can be obtained thanks to the magnetoresistive effect (see section 4.6.4.3).

An IMU s usually composed of a 3-axis gyroscope, a 3-axis accelerometer and a 3-axis magnetometer whose data are sent to a computer to calculate the global speed and position, given a known initial speed and position [Desa et al., 2009]. To illustrate this, figure 4.45 shows the basic principle of inertial motion tracking.

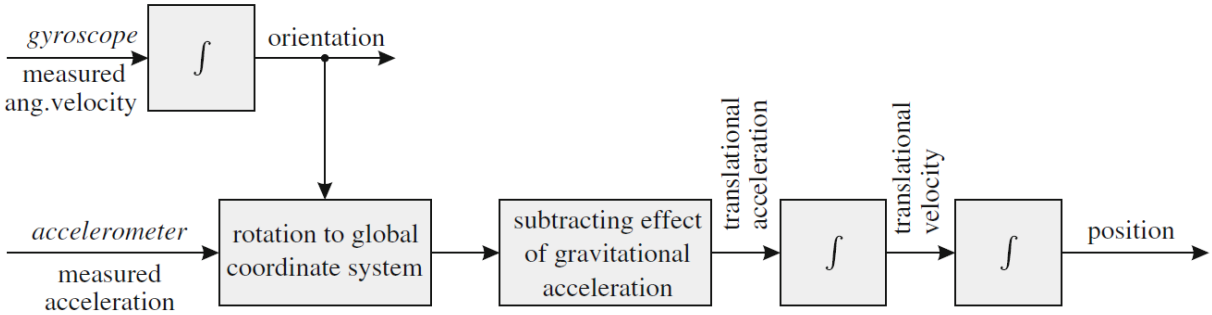

Figure 4.45: Position measurement based on inertial sensors (taken from [Mihelj et al., 2014]).

Inertial units were initially developed for attitude estimation of aerial vehicles. They have been employed for decades in navigation and more recently for unmanned vehicle tracking. Apart from localization, IMUs applications also include human-robot interaction, rehabilitation and ergonomics [Filippeschi et al., 2017].

Some commercial IMUs manufactured by Honeywell and XSens are shown in figure 4.46. The range of their products, based on MEMS technologies, can fit from heavy duty applications (TARS series) to high-volume applications (MTi 1-series). Representative characteristics of the sensors provided by these companies, as well as other information sources, are given in table 4.20.

(a) TARS series IMU from Honeywell

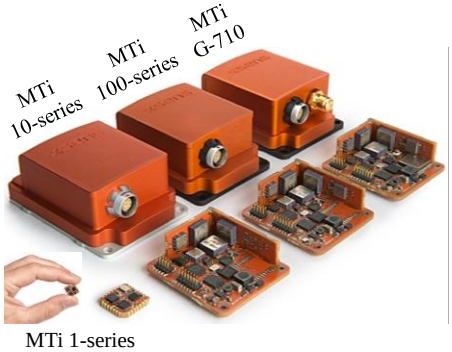

(b) IMUs from XSens

Figure 4.46: Examples of commercial IMUs.

Table 4.20: Representative characteristics of IMUs [Honeywell, 2018b, XSens, 2018, Filippeschi et al., 2017]

Sensor type	Inertial measurement unit (IMU)
Measured variable	Angle/Position
Physical phenomenon	Gyroscope effect, Acceleration
Size	$[13.2 \times 13.2]$mm – $[130 \times 135 \times 66]$mm
Measuring range	Angular speed: $\pm 75 - \pm 2000$deg/s Acceleration: ± 6 – 20g
Working frequency	100-2000Hz
Resolution	Angular speed: $1 - 40$mdeg/s Acceleration: in the order of 0.01m/s^2
Needs to equip target?	Yes: sensor moves with the target to generate data
Degrees of freedom (DoF)	6DoF measurements
Occlusion sensitive	No
Price	Relatively cheap
Strengths (✓) / Weaknesses (✗)	✓: Low power consumption ✓: Small size ✗: Suffer from drift error due to integration of acceleration
Applications	Activation or airbags, biomechanical applications for human activity recognition, in cameras for image stabilization, human-robot interaction, vibration control, missile guidance.

4.6.5.2 Conclusion

Even if IMUs represent an interesting approach which is insensitive to occlusions, their size and working frequency do not comply with the targeted applications.

Also, they natively give absolute position and orientation information. In the perspective of the development of an IC-HI tracking system, it is necessary to determine the relative handle/robot configuration. With an IMU this calculation would require to combine the IMU data with the robot's configuration obtained by forward kinematics. As a consequence, the measurement errors coming from each data source would cumulate. By precisely knowing the initial position of the handle, the data could be merged using a Kalman filter to increase the accuracy of the system. However working frequencies for small sizes IMUs remain insufficient.

4.6.6 Optical sensors

Optical sensors also known as photodetectors are devices that convert light rays into an electrical signal [Dhiraj, 2012]. These type of sensors find applications in physics, chemistry, biology, medicine, telecommunications, instrumentation, photolithography on semiconductor chips, particle detection as well as object tracking etc. [Haus, 2012].

While it was shown in section 4.5.4 that no existing 6DoF optical tracker fits our requirements (laser triangulation systems presented in section 4.5.4.2 for example are too cumbersome while photodiodes arrangements found in the Maglev haptic interface

presented in section 4.5.4.7 are complex and bulky), it seems that using optical sensors for object tracking, which is of main interest for the present work, remains interesting. In fact, despite different specifications which led for the SPACE MOUSE presented in section 4.5.4.7 to an insufficient workspace, and despite integration and fine-tuning issues in the 6DoF contactless sensor presented in appendix B, which led to an insufficient bandwidth, specifically designed arrangements of photodetectors still have the potential to fit our requirements. Elementary sensors can indeed have a high resolution, a range of measurement compliant with our application and an acquisition frequency potentially higher than in previous examples. The question is then about the optimal choice of such elementary sensors that could be integrated in a compact manner to get a tracker fully compatible with our design drivers.

Photodetectors (or light sensors) can be divided, based on their operating principle, in three major categories [Hamamatsu, 2007]:

- **external photoelectric effect sensors**, like photomultipliers, which principle of operation will be explained below,
- **internal photoelectric photodetectors** which can be further divided into photoconductive types like photoresistors (which are characterized by an increase of their electrical conductivity when they are exposed to light) and photovoltaic types like photodiodes (which generate a voltage upon exposure to light), both featuring a high sensitivity and a miniature size [Hamamatsu, 2007], and
- **thermal types** (not studied here since temperature is not a metric of interest).

According to our research, the most interesting sensors in the first category are photomultipliers and in the second case PhotoDiode Arrays (PDAs), Charge Coupled Device (CCD), Complementary Metal-Oxide Semiconductor (CMOS) and Position Sensitive Detectors (PSDs). Each of these sensors will be presented in detail below.

4.6.6.1 Photomultipliers

Photomultipliers are sensors that work based on the external photoelectric effect which states that when light (with sufficient energy) hits a metal plate, photoelectrons are released from the surface of the material. An example of a photomultiplier diagram is shown in figure 4.47a. Such arrangement (typically build in a vacuum glass tube) shows how the incoming light gets amplified (based on the external photoelectric effect) when hitting several additional electrodes (dynodes). Such avalanche effect leads to a current amplification converted into a voltage thanks to resistors. The voltage obtained is proportional to the incoming light intensity on the photocathode.

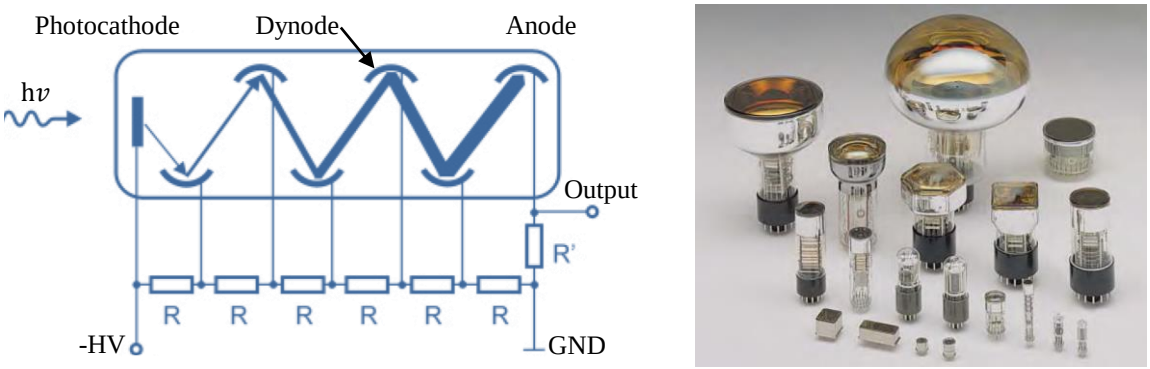

(a) Photomultiplier diagram

(b) Photomultipliers samples from Hamamatsu

Figure 4.47: Photomultiplier diagram and commercial samples.

Several fields of applications are reported for such devices [Hamamatsu, 2007]: spectrophotometry, medical equipment, biotechnology, high-energy physics experiments, environmental measurement, radiation monitors, industrial measurements, aerospace applications, and mass spectrometry etc. Even though these sensors provide a high frequency response ($8.7 - 111$MHz according to [Hamamatsu, 2016]), they require high operating voltages ($500 - 3000$V applied across the anode and cathode) and are complex to use (they require a voltage divider circuit) [Hamamatsu, 2007]. Furthermore, as shown in 4.47b which illustrates samples of photomultipliers manufactured by Hamamatsu, they can attain relatively important sizes ($13 - 127$mm diameters [Hamamatsu, 2016]).

4.6.6.2 Photodiode arrays

Before introducing these sensors, a brief description of the working principle of a photodiode will be provided.

4.6.6.2.1 Photodiodes Photodiodes are sensors that generate an electrical signal (current or voltage) when a P-N junction is irradiated by light photons.

In a N-type semiconductor the number of free electrons is superior to the number of holes (positive charges), meanwhile in an P-type semiconductor the number of holes is superior to the number of free electrons. When both are combined, the region located at the P-N junction, called the depletion layer, acts as an insulating region (see Fig.4.48). The association of these two types of materials represents one of the most common semiconductor devices, a diode.

This junction allows the passage of current only in one direction if a positive voltage (forward bias) is applied on the ends of the P-N junction, i.e. the diode is acting as a closed switch (see Fig.4.49a). On the contrary, if the applied voltage is inverted (reverse bias), the P-N junction will act as an open switch (see Fig.4.49b).

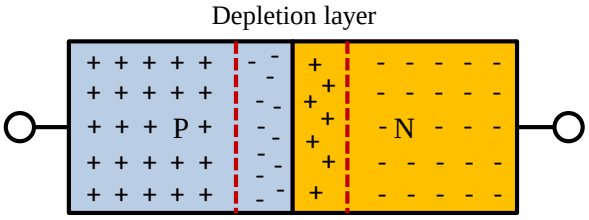

Figure 4.48: Main elements of a P-N junction.

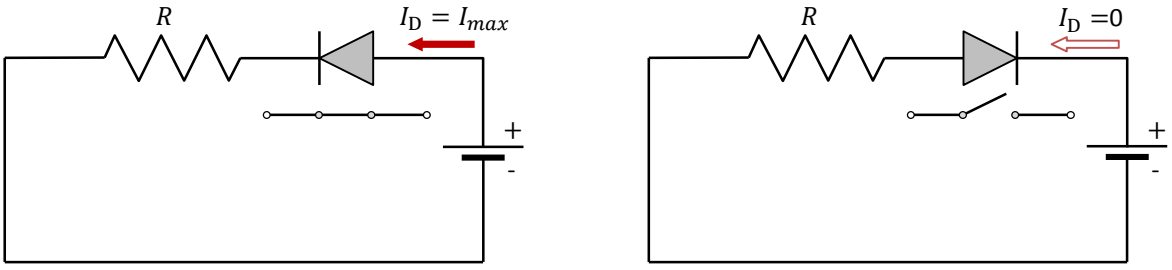

(a) Forward bias (b) Reverse bias

Figure 4.49: Forward and reverse bias of a P-N junction.

Unlike diodes, the P-N junction of photodiodes is made with a light-sensitive semiconductor. Depending on the material, the junction will be sensible to several ranges of wavelengths [Arbind, 2017]:

- from 190 to 1100nm for Silicon,
- from 400 to 1700nm for Germanium,
- from 800 to 2600nm for Indium Gallium Arsenide and
- from 1000 to 3500nm for Lead Sulphide.

These components are usually encapsulated in a package with a window allowing the light to enter into the P-N junction (see Fig.4.50a). The symbol of a photodiode is shown in figure 4.50b.

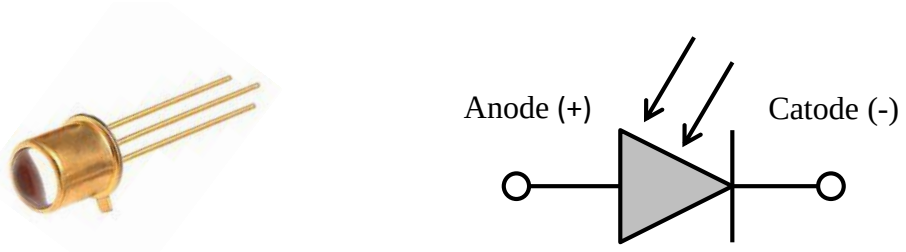

(a) SD5421-002 Photodiode p-i-n from Honeywell (b) Photodiode symbol

Figure 4.50: Photodiode sensor.

Photodiodes can also have a P-I-N structure, i.e. the photodiode contains an intrinsic region (undoped semiconductor) between the P and N semiconductors. Most of the photons are then absorbed by the intrinsic region which generates charged particles that can efficiently contribute to the photocurrent generation. As they collect photons more efficiently than P-N photodiodes., P-I-N photodiodes are the most wide spread. They are suitable for applications that require higher bandwidths.

4.6.6.2.2 Photodiode arrays Photodiode arrays (PDAs) consist in several photodiodes disposed in a line. Their principle of operation is illustrated in figure 4.51a. The incident light on each diode (pixel) generates a photocurrent which is integrated by an integration circuit associated to that pixel. During the integration period, a sampling capacitor connects to the output of the integrator through an analog switch. The amount of charge accumulated in each pixel is directly proportional to the light intensity and the integration time. The charge stored in the sampling capacitors is then sequentially connected to a charge-coupled output amplifier that generates a voltage on the analog output.

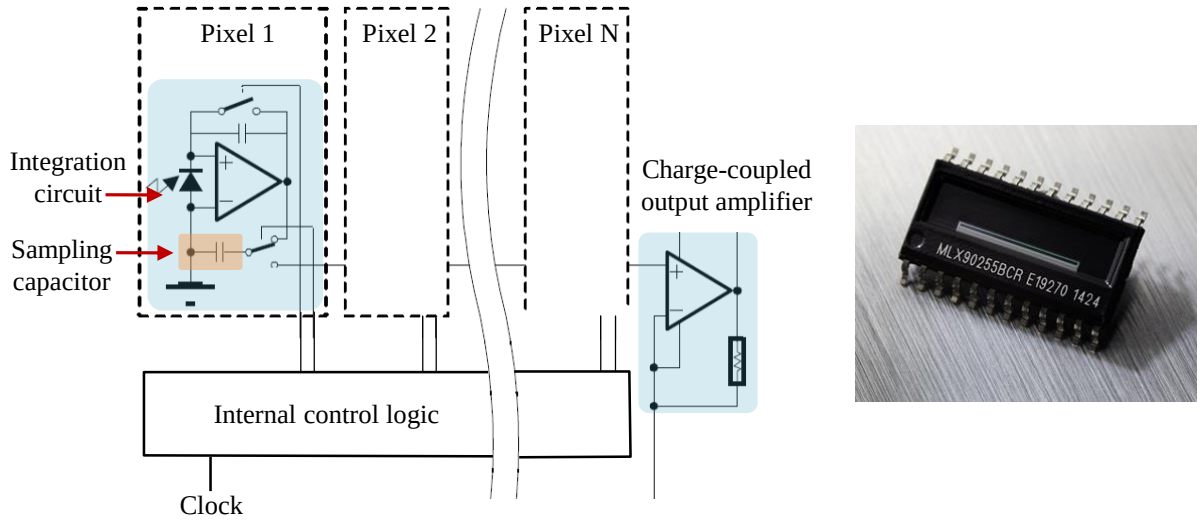

(a) Simplified functional diagram (adapted from MLX90255-BC datasheet)

(b) MLX90255-BC photodiodes array from Melexis

Figure 4.51: Linear array of photodiodes.

Commercial photodiodes are available in the market (see Fig.4.51b). They can also be found under the name of linear optical arrays. Table 4.21 shows representative characteristics of some commercially available PDAs. The provided characteristics are issued from Melexis and AMS catalogues.

Table 4.21: Representative characteristics of PDAs.

Sensor type	Photodiode arrays (PDAs)
Measured variable	Light intensity
Physical phenomenon	Conversion of light into electrical current
Size	$[8.8 \times 0.64 \times 1]$mm $-$ $[10.25 \times 15.34 \times 2.54]$mm
Measuring range	Wavelength: $400 - 1000$nm Linear array length: 8.6mm ($\approx 128 \times 1$ pixels)
Time response	Sensor integration time of all pixels: 0.033ms (min), 15ms (typ) and 100ms (max)
Resolution	300-400 DPI (dots per inch)
Needs to equip target?	Yes, target should provide any detectable light source
Degrees of freedom (DoF)	1DoF, 6DoF possible employing a sensor arrangement
Occlusion sensitive	Yes
Price	Cheap
Strengths (✓) / Weaknesses (✗)	✓: Compact ✗: All the pixels should be read and analyzed to determine the position of a light spot along the pixel array line
Applications	Linear and rotary position encoder, spectrometer and bio-metrical applications, optical character recognition (OCR) and barcode reading

4.6.6.3 CCD arrays

Charged-coupled device (CCD) sensors were invented in 1969 at AT&T Bell Labs by Willard Boyle and George E. Smith [Alfaraj, 2017]. Each pixel of these optical arrays is made of a metal-oxyde-semiconductor capacitor (MOSCAP). A MOSCAP consists in three main elements: a metal electrode (also called gate), an insulating film and P-type semiconductor (see Fig.4.52). Each pixel can be then considered to behave as a capacitor.

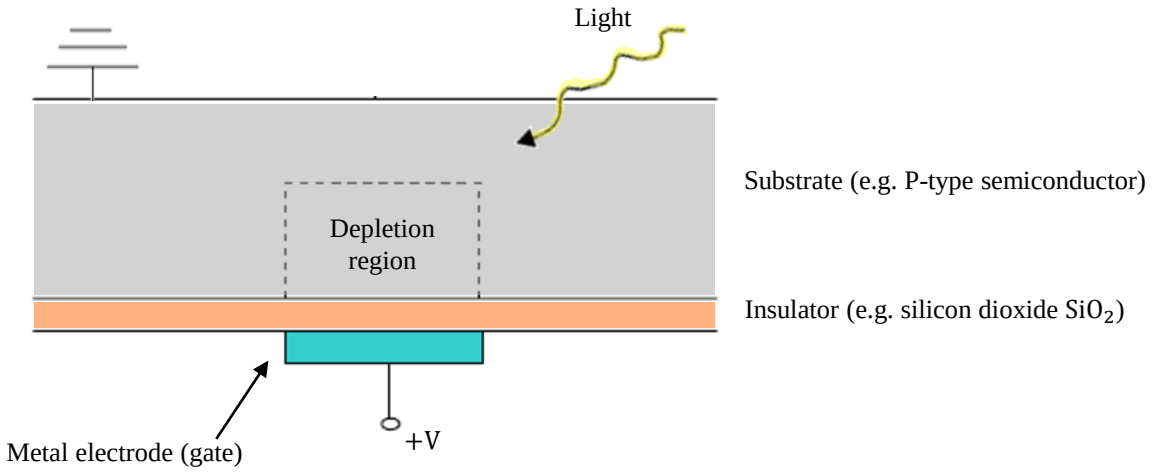

Figure 4.52: MOSCAP pixel simplified diagram.

During light incidence a charge is generated into each pixel. In a CCD device, the stored charges are transported across the matrix and read at one corner of the array (see Fig.4.53a).

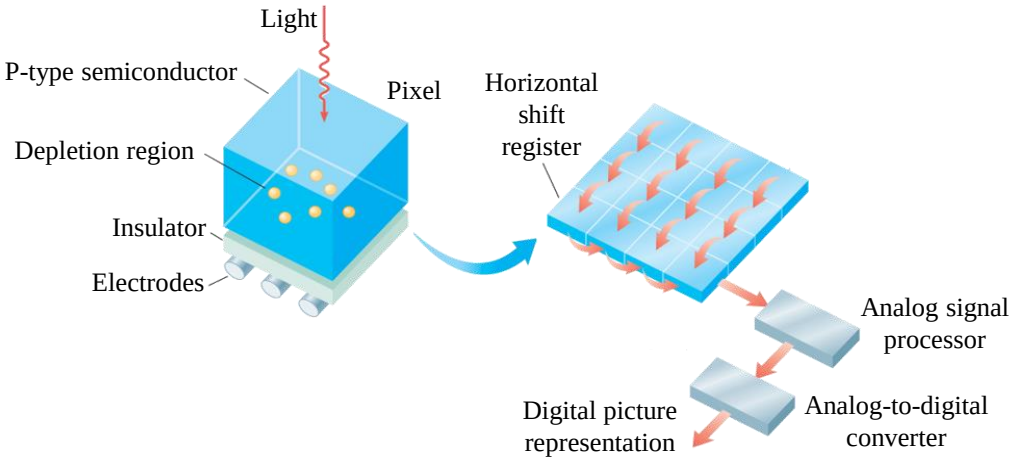

(a) Image detection and processing in a CCD sensor

(b) KAF-8300 CCD sensor from ON Semiconductor

Figure 4.53: Charged coupled device sensor. (a) adapted from [Alfaraj, 2017].

CCD sensors are commercially available (see Fig.4.53b). Table 4.22 resumes representative characteristics of some of these sensors. The presented characteristics are issued from ON Semiconductors catalogue.

Table 4.22: Representative characteristics of CCDs.

Sensor type	CCD
Measured variable	Light intensity
Physical phenomenon	Conversion of light into electric current (MOSCAP pixel)
Size	$[20 \times 30 \times 4]$mm – $[59 \times 48 \times 7]$mm
Measuring range	Wavelength: $400 - 1000$nm Array dimensions: $[512 \times 512]$pixels – $[8304 \times 6220]$pixels
Working frequency	1-20 fps (frames per second)
Resolution	Pixel size: $[5.4 \times 5.4]\mu$m $-$ $[24 \times 24]\mu$m
Needs to equip target?	Yes, target should provide any detectable light source
Degrees of freedom (DoF)	2DoF, 6DoF possible employing a sensor arrangement
Occlusion sensitive	Yes
Price	Relatively expensive
Strengths (✓) / Weaknesses (✗)	✓: Compact ✓: Mature technology ✗: Important power consumption ✗: Low noise ✗: Needs external analog-to-digital converter
Applications	Machine vision, UV-VIS-IR spectroscopy, digital oscilloscopes, scientific imaging

4.6.6.4 CMOS arrays

Unlike CCD sensors, each pixel of a Complementary Metal-Oxide Semiconductor (CMOS) array contains an *in-situ* circuit providing charge conversion and amplification (see Fig.4.54a). As a consequence, CMOS arrays are more flexible than CCD imagers in the sense that the accumulated charge on each pixel of the array can be read individually.

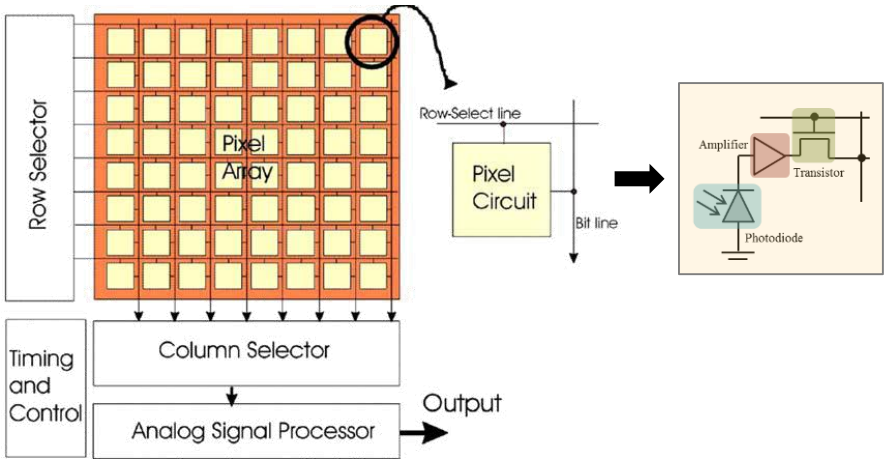

(a) CMOS image sensor floorplan

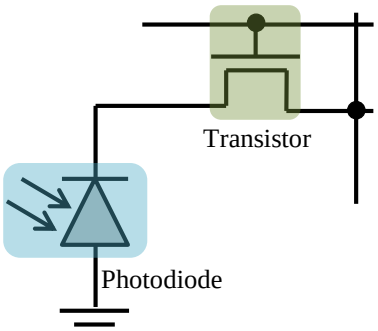

(b) Passive pixel sensor

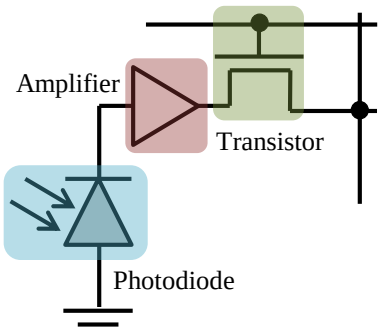

(c) Active pixel sensor

Figure 4.54: CMOS image sensor floorplan and common pixel types. (a) adapted from [Bigas et al., 2006].

Since the mid 60s, a combination of either P-N or P-N-P junctions have been employed for the conversion of light into an electronic signal [Titus et al., 2011]. Research works not only focused on the conversion part but also on how to retrieve these signals from the arrays of pixels. During the 70s CMOS sensors lost popularity in comparison to CCDs, since the later provided a more interesting fill factor (ratio of light-sensitive surface to entire pixel surface). CMOS require in fact transistors at each pixel. Also, noise in CCD was considerably less than in CMOS imagers. Finally in the early 90s, improvements in CMOS manufacturing technology and a demand to decrease power consumption for devices employing batteries made CMOS to regain interest as a viable imaging device. CMOS arrays can make use of two types of pixel circuits:

- **Passive pixel sensors** (PPS) which were employed in the first CMOS imagers: these

sensors are based on photodiodes without internal amplification stage. They only contain a transistor allowing to connect the elementary sensor (photodiode) to the readout structure (see Fig.4.54b). These sensors suffered from low sensitivity (amount of generated charge in function of the received light) and high noise.

- **Active pixel sensors** (APS): contrary to PPS, APS can contain several transistors per pixel and an amplification stage (see Fig.4.54c). Such combination is known for improving the performance of the pixel, e.g. the power dissipation of a pixel is lower than in CCDs since each amplifier is activated during readout.

CMOS sensors are commercially available (see Fig.4.55). Table 4.23 resumes representative characteristics of some of these sensors. The presented characteristics are issued from ON Semiconductors catalogue.

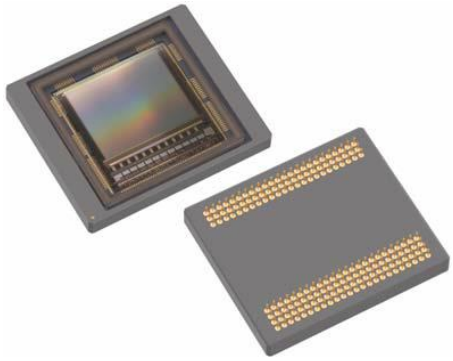

NOIL2SM1300A CMOS high speed sensor from ON Semiconductors

Figure 4.55: Commercial CMOS imager.

Table 4.23: Representative characteristics of CMOS imagers.

Sensor type	CMOS
Measured variable	Light intensity
Physical phenomenon	Conversion of light into electric current (PPS or APS pixels)
Size	$[11.5 \times 11.5 \times 1.4]$mm – $[36 \times 31 \times 6.8]$mm
Measuring range	Wavelength: $400 - 1000$nm Array dimensions: $[640 \times 480]$pixels – $[2210 \times 3002]$pixels
Working frequency	$5 - 815$ fps (frames per second)
Resolution	Pixel size: $[3 \times 3]\mu$m – $[14 \times 14]\mu$m
Needs to equip target?	Yes, target should provide any detectable light source
Degrees of freedom (DoF)	2DoF, 6DoF possible employing a sensor arrangement
Occlusion sensitive	Yes
Price	Relatively cheap
Strengths (✓) / Weaknesses (✗)	✓: Individual pixel readout ✓: Low power consumption ✓: Cheaper than CCDs ✓: Faster than CCDs ✗: Face lower fill factor than CCDs ✗: Less sensitive than CCDs
Applications	Space, automotive, medical, digital photography, machine vision, motion monitoring, security, barcode scanning.

4.6.6.5 Position sensitive detectors

A PSD is composed of a uniform resistive layer formed on one or both surfaces of a high-resistivity semiconductor substrate and a pair of output electrodes placed at both ends of the resistive layer for extracting position signals. When a light beam strikes on its photosensitive area, the light incident on the detector is converted into an electrical current (photocurrent) that is divided between the contacts in proportion to the resistance of the active layer (see Fig.4.56). This phenomenon is called lateral photo-effect [Woltring, 1975].

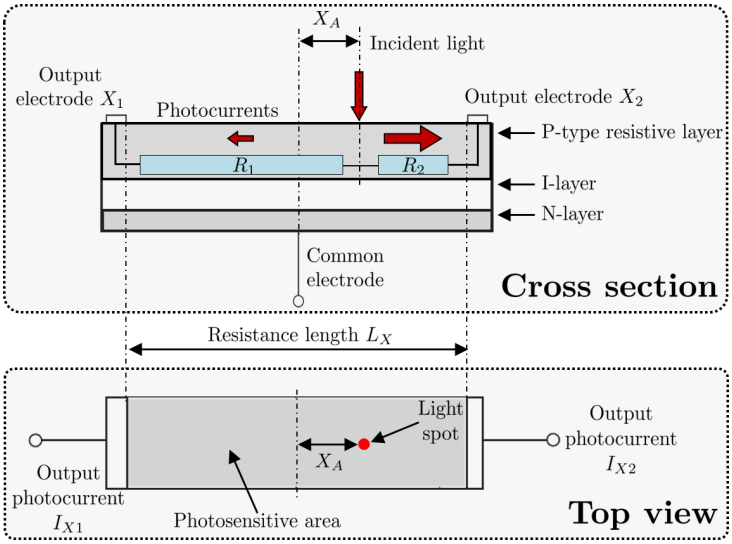

Figure 4.56: Schematic view of a one-dimensional PSD (adapted from [Hamamatsu, 2014]).

The relation between the location of the incident light and the occurring photocurrents is given by (4.11), where Lx is the length of the photosensitive area and X_A the distance from the electrical center of the PSD to the light input position.

$$\frac{I_{X_2} - I_{X_1}}{I_{X_1} + I_{X_2}} = \frac{2X_A}{Lx} \tag{4.11}$$

PSDs are commonly used in non-contact distance measurement systems using the triangulation principle for various height and vibration measurements. They are commercially available either in 1D (see Fig.4.57a) or in 2D (see Fig.4.57b) formats.

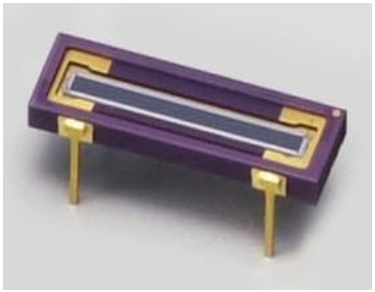

(a) S3932 1D PSD from Hamamatsu

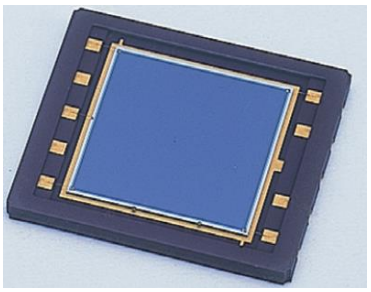

(b) S5991-01 2D PSD from Hamamatsu

Figure 4.57: Commercial 1D and 2D PSDs.

Table 4.24 provides representative characteristics of commercially available PSDs. The provided characteristics were issued from Hamamatsu catalogue.

Table 4.24: Representative characteristics of PSDs.

Sensor type	Position sensitive detector (PSD)
Measured variable	Generated photocurrent
Physical phenomenon	Conversion of light into electric current (lateral photo-effect)
Size	Package size: 1D: [4.1 × 4.8 × 1.8]mm to [55 × 5 × 2.5]mm 2D: [8.8 × 10.6 × 1.2]mm to [28 × 28 × 5]mm
Measuring range	Wavelength: 320nm – 1100nm Photosensitive area size: 1D: 2 to 37mm 2D: [4 × 4]mm to [12 × 12]mm
Working frequency	100kHz – 1MHz
Error / Resolution	1D, 2D Position error: 10µm – 150µm / 2D Resolution: 0.4mm – 1mm
Needs to equip target?	Yes, target should provide any detectable light source
Degrees of freedom (DoF)	1DoF, 2DoF, 6DoF (employing a sensor arrangement)
Occlusion sensitive	Yes
Price	Relatively cheap
Strengths (✓) / Weaknesses (✗)	✓: Compact ✓: High speed ✓: Simple to use ✗: Require precise current measurement equipment
Applications	Non-contact distance measurement, e.g. height and vibration measurements.

4.6.6.6 Conclusion

The working principle and characteristics of several optical elementary sensors, able to provide displacement and position information, were presented in the present section.

Photomultipliers where quickly discarded as they are complex to use and cumbersome. Remained on one hand multichannel sensors such as photodiodes arrays, CCD and CMOS sensors, and on the other hand PSDs, which consist in a large photodiode able to provide the analog coordinates of a spot of light.

Multichannel optical sensors are compact and provide interesting characteristics in terms of resolution, i.e. the size of their pixels is in the order of few μm. On the other hand, these sensors behave basically as a camera and in general one measurement requires reading all the pixels of the imager. This has the disadvantage of an important acquisition time: each pixel requires a minimum time for its stored charge to be converted into an electrical signal, then this electrical signal needs to be converted in to a digital one and finally it is necessary to add the time needed for image processing in order to obtain the information of interest, i.e. the position of the incident light spot. With a number of pixels ranging from 128 (in the case of PDAs) to $\approx 6,630,000$ (in the case of large CMOS), this considerably slows down the attainable sampling rate. Based on the explored catalogues,

full image sampling rates remains limited to between 1Hz and ≈ 800Hz. This rate remains below our requirements to have a control loop working at a frequency higher than 1kHz. Furthermore, these sensors are relatively complex to use.

In this context, PSDs represent a very interesting option. They remain compact sensors and provide interesting characteristics in terms of acquisition frequency (100kHz − 1MHz) and position errors (10μm − 150μm). These analog sensors are also very simple-to-use, e.g. in a 1D PSD the position of the center of gravity of a light spot can be determined by directly measuring two photocurrents and making only three operations (two additions and one division).

4.6.7 Global conclusion on elementary sensors for IC-HI tracking systems

The working principle of several types of elementary sensors, in particular ultrasonic, capacitive, magnetic, inertial and optical sensors able to provide distance and/or displacement information, were presented from sections 4.6.2 to 4.6.6, along with their technical characteristics (issued from the catalogs of important sensor suppliers). Having first described in a simplified and easy to understand yet non-exhaustive manner their working principle allowed to better interpret the technical aspects provided by manufacturers. The presented study allowed to position the suitability of current commercially available technologies in reference to the design drivers of an IC-HI tracking system of type CT-HI.

After a thorough study of the available sensing technologies and inspired by the system developed in [Diallo, 2014] (see Appendix B) we chose to focus on linear PSDs for the targeted application. PSDs have proven to be an adapted technological solution in the case of non-contact tracking systems (see section 4.5.4.7). Motivated by the simplicity and potential low cost of the light source, slit and linear optical sensor arrangement, a linear PSD was chosen for the development of our IC-HI tracking system.

4.7 Modeling and experimental characterization of a 1DoF non-contact displacement sensor

As stated at the beginning of this chapter, the global aim of the current study is the development of a 6DoF tracking system that can be used to efficiently measure the configuration of the handle of an IC-HI. To this end, we first derived important design drivers for such a system. Then the literature on tracking systems and non-contact sensing technologies was studied and their performances were compared to the defined design criteria. We concluded from this study that a custom designed measurement system based on optical elementary sensors was the most promising solution for the intended application.

We more specifically focused our attention on a system which will be denoted here as Emitter-Receptor-Slit (ERS) sensor. This system, inspired by the Space Mouse, is illustrated by figure 4.58. It is composed of an infrared light source, a slit and a linear position sensitive detector (PSD).

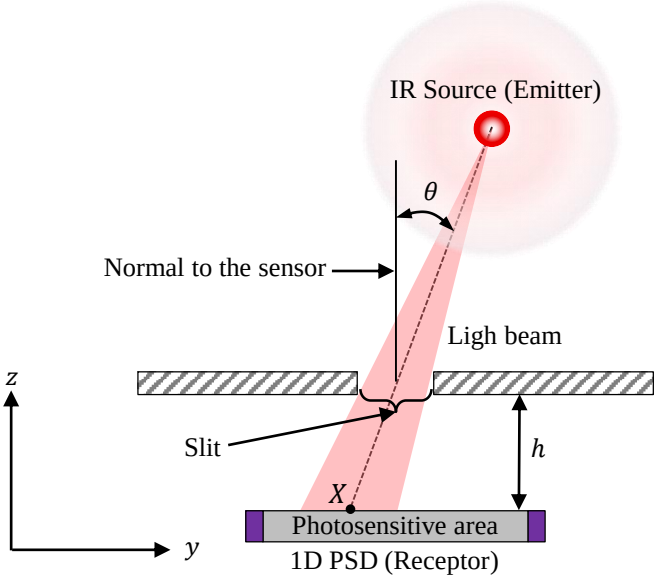

Figure 4.58: Emitter-Receptor-Slit principle.

Its principle of operation is the following: the angle θ between the normal to the sensor and the line going from the source to the slit is deduced from the position X of the image of the source on the sensor, provided the distance h between the sensor and the slit is known. In space, this angle defines a plane. The position of the source can easily be obtained by repeating this operation for three different slits, the source being at the intersection of the three planes (see Appendix B for details).

While simple in theory, this principle requires however in practice an efficient model able to predict the angle θ from the distance X. The first step towards the development of such an inverse model is to better understand the behavior of the system, which requires the development of a realistic geometric and radiometric modeling of the source, slit and sensor. The aim of the following is to present such a direct model able to estimate X from θ, as well as its experimental validation.

4.7.1 Basic concepts of radiometry

Light sources can emit energy in a wide range of wavelengths, only some of them being visible. Indeed, the spectrum of radiant energy waves that we call light ranges approximately from 380nm to 770nm. Wavelengths shorter (ultra violet) or longer (infrared) than these do not produce a visual response in the eye [Ryer, 1997]. As a consequence, depending on the wavelengths of interest, the measurement of the propagated energy in

the electromagnetic waves radiated by light sources can use two approaches: the photometric approach, which refers only to the part of the radiant power produced by the source that is perceived by the human eye as light, and the radiometric approach, which is more general as it takes into account the entire radiant power produced by the source.

In the present application, in order to ensure the best possible sensitivity to handle movements, it is important that the sensor is not perturbed by external conditions, especially ambient light. Therefore, and after a careful analysis of the available sensors and light sources, we decided to rely on components working in the infrared spectrum (>770nm). The attention being given to these wavelengths, in particular in quantifying the power emitted by an infrared emitting diode (IRED), we will deal here with the radiometric approach.

It is worth noting that the sensor, as shown on figure 4.58, will not see the entire light emitted by the source, but only the part of it that:

- passes through the slit and
- illuminates the active area of the sensor.

As a consequence, we will not consider here the radiant power or radiant flux Φ representing the total power (light) radiated by the source, but only the part of it which illuminates the active area of the sensor. Therefore we will use the notion of radiant intensity, denoted here as I_e, which refers to the energy radiated by the source into the unit solid angle in a unit of time. This is the power per unit solid angle and it is typically given in mW/sr by IRED's constructors.

The computation of the total emitted power on the active area of the sensor requires to know the corresponding solid angle. Here we will consider that the illuminated sensor surface, as seen from the source, can be modeled as a rectangular plate (a rectangular slit is easy to manufacture and most measuring devices themselves have a rectangular window or sensitive surface [Khadjavi, 1968]) of size $a \times b$ (area ab) at a distance d from the source. Taking the center of the plate as a reference (i.e. considering only the configuration where the vector normal to the plate surface starting at the plate center points to the source, which means that the plate surface is perpendicular to the line of sight [Mathar, 2015]), the associated solid angle is given by (4.12).

$$\Omega(a, b, d) = 4 \arccos \sqrt{\frac{1 + \alpha^2 + \beta^2}{(1 + \alpha^2)(1 + \beta^2)}} \tag{4.12}$$

With $\alpha = a/(2d)$ and $\beta = b/(2d)$.

The presented concepts will be used in the following sections to establish a model of the response of an ERS system.

4.7.2 Model of a emitter-receptor-slit sensor

When a slit is placed in the field of view of a light source, the light passing through it builds a light beam and its shape is mainly determined by the slit geometry. When the light beam hits the photosensitive area of the receptor, a certain amount of power is transmitted to it (see Fig.4.59).

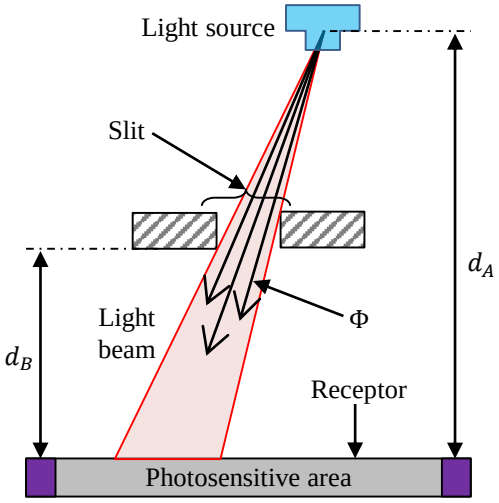

Figure 4.59: Sagittal view of an ERS system illustrating its main elements. Here d_A and d_B are distances perpendicular to the receptor's surface.

The received power does not only depend on the geometry of the light beam but as well on the characteristics of the light source and the irradiated portion of the receptor's photosensitive area. In the following subsections we will present the characteristics of the light beam formed by an ERS system that uses one IRED (emitter) and one linear PSD (receptor).

We are interested here in modeling the response of the ERS system in order to predict two outputs:

- the position of the light spot X_A (see Fig.4.56): our aim is to get a relationship between the position of the source and X_A that can be inverted in the future to compute the angle θ of the plane in which the source lies from the measurement X_A, and
- the total generated photocurrent $I_O = I_{X_1} + I_{X_2}$: this data is useful to compute the theoretical limits of the workspace in which the source can move. In practice, we intend to use this information to check for each position of the source if the sensor is not insufficiently illuminated (in this case the signal/noise ratio would be insufficient) nor saturated. Indeed even if the position X_A can still be computed from θ in such cases, the sensor will not be useful in practice as X_A will not be exploitable for the calculation of θ.

4.7.2.1 IRED-PSD slit-based system

The light beam shape generated by this ERS system is similar to a pyramid of rectangular base. As it can be observed in figure 4.60, only a part of its base intersects with the PSD photosensitive area. This intersection represents the light spot A_{PSD}. The associated light beam is called here PSD light beam (PLB). In the present case we suppose that the position X_A corresponds to the geometrical center of the light spot A_{PSD}. As the IRED translates in space, the shape of the PLB varies. These variations let us identify other geometrical elements illustrated in figure 4.61. The amount of solid angle contained in the PLB can then be estimated using (4.12).

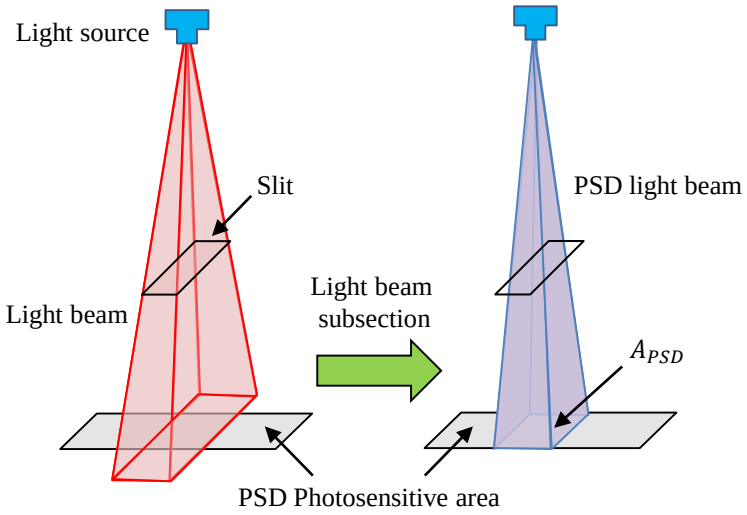

Figure 4.60: Light beam shaped by the slit (left) and its subsection illuminating the PSD active area (right).

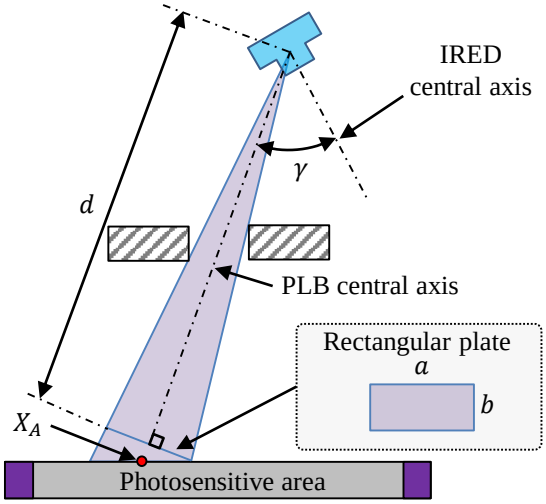

Figure 4.61: Geometrical description of the PLB. The position of the center of gravity X_A does not necessarily intersects with the PSD light beam central axis. The rectangular plate is perpendicular to the PLB central axis and its dimension a is parallel to the photosensitive area.

4.7.2.2 Photocurrent calculation

The generated photocurrent of an isotropic IRED can be calculated using:

$$I_O = P_{psd}S + I_D = \Omega I_e(I_F)S + I_D \tag{4.13}$$

where,

P_{psd} represents the power received on the PSD photosensitive area (in watt, W),
S is the photoresponsivity (a conversion factor of power into current which is given by the PSD constructor in A/W) and
I_D stands for the PSD dark current (in A).

In the very right part of (4.13),

Ω is the PSD light beam (PLB) corresponding solide angle and
I_e is the radiant intensity (in W/sr), function of
I_F which is the forward current flowing through the IRED (in A).

IREDs are in practice non-isotropic light sources. This means that depending on the view angle γ in reference to the IRED central axis, the emitted power will vary according to a certain profile (see Fig.4.62). This variation is regulated by the relative radiant intensity denoted $I_{e_{Rel}}$. In order to take this power variation into account, we can add the relative radiant intensity $I_{e_{Rel}}(\gamma)$ to (4.13) as shown in (4.14).

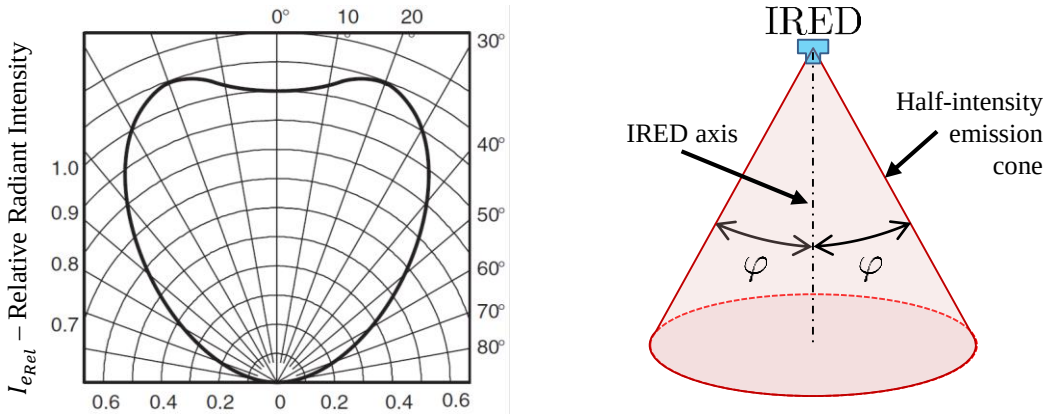

Figure 4.62: Relative radiant intensity profile for IRED CQY36N (left) and IRED half-intensity emission cone (right). At a view angle $\gamma = \varphi$, the emitted power corresponds to half of the total radiant intensity I_e.

$$I_O = \Omega I_e(I_F)I_{e_{Rel}}(\gamma)S + I_D \tag{4.14}$$

It is worth noting that, as can be seen from the left part of the figure 4.62, an IRED emits a light that is sufficient to be seen by the sensor only in a certain cone. As in the case of an IC-HI there can momentarily be an important angular offset between the handle and the end-effector of the robot when the former is manipulated by the user, it is important that the IRED (which is mounted on the handle) has the largest possible half-intensity emission cone so that it continues to illuminate the sensor even for large angulations of the handle relative to the end effector (on which the sensor is mounted). After a careful review of the manufacturers' catalogues, we selected for our study an IRED CQY36N from VISHAY.

Equation (4.14) assumes that the relative radiant intensity for a given value of γ is representative of the $I_{e_{Rel}}$ distribution inside the solid angle contained in the PLB. This assumption can be considered as valid as long as the slit width is small. This constraint will guide our design.

In order to ease the calculation of the aforementioned geometrical elements, a simulator of the ERS system was developed using Matlab (see Fig.4.63). The ERS simulator allows to calculate the response for any number of ERS arbitrarily positioned and oriented in space.

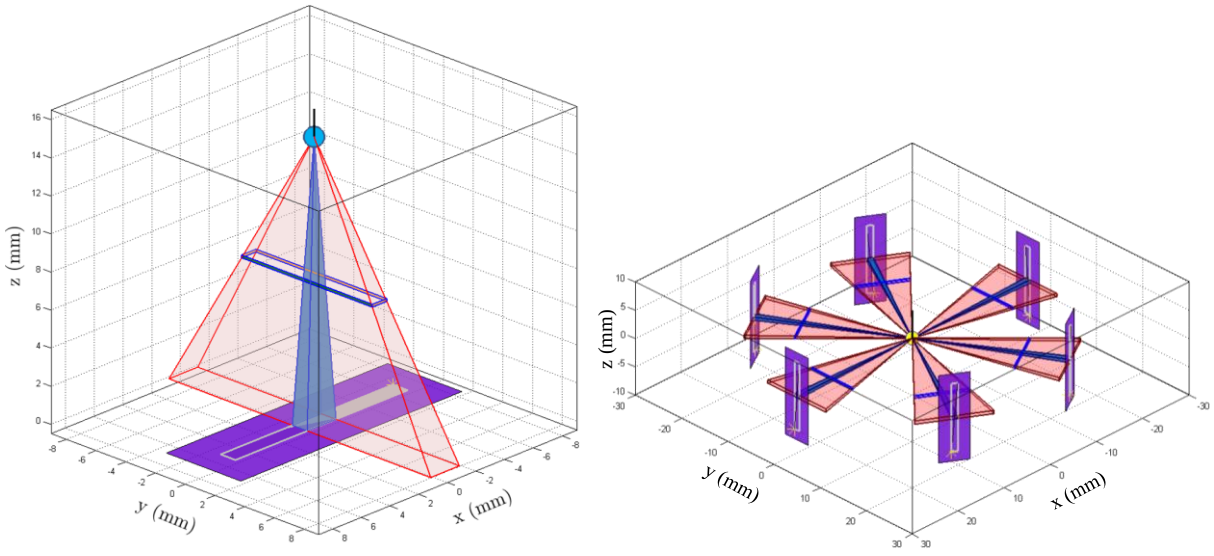

Figure 4.63: Single (left) and 6 ERS (right) configurations simulation.

4.7.3 Experimental results

In order to be able to evaluate complex cases, e.g. an arrangement of several ERS systems, the elementary sensor model should provide a response as close as possible to that of the real components. To validate the pertinence of the proposed model, a test bench of a single ERS system was built and first experiments were performed. In the following paragraphs the test bench description, performed experiments and results are presented.

4.7.3.1 ERS Test Bench

The test bench is composed of two sub-assemblies which are denoted here as the Emitter Sub-Assembly (EmSA) and Receptor Sub-Assembly (ReSA). The EmSA can translate in three orthogonal axes, meanwhile the ReSA is static (see Fig.4.64).

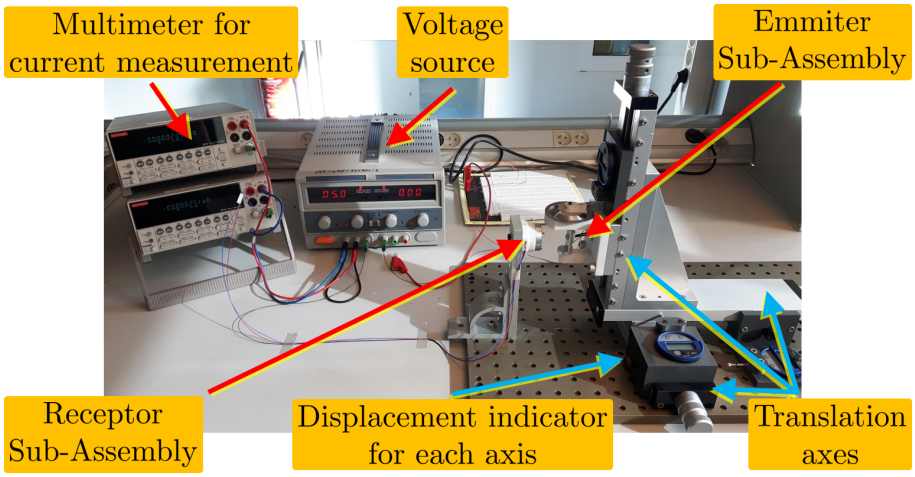

Figure 4.64: ERS test bench main elements

The EmSA (see Fig.4.65) is composed of the emitter CQY36N made by VISHAY. This IRED is particularly interesting because of its big half-intensity emission angle $\varphi = \pm 55\text{deg}$. As previously explained, a big angle allows to increase the space in which the IRED can translate and still send a sufficient amount of radiant power through the slit. The emitter presents a radiant intensity of $I_e \approx 3.16\text{mW/sr}$ at a forward current of $I_F = 100\text{mA}$.

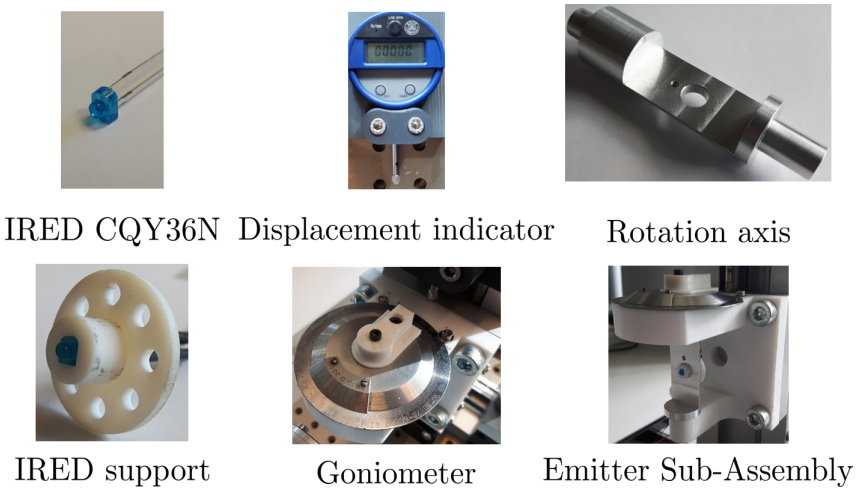

Figure 4.65: Emitter Sub-Assembly's main elements. From left to right, from top to bottom: an IRED CQY36N from VISHAY. A ROCHPROFIL displacement indicator of 0.01mm resolution allowing to measure translations on each axis. The rotation axis that hosts the IRED support and which rotation axis is coincident with the IRED's chip. The IRED support that can be rotated around the IRED's central axis by steps of 45°. A goniometer allows to quantify the rotation on the vertical axis. Finally the complete Emitter Sub-Assembly.

The ReSA (see Fig.4.66) is composed of a receptor support which was specially designed to host the one-dimensional PSD S3932 made by HAMAMATSU. This receptor provides a photosensitive area of 1mm × 12mm and presents a photoresponsivity of $S \approx 0.54\text{A/W}$ at a wavelength of $\lambda = 950\text{nm}$ (corresponding to the IRED wavelength). Its maximal dark current is $I_D = 20\text{nA}$ when the reverse voltage is equal to $V_R = 5\text{V}$.

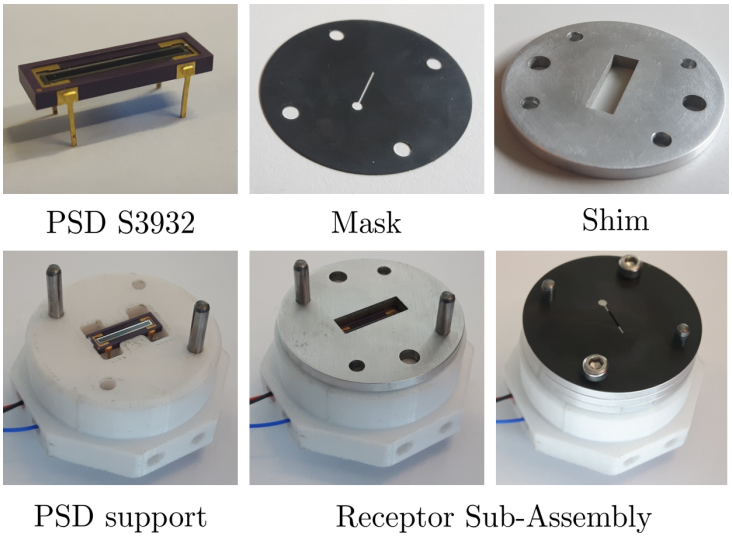

Figure 4.66: Receptor Sub-Assembly main elements. From left to right, from top to bottom: one-dimensional PSD S3932 by HAMAMATSU. A 0.16mm thick dark steel mask, containing a slit that can be mounted on the PSD support. The slit width equals 0.4mm and it is oriented perpendicular to the PSD photosensitive area, dividing it into two halves. Aluminum shims of 2.5mm height allow to position the slit at a distance d_B from the PSD surface. A PSD support specially designed to host the one-dimensional PSD S3932. Finally the complete Receptor Sub-Assembly

The aluminium shims shown in figure 4.66 only allow to set the slit at the desired distance from the sensor surface. It is worth noting that we also designed a shim allowing to further integrate an IR filter above the sensor in order to reduce the pollution due to the visible light (see Fig.4.67). However preliminary tests showed that, in the current testing environment, the visible light had no significant influence on the measured photocurrents. Thus it was not used in the reported experiments.

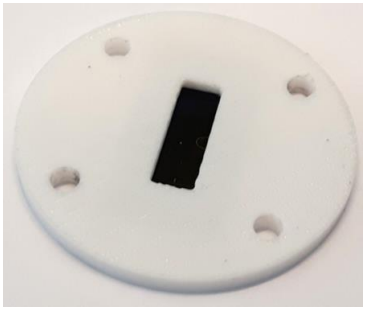

Figure 4.67: Shim of 2.5mm height containing a 1mm thick OptoliteTM infrared filter made by Instrument Plastics.

Both sub-assemblies were mounted parallel to each other on a precision table. Their initial relative positioning is adjusted using a plastic tube of known length that defines a perpendicular distance of 32mm between the IRED chip and the PSD surface (see Fig.4.68).

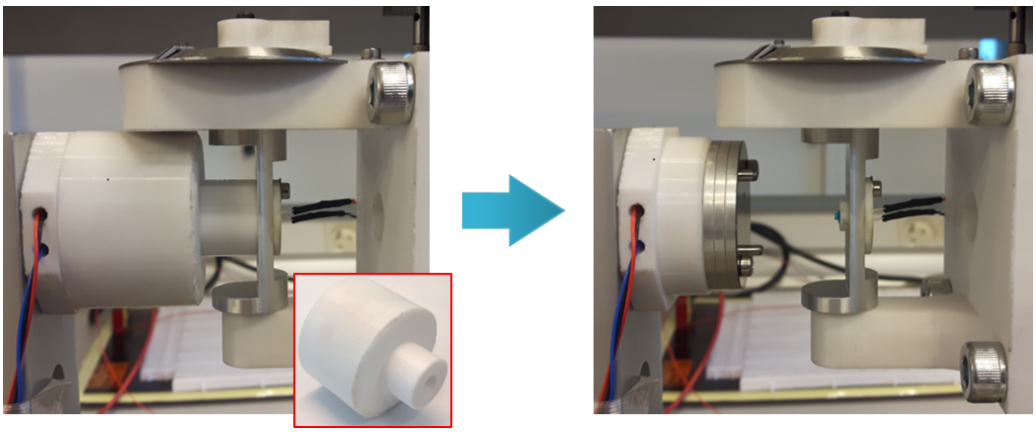

Figure 4.68: Positioning at the zero reference by means of the centering tube. At this position the IRED central axis is coincident with the center of the photosensitive area of the PSD.

4.7.3.2 Experiment 1: Description and Results

The proposed experiment aims to compare the calculated value of the light spot position X_A with the real one. The IRED chip is positioned at a distance of $d_A = 15$mm, which remains constant, from the PSD surface and the slit at a distance of $d_B = 7.5$mm from the same surface. The IRED is translated, with its central axis normal to the PSD surface, along the PSD x_{PSD} axis (see Fig.4.69). This configuration would make that the displacement of the IRED is almost equivalent to that of the light spot.

The displacement interval ranged from -5.5 to 5.5mm, with a step of 0.5mm, providing a total of 23 samples of I_{X1} and I_{X2}. This range guaranties that the light spot remains geometrically inside the photosensitive area.

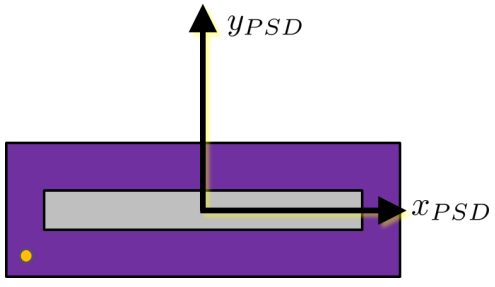

Figure 4.69: PSD reference frame seen by the IRED. The frame has its origin at the geometrical center of the photosensitive area and the x_{PSD} axis is parallel to it.

Figure 4.70 shows the resulting X_A position for the proposed experiment. It can be observed that the calculated and measured values are very similar, however there

exists a gap that will be denoted here as absolute error $|\varepsilon|$. The average absolute error is $|\varepsilon_{avg}| \approx 0.2591$mm, the maximum error being equal to $|\varepsilon_{max}| = 1.1542$mm and the minimum error to $|\varepsilon_{min}| = 0.0058$mm.

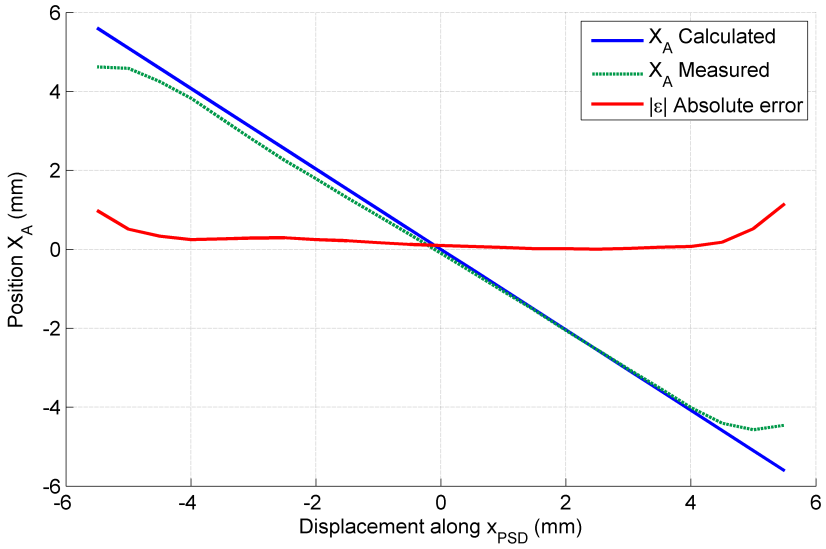

Figure 4.70: Comparison of the calculated and measured values of the position X_A of the light spot on the sensor. When the IRED translates in the positive direction of x_{PSD}, the light spot moves in the opposite direction and vice versa.

It is worth noting that the light spot position is measured using a specific part of the photosensitive area. For a PSD which photosensitive area length is $Lx \leq 12$mm, the recommended useful area length is only $Lx \times 0.75$. This corresponds to a value of 9mm for the PSD S3932, i.e. 4.5mm on each side of the photosensitive area. It can interestingly be observed that this area corresponds with a range where $|\varepsilon|$ is low. Indeed it can be seen that the average error $|\varepsilon_{avg}|$ remains low for $-4\text{mm} < x_{PSD} < 4\text{mm}$, i.e. $|\varepsilon_{avg}| \approx 0.1332$mm. On the contrary, it is observed that $|\varepsilon|$ rises as the light spot approaches the ends of the photosensitive area.

Figure 4.71 shows the amount of generated photocurrent I_O for this experiment. The calculated values of I_O preserve a similar order of magnitude in comparison to the measured values. However, the curve profiles are different. A possible explanation is that the theoretical value of $I_{e_{Rel}}$ given in the datasheet differs from that of the real IRED's behavior. This hypothesis was tested in a second experiment reported in [De La Cruz et al., 2018]. The obtained results better fit experimental data but some differences remain. Also, the procedure is too specific and cannot be a viable solution on the context of a generic development. Fortunately, the results plotted in 4.71 are sufficient to estimate the envelope of the useful domain.

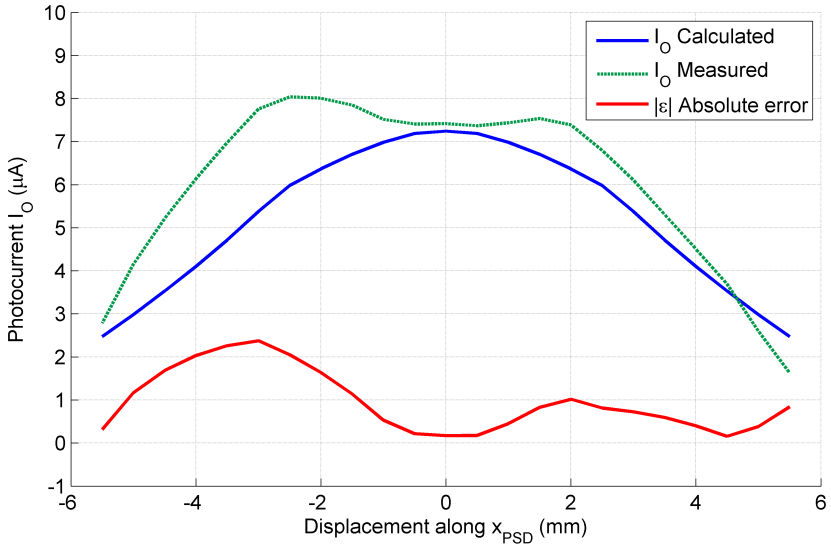

Figure 4.71: Calculated and measured values of the total photocurrent I_O generated by the sensor.

4.7.3.3 Experiment 2: Description and Results

In this experiment, the IRED is again translated, with its central axis normal to the PSD surface, along the PSD x_{PSD} axis. This time however the distance d_A takes different values, aiming to further explore the output of the PSD in various conditions. In figure 4.72, we can observe that the model fits well experimental measures when the IRED is far away from the sensor, while a visible difference exists at closer distances.

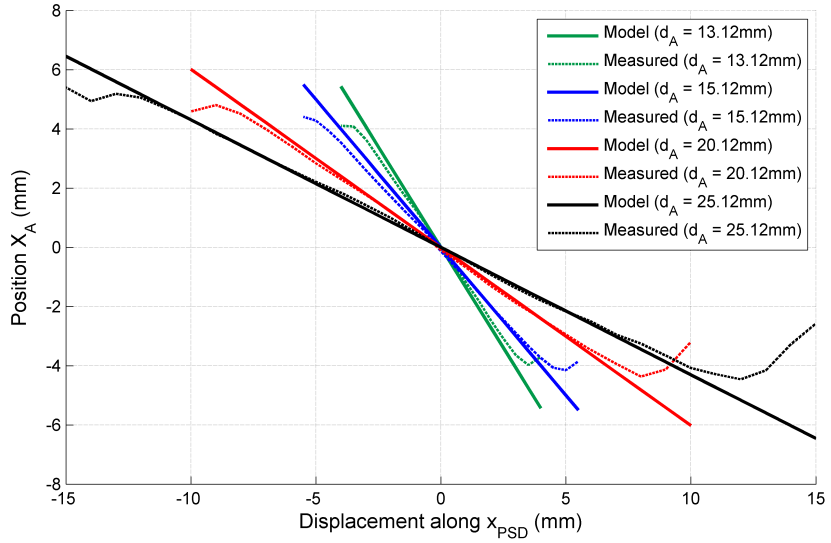

Figure 4.72: Comparison of the calculated and measured values of the position X_A of the light spot for different values of the distance d_A between the IRED and the sensor.

This can be explained by the fact that at long distances the radiant intensity distribution inside the light beam is relatively homogeneous, while at closer distances this is no more

the case. To cope with this issue, the inhomogeneity of the radiant intensity should be taken into account in the sensor model.

The total generated photocurrents corresponding to the same four values of d_A are shown in Fig.4.73. This confirms that despite the difference of photocurrent profiles, the order magnitude of theoretical photocurrent I_O remains close to the measured values. This result allows to conclude that our model is sufficient to estimate at what distances the IRED could saturate or not sufficiently illuminate the PSD.

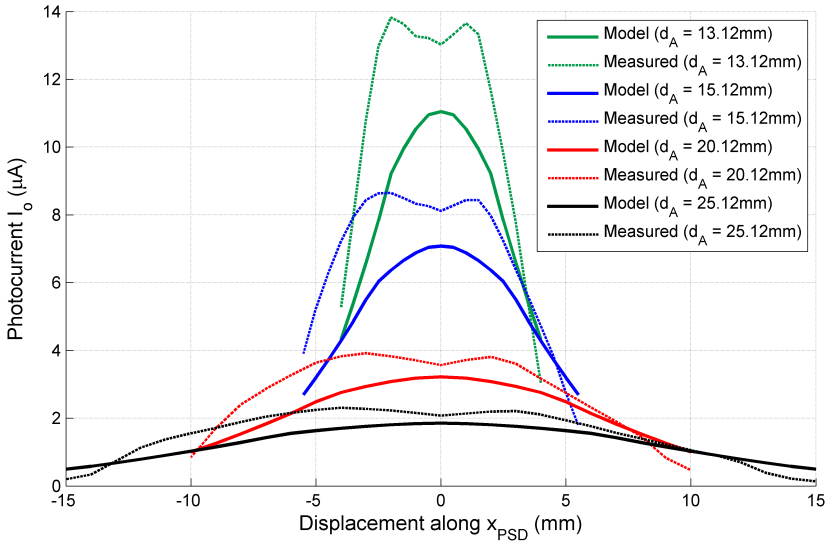

Figure 4.73: Calculated and measured values of the total photocurrent I_0 generated by the sensor for different values of the distance d_A between the IRED and the sensor.

4.7.4 Conclusion

IC-HI devices require high performances short range non-contact tracking systems to measure the configuration of the tool relative to the robot's end-effector. After a thorough study of the technological solutions that could potentially solve this problem, ERS systems associating an IRED and a linear PSD appeared to be the most suitable solution therefore, allowing a very simple yet efficient implementation of such sensors.

To validate their interest and performances, a mathematical model and experimental characterization of such system was proposed. Radiometry concepts and geometrical elements of the ERS system were detailed in order to calculate the position of the light spot's center of gravity and the amount of radiant flux being received by the photodetector. Elements of conversion of power into photocurrent were also given and a test bench of a single ERS system was built and tested in two displacement tasks.

The similarity found between the calculated positions X_A and the measured values is particularly promising and the proposed displacement model worked particularly well at long distances. At shorter distances, however, we observe more difference between the

model and the experimental data. To improve these results, the ERS model should be improved, e.g. by better determining the position of the center of gravity of the light beam, taking into account the radiant intensity distribution inside it.

On the other hand, the evaluation of the total light intensity received by the PSD seems sufficient in practice to estimate at what distances the IRED could saturate or not sufficiently illuminate the PSD.

It is worth noting that the use of our test bench requires long and tedious manual manipulations to change the position of the light source and report the results in tables. Another point of improvement would be to build an automated test bench to extend the case study range.

4.8 Chapter conclusion

The present chapter provided a contribution to the design of a 6DoF contactless tracking system for an IC-HI allowing tool interaction.

We first showed that, while sharing several requirements with general VR trackers (e.g. robust 6 DoF tracking at a high frequency), an IC-HI tracking system has also specific design drivers. As an example, while VR trackers raise the major challenge of non-invasive position measurement of different body parts in an unlimited workspace, usually using external sensors, a local tracking system is better suited for the later which requires only a small workspace with however a higher accuracy. Also, a tool-based IC-HI tolerates that the target is equipped with sensor parts (i.e. emitters or receptors). These considerations allowed us introduce the design drivers of an IC-HI device (required measuring range, working frequency, precision and size).

Then we made a thorough review of the technological solutions that could fit these requirements. We first considered existing integrated tracking systems and showed that none of them is suitable off the shelf. As a consequence, we proposed to develop a custom designed solution. To this end, elementary sensors were presented in terms of their working principle and technical characteristics. Conclusions for each type of technology were given with a particular focus on their ability to comply with the searched values of the design drivers. Emitter-Receptor-Slit (ERS) system composed of an IRED illuminating a linear PSD through a thin and narrow slit appeared to be the most suitable solution therefore.

Thus we developed a mathematical model of such an ERS and made its preliminary characterization using an experimental test bench. Our results proved that our model allows to efficiently predict both the position of the light spot and the total generated photocurrent. While it would still be interesting to extend the characterization of such 1DoF sensor, we can conclude that such ERS system is a promising solution for the construction of a 6DoF IC-HI tracking module.

It will however be required therefore to invert the relationship between the position of the source and the position of the spot. Our aim in the future is to do so in order to allow computing the equation of the plane, in which the source lies, from the sensor's response. This will give the opportunity to compute the 3D position of a source (assumed to be punctual) by repeating this operation with three different ERS systems, the source being at the intersection of the three planes. By doing so for at least 3 IREDs mounted on the handle, it will be possible to get the later's full configuration in space.

The second part of our model (allowing to compute the theoretical limits of the workspace in which the source can move) will be particularly useful when designing and optimizing such a 3DoF or 6DoF sensor as it will allow to verify that for any possible handle configuration no sensor is insufficiently illuminated nor saturated.

General Conclusion and Perspectives

General Conclusion

Force feedback interfaces are robotic systems allowing natural motion interactions with virtual or remote environments. They are employed in several domains such as remote handling, manufacturing, entertainment, education, medicine and rehabilitation, just to mention the most popular. In virtual reality applications, the user typically holds a handle that is mechanically linked to the end-effector of the robot. This link has a non-negligible influence since the presence of the robot can be felt even in free space, decreasing the realism of the interaction.

Intermittent contact haptic interfaces are a promising technological development aiming to cope with this issue. These interfaces track and closely follow (without contact) the user movements in free space and come to his/her contact only when force feedback is required. This way IC haptic interfaces aim to provide more realistic interactions with virtual environments.

Their design and objective evaluation are however particularly complex and there are still challenges to be met. It was then considered important to focus our research in three directions:

1. evaluation of the benefits of the IC paradigm compared to classical haptic interfaces: this research was based on the use of an existing 2DoF device providing finger interactions,
2. improvement of the performances of IC haptic interfaces for force rendering at high speeds: this activity was supported by the same 2DoF device, and
3. the extension of the IC paradigm to provide tool-based interactions in 6DoF: this development relied on a 1DoF prototype.

The main results of our work are the following.

The evaluation of the benefits of the IC paradigm was performed through three experiments: stiffness identification, target pointing and blind obstacle detection. Two kinds of criteria were taken into account for comparing IC and classical haptic interfaces: on one

hand quantitative data informing on the quality of the force rendering and on the other hand qualitative elements allowing to take into account the perception of the users. This research was based on the use of an existing 2DoF device providing finger interactions. The performed psychophysical tests showed that human operators managed to perform the proposed elementary virtual reality tasks with an IC device as efficiently as with a CC device. This is particularly encouraging taking into account that learning to manipulate the IC interface was not straightforward.

The same IC device was also tested under a different free space to contact transition strategy intended to improve its performances, and in particular to enlarge its capability to approach virtual objects at high speeds. Indeed it was found that the quality of the force rendering relies on an adequate free space to contact transition at adapted speeds, then on the ability of the device to display mechanical properties corresponding to different virtual objects. The former is of a particular importance since the interface should be completely stabilized when the user touches it, giving the impression to touch a static object. With the existing control schemes however, this is the case only at relatively low speeds. The new solution we proposed is intended to cope with this issue. In this approach, we exploit the time taken just before contact by the finger to travel the existing gap between the user's finger and the IC end-effector to apply a purely dissipative force on the device. This way the kinetic energy of the robot is reduced before the user's finger touches it and the user encounters a quasistatic interface. The stabilization stage avoids transmitting to the user unexpected jerks. The experiments performed to validate this approach showed that the contact sensation was perceived as more natural with the new control scheme at high speeds (0.4m/s in the present work). Furthermore, the visuo-haptic delay remained lower than 40ms, i.e. it was imperceptible.

Finally, the main design specifications (range of measurement, accuracy, size and working frequency) of the tracking system of a 6DoF IC haptic interface aiming to provide tool interactions were explained. Available tracking systems and non-contact sensing technologies were explored and their pertinence regarding the targeted application (development of a 6DoF IC traking system) was discussed. Finally, a 1DoF IC tracking sensor (called ERS system which stands for Emitter-Receptor-Slit) based on a linear position sensitive detector, a slit and an infrared LED was introduced and modeled. Preliminary measurements allowed us to validate this model and to conclude that such ERS system is a promising solution for the construction of a 6DoF IC-HI tracking module.

Short Term Perspectives

The short term perspectives provided here concern the development of the 6DoF IC interface tracking system. These perspectives are:

- To develop an automated test bench for the 1DoF IC tracking system in order to

exhaustively characterize its response, i.e. correlate the displacements of the light source with the sensor position measurements and the total generated photocurrent.

- To employ the existing ERS simulator to find a direct model (i.e. allowing to compute the response of the sensor knowing the position of the source) that is the closest possible to the real behavior of the system.
- To inverse this relation in order to get a useful inverse model allowing to compute the equation of the plane in which the source lies based on the generated photocurrents of the sensor.
- To simulate a sensor composed of n ERS systems in order to find a pertinent arrangement allowing to obtain a transformation matrix connecting the sensor readings to the coordinates of a 3D point or directly to a 6DoF information.
- To perform simulations to optimize the sensing space based on the targeted volume.
- To perform the housing design and electronic integration of sensors as well as light sources on a handle.
- To perform its integration on the end-effector of a robot.
- To design the tracking control strategy in 3DoF and 6DoF.

Long Term Perspectives

The long term perspectives assume the existence of a 6DoF tracking system. The proposed perspectives are the following:

- To develop a 3DoF force feedback system with embedded 3DoF tracking system.
- To develop of a 6DoF force feedback system able to track and constraint the tool in 6DoF.
- To perform its integration on the end-effector of a robot.
- To design the free space to contact control strategy in 3DoF and 6DoF.
- To perform psychophysical evaluations as detailed in the present report but employing a robot with low mechanical transparency.

Author's publications

- Oscar De La Cruz Fierro, Wael Bachta, Florian Gosselin, Guillaume Morel. A New Control Strategy for the Improvement of Contact Rendering with Encounter-type Haptic Displays. *In Proceedings of the 14th International Conference on Informatics in Control, Automation and Robotics (ICINCO)*, 2017.
- Oscar De La Cruz, Florian Gosselin, Wael Bachta, Guillaume Morel. Contributions to the Design of a 6 DoF Contactless Sensor Intended for Intermittent Contact Haptic Interfaces. *In Proceedings of the 3rd International Conference on Advanced Robotics and Mechatronics (ICARM)*, 2018. *Best Conference Paper Award.*

Bibliography

[3D Systems, 2018] 3D Systems (2018). Touch haptic device. https://www.3dsystems.com/haptics-devices/touch. [Online accessed: 30-July-2018].

[Achhammer et al., 2010] Achhammer, A., Weber, C., Peer, A., and Buss, M. (2010). Improvement of model-mediated teleoperation using a new hybrid environment estimation technique. In *IEEE International Conference on Robotics and Automation (ICRA)*, pages 5358–5363.

[Advanced Scientific Concepts Inc., 2018] Advanced Scientific Concepts Inc. (2018). Products. http://www.advancedscientificconcepts.com/index.html. [Online accessed: 16-October-2018].

[Aggarwal and Ara, 2009] Aggarwal, R. and Ara, D. (2009). From scalpel to simulator: A surgical journey. *Surgery*, 145(1):1–4.

[Alfaraj, 2017] Alfaraj, N. (2017). A review of charge-coupled device image sensors. Technical report.

[Arbind, 2017] Arbind, M. (2017). Photodiode. *The Himalayan Physics*, 4(4).

[Avizzano et al., 2002] Avizzano, C. A., Solis, J., Frisoli, A., and Bergamasco, M. (2002). Motor learning skill experiments using haptic interface capabilities. In *Proceedings of the IEEE International Workshop on Robot and Human Interactive Communication Proceedings*, pages 198–203.

[Azuma and Ward, 1991] Azuma, R. and Ward, M. (1991). Space Resection by Collinearity: Mathematics Behind the Optical Ceiling Head-Tracker. Technical report, University of North Carolina at Chapel Hill.

[Basdogan et al., 2000] Basdogan, C., Ho, C.-H., Srinivasan, M. A., and Slater, M. (2000). An Experimental Study on the Role of Touch in Shared Virtual Environments. *ACM Trans. Comput.-Hum. Interact.*, 7(4):443–460.

[Bergamasco, 1995] Bergamasco, M. (1995). Haptic interfaces: the study of force and tactile feedback systems. In *Proceedings of the IEEE International Workshop on Robot and Human Communication*, pages 15–20.

[Berkelman, 1999] Berkelman, P. (1999). *Tool-Based Haptic Interaction with Dynamic Physical Simulations using Lorentz Magnetic Levitation*. PhD dissertation, Carnegie Mellon University.

[Bigas et al., 2006] Bigas, M., Cabruja, E., Forest, J., and Salvi, J. (2006). Review of cmos image sensors. *Microelectronics Journal*, 37:433–451.

[Bolopion and Régnier, 2013] Bolopion, A. and Régnier, S. (2013). A review of haptic feedback teleoperation systems for micromanipulation and microassembly. *IEEE Transactions on Automation Science and Engineering*, 10(3):496–502.

[Borro et al., 2004] Borro, D., Savall, J., Amundarain, A., Gil, J. J., Garcia-Alonso, A., and Matey, L. (2004). A large haptic device for aircraft engine maintainability. *IEEE Computer Graphics and Applications*, 24(6):70–74.

[Bowyer et al., 2014] Bowyer, S. A., Davies, B. L., and Baena, F. R. y. (2014). Active constraints/virtual fixtures: A survey. *IEEE Transactions on Robotics*, 30(1):138–157.

[Brooks et al., 1990] Brooks, Jr., F. P., Ouh-Young, M., Batter, J. J., and Jerome Kilpatrick, P. (1990). Project gropehaptic displays for scientific visualization. In *Proceedings of the Annual Conference on Computer Graphics and Interactive Techniques*, SIGGRAPH '90, pages 177–185. ACM.

[Bruce et al., 2014] Bruce, V., Georgeson, M. A., and Green, P. R. (2014). *Visual Perception: Physiology, Psychology and Ecology*. Psychology Press.

[Burdea, 2008] Burdea, G. C. (2008). The role of haptics in physical rehabilitation.

[Campion, 2011] Campion, G. (2011). Literature Review. In *The Synthesis of Three Dimensional Haptic Textures: Geometry, Control, and Psychophysics*, Springer Series on Touch and Haptic Systems, pages 7–44. Springer London.

[Chabrier, 2018] Chabrier, A. (2018). *Étude théorique et expérimentale d'une interface à retour d'effort augmenté*. PhD dissertation, Sorbonne Université.

[Chabrier et al., 2017] Chabrier, A., Gonzalez, F., Gosselin, F., and Bachta, W. (2017). Design and experimental evaluation of an infrared instrumentation for haptic interfaces. In *Proceedings of the IEEE International Instrumentation and Measurement Technology Conference*, pages 1–6.

[Chun et al., 2004] Chun, K., Verplank, B., Barbagli, F., and Salisbury, K. (2004). Evaluating haptics and 3d stereo displays using Fitts' law. In *Proceedings of the International Conference on Creating, Connecting and Collaborating through Computing*, pages 53–58.

[Clarke and Braginski, 2005] Clarke, J. and Braginski, A. I. (2005). Introduction. In Clarke, J. and Braginski, A. I., editors, *The SQUID Handbook*, pages 2–28. Wiley-Blackwell.

[Clarte, 2018] Clarte (2018). Lobbybot. https://www.clarte-lab.fr/projets/tous-nos-projets/15-lobbybot. [Online accessed: 01-August-2018].

[Couroussé, 2007] Couroussé, D. (2007). Mechanical impedance. In *Enaction and Enactive Interfaces : A Handbook of terms*, number <hal-00978979>, pages 194–196.

[Desa et al., 2009] Desa, H., Sofian, M., and Azfar, A. (2009). Study of inertial measurement unit sensor. In *Proceedings of the International Conference on Man-Machine Systems*.

[De La Cruz et al., 2018] De La Cruz, O., Gosselin, F., Bachta, W., and Morel, G. (2018). Contributions to the Design of a 6DoF Contactless Sensor Intended for Intermittent Contact Haptic Interfaces. In *Proceedings of the IEEE International Conference on Advanced and Robotics and Mechatronics*.

[Dhiraj, 2012] Dhiraj, A. (2012). Optical sensors and their applications. *Journal of Scientific Research and Reviews*, 1(5):60–68.

[Diallo, 2014] Diallo, D. (2014). Développement d'un Capteur 6D de Suivi de Position et d'Orientation pour une Interface Haptique à Contacts Intermittents. Rapport de stage.

[Diaz et al., 2010] Diaz, I., Gil, J. J., and Hulin, T. (2010). Stability Boundary and Transparency for Haptic Rendering. In *Advances in Haptics*, pages 103–125.

[Drung et al., 2007] Drung, D., Abmann, C., Beyer, J., Kirste, A., Peters, M., Ruede, F., and Schurig, T. (2007). Highly Sensitive and Easy-to-Use SQUID Sensors. *IEEE Transactions on Applied Superconductivity*, 17(2):699–704.

[Elgammal and Lee, 2009] Elgammal, A. and Lee, C.-S. (2009). Tracking people on a torus. *IEEE transactions on pattern analysis and machine intelligence*, 31(3).

[Elgendi et al., 2012a] Elgendi, M., Picon, F., and Magnenat-Thalmann, N. (2012a). Real-Time Speed Detection of Hand Gesture using Kinect.

[Elgendi et al., 2012b] Elgendi, M., Picon, F., and Thalmann, N. (2012b). Real-time speed detection of hand gesture using kinect. In *Proceedings of the Workshop on Autonomous Social Robots and Virtual Humans, Annual Conference on Computer Animation and Social Agents*.

[Farnell, 2018] Farnell (2018). Capteurs à ultrasons. https://fr.farnell.com/. [Online accessed: 27-September-2018].

[Field et al., 2011] Field, M., Pan, Z., Stirling, D., and Naghdy, F. (2011). Human motion capture sensors and analysis in robotics. *Industrial Robot: An International Journal*, 38:163–171.

[Filippeschi et al., 2017] Filippeschi, A., Schmitz, N., Miezal, M., Bleser, G., Ruffaldi, E., and Stricker, D. (2017). Survey of Motion Tracking Methods Based on Inertial Sensors: A Focus on Upper Limb Human Motion. *Sensors (Basel, Switzerland)*, 17(6).

[Force Dimension, 2018] Force Dimension (2018). sigma.7. http://www.forcedimension.com/products/sigma-7/overview. [Online accessed: 30-July-2018].

[Forrest et al., 2009] Forrest, N., Baillie, S., and Tan, H. Z. (2009). Haptic stiffness identification by veterinarians and novices: A comparison. In *Proceedings of the EuroHaptics Conference, and Symposium on Haptic Interfaces for Virtual Environment and Teleoperator Systems*, pages 646–651.

[Geng, 2011] Geng, J. (2011). Structured-light 3d surface imaging: a tutorial. *Advances in Optics and Photonics*, 3(2):128–160.

[Gescheider, 2013] Gescheider, G. A. (2013). *Psychophysics: The Fundamentals*. Psychology Press.

[Gonzalez, 2015] Gonzalez, F. (2015). *Contributions au développement d'une interface haptique à contacts intermittents*. PhD dissertation, Université Pierre et Marie Curie - Paris VI.

[Gonzalez et al., 2015] Gonzalez, F., Bachta, W., and Gosselin, F. (2015). Smooth transition-based control of encounter-type haptic devices. In *Proceedings of the IEEE International Conference on Robotics and Automation*, pages 291–297.

[Gosselin et al., 2013] Gosselin, F., Bouchigny, S., Mégard, C., Taha, F., Delcampe, P., and d'Hauthuille, C. (2013). Haptic systems for training sensorimotor skills: A use case in surgery. *Robotics and Autonomous Systems*, 61(4):380–389.

[Gosselin et al., 2011] Gosselin, F., Ferlay, F., Bouchigny, S., Mégard, C., and Taha, F. (2011). Specification and design of a new haptic interface for maxillo facial surgery. In *2011 IEEE International Conference on Robotics and Automation*, pages 737–744.

[Gosselin and Louveau, 2010] Gosselin, F. and Louveau, P. (2010). *Proces verbal de recette: Virtuose 6D Médical EVO II*. CEA, LIST.

[Grenier, 1991] Grenier, T. M. (1991). Hand anthropometry of u.s. army personnel. Technical report. AD-A244533.

[Gueuning et al., 1996] Gueuning, F., Varlan, M., Eugene, C., and Dupuis, P. (1996). Accurate distance measurement by an autonomous ultrasonic system combining time-of-flight and phase-shift methods. In *Quality Measurement: The Indispensable Bridge between Theory and Reality (No Measurements? No Science! Joint Conference - 1996: IEEE Instrumentation and Measurement Technology Conference and IMEKO Tec*, pages 399–404 vol.1.

[Hamamatsu, 2007] Hamamatsu (2007). *Photomultiplier Tubes, Basics and Applications*. 3 edition.

[Hamamatsu, 2014] Hamamatsu (2014). "si photodiodes" in Opto-semiconductor Handbook.

[Hamamatsu, 2016] Hamamatsu (2016). Photomultiplier tubes and related products. https://www.hamamatsu.com/eu/en/product/optical-sensors/pmt/catalog/index.html. [Online accessed: 23-November-2018].

[Hannaford and Okamura, 2016] Hannaford, B. and Okamura, A. M. (2016). Haptics. In Siciliano, B. and Khatib, O., editors, *Handbook of Robotics*, pages 1063–1083. Springer Berlin Heidelberg.

[Haption, 2018] Haption (2018). Virtuose 6d. https://www.haption.com/fr/products-fr/virtuose-6d-fr.html. [Online accessed: 30-July-2018].

[Hassan et al., 2010] Hassan, A. H., Al-Fraidi, A. A., and Al-Saeed, S. H. (2010). Corticotomy-Assisted Orthodontic Treatment: Review. *The Open Dentistry Journal*, 4:159–164.

[Hatzfeld and Kern, 2009] Hatzfeld, C. and Kern, T. A. (2009). *Engineering Haptic Devices: A Beginner's Guide*. Springer Series on Touch and Haptic Systems. Springer-Verlag, 2 edition.

[Haus, 2012] Haus, J. (2012). Optical Sensors: Basics and Applications. *Contemporary Physics*, 53(1).

[Havig et al., 2011] Havig, P., McIntire, J., and Geiselman, E. (2011). Virtual reality in a cave: Limitations and the need for hmds. In *Proceedings of the SPIE-The International Society for Optical Engineering*.

[Hayward and Maclean, 2007] Hayward, V. and Maclean, K. E. (2007). Do it yourself haptics: part i. *IEEE Robotics Automation Magazine*, 14(4):88–104.

[Hirota and Hirose, 1993] Hirota, K. and Hirose, M. (1993). Development of surface display. In *Proceedings of the IEEE Virtual Reality Annual International Symposium*, pages 256–262.

[Hirzinger, 1999] Hirzinger, G. (1999). Intuitive Robot Motion Control - The SPACE MOUSE Story. *Journal of the Robotics Society of Japan*, 17(2):175–179.

[Honeywell, 2018a] Honeywell (2018a). Hall Effect Sensing and Applications. https://sensing.honeywell.com/hallbook.pdf. [Online accessed: 19-September-2018].

[Honeywell, 2018b] Honeywell (2018b). Inertial Measurement Units. https://sensing.honeywell.com/sensors. [Online accessed: 28-October-2018].

[Honeywell, 2018c] Honeywell (2018c). Linear Hall-effect Sensors ICs. https://sensing.honeywell.com/sensors/linear-and-angle-sensor-ics. [Online accessed: 22-October-2018].

[Horaud et al., 2016] Horaud, R., Hansard, M., Evangelidis, G., and Ménier, C. (2016). An overview of depth cameras and range scanners based on time-of-flight technologies. *Machine Vision and Applications*, 27(7):1005–1020.

[Janin et al., 1995] Janin, A. L., Zikan, K., Mizell, D., Banner, M., and Sowizral, H. A. (1995). Videometric head tracker for augmented reality applications. In *Telemanipulator and Telepresence Technologies*, volume 2351, pages 308–316. International Society for Optics and Photonics.

[Jogschies et al., 2015] Jogschies, L., Klaas, D., Kruppe, R., Rittinger, J., Taptimthong, P., Wienecke, A., Rissing, L., Wurz, M., Jogschies, L., Klaas, D., Kruppe, R., Rittinger, J., Taptimthong, P., Wienecke, A., Rissing, L., and Wurz, M. C. (2015). Recent Developments of Magnetoresistive Sensors for Industrial Applications. *Sensors*, 15(11):28665–28689.

[Jubien, 2014] Jubien, A. (2014). *Identification dynamique des robots à flexibilités articulaires*. PhD dissertation, Université de Nantes.

[Keller, 2018] Keller, P. (2018). Technologies for Precision Magnetic Field Maping. https://www.metrolab.com/resources/downloads/. [Online accessed: 22-October-2018].

[Khadjavi, 1968] Khadjavi, A. (1968). Calculation of solid angle subtended by rectangular apertures. *Journal of the Optical Society of America*, 58(10):1417–1418.

[Kirkpatrick and Douglas, 2002] Kirkpatrick, A. E. and Douglas, S. A. (2002). Application-based evaluation of haptic interfaces. In *Proceedings of the Symposium on Haptic Interfaces for Virtual Environment and Teleoperator Systems*, pages 32–39.

[Knorlein et al., 2009] Knorlein, B., Di Luca, M., and Harders, M. (2009). Influence of Visual and Haptic Delays on Stiffness Perception in Augmented Reality. In *Proceedings of the 2009 8th IEEE International Symposium on Mixed and Augmented Reality*, pages 49–52.

[Lawrence et al., 2000] Lawrence, D. A., Pao, L. Y., Dougherty, A. M., Salada, M. A., and Pavlou, Y. (2000). Rate-hardness: a new performance metric for haptic interfaces. *IEEE Transactions on Robotics and Automation*, 16(4):357–371.

[Lederman and Klatzky, 1990] Lederman, S. J. and Klatzky, R. L. (1990). Haptic exploration and object representation. In Godale, M. A., editor, *Vision and action : The control of grasping*, pages 98–109. New Jersey: Ablex.

[Lenz and Edelstein, 2006] Lenz, J. and Edelstein, S. (2006). Magnetic sensors and their applications. *IEEE Sensors Journal*, 6(3):631–649.

[Li et al., 2008] Li, W., Zhang, Z., and Liu, Z. (2008). Expandable Data-Driven Graphical Modeling of Human Actions Based on Salient Postures. *IEEE Transactions on Circuits and Systems for Video Technology*, 18(11):1499–1510.

[M. and Taylor, 2005] M., R. and Taylor, I. (2005). Haptics for scientific visualization.

[MacKenzie, 1995] MacKenzie, I. S. (1995). Human-computer Interaction. pages 483–492. Morgan Kaufmann Publishers Inc.

[Mathar, 2015] Mathar, R., J. (2015). Solid angle of a rectangular plate. http://www.mpia.de/~mathar/public/mathar20051002.pdf. [Online accessed: 10-October-2018].

[MaxBotix, 2018] MaxBotix (2018). Innovative ultrasonic sensors. https://www.maxbotix.com/. [Online accessed: 21-October-2018].

[McNeely, 1993] McNeely, W. A. (1993). Robotic graphics: a new approach to force feedback for virtual reality. In *Proceedings of the IEEE Virtual Reality Annual International Symposium*, pages 336–341.

[Mestre, 2015] Mestre, D. R. (2015). Immersion and presence.

[Mestre, 2017] Mestre, D. R. (2017). Cave versus head-mounted displays: Ongoing thoughts. *Electronic Imaging*, 2017(3):31–35.

[Micro-Epsilon, 2018] Micro-Epsilon (2018). Laser triangulation sensors. https://www.micro-epsilon.fr/. [Online accessed: 16-October-2018].

[MicroSense, 2018] MicroSense (2018). Understanding capacitive position sensors. http://www.microsense.net. [Online accessed: 28-September-2018].

[Mihelj et al., 2014] Mihelj, M., Novak, D., and Beguš, S. (2014). *Virtual Reality Technology and Applications*. Intelligent Systems, Control and Automation: Science and Engineering. Springer Netherlands.

[MOOG, 2018] MOOG (2018). Desktop haptic interface. http://www.moog.com/products/haptics-robotics/. [Online accessed: 30-July-2018].

[MPB Technologies Inc., 2018a] MPB Technologies Inc. (2018a). Freedom 6s. http://www.mpb-technologies.ca/mpbt/mpbt_web_2009/_en/6dof/index.html. [Online accessed: 30-July-2018].

[MPB Technologies Inc., 2018b] MPB Technologies Inc. (2018b). How do you Choose a Haptic Device? http://www.mpb-technologies.ca/mpbt/mpbt_web_2009/_en/resources/articles/How%20do%20you%20choose%20a%20haptic%20device.pdf. [Online accessed: 25-October-2018].

[Nagasaki, 1989] Nagasaki, H. (1989). Asymmetric velocity and acceleration profiles of human arm movements. *Experimental Brain Research*, 74(2):319–326.

[Oakley et al., 2000] Oakley, I., McGee, M. R., Brewster, S., and Gray, P. (2000). Putting the Feel in 'Look and Feel'. In *Proceedings of the SIGCHI Conference on Human Factors in Computing Systems*, pages 415–422.

[Okamura, 2009] Okamura, A. M. (2009). Haptic feedback in robot-assisted minimally invasive surgery. *Current opinion in urology*, 19(1):102–107.

[Orozco et al., 2012] Orozco, M., Silva, J., El Saddik, A., and Petriu, E. (2012). The role of haptics in games. In El Saddik, A., editor, *Haptics Rendering and Applications*, chapter 11, pages 217–234. InTech.

[Palluel-Germain et al., 2007] Palluel-Germain, R., Bara, F., Boisferon, A. H. d., Hennion, B., Gouagout, P., and Gentaz, E. (2007). A visuo-haptic device - telemaque - increases kindergarten children's handwriting acquisition. In *Second Joint EuroHaptics Conference and Symposium on Haptic Interfaces for Virtual Environment and Teleoperator Systems*, pages 72–77.

[Passaro et al., 2017] Passaro, V. M. N., Cuccovillo, A., Vaiani, L., De Carlo, M., and Campanella, C. E. (2017). Gyroscope Technology and Applications: A Review in the Industrial Perspective. *Sensors (Basel, Switzerland)*, 17(10).

[Polhemus Inovation in Motion, 2018] Polhemus Inovation in Motion (2018). Motion tracking/all trackers. https://polhemus.com/motion-tracking/all-trackers/. [Online accessed: 16-October-2018].

[Primdahl, 1979] Primdahl, F. (1979). The fluxgate magnetometer. *Journal of Physics E: Scientific Instruments*, 12(4):241.

[Puangmali et al., 2008] Puangmali, P., Althoefer, K., Seneviratne, L. D., Murphy, D., and Dasgupta, P. (2008). State-of-the-art in force and tactile sensing for minimally invasive surgery. *IEEE Sensors Journal*, 8(4):371–381.

[Quanser Inc., 2018] Quanser Inc. (2018). High definition haptic device. https://www.quanser.com/products/hd2-high-definition-haptic-device/. [Online accessed: 30-July-2018].

[Reiner, 2004] Reiner, M. (2004). The role of haptics in immersive telecommunication environments. *IEEE Transactions on Circuits and Systems for Video Technology*, 14(3):392–401.

[Robles-De-La-Torre, 2006] Robles-De-La-Torre, G. (2006). The importance of the sense of touch in virtual and real environments. *IEEE MultiMedia*, 13(3):24–30.

[Rolland et al., 1999] Rolland, J. P., Baillot, Y., and Goon, A. A. (1999). A Survey of Tracking Technology for Virtual Environments.

[RS Components, 2018] RS Components (2018). Capteurs de proximité capacitifs. https://fr.rs-online.com/web/. [Online accessed: 29-September-2018].

[Ryer, 1997] Ryer, A. (1997). *Light Measurement Handbook*. International Light Inc.

[S. Huang et al., 2002] S. Huang, S., F. Huang, C., N. Huang, K., and S. Young, M. (2002). A high accuracy ultrasonic distance measurement system using binary frequency shift-keyed signal and phase detection. 73(10).

[Sagardia et al., 2015] Sagardia, M., Hertkorn, K., Hulin, T., Schätzle, S., Wolff, R., Hummel, J., Dodiya, J., and Gerndt, A. (2015). Vr-oos: The dlr's virtual reality simulator for telerobotic on-orbit servicing with haptic feedback. In *IEEE Aerospace Conference*, pages 1–17.

[Salisbury et al., 2004] Salisbury, K., Conti, F., and Barbagli, F. (2004). Haptic rendering: introductory concepts. *IEEE Computer Graphics and Applications*, 24(2):24–32.

[Samur, 2012] Samur, E. (2012). *Performance Metrics for Haptic Interfaces*. Springer Series on Touch and Haptic Systems. Springer-Verlag.

[Samur et al., 2007] Samur, E., Wang, F., Spaelter, U., and Bleuler, H. (2007). Generic and systematic evaluation of haptic interfaces based on testbeds. In *Proceedings of the IEEE/RSJ International Conference on Intelligent Robots and Systems*, pages 2113–2119.

[Sankaranarayanan et al., 2003] Sankaranarayanan, G., Weghorst, S., Sanner, M., Gillet, A., and Olson, A. (2003). Role of haptics in teaching structural molecular biology. In *Proceedings of the 11th Symposium on Haptic Interfaces for Virtual Environment and Teleoperator Systems*, pages 363–366.

[Shamir, 2006] Shamir, A. (2006). An overview of Optical Gyroscopes Theory , Practical Aspects , Applications and Future Trends. Technical report.

[Sherman and Craig, 2003] Sherman, W. R. and Craig, A. B. (2003). Chapter 1 - introduction to virtual reality. In Sherman, W. R. and Craig, A. B., editors, *Understanding Virtual Reality*, The Morgan Kaufmann Series in Computer Graphics, pages 5 – 37. Morgan Kaufmann.

[Shon et al., 2007] Shon, A. P., Storz, J. J., and Rao, R. P. N. (2007). Towards a Real-Time Bayesian Imitation System for a Humanoid Robot. In *Proceedings of the IEEE International Conference on Robotics and Automation*, pages 2847–2852.

[Sigal et al., 2009] Sigal, L., Balan, A. O., and Black, M. J. (2009). HumanEva: Synchronized Video and Motion Capture Dataset and Baseline Algorithm for Evaluation of Articulated Human Motion. *International Journal of Computer Vision*, 87(1):4–27.

[Sony, 2018] Sony (2018). Sony Depth Sensing Solutions. https://www.sony-depthsensing.com/. [Online accessed: 16-October-2018].

[ST Microelectronics, 2016] ST Microelectronics (2016). Vl6180x proximity and ambient light sensing (ALS) module, Docid026171 Rev 7. [Online accessed: 18-February-2019].

[Tachi et al., 1994] Tachi, S., Maeda, T., Hirata, R., and Hoshino, H. (1994). A construction method of virtual haptic space. In *Proceedings of the International Conference on Artificial Reality and Tele-Existence*, pages 131–138.

[Tamar and Neville, 1985] Tamar, F. and Neville, H. (1985). The Coordination of Arm Movements: An Experimentally Confirmed Mathematical Model. *The Journal of Neuroscience*, 5:1688–1703.

[Terzic et al., 2012] Terzic, E., Terzic, J., Nagarajah, R., and Alamgir, M. (2012). Capacitive Sensing Technology. In Terzic, E., Terzic, J., Nagarajah, R., and Alamgir, M., editors, *A Neural Network Approach to Fluid Quantity Measurement in Dynamic Environments*, pages 11–37. Springer London.

[TE Connectivity Sensors, 2018a] TE Connectivity Sensors (2018a). Basics of Magnetoresistive (MR) Sensors. https://www.te.com/content/dam/te-com/documents/sensors/global/basics-magnetoresistive-mr-sensors-white-paper.pdf. [Online accessed: 22-October-2018].

[TE Connectivity Sensors, 2018b] TE Connectivity Sensors (2018b). KMT37 Magnetic Angle Sensor. https://www.te.com/usa-en/home.html. [Online accessed: 22-October-2018].

[TE Connectivity Sensors, 2018c] TE Connectivity Sensors (2018c). KMXP Series - AMR Linear Position Sensors. https://www.te.com/usa-en/home.html. [Online accessed: 22-October-2018].

[Texas Instruments, 2018] Texas Instruments (2018). Drv425 integrated fluxgate magnetic sensor ic for open-loop applications. http://www.ti.com. [Online accessed: 22-October-2018].

[Titus et al., 2011] Titus, A. H., Cheung, M. C.-K., and Chodavarapu, V. P. (2011). Cmos photodetectors. In Park, J.-W., editor, *Photodiodes*, chapter 4. IntechOpen.

[Tumanski, 2013] Tumanski, S. (2013). Modern magnetic field sensors - a review. In *International Symposium on Electromagnetic Fields*.

[Unger et al., 2001] Unger, B. J., Nicolaidis, A., Berkelman, P. J., Thompson, A., Klatzky, R. L., and Hollis, R. L. (2001). Comparison of 3-D haptic peg-in-hole tasks in real and virtual environments. In *Proceedings of the 2001 IEEE/RSJ International Conference on Intelligent Robots and Systems*, pages 1751–1756.

[Velodyne, 2018] Velodyne (2018). Products. https://www.velodynelidar.com/. [Online accessed: 16-October-2018].

[Vogels, 2004] Vogels, I. M. L. C. (2004). Detection of temporal delays in visual-haptic interfaces. *Human Factors*, 46(1):118–134.

[Welch et al., 2001] Welch, G., Bishop, G., Vicci, L., Brumback, S., Keller, K., and Colucci, D. (2001). High-Performance Wide-Area Optical Tracking: The HiBall Tracking System. *Presence*, 10(1):1–21.

[Westebring et al., 2008] Westebring, E., Goossens, R., Jakimowicz, J., and Dankelman, J. (2008). Haptics in minimally invasive surgery - a review. *Minimally invasive therapy & allied technologies : MITAT : official journal of the Society for Minimally Invasive Therapy*, 17:3–16.

[Woltring, 1975] Woltring, H. J. (1975). Single- and dual-axis lateral photodetectors of rectangular shape. *IEEE Transactions on Electron Devices*, 22(8):581–590.

[Xia, 2016] Xia, P. (2016). Haptics for product design and manufacturing simulation. *IEEE Transactions on Haptics*, 9(3):358–375.

[XSens, 2018] XSens (2018). XSens Products. https://www.xsens.com/. [Online accessed: 28-October-2018].

[Yokokohji et al., 1996] Yokokohji, Y., Hollis, R. L., and Kanade, T. (1996). What you can see is what you can feel-development of a visual/haptic interface to virtual environment. In *Proceedings of the IEEE 1996 Virtual Reality Annual International Symposium*, pages 46–53.

[Yokokohji et al., 2001] Yokokohji, Y., Kinoshita, J., and Yoshikawa, T. (2001). Path planning for encountered-type haptic devices that render multiple objects in 3d space. In *Proceedings of the IEEE Virtual Reality Conference*, pages 271–278.

[Yokokohji et al., 1999] Yokokohji, Y., L. Hollis, R., and Kanade, T. (1999). WYSIWYF display: A visual/haptic interface to virtual environment. *Presence*, 8(4):412–434.

[Yokokohji et al., 2004] Yokokohji, Y., Muramori, N., Sato, Y., Kikura, T., and Yoshikawa, T. (2004). Design and path planning of an encountered-type haptic display for multiple fingertip contacts based on the observation of human grasping behavior. In *Proceedings of the IEEE International Conference on Robotics and Automation*, pages 1986–1991.

[Yoshikawa and Nagura, 1997] Yoshikawa, T. and Nagura, A. (1997). A touch and force display system for haptic interface. In *Proceedings of the IEEE International Conference on Robotics and Automation*, pages 3018–3024.

[Yoshikawa and Nagura, 1999] Yoshikawa, T. and Nagura, A. (1999). A three-dimensional touch/force display system for haptic interface. In *Proceedings of the IEEE International Conference on Robotics and Automation*, pages 2943–2951.

[Zhang et al., 2017] Zhang, H., Zhang, Y., Wang, D., and Lu, L. (2017). DentalTouch: A haptic display with high stiffness and low inertia. In *Proceedings of the IEEE World Haptics Conference*, pages 388–393.

Appendix A

Description of the 2DoF Intermittent Contact Haptic Interface

The robot used for the experiments presented in chapter 2 and chapter 3 is a 2 degrees of freedom close-tracking-type intermittent contact haptic interface (CT-HI).

It is composed of two links 0.25m long each (see Fig.A.1) actuated by two Maxon RE-35 DC motors and cable capstan reducers, allowing a particularly transparent behavior. 1000ppt encoders disposed on the motor's axes are used for position sensing and counterweights mounted on each axis allow gravity compensation.

Figure A.1: 2DoF Close-tracking haptic interface developed at CEA, LIST.

As described in [Gonzalez, 2015], it is equipped with a CT-HI, or IC-HI, ring-like end-effector. This ring has an inner diameter of 24mm, which allows a gap between a medium-sized index finger and the ring which is sufficient to track and follow this finger at medium speeds (i.e. theoretically up to 1.26m/s in flexion-extension and 0.26m/s in abduction-adduction) without user-robot collisions. Sixteen Vishay VCNL4000 infrared proximity sensors distributed over the inner side of the ring make possible the measurement of their distance from the finger's skin (a small diaphragm in front of each sensor's allows to focus the IR light which is emitted only in front of it, see Fig.A.2).

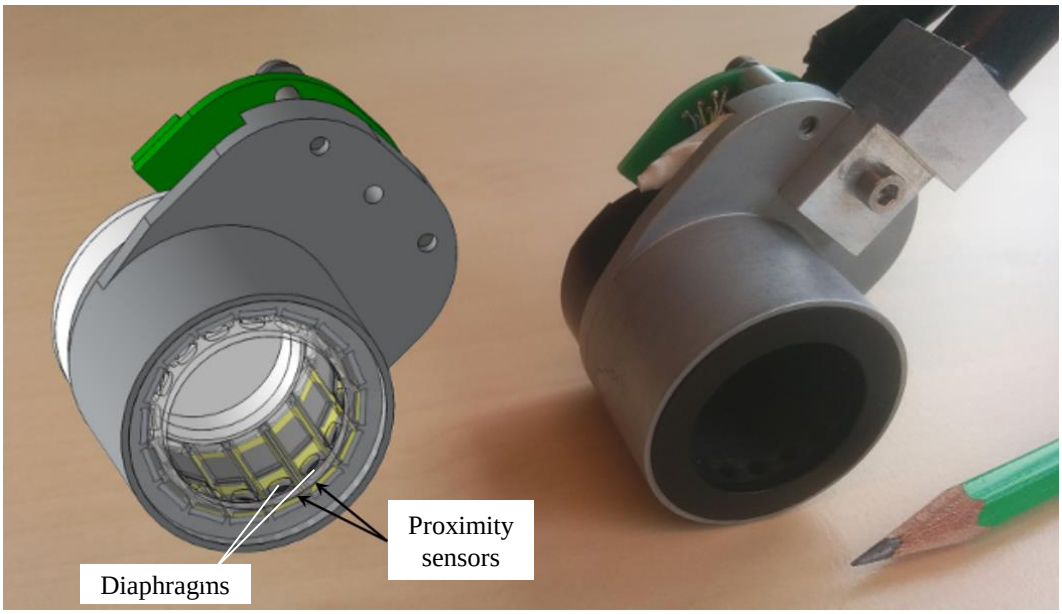

Figure A.2: Ring-like CT-HI end-effector (picture from [Gonzalez, 2015]).

ATMega328P microcontrollers retrieve and send proximity sensor measurements to the haptic interface controller trough a fast serial bus at a rate of 400kbps. Estimation of the finger's location is computed as the center of the polygon build from the measurements (see Fig.A.3).

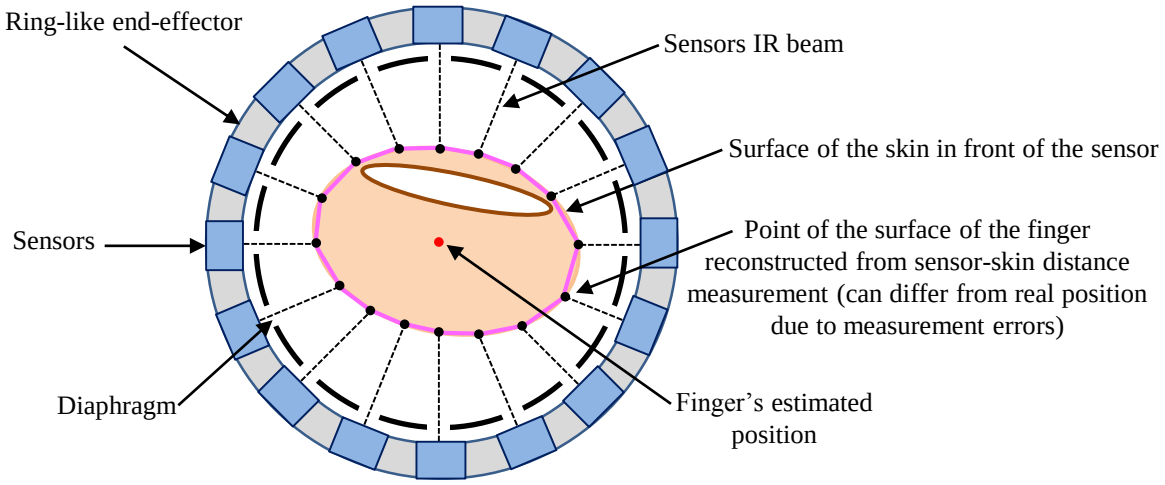

Figure A.3: Principle of operation of the finger's position measurement.

The controller is composed of a PC104 computer running Xenomai realtime operating system and a servo-drive controlling both motors. A telerobotics library acquires the state of the robot, computes the finger's position and sends the reference torques to the servo-drive at a rate of 1kHz to allow tracking of the user's finger. Rate mismatch between the control loop (1kHz) and the estimation of the finger's center (300Hz) is handled by a Kalman filter committed to extrapolate the finger's position.

Appendix B

Description of the 6DoF Non-contact Handle Tracking System Prototype Developed at CEA, LIST

CEA, LIST has developed a 6DoF tracking system prototype in 2014 [Diallo, 2014]. This system is composed of three 3DoF elements each composed of 3 elementary 1DoF sensors. Indeed an efficient solution to obtain the 6DoF pose of a target, in this case a handle, is to compute the position of at least three points laying on it, as usually done in IR based motion capture systems.

In the following sections we will present its principle of operation. We will first introduce the 1DoF sensor, then the concept of 3DoF sensors. Then the principle of the 6DoF tracking system will be explained. Finally technical specifications of the developed prototype will be provided.

B.1 1DoF Sensors

To design a multi-DoF position sensor, it was proposed in [Diallo, 2014] to rely on elementary angular sensors obtained by placing an IR light source over a slit projecting a light or shadow pattern on a linear optical sensor perpendicular to it (here an array of photodiodes, see Fig.B.1).

As it can be observed, the light emitted by the IR source, passing through the slit and hitting the sensor lies in a plane. The angle between this plane and the normal to the sensor can be computed from the measurement of the position of the generated light spot that hits the surface of the optical detector.

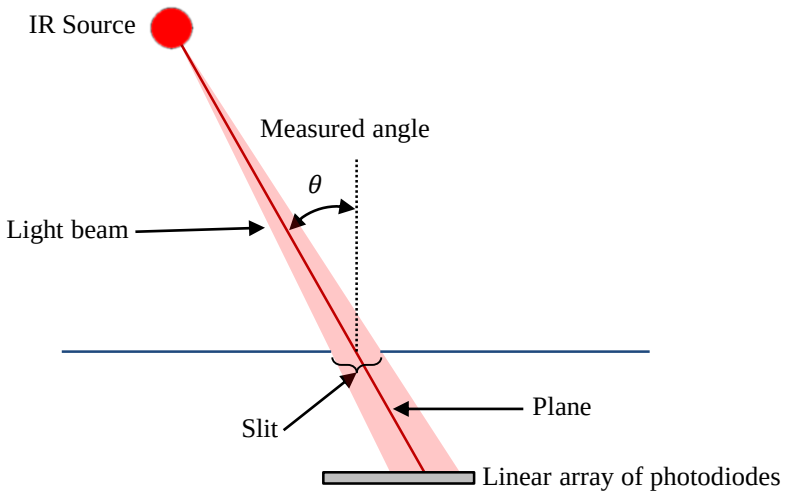

Figure B.1: Angular sensor elements.

B.2 3DoF Sensor principle

Based on the basic configuration presented in section B.1, a 3DoF sensor can easily be obtained by placing the same IR light source over a set of three linear optical sensors, disposed below three slits perpendicularly to them (see Fig.B.2). Each angular sensor provides then information allowing to define the coordinates of a plane passing through the source, the slit and the shadow line. The 3D coordinates of the light source (assumed as punctual) can then be obtained by finding the intersection between the three planes, each one related to a slit/sensor pair.

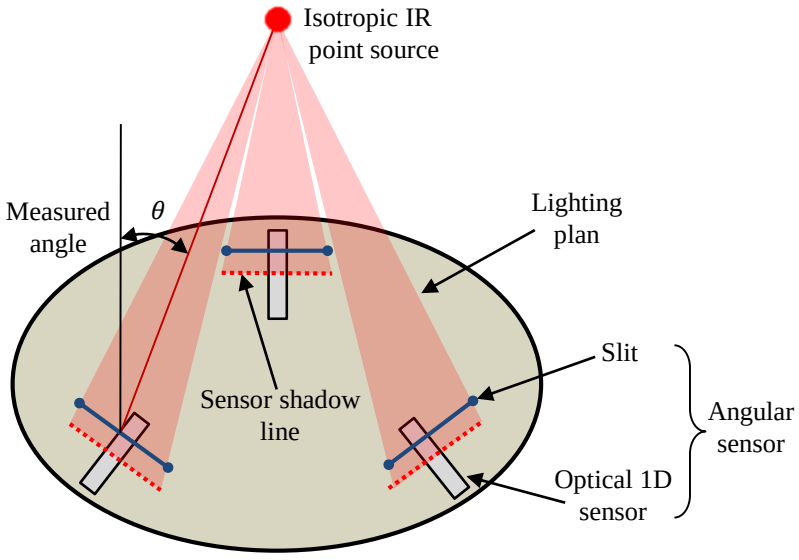

Figure B.2: 3D sensor elements.

In practice, the three angular sensors (slit/sensor pairs) are arranged on a disk of radius R at 120deg ($2\pi/3$) from each other (see Fig.B.3). Their position vector is denoted here $\boldsymbol{P}_i$, the center of the circle being assumed as the origin $(0, 0)$.

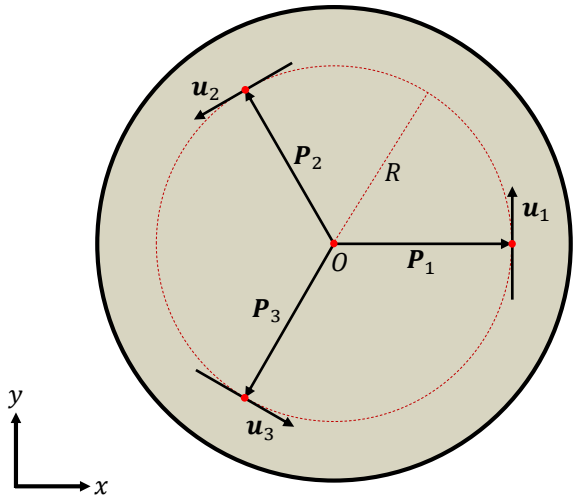

Figure B.3: Placement of the angular sensors on the circular base.

Each angular sensor returns the value of the angle θ_i between the normal to the disk and the corresponding plane. This angle is measured around the vector axis $\boldsymbol{u}_i$ which represents the shadow line shown in figure B.2.

The position vectors of the points $\boldsymbol{P}_i$ are defined as follows:

$$\begin{aligned} \boldsymbol{P}_1 &= R \times [1\ 0\ 0], \\ \boldsymbol{P}_2 &= R \times [\cos(2\pi/3)\ \ \sin(2\pi/3)\ 0] \text{ and} \\ \boldsymbol{P}_3 &= R \times [\cos(4\pi/3)\ \ \sin(4\pi/3)\ 0]. \end{aligned} \tag{B.1}$$

The shadow line axis vectors are defined as:

$$\begin{aligned} \boldsymbol{u}_1 &= [0\ 1\ 0], \\ \boldsymbol{u}_2 &= [\cos(7\pi/6)\ \ \sin(7\pi/6)\ 0] \text{ and} \\ \boldsymbol{u}_3 &= [\cos(11\pi/6)\ \ \sin(11\pi/6)\ 0]. \end{aligned} \tag{B.2}$$

In addition, the vector normal to the disk, and therefore normal to the sensors, is defined as $\boldsymbol{v} = [0\ 0\ 1]$.

Let's denote here $\boldsymbol{v}_i'$ the vectors normal to the searched planes. These vectors form an angle $\gamma_i = \pi/2 - \theta_i$ with the normal to the sensors (see Fig.B.4).

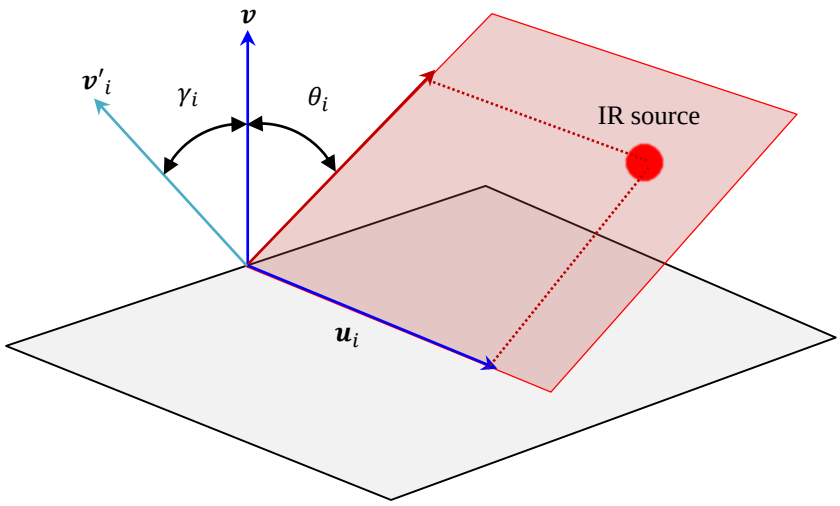

Figure B.4: Representation of vectors in space.

Based on these resources the vectors $\vec{v'}_i$ are defined as follows:

$$\boldsymbol{v}_i' = \boldsymbol{v}\cos(\gamma_i) + (\boldsymbol{u}_i \wedge \boldsymbol{v})\sin(\gamma_i) \tag{B.3}$$

The equations of the planes corresponding to the angular sensors i containing the points P_i are:

$$\begin{aligned} &\mathcal{P}_1 : \sin(\gamma_1)X + \cos(\gamma_1)Z = d_1 \text{ with} \\ &d_1 = R\sin(\gamma_1) \end{aligned} \tag{B.4}$$

$$\begin{aligned} &\mathcal{P}_2 : \sin(7\pi/6)\sin(\gamma_2)X - \cos(7\pi/6)\sin(\gamma_2)Y + \cos(\gamma_2)Z = d_2 \text{ with} \\ &d_2 = R\sin(\gamma_2)[\cos(2\pi/3)\sin(7\pi/6) - \sin(2\pi/3)\cos(7\pi/6)] \end{aligned} \tag{B.5}$$

$$\begin{aligned} &\mathcal{P}_3 : \sin(11\pi/6)\sin(\gamma_3)X - \cos(11\pi/6)\sin(\gamma_3)Y + \cos(\gamma_3)Z = d_3 \text{ with} \\ &d_3 = R\sin(\gamma_3)[\cos(4\pi/3)\sin(11\pi/6) - \sin(4\pi/3)\cos(11\pi/6)] \end{aligned} \tag{B.6}$$

In order to find the position of the IR light source, which is the intersection between these planes, it is required to solve the following equations system:

$$\begin{bmatrix} \sin(\gamma_1) & 0 & \cos(\gamma_1) \\ \sin(7\pi/6)\sin(\gamma_2) & -\cos(7\pi/6)\sin(\gamma_2) & \cos(\gamma_2) \\ \sin(11\pi/6)\sin(\gamma_3) & -\cos(11\pi/6)\sin(\gamma_3) & \cos(\gamma_3) \end{bmatrix} \begin{bmatrix} X \\ Y \\ Z \end{bmatrix} = \begin{bmatrix} d_1 \\ d_2 \\ d_3 \end{bmatrix} \tag{B.7}$$

B.3 6DoF Tracking system

As previously explained, it is possible to obtain the 6DoF pose of a target from the position of at least three points located on it. The pose of the handle can thus be obtained with an arrangement of at least three 3D sensors.

Two solutions can be envisaged therefore:

- It is possible to use 3 independent 3D sensors to compute the Cartesian coordinates of three points laying on the target (see Fig.B.5). This strategy has the advantage of allowing a simultaneous computation of the three points in space, which maximizes the acquisition frequency. It requires however to employ nine slit/sensor pairs, which makes the entire system more cumbersome, which is not desired.

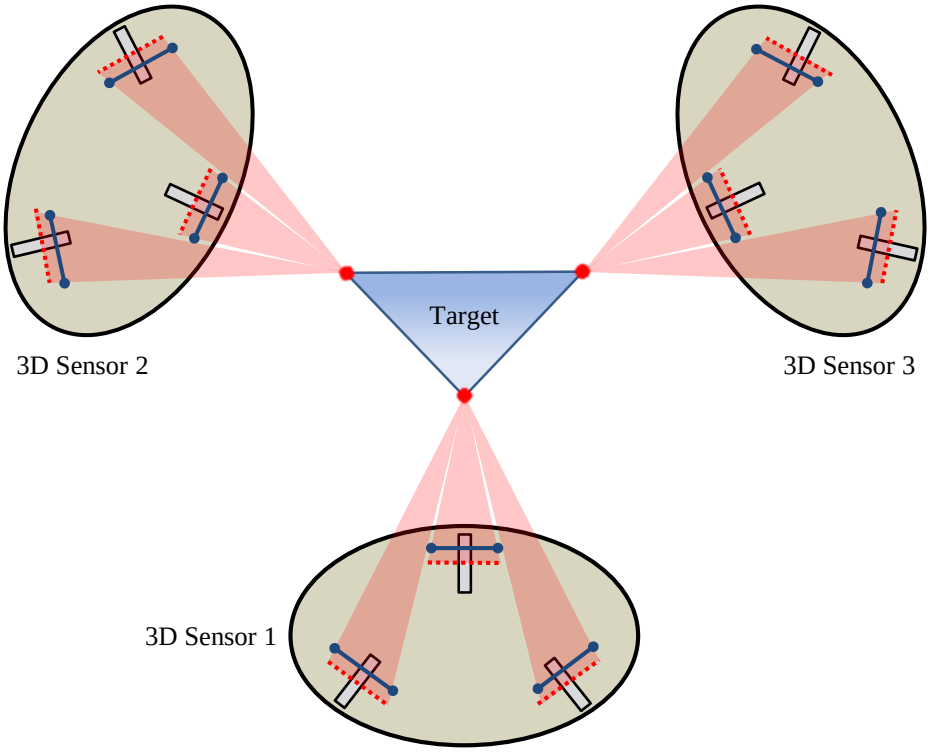

Figure B.5: Set of three 3D sensors maximizing the acquisition frequency.

- Another approach consists in calculating the three targets poses alternatively, i.e. to employ only one 3D sensor that will provide the 3D coordinates of each light source one after another (see Fig.B.6).

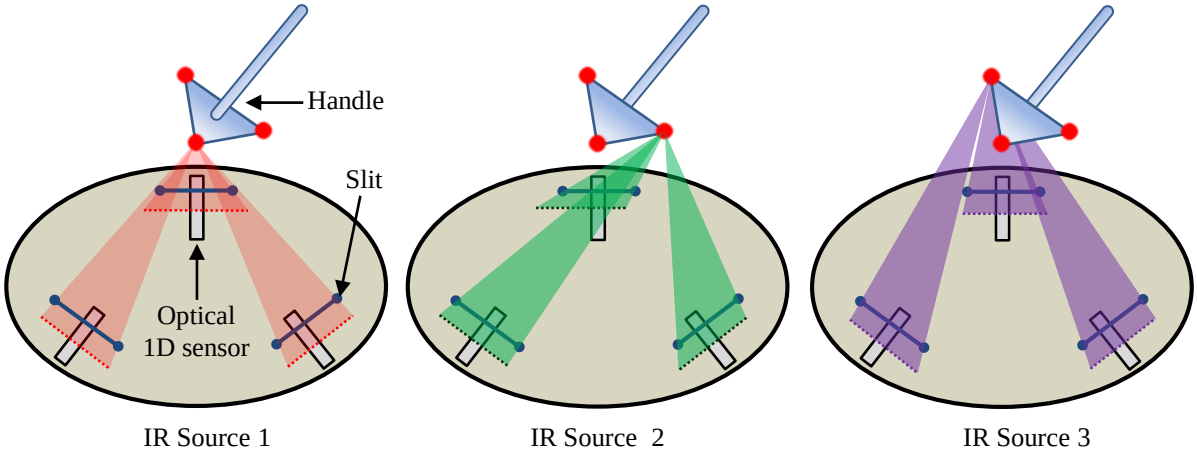

Figure B.6: Alternated employ of a 3D sensor, maximizing the compactness.

This solution is more compact. However, the 6DoF pose of the target can only be calculated upon completion of the computation of the three points. As a consequence, the acquisition frequency is only a third of the previous approach. Still, if the bandwidth of the 3D acquisition system is high enough, the position of three points can be computed sufficiently fast.

The later approach being much more compact, it was employed for the development of the prototype.

Assuming that the three IR light sources attached to the handle form an equilateral triangle whose vertices are denoted A, B and C, the position of the handle can be defined as the center of the triangle located at the point G defined as:

$$\begin{aligned} X_G &= (X_A + X_B + X_C)/3 \\ Y_G &= (Y_A + Y_B + Y_C)/3 \\ Z_G &= (Z_A + Z_B + Z_C)/3 \end{aligned} \tag{B.8}$$

This triangle lies in a plane whose normal vector can be denoted as $\boldsymbol{t}$. The following identities are then verified:

$$\begin{aligned} \boldsymbol{GA} \cdot \boldsymbol{t} &= 0, \\ \boldsymbol{GB} \cdot \boldsymbol{t} &= 0 \text{ and} \\ \boldsymbol{GC} \cdot \boldsymbol{t} &= 0 \end{aligned} \tag{B.9}$$

Thus the components $[t_x, t_y, t_z]$ of vector $\boldsymbol{t}$ can be found by solving the following equations system:

$$\begin{bmatrix} X_A - X_G & Y_A - Y_G & Z_A - Z_G \\ X_B - X_G & Y_B - Y_G & Z_B - Z_G \\ X_C - X_G & Y_C - Y_C & Z_C - Z_G \end{bmatrix} \begin{bmatrix} t_x \\ t_y \\ t_z \end{bmatrix} = \begin{bmatrix} 0 \\ 0 \\ 0 \end{bmatrix} \tag{B.10}$$

Then, once normalized, the vector $\boldsymbol{t}_{norm} = \boldsymbol{t}/|\boldsymbol{t}|$ can be used as one of the orientation vectors of the handle, i.e. as one of the columns of its transformation matrix $\mathbf{T}_{handle}$, for example the last one $\boldsymbol{a}_{handle}$ which is usually associated with the vector normal to the body of reference. It can be completed with the unit vector $\boldsymbol{GA}/|\boldsymbol{GA}|$, which has the advantage of being perpendicular to $\boldsymbol{t}$ and can thus be used as another column of $\mathbf{T}_{handle}$, for example the first one $\boldsymbol{s}_{handle}$. The second column $\boldsymbol{n}_{handle}$ can be easily obtained as the crossproduct between $\boldsymbol{a}_{handle}$ and $\boldsymbol{s}_{handle}$.

The handle transformation matrix is then obtained as:

$$\begin{aligned} \mathbf{T}_{handle} &= \begin{bmatrix} \boldsymbol{s}_{handle} & \boldsymbol{n}_{handle} & \boldsymbol{a}_{handle} & [X_G, Y_G, Z_G]^T \\ 0 & 0 & 0 & 1 \end{bmatrix} \\ &= \begin{bmatrix} \boldsymbol{GA}/|\boldsymbol{GA}| & \boldsymbol{t}/|\boldsymbol{t}| \wedge \boldsymbol{GA}/|\boldsymbol{GA}| & \boldsymbol{t}/|\boldsymbol{t}| & [X_G, Y_G, Z_G]^T \\ 0 & 0 & 0 & 1 \end{bmatrix} \end{aligned} \tag{B.11}$$

B.4 Prototype main characteristics

The developed prototype of the tracking system, whose final design is still confidential and cannot be shown here, employs three linear arrays of photodiodes (ref. MLX75306) mounted on a disk in order to measure the intensity of the light emitted by three IR light sources mounted on a pen-like target and filtered by three masks which are perpendicular to the sensors. The current characteristics of the prototype are the following:

- **System working frequency:** < 300Hz,
- **Precision:** $< 10^{-1}$mm and
- **Workspace:** ± 10mm.